

# POLITECNICO DI TORINO

Master's Degree in Environmental and Land  
Engineering



Master's Degree Thesis

## Sustainable Earth Monitoring: Geospatial Analysis for Assessing Environmental Impacts in Moroccan Phosphate Mining

Supervisor

PROFESSOR PIERO BOCCARDO

Candidate

SEYEDEH FAHIMEH MIRNEZAMI ZIYABARI

Co-Supervisor

SUSANNA GRITA (PHD CANDIDATE)

December 2024





# Summary

This thesis investigates the environmental implications of phosphate mining in Morocco's Khouribga region. Phosphate rock is essential for agriculture, industry, and emerging technologies due to its high phosphorus content and the presence of rare earth elements (REE) and uranium. However, the mining processes release dust and tailings containing potentially toxic metals (PTMs), including cadmium and chromium, which contaminate soil, water, and air, posing risks to ecosystems and human health.

The study leverages remote sensing technologies, EMIT and ECOSTRESS sensors, to evaluate mineral distributions and environmental impacts in Morocco's Khouribga phosphate mining region. EMIT's hyperspectral imaging captures unique spectral features of minerals, while ECOSTRESS, is repurposed here to differentiate critical minerals like quartz and apatite. Together, these sensors facilitate mineral detection in challenging conditions by addressing issues like overlapping or featureless spectral responses in certain SWIR wavelengths, allowing for a more detailed understanding of mineral presence and distribution across the mining landscape.

Using the Modified Soil-Adjusted Vegetation Index (MSAVI) and Albedo indices, a multi-temporal analysis spanning over 40 years reveals significant environmental changes in the Khouribga phosphate mine area. This analysis highlights a marked progression from mild to severe desertification, particularly in regions experiencing intensive mining activities, characterized by a decline in vegetation cover and an increase in barren land.

The study employs NDVI to monitor both seasonal and long-term dynamics in response to mining. These indices indicate recurring patterns of vegetation decline and recovery, emphasizing the environmental pressures exerted by mining operations.

These findings highlight the importance of sustainable mining practices like reforestation and erosion control to reduce environmental degradation and enhance ecosystem resilience. This research provides a framework for using remote sensing to monitor mining impacts, guiding land management strategies that balance resource extraction with sustainability in semi-arid mining regions.



# Acknowledgements

First and foremost, I would like to extend my heartfelt thanks to Professor Piero Boccardo. His steady guidance has been instrumental throughout this journey. With his patience and wisdom, he turned moments of confusion into invaluable opportunities for growth. I am deeply grateful for his unwavering belief in my potential and his supportive presence.

My heartfelt thanks also go to Susanna Grita, whose encouragement and technical expertise were a constant source of reassurance. Her kindness and continuous support helped me get through the most difficult phases of this journey.

I can't thank Mr. Komai enough for always believing in me. His support has meant the world to me, and I truly wouldn't be where I am today without him. He's been a guiding light, and I'm forever grateful for his encouragement and trust.

To my classmate and dear friend Shahabeddin Sahraian, thank you for being there every step of the way. Your support, encouragement, and the many moments of shared understanding reminded me that I was never alone. You made the hard days easier and I am so grateful for your presence.

To my little brother Mohammadhossein, you have been my silent strength. Your love and the simple fact that you were always there meant more to me than I can express. You brought light into the most difficult moments, and I couldn't have done this without you.

To my parents, thank you for always being there for me with your love and support. Your belief in me gave me the courage to keep going, even when things felt impossible. Every step I've taken has been built on the sacrifices you've made and the strength you've given me. I am endlessly grateful to you, and I hope this work reflects how much you mean to me.





# Table of Contents

<b>List of Tables</b>	x
<b>List of Figures</b>	xiv
<b>1 Introduction</b>	1
<b>2 Literature Review</b>	6
2.0.1 Moroccan's phosphate . . . . .	7
2.0.2 Moroccan's climate . . . . .	9
2.0.3 Environmental Impacts of Mining Dust . . . . .	11
2.0.4 Desertification Index . . . . .	12
2.0.5 Using Band Math for Mineral Detection: Integrating EMIT and ECOSTRESS Satellites . . . . .	13
2.0.6 Band Math for Single Feature Extraction . . . . .	14
2.0.7 EMIT Satellite and Mineral Dust Mapping . . . . .	15
2.0.8 ECOSTRESS Satellite and Thermal Infrared Detection . . .	18
2.0.9 Spectral properties of minerals . . . . .	20
2.0.10 Spectral properties of apatite . . . . .	20
2.0.11 Spectral properties of Quartz . . . . .	21
2.0.12 Spectral properties of Dolomite . . . . .	23
2.0.13 Spectral properties of Calcite . . . . .	24
2.0.14 Spectral properties of gypsum . . . . .	25
2.0.15 Spectral properties of Sepiolite . . . . .	27
2.0.16 Spectral properties of Kaolinite . . . . .	28
2.0.17 Spectral properties of Illite . . . . .	29
2.0.18 Spectral properties of Palygorskite . . . . .	30
2.0.19 Spectral properties of Glauconite . . . . .	31
2.0.20 Spectral properties of Iron Oxides (Hematite and Goethite) .	32
<b>3 Methodology</b>	33
3.1 Methodology of Multi-Temporal NDVI Analysis . . . . .	34

3.1.1	NDVI Analysis for year 2023 . . . . .	34
3.1.2	Multi-Temporal NDVI Analysis for Land Cover Classification and Vegetation Dynamics . . . . .	35
3.2	Methodology of Desertification Index . . . . .	36
3.2.1	Indices for Desertification Assessment . . . . .	36
3.2.2	Scatter Plot Analysis: Albedo vs. MSAVI . . . . .	37
3.2.3	Approach to Pixel Classification . . . . .	38
3.3	Methodology for Mineral Detection in Phosphate Mines Using Hy- perspectral Analysis (ECOSTRESS/EMIT) . . . . .	39
3.3.1	Literature Review for Mineral Identification . . . . .	39
3.3.2	Literature Review for Spectral Signatures in SWIR and TIR . . . . .	40
3.3.3	ECOSTRESS Image Processing . . . . .	41
3.3.4	EMIT Image Processing . . . . .	43
3.3.5	Spectral Library Resampling . . . . .	44
3.3.6	Development of Band Math Equations for Mineral Feature Detection . . . . .	44
3.3.7	Raster Color Slice for Mineral Visualization . . . . .	44
3.3.8	Validation . . . . .	45
<b>4</b>	<b>Results and Discussion</b> . . . . .	<b>46</b>
4.1	Results of NDVI Analysis . . . . .	47
4.1.1	NDVI for the year 2023 . . . . .	47
4.1.2	Color-Sliced NDVI (Detailed Vegetation Health Classification) . . . . .	49
4.1.3	Multi temporal Time Series of NDVI for 40-year period . . . . .	51
4.2	Results of Desertification Index . . . . .	58
4.3	Result of Mineral Detection in Phosphate Mines Using EMIT satellite . . . . .	78
4.3.1	Dolomite in EMIT . . . . .	81
4.3.2	Calcite in EMIT . . . . .	85
4.3.3	Gypsum in EMIT . . . . .	89
4.3.4	Sepiolite in EMIT . . . . .	95
4.3.5	Kaolinite in EMIT . . . . .	100
4.3.6	Illite in EMIT . . . . .	105
4.3.7	Palygorskite in EMIT . . . . .	109
4.3.8	Glauconite in EMIT . . . . .	113
4.3.9	Hematite in EMIT . . . . .	117
4.4	Result of Mineral Detection in Phosphate Mines Using ECOSTRESS satellite . . . . .	122
4.4.1	Apatite In ECOSTRESS . . . . .	123
4.4.2	Quartz In ECOSTRESS . . . . .	127
4.4.3	Dolomite In ECOSTRESS . . . . .	131
4.4.4	Calcite In ECOSTRESS . . . . .	134

<b>5 Conclusion</b>	<b>137</b>
5.0.1 Multitemporal and Vegetation Analysis . . . . .	138
5.0.2 Desertification and Land Degradation . . . . .	139
5.0.3 Key Findings of NDVI and Desertification Analysis . . . . .	142
5.0.4 Limitations of NDVI and Desertification Analysis . . . . .	144
5.0.5 Mineral Grouping and Shapefile Layout . . . . .	145
5.0.6 Key Findings of mineral detection . . . . .	154
5.0.7 Limitations of mineral detection . . . . .	155
<b>Bibliography</b>	<b>157</b>



# List of Tables

2.1	EMIT Imaging System: Optical and Spectral Parameters [42]	17
2.2	Spectral and Spatial Characteristics of ECOSTRESS Thermal Infrared Bands [45]	18
3.1	Data sources for NDVI analysis	34
3.2	Data sources for multi-temporal NDVI analysis	35
3.3	Data sources for Desertification Index analysis	36
4.1	Land Cover and Vegetation Area Classification (Km <sup>2</sup> ) from 1985 to 2023	56
4.2	Spectral Features and Wavelength Characteristics of Minerals at Khouribga Phosphate Mine	79
4.3	Spectral Signatures, Reflectance Value Ratios, and Band Ratios of Minerals Using EMIT Data	80
4.4	spectral signature of Dolomite observed in the SWIR range at a wavelength of 2308 nm corresponding to EMIT band 260.	81
4.5	Reflectance Values and Band Math Calculation for Dolomite at Spectral Signature of 2310 nm. This table presents the reflectance values and band math calculations for Dolomite with fine, medium, and coarse grain sizes, calculated using Perkin and Beckman spectral analyzers, with data sourced from the ASTER library embedded in ENVI.	81
4.6	spectral signature of Calcite observed in the SWIR range at a wavelength of 2330 nm corresponding to EMIT band 263.	85
4.7	Reflectance Values and Band Math Calculation for Calcite at Spectral Signature of 2330 nm. This table presents the reflectance values and band math calculations for Calcite with fine, medium, and coarse grain sizes, calculated using Perkin and Beckman spectral analyzers, with data sourced from the ASTER library embedded in ENVI.	85

4.8	spectral signature of Gypsum observed in the SWIR range at a wavelength of 1200 nm, 1660 nm, and 2210 nm corresponding to EMIT band 111, 173, and 247 respectively. . . . .	89
4.9	Reflectance Values and Band Math Calculation for Gypsum at Spectral Signature of 1200 nm. This table presents the reflectance values and band math calculations for Gypsum with fine, medium, and coarse grain sizes, calculated using Perkin and Beckman spectral analyzers, with data sourced from the ASTER library embedded in ENVI. . . . .	89
4.10	Reflectance Values and Band Math Calculation for Gypsum at Spectral Signature of 1660 nm. This table presents the reflectance values and band math calculations for Gypsum with fine, medium, and coarse grain sizes, calculated using Perkin and Beckman spectral analyzers, with data sourced from the ASTER library embedded in ENVI. . . . .	90
4.11	Reflectance Values and Band Math Calculation for Gypsum at Spectral Signature of 2210 nm. This table presents the reflectance values and band math calculations for Gypsum with fine, medium, and coarse grain sizes, calculated using Perkin and Beckman spectral analyzers, with data sourced from the ASTER library embedded in ENVI. . . . .	90
4.12	spectral signature of Sepiolite observed in the SWIR range at a wavelength of 2137 nm and 2330 nm corresponding to EMIT band 237 and 263 respectively. . . . .	95
4.13	Reflectance Values and Band Math Calculation for Sepiolite at Spectral Signature of 2137 nm. This table presents the reflectance values and band math calculations for Sepiolite with fine, medium, and coarse grain sizes, calculated using Perkin and Beckman spectral analyzers, with data sourced from the ASTER library embedded in ENVI. . . . .	95
4.14	Reflectance Values and Band Math Calculation for Sepiolite at Spectral Signature of 2330 nm. This table presents the reflectance values and band math calculations for Sepiolite with fine, medium, and coarse grain sizes, calculated using Perkin and Beckman spectral analyzers, with data sourced from the ASTER library embedded in ENVI. . . . .	96
4.15	spectral signature of Kaolinite observed in the SWIR range at a wavelength of 2204 nm and 2334 nm corresponding to EMIT band 246 and 250 respectively. . . . .	100

4.16	Reflectance Values and Band Math Calculation for Kaolinite at Spectral Signature of 2204 nm. This table presents the reflectance values and band math calculation for Kaolinite with fine grain size, calculated using Perkin and Beckman spectral analyzers, with data sourced from the ASTER library embedded in ENVI. . . . .	100
4.17	Reflectance Values and Band Math Calculation for Kaolinite at Spectral Signature of 2234 nm. This table presents the reflectance values and band math calculations for Kaolinite with fine grain size. The values were calculated using Perkin and Beckman spectral analyzers, with data sourced from the ASTER library embedded in ENVI. . . . .	101
4.18	spectral signature of Illite observed in the SWIR range at a wavelength of 2211 nm corresponding to EMIT band 247. . . . .	105
4.19	Reflectance Values and Band Math Calculation for Illite at Spectral Signature of 2211 nm. This table presents the reflectance values and band math calculations for Illite with fine grain size. The values were calculated using Perkin and Beckman spectral analyzers, with data sourced from the ASTER library embedded in ENVI. . . . .	105
4.20	spectral signature of Palygorskite observed in the SWIR range at a wavelength of 2211 nm corresponding to EMIT band 247. . . . .	109
4.21	Reflectance Values and Band Math Calculation for Palygorskite at Spectral Signature of 2211 nm. This table presents the reflectance values and band math calculations for Palygorskite with fine grain size. The values were calculated using Perkin and Beckman spectral analyzers, with data sourced from the ASTER library embedded in ENVI. . . . .	109
4.22	spectral signature of Glauconite observed in the SWIR range at a wavelength of 2308 nm corresponding to EMIT band 250 respectively.	113
4.23	Reflectance Values and Band Math Calculation for Glauconite at Spectral Signature of 2308 nm. This table presents the reflectance values and band math calculations for Glauconite with fine, medium, and coarse grain sizes. The values were calculated using Perkin and Beckman spectral analyzers, with data sourced from the ASTER library embedded in ENVI. . . . .	113
4.24	spectral signature of Hematite observed in the SWIR range at a wavelength of 551 nm and 860 nm corresponding to EMIT band 24 and band 43. . . . .	117

4.25	Reflectance Values and Band Math Calculation for Hematite at Spectral Signature of 551 nm. This table presents the reflectance values and band math calculations for Hematite with fine, medium, and coarse grain sizes, calculated using Perkin and Beckman spectral analyzers, with data sourced from the ASTER library embedded in ENVI. . . . .	117
4.26	Reflectance Values and Band Math Calculation for Hematite at Spectral Signature of 860 nm. This table presents the reflectance values and band math calculations for Hematite with fine, medium, and coarse grain sizes, calculated using Perkin and Beckman spectral analyzers, with data sourced from the ASTER library embedded in ENVI. . . . .	118
4.27	Spectral Signatures, Reflectance Value Ratio, and Band Ratios of Minerals Using ECOSTRESS Data. . . . .	122
4.28	Reflectance Values and Band Math Calculation for Apatite at a Spectral Signature of 9620 nm. This table presents the reflectance values and band math calculations for Apatite with fine, medium, and coarse grain sizes. The values were calculated using Nicolet spectral analyzers, with data sourced from the ASTER library embedded in ENVI. . . . .	123
4.29	Reflectance Values and Band Math Calculation for Quartz at a Spectral Signature of 9330 nm. This table presents the reflectance values and band math calculations for Quartz with fine, medium, and coarse grain sizes. The values were calculated using Nicolet spectral analyzers, with data sourced from the ASTER library embedded in ENVI. . . . .	127
4.30	Reflectance Values and Band Math Calculation for Dolomite at a Spectral Signature of 11350 nm. This table presents the reflectance values and band math calculations for Dolomite with fine, medium, and coarse grain sizes. The values were calculated using Nicolet spectral analyzers, with data sourced from the ASTER library embedded in ENVI. . . . .	131
4.31	Reflectance Values and Band Math Calculation for Calcite at a Spectral Signature of 11430 nm. This table presents the reflectance values and band math calculations for Calcite with fine, medium, and coarse grain sizes. The values were calculated using Nicolet spectral analyzers, with data sourced from the ASTER library embedded in ENVI. . . . .	134

# List of Figures

1.1	Khouribga mine Map . . . . .	3
2.1	A simplified geological map of Morocco showing the distribution of phosphate deposits across various structural regions of the country (modified based on Piqué, 1994, [20] . . . . .	8
2.2	Photographs of the Moroccan apatite ores: (A) High Atlas Imilchil apatite gems [16] (B) Dakhla Gleibat Lafhouda iron oxide–apatite ore associated with carbonatite complex [24] . . . . .	9
2.3	True absorption band depth and relative absorption band depth . .	14
2.4	Diagram of the EMIT instrument that was installed on the International Space Station on July 24, 2022 [40]. . . . .	16
2.5	Reflectance Spectrum of Fluorapatite ( $\text{Ca}_5(\text{PO}_4)_3\text{F}$ ) from the USGS Spectral Library . . . . .	20
2.6	Reflectance Spectrum of Quartz ( $\text{SiO}_2$ ) from the USGS Spectral Library . . . . .	21
2.7	Reflectance Spectrum of Dolomite ( $\text{CaMg}(\text{CO}_3)_2$ ) from the USGS Spectral Library . . . . .	23
2.8	Reflectance Spectrum of Calcite ( $\text{CaCO}_3$ ) from the USGS Spectral Library . . . . .	24
2.9	Reflectance Spectrum of Gypsum ( $\text{CaSO}_4 \cdot 2\text{H}_2\text{O}$ ) from the USGS Spectral Library . . . . .	25
2.10	Reflectance Spectrum of Sepiolite ( $\text{Mg}_4\text{Si}_4\text{O}_{15}(\text{OH})_2 \cdot \text{H}_2\text{O}$ ) from the USGS Spectral Library . . . . .	27
2.11	Reflectance Spectrum of Kaolinite ( $\text{Al}_2\text{Si}_2\text{O}_5(\text{OH})_4$ ) From the USGS Spectral Library . . . . .	28
2.12	Reflectance Spectrum of Illite ( $(\text{Mg}, \text{Al})_2\text{Si}_4\text{O}_{10}(\text{OH}) \cdot 4\text{H}_2\text{O}$ ) From the USGS Spectral Library . . . . .	29
2.13	Reflectance Spectrum of Palygorskite ( $(\text{Mg}, \text{Al})_2\text{Si}_4\text{O}_{10}(\text{OH}) \cdot 4\text{H}_2\text{O}$ ) From the USGS Spectral Library . . . . .	30
2.14	Reflectance Spectrum of Glauconite( $(\text{K}, \text{Na}(\text{Fe}^{3+}, \text{Al}, \text{Mg})_2(\text{Si}, \text{Al})_4\text{O}_{10}(\text{OH})_2$ ) From the USGS Spectral Library . . . . .	31

2.15	Reflectance Spectrum of Hematite $\text{Fe}_2\text{O}_3$ From the USGS Spectral Library . . . . .	32
2.16	Reflectance Spectrum of Goethite $\text{FeO}(\text{OH})$ From the USGS Spectral Library . . . . .	32
3.1	Albedo-MSAVI spatial features [37] . . . . .	38
4.1	NDVI result for different months of 2023 . . . . .	48
4.2	Classification table for raster color slice of 2023 . . . . .	49
4.3	Color sliced NDVI trend for the year 1985 . . . . .	52
4.4	Color sliced NDVI trend for the year 1991 . . . . .	52
4.5	Color sliced NDVI trend for the year 1999 . . . . .	53
4.6	Color sliced NDVI trend for the year 2004 . . . . .	53
4.7	Color sliced NDVI trend for the year 2009 . . . . .	54
4.8	Color sliced NDVI trend for the year 2014 . . . . .	54
4.9	Color sliced NDVI trend for the year 2017 . . . . .	55
4.10	Color sliced NDVI trend for the year 2024 . . . . .	55
4.11	Trends in Vegetation Classification Areas (1985-2023): Bare Land, Shrub, Cultivation, and Forest . . . . .	56
4.12	The classification of desertification for Khouribga region . . . . .	58
4.13	Desertification Index Assessment of the Khouribga Region: A Landsat-Based Temporal Study (1985–2024) . . . . .	59
4.14	Albedo and MSAVI for Desertification Assessment in the Khouribga Region: 1985 . . . . .	60
4.15	Albedo vs MSAVI scatter plot: 1985 . . . . .	60
4.16	Spatial Distribution and Classification of Desertification: 1985 . . . . .	61
4.17	Albedo and MSAVI for Desertification Assessment in the Khouribga Region: 1991 . . . . .	62
4.18	Albedo vs MSAVI scatter plot: 1991 . . . . .	62
4.19	Spatial Distribution and Classification of Desertification: 1991 . . . . .	63
4.20	Albedo and MSAVI for Desertification Assessment in the Khouribga Region: 1999 . . . . .	64
4.21	Albedo vs MSAVI scatter plot: 1999 . . . . .	64
4.22	Spatial Distribution and Classification of Desertification: 1999 . . . . .	65
4.23	Albedo and MSAVI for Desertification Assessment in the Khouribga Region: 2005 . . . . .	66
4.24	Albedo vs MSAVI scatter plot: 2005 . . . . .	66
4.25	Spatial Distribution and Classification of Desertification: 2005 . . . . .	67
4.26	Albedo and MSAVI for Desertification Assessment in the Khouribga Region: 2009 . . . . .	68
4.27	Albedo vs MSAVI scatter plot: 2009 . . . . .	68

4.28	Spatial Distribution and Classification of Desertification: 2009 . . .	69
4.29	Albedo and MSAVI for Desertification Assessment in the Khouribga Region: 2014 . . . . .	70
4.30	Albedo vs MSAVI scatter plot: 2014 . . . . .	70
4.31	Spatial Distribution and Classification of Desertification: 2014 . . .	71
4.32	Albedo and MSAVI for Desertification Assessment in the Khouribga Region: 2017 . . . . .	72
4.33	Albedo vs MSAVI scatter plot: 2017 . . . . .	72
4.34	Spatial Distribution and Classification of Desertification: 2017 . . .	73
4.35	Albedo and MSAVI for Desertification Assessment in the Khouribga Region: 2023 . . . . .	74
4.36	Albedo vs MSAVI scatter plot: 2023 . . . . .	74
4.37	Spatial Distribution and Classification of Desertification: 2023 . . .	75
4.38	Albedo and MSAVI for Desertification Assessment in the Khouribga Region: 2024 . . . . .	76
4.39	Albedo vs MSAVI scatter plot: 2024 . . . . .	76
4.40	Spatial Distribution and Classification of Desertification: 2024 . . .	77
4.41	Resampled Spectral Reflectance of Dolomite for fine, medium, and coarse grain size, adjusted to the EMIT sensor resolution. . . . .	82
4.42	EMIT image of dolomite after application of relative band math at 2308 nm wavelength. . . . .	82
4.43	results of relative band math after applying raster color slice: The red color represents the range between 2.09 to 2.136, corresponding to the presence of the fine grain dolomite. . . . .	83
4.44	A comparison of the selected dolomite spectra from the ENVI spectral library (in red) with spectral profiles collected from multiple locations within the study area (in black) . . . . .	84
4.45	Resampled Spectral Reflectance of Calcite for fine, medium, and coarse grain size, adjusted to the EMIT sensor resolution. . . . .	86
4.46	EMIT image of calcite after application of relative band math at 2330 nm wavelength. . . . .	86
4.47	results of relative band math after applying raster color slice: The red color represents the range between 2.220 to 2.270, corresponding to the presence of the fine grain calcite. . . . .	87
4.48	A comparison of the selected calcite spectra from the ENVI spectral library (in red) with spectral profiles collected from multiple locations within the study area (in black) . . . . .	88
4.49	Resampled Spectral Reflectance of Gypsum for fine, medium, and coarse grain size, adjusted to the EMIT sensor resolution. . . . .	90
4.50	EMIT image of gypsum after application of relative band math at 1200 nm wavelength. . . . .	91

4.51	results of relative band math after applying raster color slice: The red color represents the range between 2.05 to 2.09 and 2.24 to 2.3 corresponding to the presence of the fine grain gypsum. . . . .	91
4.52	EMIT image of gypsum after application of relative band math at 1660 nm wavelength. . . . .	92
4.53	results of relative band math after applying raster color slice: The red color represents the range between 0.540 to 0.8, corresponding to the presence of the fine grain gypsum. . . . .	92
4.54	EMIT image of gypsum after application of relative band math at 2210 nm wavelength. . . . .	93
4.55	results of relative band math after applying raster color slice: The red color represents the range between 2.25 to 2.35, corresponding to the presence of the fine grain gypsum. . . . .	93
4.56	A comparison of the selected gypsum spectra from the ENVI spectral library (in red) with spectral profiles collected from multiple locations within the study area (in black) indicates notable similarities in 2210 nm. . . . .	94
4.57	Resampled Spectral Reflectance of Sepiolite for fine, medium, and coarse grain size, adjusted to the EMIT sensor resolution. . . . .	96
4.58	EMIT image of Sepiolite after application of relative band math at 2137 nm wavelength. . . . .	97
4.59	results of relative band math after applying raster color slice: The red color represents the range between 0.55 to 0.7, corresponding to the presence of the fine grain sepiolite. . . . .	97
4.60	EMIT image of sepiolite after application of relative band math at 2330 nm wavelength. . . . .	98
4.61	results of relative band math after applying raster color slice: The red color represents the range between 1.7 to 1.8, corresponding to the presence of the medium and coarse grain sepiolite. . . . .	98
4.62	A comparison of the selected sepiolite spectra from the ENVI spectral library (in red) with spectral profiles collected from multiple locations within the study area (in black) indicates weak similarities in 2137 nm and good similarities in 2330 nm. . . . .	99
4.63	Resampled Spectral Reflectance of Kaolinite for fine, medium, and coarse grain size, adjusted to the EMIT sensor resolution. . . . .	101
4.64	EMIT image of Kaolinite after application of relative band math at 2204 nm wavelength. . . . .	102
4.65	results of relative band math after applying raster color slice: The red color represents the range between 2.34 to 2.78, corresponding to the presence of the fine grain Kaolinite. . . . .	102



4.66	EMIT image of Kaolinite after application of relative band math at 2234 nm wavelength. . . . .	103
4.67	results of relative band math after applying raster color slice: The red color represents the range between 0.54 to 0.65, corresponding to the presence of the fine grain Kaolinite. . . . .	103
4.68	A comparison of the selected kaolinite spectra from the ENVI spectral library (in red) with spectral profiles collected from multiple locations within the study area (in black) indicates moderate similarities in 2200 nm and 2234 nm. . . . .	104
4.69	Resampled Spectral Reflectance of Illite for fine grain size, adjusted to the EMIT sensor resolution. . . . .	106
4.70	EMIT image of Illite after application of relative band math at 2211 nm wavelength. . . . .	106
4.71	results of relative band math after applying raster color slice: The red color represents the range between 2.1 to 2.25, corresponding to the presence of the fine grain Illite. . . . .	107
4.72	A comparison of the selected illite spectra from the ENVI spectral library (in red) with spectral profiles collected from multiple locations within the study area (in black) indicates notable similarities in 2211 nm. . . . .	108
4.73	Resampled Spectral Reflectance of Palygorskite for fine grain size, adjusted to the EMIT sensor resolution. . . . .	110
4.74	EMIT image of Palygorskite after application of relative band math at 2211 nm wavelength. . . . .	110
4.75	results of relative band math after applying raster color slice: The red color represents the range between 2.1 to 2.2, corresponding to the presence of the fine grain Palygorskite. . . . .	111
4.76	A comparison of the selected Palygorskite spectra from the ENVI spectral library (in red) with spectral profiles collected from multiple locations within the study area (in black) indicates notable similarities in 2211 nm. . . . .	112
4.77	Resampled Spectral Reflectance of glauconite for fine, grain size, adjusted to the EMIT sensor resolution. . . . .	114
4.78	EMIT image of Glauconite after application of relative band math at 2308 nm wavelength. . . . .	114
4.79	results of relative band math after applying raster color slice: The red color represents the range between 2.05 to 2.25, corresponding to the presence of the fine grain glauconite. . . . .	115

4.80	A comparison of the selected Glauconite spectra from the ENVI spectral library (in red) with spectral profiles collected from multiple locations within the study area (in black) indicates notable similarities in 2203 nm. . . . .	116
4.81	Resampled Spectral Reflectance of Hematite for fine, medium, and coarse grain size, adjusted to the EMIT sensor resolution. . . . .	118
4.82	EMIT image of Hematite after application of relative band math at 551 nm wavelength. . . . .	119
4.83	results of relative band math after applying raster color slice: The red color represents the range between 2.7 to 3.6, corresponding to the presence of the fine grain Hematite. . . . .	119
4.84	EMIT image of Hematite after application of relative band math at 860 nm wavelength. . . . .	120
4.85	results of relative band math after applying raster color slice: The red color represents the range between 2.4 to 2.5, corresponding to the presence of the fine grain Hematite. . . . .	120
4.86	A comparison of the selected hematite spectra from the ENVI spectral library (in red) with spectral profiles collected from multiple locations within the study area (in black) indicates notable similarities in 551 nm and 860 nm. . . . .	121
4.87	(a) Spectral Reflectance and (b) Resampled Spectral Reflectance of Apatite for fine, medium, and coarse grain size, adjusted to the ECOSTRESS sensor resolution. . . . .	124
4.88	Spectral Reflectance and Resampled Spectral Reflectance of Apatite for fine, medium, and coarse grain size in one frame. . . . .	124
4.89	ECOSTRESS image of Apatite after application of relative band math at 9160 nm wavelength. . . . .	125
4.90	results of relative band math after applying raster color slice: The red color represents the range between 1.3 to 1.6, corresponding to the presence of the fine grain Apatite. . . . .	125
4.91	A comparison of the selected apatite spectra from the ENVI spectral library (in red) with spectral profiles collected from multiple locations within the study area (in black). . . . .	126
4.92	(a) Spectral Reflectance and (b) Resampled Spectral Reflectance of Quartz for fine, medium, and coarse grain size, adjusted to the ECOSTRESS sensor resolution. . . . .	128
4.93	Spectral Reflectance and Resampled Spectral Reflectance of Quartz for fine, medium, and coarse grain size in one frame. . . . .	128
4.94	ECOSTRESS image of Quartz after application of relative band math at 9330 nm wavelength. . . . .	129

4.95	results of relative band math after applying raster color slice: The red color represents the range between 0.03 to 0.25, corresponding to the presence of the fine grain Quartz. . . . .	129
4.96	A comparison of the selected quartz spectra from the ENVI spectral library (in red) with spectral profiles collected from multiple locations within the study area (in black) indicates notable similarities in 9330 nm. . . . .	130
4.97	(a) Spectral Reflectance and (b) Resampled Spectral Reflectance of Dolomite for fine, medium, and coarse grain size, adjusted to the ECOSTRESS sensor resolution. . . . .	132
4.98	ECOSTRESS image of Dolomite after application of relative band math at 11350 nm wavelength. . . . .	132
4.99	ECOSTRESS image of Dolomite after application of relative band math at 11430 nm wavelength. . . . .	133
4.100	results of relative band math after applying raster color slice: The red color represents the range between 3.4 - 3.78 corresponding to the presence of the fine grain Calcite. . . . .	133
4.101	(a) Spectral Reflectance and (b) Resampled Spectral Reflectance of Calcite for fine, medium, and coarse grain size, adjusted to the ECOSTRESS sensor resolution. . . . .	135
4.102	ECOSTRESS image of Calcite after application of relative band math at 11430 nm wavelength. . . . .	135
4.103	ECOSTRESS image of Calcite after application of relative band math at 11430 nm wavelength . . . . .	136
4.104	results of relative band math after applying raster color slice: The red color represents the range between 0.1 to 0.3 and 0.75 to 0.95 corresponding to the presence of the fine grain Calcite. . . . .	136
5.1	Multi-temporal NDVI of the Khouribga mine region from 1985 to 2023, showing vegetation and land cover changes . . . . .	139
5.2	multi-temporal desertification trend of the Khouribga mine region over the past four decades . . . . .	140
5.3	Scatter plot of multi-temporal desertification trend of Khouribga mine	141
5.4	Calcite (in red) and dolomite (in blue) shapefile layout in EMIT. . .	146
5.5	Shapefile (in green) represents the presence of Calcite in ECOSTRESS. . . . .	147
5.6	Shapefile (in green) represents the presence of dolomite in ECOSTRESS.	147
5.7	sepiolite (in blue), kaolinite dolomite (in purple), illite (in red) and palygorskite (in green) shapefile layout in EMIT. . . . .	149
5.8	Shapefile (in red) represents the presence of hematite in EMIT. . .	150

5.9	Stability of hematite, goethite, ferric hydroxide, and hydroxyl salts depending on temperature and pH . . . . .	151
5.10	Shapefile (in red) represents the presence of gypsum in EMIT . . .	152
5.11	Apatite (in green) and quartz (in red) in ECOSTRESS . . . . .	153
5.12	The capability of various satellites to detect different minerals. . . .	154



# Chapter 1

## Introduction

Phosphate rocks are the most significant phosphorus-bearing raw material in the fertilizer industry. They serve as the primary source of phosphorus (P), an essential element for agriculture and various industrial applications, including animal feed, cosmetics, and electronic [1]. Phosphate rocks are also likely to contain significant quantities of rare earth elements (REE), positioning them as a potential REE resource due to their widespread production globally [2]. Similarly, phosphate rocks are considered an unconventional source of uranium, particularly in certain deposits where uranium concentrations can be high [2].

One of the biggest challenges humanity faces is ensuring a stable phosphate supply. Proactive strategies are needed to address this, such as recycling waste from phosphate mining, processing, and exploring new potential phosphate ore resources [3]. Marine-origin sedimentary phosphorites are currently the main raw material for the phosphate industry, making up about 90% of global phosphate rock production [4]. Approximately 10% of phosphate rocks come from igneous sources, while the remainder is sourced from residual and guano-type sedimentary deposits. Both igneous and sedimentary rock sources have distinct advantages and drawbacks related to their chemical composition, geographic distribution, and feasibility for exploitation [1].

Morocco, situated in northwestern Africa, is a key player in global phosphate production, holding over 70% of the world's known phosphate reserves. The sedimentary phosphate deposits here, spanning the upper Cretaceous to lower Eocene period, are among the largest globally, with major deposits found in basins like Ouled Abdoun, Ganntour, Meskala, and Oued Ed-Dahab [5]. Given Morocco's substantial reserve-to-production ratio, the country is positioned as a long-term global phosphate supplier, with reserves estimated to last over 1,300 years at current production rates [6]. Morocco's phosphate production has seen a 43% increase over the past decade, underscoring its growing role in the international phosphate market [3].

Morocco's climate, influenced by the Atlantic Ocean, the Mediterranean Sea, and the Sahara Desert, varies from sub-humid and semi-arid conditions in the north to arid and desert-like conditions in the south [7]. As one of the most climate-vulnerable regions in North Africa and the Mediterranean, Morocco experiences fluctuating precipitation patterns, significantly impacted by mid-latitude storms and the North Atlantic Oscillation (NAO), which drive seasonal droughts and occasional extreme rainfall events [8] [9]. Climate models project that Morocco, like the broader Mediterranean region, will face increased temperatures and a decrease in annual precipitation in the future, trends that amplify the risk of recurrent droughts and create challenges for water resources and agriculture [10]. These climate vulnerabilities, coupled with intensive land use from industries such as phosphate mining, intensify the environmental challenges facing Morocco.

Phosphate mining, particularly in Morocco's Khouribga region, produces dust and

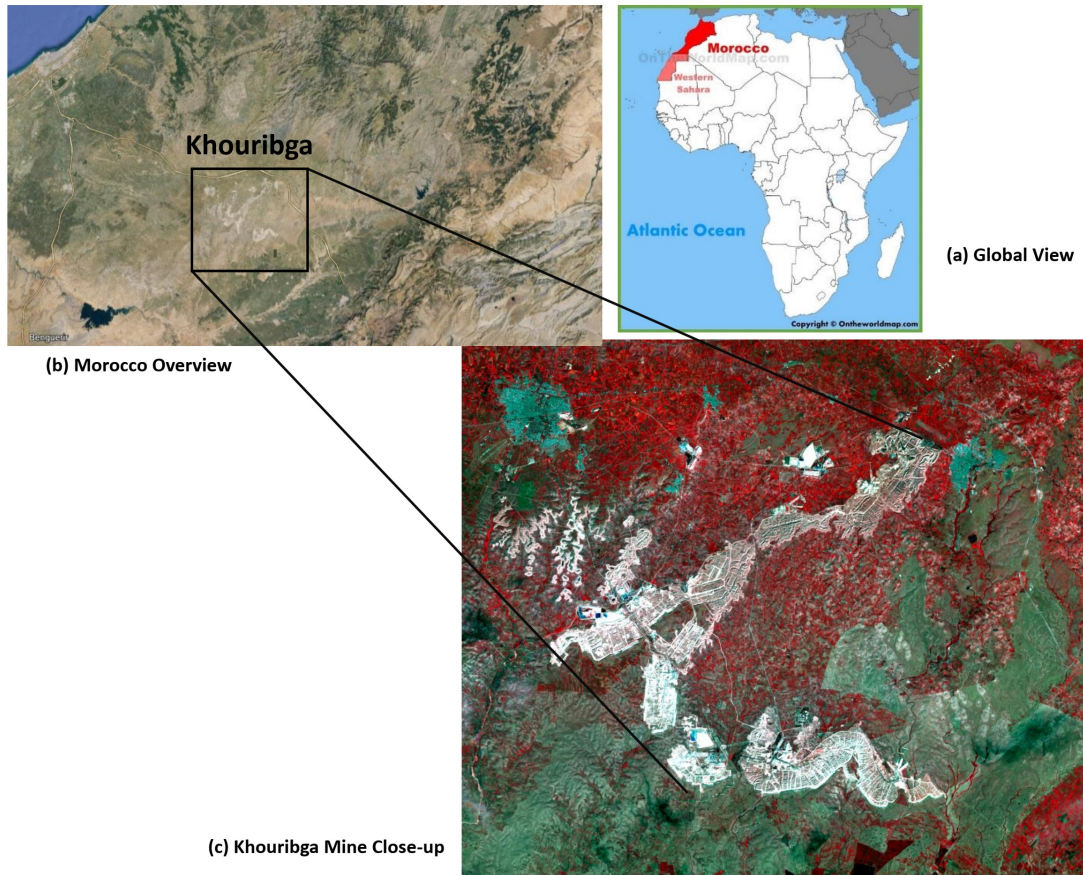


**Figure 1.1:** Khouribga mine Map

tailings laden with potentially toxic metals (PTMs) like cadmium, chromium, and zinc, which pose significant risks to soil, water, and air quality [11]. These dust emissions not only impact the health of nearby communities through inhalation and ingestion but also lead to long-term ecological degradation by contaminating soils, polluting groundwater, and disrupting local flora and fauna. Effective management of mining waste is crucial to mitigate these environmental risks and safeguard human health, as exposure to PTMs from mine tailings may lead to both carcinogenic and non-carcinogenic health effects [12] [13].

Phosphate mining operations impact the environment significantly, particularly in regions like Morocco's Khouribga Basin. Mining processes generate extensive dust emissions, containing potentially toxic metals (PTMs) such as cadmium, zinc, and chromium, which can harm local ecosystems and public health. This dust, generated through mining processes like excavation, blasting, and beneficiation, can be carried through air and water, impacting nearby communities and agriculture. In Khouribga, contamination from PTMs has been detected in groundwater, raising



health concerns for communities dependent on these water sources for drinking and irrigation [11] [14]. Mining activities also degrade the soil, reducing its fertility and increasing erosion rates, further exacerbating land degradation in affected regions. These environmental impacts highlight the need for advanced monitoring and mitigation strategies to reduce PTM exposure and to manage land degradation sustainably.

Geospatial tools and remote sensing techniques have proven effective in monitoring environmental changes associated with mining activities. By utilizing indices such as the Normalized Difference Vegetation Index (NDVI) and the Modified Soil-Adjusted Vegetation Index (MSAVI) alongside surface albedo measurements, remote sensing enables comprehensive analysis of vegetation loss and soil degradation. These indices are valuable for assessing desertification, especially in semi-arid regions where climate stress and land use accelerate degradation. This thesis employs these geospatial tools to evaluate the environmental impacts of phosphate mining, focusing on multitemporal and desertification analyses. Through remote sensing, a systematic approach to assessing vegetation dynamics and soil health is developed, offering insights into the environmental changes driven by both mining activities and regional climate patterns. Such an approach provides a robust framework for sustainable mining management, supporting environmental conservation in Morocco's phosphate-rich regions.

Recent advancements in spaceborne imaging, with satellites like the Earth Surface Mineral Dust Source Investigation (EMIT) and the ECOSystem Spaceborne Thermal Radiometer Experiment on Space Station (ECOSTRESS), have significantly enhanced our capabilities for mineral and environmental analysis. EMIT, operating in visible to shortwave infrared (SWIR) wavelengths, is adept at identifying minerals through their unique spectral absorption features. In contrast, ECOSTRESS, capturing thermal infrared (TIR) wavelengths, provides detailed thermal data, supporting analyses of surface temperature and water stress. Together, EMIT and ECOSTRESS offer a synergistic approach to detecting mineral dust sources and emissions, especially in remote or arid regions where ground-based monitoring is limited. These advanced platforms facilitate comprehensive mineral and environmental assessments, particularly in mining-intensive landscapes like those in Morocco.

This thesis employs Band Math for Single Feature Extraction, a method designed to detect specific spectral features that identify unique mineral signatures. By isolating characteristic absorption bands through calculated band ratios, this technique facilitates precise and efficient mineral detection. Initially developed for airborne sensors, Band Math has been adapted for spaceborne platforms such as EMIT and ECOSTRESS, enabling large-scale mineral mapping without the need for extensive fieldwork. The integration of EMIT's spectral data with ECOSTRESS's high-resolution thermal imagery provides an innovative framework for mineral

distribution analysis.

The primary objective of this research is to detect and map mineral distributions in Morocco's phosphate mining regions using advanced remote sensing techniques. By establishing a remote, replicable methodology, this approach highlights the potential for identifying spectral anomalies and regions of interest for further investigation, complementing and supporting field surveys. While remote sensing provides valuable surface-level insights, fieldwork remains essential in geology for comprehensive exploration and validation. The findings aim to simplify the preliminary stages of mineral exploration, optimize resource management, and broaden the applications of remote sensing technologies.

In addition to mineral detection, this thesis assesses the environmental impacts of mining-related land degradation, with a specific focus on desertification. Using multitemporal analyses of vegetation indices, such as NDVI and MSAVI, the study evaluates changes in vegetation health and land cover over time. By combining these indices with mineral mapping, the research highlights the interplay between resource extraction, vegetation decline, and soil degradation. This approach offers valuable insights into the environmental consequences of mining and supports the development of strategies to mitigate its impact on arid and semi-arid ecosystems. In the broader context of sustainable mining practices, this thesis forms part of an extended research initiative. While this study focuses on environmental impacts in the Khouribga phosphate region, it complements parallel work by a colleague on Morocco's Youssoufia phosphate mine. Together, these studies aim to build a comprehensive assessment of Morocco's phosphate mining sector, offering a nuanced understanding of mineral-associated environmental challenges across different regional contexts. Thus, this research contributes not only to the scientific understanding of phosphate mining's environmental footprint but also to the overarching goal of sustainable resource management in climate-sensitive areas.

## Chapter 2

# Literature Review

## 2.0.1 Moroccan's phosphate

Moroccan sedimentary phosphate deposits are globally notable due to their vast extent and abundant resources, comprising over 70% of the world's phosphate reserves. This country is located in the northwestern corner of the African continent and stretches from 21°N to 37°N. It borders the Mediterranean Sea to the north and the Atlantic Ocean to the west. Moroccan's phosphate rocks are predominantly from the upper Cretaceous to lower Eocene stratigraphic period. They are found across multiple sedimentary basins, varying in surface area and phosphate content. [5]

Phosphorus in phosphate rocks is typically found combined with other elements as phosphate minerals, with the apatite group being the most widespread type [15]. In addition to sedimentary phosphates, Morocco contains several carbonatite and carbonatite-alkaline complexes that may harbor potential resources of igneous phosphate and critical metals [16]. Marine sedimentary phosphates contain various phosphate particles, called "phosclates," which include skeletal grains (such as bioclasts, shark teeth, and bone fragments) and non-skeletal grains (like peloids, coprolites, and aggregates). These particles are mixed with non-phosphate materials like quartz, calcite, dolomite, and clay minerals [17].

Non-apatitic phosphate minerals are typically secondary ferrous and aluminous minerals formed by the alteration of primary phosphates. The main phosphate mineral is carbonate fluorapatite (CFA), previously known as francolite [18].

In Morocco, the most significant sedimentary phosphate deposits are primarily located in four basins: Ouled Abdoun, Ganntour, Meskala, and Oued Ed-Dahab. Smaller, less economically significant deposits are also found in areas like Middle Atlas, Beni Mellal, High Atlas, Marrakesh High Atlas northern basins, Souss, and Ouarzazate basins [5]. These deposits are part of the Mediterranean (Tethyan) phosphogenic province and were formed between the Upper Cretaceous and Paleogene periods, specifically from the Maastrichtian to the Ypresian [19].

Data on Moroccan sedimentary phosphates indicate that, like other regional phosphate rocks, they primarily consist of francolite and associated gangue minerals such as calcite, dolomite, quartz, gypsum, and various clay minerals (smectite, Illite, Palygorskite, sepiolite, kaolinite). Accessory minerals include glauconite, sulfides (mainly pyrite), iron oxides (hematite and goethite), and feldspar [21]. Phosphate reserves are dynamic and can change over time due to factors such as production rates, the discovery of new reserves, and the reclassification of resources and reserves. The most comprehensive study on phosphate reserves and resources is by Steven Van Kauwenbergh in 2010 [22], which compiles various previous studies and indicates that reserve estimates range from 15,000 MMT to over 1,000,000 MMT, while resource estimates range from approximately 91,000 MMT to over 1,000,000 MMT. Currently, the USGS is the only major geological survey providing

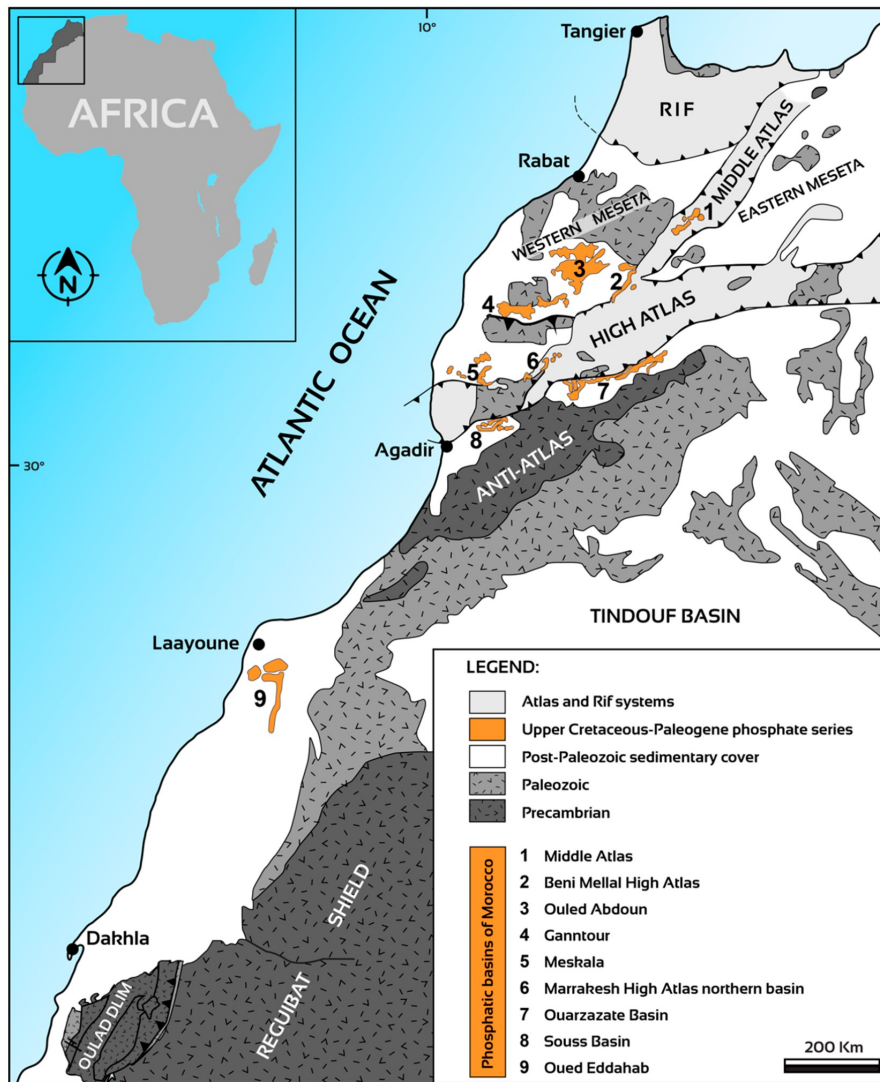


**Figure 2.1:** A simplified geological map of Morocco showing the distribution of phosphate deposits across various structural regions of the country (modified based on Piqué, 1994, [20])

up-to-date global phosphate rock reserves data, reporting that global resources exceed 300,000 billion tons and reserves are about 71,000 MMT [23]. Morocco has the largest phosphate reserves, holding 70-75% (around 50,000 MMT) of the world's known phosphate reserves [23].

Despite the increase in phosphate production since 2010, estimated reserves have remained unchanged, highlighting the need to reevaluate Morocco's phosphate resources and reserves given their global significance.

Morocco, with the largest reserves, is expected to see its share increase due to a high reserve-to-production ratio. China leads global phosphate production with 40%, Morocco follows with 17%, and the USA contributes 11%. China surpassed the USA in 2006, and Morocco overtook the USA in 2017 [6]. Morocco's reserve-to-production ratio is over 1300 years, much higher than other countries, but this does not account for potential changes in reserve classification. Morocco's phosphate production has risen by 43% from 25,000 MT in 2010 to 37,000 MT in 2020 [3].

graphicx

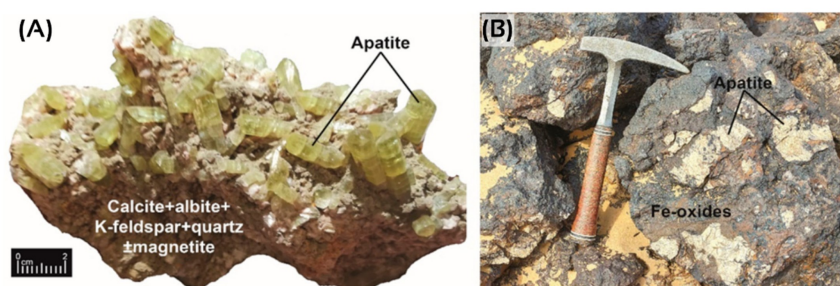


**Figure 2.2:** Photographs of the Moroccan apatite ores: (A) High Atlas Imilchil apatite gems [16] (B) Dakhla Gleibat Lafhouda iron oxide-apatite ore associated with carbonatite complex [24]

## 2.0.2 Moroccan's climate

The Moroccan climate is characterized by the influences of the Atlantic, the Mediterranean, and the Sahara [7]. Studies at global, regional, and national levels have shown that Morocco is one of the most climatically vulnerable areas in the Mediterranean and North Africa [8].

this results in a sub-humid to semi-arid climate in the north and an arid to desert-like climate in the south. Storms in the mid-latitudes have a significant impact on precipitation, especially in the wettest regions [7]. The large-scale North Atlantic circulation (extratropical circulation modes) can lead to normal, dry, or wet conditions in winter, depending on the specific weather regime [9].

In particular, weather patterns similar to the positive (negative) phase of the North Atlantic Oscillation (NAO) are generally associated with dry (humid) conditions. Very humid conditions in the northeastern part of the country can be caused by blockages in the Mediterranean pressure systems (e.g. El Hoceima in November 2003). Tropical storms moving up the Atlantic coast have often resulted in extreme precipitation events (e.g. Tantan in August 2003, Casablanca in November 2010),

which is consistent with previous studies on tropical-extra-tropical interactions in the region [25].

Driouech et al. [9] observed a trend towards warmer and drier conditions in numerous regions, based on data from 17 meteorological stations from the period 1961 to 2008.

Donat et al. [26] identified positive trends in mean temperature and warm extremes, along with decreasing trends in cold events, using data from 10 meteorological stations. Filahi et al. [27] noted decreasing precipitation trends, particularly in the country's interior and at stations with long-term records (approximately four decades). While these studies indicate an increase in persistent drought [28]. Changes in extreme precipitation events were found to be less [27].

Regarding future changes, most climate model projections concur that the Moroccan climate will align with trends observed across the entire Mediterranean region. These projections indicate an increase in both mean and high temperatures, along with a decrease in total annual precipitation [10].

Negative climate effects have already been observed. droughts are recurrent and becoming more frequent and, perhaps, more severe. For example, the dry conditions during 1982–1983 and 1994–1995, two of the most widespread droughts to affect the country, resulted in a significant drop in water reserves. This impacted not only irrigated agriculture but also drinking water supplies and electricity production [29]. Official drought declarations, triggering government emergency relief, were made in 1992–95, 1998–2001, 2005, 2007, and 2015–2016 [29]. The most recent drought, from November 2015 to spring 2016, caused a three percent decline in economic growth due to decreased agricultural output, particularly in cereal production. Mitigation actions, including crop insurance, were limited. The citrus and olive value chains also saw output declines and increased sensitivity to water shortages during the 2015–16 drought [29].

The Moroccan climate's vulnerability to changing weather patterns, coupled with the environmental challenges posed by phosphate mining, highlights the complex interaction between natural and human-induced factors. Morocco's semi-arid to arid conditions, intensified by the North Atlantic Oscillation (NAO) and frequent droughts, significantly impact water resources and agricultural output, as seen during events like the 2015-2016 drought. While climate shifts pose their challenges, human activities—such as phosphate mining—introduce additional environmental pressures, notably in the form of dust pollution and resource depletion. So, a literature review is dedicated to the environmental impact of dust on the area.

### 2.0.3 Environmental Impacts of Mining Dust

Dust generation in phosphate mining arises from activities like vehicle traffic, blasting, excavation, and beneficiation processes like crushing and drying [30]. Sediments and tailings in phosphate mining areas often have higher concentrations of PTMs, with fine particles accumulating more harmful metals, such as Cd, Zn, and Cr [11]. The environmental impact of dust generation in industries like mining is increasingly studied due to stricter regulations on emissions, air quality, and pollution. Public awareness has also grown regarding the environmental consequences of such activities [30]

In recent decades, the mining industry's legacy of environmental damage has heightened public concern over the industry's ability to manage its environmental footprint. As mining operations expand, the demand for improved management of environmental impacts grows. Governments have responded by imposing stricter regulations to safeguard ecosystems and communities living near mining sites [30]. Phosphate mining, in particular, presents significant environmental challenges. The extraction process can increase concentrations of toxic metals and radioactive elements in water bodies and the surrounding environment. The following major impacts are often observed:

**1. Water Contamination:** Phosphate mining can lead to large quantities of dust and powder being transported by water, contaminating nearby aquatic ecosystems. Acid mine drainage can also lead to groundwater contamination following rainfall [31].

In regions like Morocco, groundwater is a vital resource, especially in rural areas. However, the Khouribga phosphate mining region threatens groundwater quality. Studies on 90 well samples from the region indicate that while most samples meet standards for pH, conductivity, and various minerals, nitrate levels exceed safe limits for consumption, posing a significant health risk for infants and pregnant women [14].

The groundwater in Khouribga exhibits chemical heterogeneity, with dominant facies being calcium sulfate-magnesium and calcium bicarbonate-magnesium. These findings, supported by principal component analysis, highlight the ongoing need for groundwater preservation and management in phosphate mining areas to safeguard public health [14].

**2. Soil Contamination:** The disposal of mine tailings often leads to the accumulation of hazardous trace metals like uranium (U), cadmium (Cd), and chromium (Cr) in soils, which can pose risks to both the environment and human health [32].

**3. Air Pollution:** Mining operations release dust and emissions from blasting, crushing, and ore transportation, negatively affecting air quality. Winds can carry



this dust to nearby communities, impacting health and polluting homes and farmland [33].

**4. Soil degradation:** Phosphate mine wastes cover large areas, making soil susceptible to erosion and metal contamination and reducing fertility [34].

**5. Landscape degradation:** The waste rock piles and tailing ponds associated with phosphate mining alter the landscape and degrade natural aesthetics [35].

**6. Fauna and flora impact:** Phosphate extraction destroys habitats, harming local ecosystems and species. Pollution from mining can also weaken plant and animal health in affected areas [36].

**7. Health and Environmental Risks of PTMs:** The pollution generated by phosphate mining poses significant health risks, particularly due to potentially toxic metals (PTMs) like Cr, Ni, As, and Cd. These metals can cause both carcinogenic and non-carcinogenic effects, especially when exposure exceeds acceptable thresholds [12].

These metals do not degrade easily and can accumulate in soils and sediments, where they can enter human systems through inhalation, ingestion, or dermal contact. Over the past few decades, research has focused on understanding the distribution and sources of PTM contamination in mining regions [13].

Phosphate mining, especially, generates dust and airborne particulate matter (PM) that threatens both the environment and human health [11]. Exposure to PTM fractions may not immediately lead to significant health risks, according to some risk assessments. However, ingestion of contaminated soil or mine tailings can significantly increase health risks, especially for children, who are more vulnerable to the harmful effects of PTMs [11]. Effective management of contaminated soils and mine tailings is crucial for reducing these risks [11].

**8. Potential Human Health Risk:** Health risk assessments for PTMs from phosphate mining typically evaluate both non-carcinogenic and carcinogenic effects. The hazard quotient (HQ) and hazard index (HI) are used to measure non-carcinogenic risks, while the cancer index assesses the likelihood of developing cancer from exposure. Studies have shown that children are more susceptible to PTM exposure than adults, particularly through ingestion. While non-carcinogenic risks may remain under threshold values ( $HI < 1$ ), carcinogenic risks—especially for Cd—exceed acceptable levels for both children and adults [13].

## 2.0.4 Desertification Index

The dual pressures of climate change and human-induced land degradation, such as through mining, intensify desertification processes in Morocco. As vegetation is lost due to both natural and anthropogenic factors, surface albedo increases, signaling a shift towards more degraded landscapes.

Desertification ranks among the top global environmental challenges and is a significant cause of degradation in semi-arid grasslands. Understanding the ecological conditions of these regions and tracking their temporal and spatial changes is essential for effective environmental protection and land management at both regional and local scales. Remote sensing technology has become a widely used tool in monitoring and assessing desertification due to its broad observational range, extensive data collection, fast updates, and high accuracy [37].

In semi-arid grasslands, the traditional NDVI (Normalized Difference Vegetation Index) is often less effective due to sparse vegetation cover and the influence of soil and moisture on the index. MSAVI (Modified Soil Adjusted Vegetation Index), on the other hand, adjusts for soil background effects, increasing the sensitivity of vegetation detection in such environments. As desertification progresses, surface vegetation decreases, leading to lower vegetation index values, making MSAVI an ideal biophysical parameter for measuring the extent of desertification in these areas [37].

Additionally, surface albedo is another key indicator of desertification. As vegetation cover declines, surface moisture and roughness decrease, increasing surface albedo. Studies have shown that higher albedo values correspond to more severe levels of desertification. This makes albedo a useful physical parameter for assessing land degradation [37].

By combining MSAVI and albedo in a quantitative model, this study provides a straightforward yet effective method for remote sensing-based desertification monitoring in semi-arid grasslands. The model offers a valuable tool for understanding the impact of desertification on surface characteristics and can guide future environmental management efforts [37].

### **2.0.5 Using Band Math for Mineral Detection: Integrating EMIT and ECOSTRESS Satellites**

The exploration of Earth's mineral compositions from space has seen significant advancements with the deployment of satellites like EMIT and ECOSTRESS. Remote sensing methods, particularly the technique known as Band Math for Single Feature Extraction, are critical in detecting and mapping minerals. This article delves into the process of using band math for feature extraction and how it is applied in conjunction with data from the EMIT and ECOSTRESS satellites to enhance our understanding of mineral dust, climate effects, and environmental changes.

## 2.0.6 Band Math for Single Feature Extraction

Band Math for Single Feature Extraction is a remote sensing technique used to highlight specific spectral features that are indicative of certain minerals. This method involves identifying absorption features within a mineral's spectral signature by analyzing reflectance values at specific wavelengths.

Absorption band-depth images were pioneered by Brickey et al [38] and Crowley et al [39] to map mineral distributions using radiometrically-corrected Airborne Imaging Spectrometer data. This method involves analyzing specific wavelengths in the shortwave infrared (SWIR) spectrum to define the depth of absorption features, which are indicative of certain minerals. The process entails calculating ratios that highlight these absorption features. To create an absorption band-depth image, the sum of the reflectance values from several spectral bands positioned at the shoulders of the absorption feature is divided by the sum of the reflectance values from one or more bands located at the center of the absorption feature, where the reflectance is at a minimum. This approach involves including as many bands as possible to reduce the effects of noise, resulting in a one-band image where pixel values correspond to the depth of the absorption feature at the wavelength of the reflectance minimum.

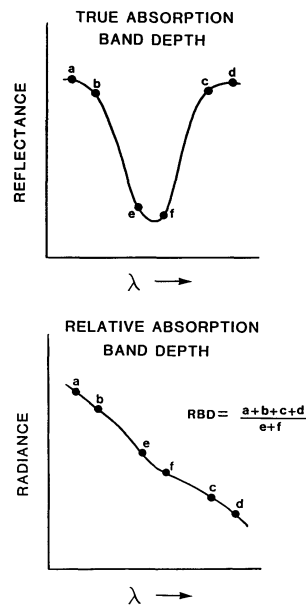


**Figure 2.3:** True absorption band depth and relative absorption band depth [39]

## 2.0.7 EMIT Satellite and Mineral Dust Mapping

Each year, millions of tons of dust are lifted from the world's driest and least vegetated regions, carried by the wind, and dispersed across the globe. This dust is made up of minerals and chemicals that reflect the composition of the rocks and soil where it originates. The color of the dust varies depending on its mineral content: for example, iron-rich dust appears dark red and absorbs more solar energy, while clay-heavy dust is pale yellow or white and reflects more sunlight. This dust influences Earth's atmospheric temperatures through a process known as radiative forcing. However, a lack of detailed data on dust from desert regions—where it is most abundant—means that much of the information available comes from agricultural areas, which are studied more often due to their relevance to farming. As a result, climate models often rely on fewer than 5,000 dust samples, leading to generalized assumptions about dust composition. These models tend to depict dust as yellow, the average color found in global samples, which creates considerable uncertainty about whether dust has a cooling or warming effect on the planet[40]. Airborne dust affects more than just our respiratory health, like causing nasal congestion or lung irritation, and creating physical annoyances such as a layer of grit on car windshields. Studies have found that dust can help fertilize rainforests and trigger algae blooms, impact snowmelt speeds, and possibly even influence weather and climate patterns. To better understand the climate-related effects of dust, NASA's Earth Surface Mineral Dust Source Investigation (EMIT) mission is working to deepen our knowledge of these impacts[40].

EMIT, positioned on the International Space Station (ISS), collects detailed data on the color and composition of Earth's dry, dust-prone regions, which generate mineral dust that can travel long distances through the air. Darker dust absorbs more sunlight, raising the surrounding air temperature, while lighter dust reflects sunlight, contributing to cooling the air.

EMIT, operated by NASA's Jet Propulsion Laboratory (JPL), provides much more detailed information about the surface minerals in dust-generating areas. This valuable data will assist scientists in improving climate models, which currently account for the temperature effects of dust but often depend on assumptions regarding its color[40].

EMIT targets ten key minerals commonly found in dust sources, each of which responds uniquely to light and heat. By determining the prevalence of these minerals in different regions, scientists can address knowledge gaps and gain a better understanding of how atmospheric dust influences warming or cooling on both global and regional scales, as well as the extent of these effects. These temperature fluctuations can affect atmospheric conditions, ultimately influencing the timing and distribution of precipitation. [40].

**EMIT’s Science Goals and Objectives:**

1. To gather remote sensing data on the distribution of surface minerals—such as hematite, goethite, illite, vermiculite, calcite, dolomite, montmorillonite, kaolinite, chlorite, and gypsum—in arid regions between 50 degrees north and south latitudes across Africa, Asia, North America, South America, and Australia.
2. To improve our understanding of how mineral dust affects heating and cooling in Earth’s atmosphere.
3. To improve predictions regarding how future climate scenarios may influence the amount and types of mineral dust released into the atmosphere [40].

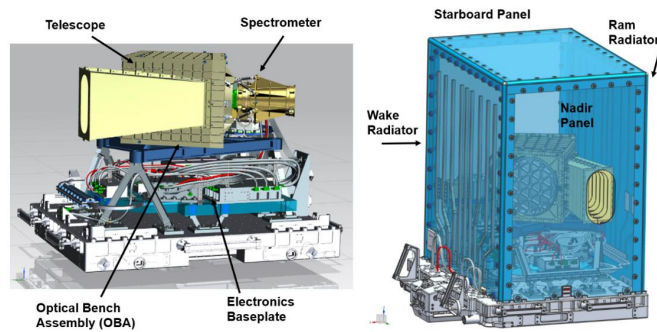


**Figure 2.4:** Diagram of the EMIT instrument that was installed on the International Space Station on July 24, 2022 [40].

EMIT is the first experiment aboard the International Space Station (ISS) dedicated specifically to studying mineral dust sources, making it the only instrument of its kind on any spacecraft. While on the ISS, EMIT orbits Earth at a speed of 8 kilometers per second, completing one full orbit approximately every 90 minutes and making about 16 orbits each day. It was launched on a SpaceX resupply mission on July 14, 2022, and installed on the ExPRESS Logistics Carrier 1 (ELC1), an essential platform for external instruments on the ISS. Over the next year, EMIT will map the surface composition of mineral dust sources in arid regions, contributing to a deeper understanding of the mineral dust cycle [41].

EMIT employs an imaging spectrometer to capture the spectrum at each point in an image. It gathers sunlight that is reflected from Earth’s surface minerals using a telescope and spectrometer system, which directs the light onto a detector array sensitive to visible and short-wavelength infrared light. Each mineral has a unique spectral signature within this range. The detector records the spectrum from a 1,240-point cross-track sample of EMIT’s swath, while the ISS’s movement in orbit provides the along-track data for the image. The collected image data is calibrated for spectral radiance, corrected for atmospheric effects, and analyzed to determine the mineral composition, enabling EMIT to meet its scientific goals [42].

EMIT functions within a wavelength range of 380 to 2500 nm, utilizing a single cryogenic Focal Plane Array (FPA) with channel spacing of approximately 7.5 nm. Its 74 km swath width and 60 m ground sampling resolution enable detailed mineralogical analysis of fallow agricultural fields. However, certain spectral bands, notably those between 1.320 to 1.439 nm and 1.766 to 1.967 nm, are considered unsuitable due to interference from atmospheric conditions, particularly water absorption [43].

<b>F-number</b>	F/1.8
<b>Cross-track FOV</b>	11°
<b>IFOV (cross-track x along-track)</b>	155 x 71 rad
<b>Focal length</b>	193.5 mm
<b>Entrance pupil aperture</b>	110 mm
<b>Spectral Range</b>	381 – 2493 nm
<b>Spectral Sampling</b>	7.5 nm
<b>Spectral Resolution</b>	60 m
<b>Number of Bands</b>	285

**Table 2.1:** EMIT Imaging System: Optical and Spectral Parameters [42]

## 2.0.8 ECOSTRESS Satellite and Thermal Infrared Detection

EMIT specializes in observing the visible to shortwave infrared (SWIR) spectrum, while ECOSTRESS operates in the thermal infrared (TIR) range to study Earth’s surface temperature and monitor water stress in ecosystems. The ECOSTRESS mission, short for the ECOSystem Spaceborne Thermal Radiometer Experiment on Space Station, focuses on tracking plant transpiration—the release of water vapor from leaves—and overall evapotranspiration (ET), which combines evaporation from soil and plant surfaces. By providing high-resolution TIR data, the mission offers valuable insights into water usage and stress in plants [44].

Mounted on the International Space Station (ISS), ECOSTRESS addresses three critical scientific objectives: understanding how terrestrial ecosystems react to shifts in water availability, examining how daily vegetation water stress influences the global carbon cycle, and improving agricultural sustainability by enhancing water use monitoring and drought forecasting. To achieve these aims, ECOSTRESS identifies water stress thresholds for vulnerable ecosystems, uncovers barriers to plant water uptake, and analyzes agricultural water consumption across the U.S., contributing to more accurate drought predictions and better resource management [44].

While ECOSTRESS primarily focuses on evaluating plant water stress and mea-

Description	Value	Unit	Notes
Measured band centers	Band 1 – 8.29	μm	May 15 2019 – May 17, 2023, Three Band data Transition April 28, 2023 – May 17, 2023, Three and Five Band data May 18, 2023 – Present, Five Band data only mode
	Band 2 – 8.78		
	Band 3 – 9.20		
	Band 4 – 10.49 Band 5 – 12.09		
Measured FWHM per band	Band 1 – 0.345	μm	
	Band 2 – 0.310		
	Band 3 – 0.396		
	Band 4 – 0.410		
	Band 5 – 0.611		
Pixel size at nadir	69x38	m	2 pixels in cross-track and 1 pixel in down track
Swath width	384	km	
Scene size	5400x5632	pixels	

**Table 2.2:** Spectral and Spatial Characteristics of ECOSTRESS Thermal Infrared Bands [45]

asuring evapotranspiration (ET), it also offers the unique capability to identify surface minerals through its thermal infrared (TIR) observations. By analyzing TIR data, researchers can generate mineralogical maps that leverage the distinct thermal emission properties of various minerals. These thermal signatures, captured with ECOSTRESS’s high-resolution capabilities, allow for precise identification of surface compositions.

This added functionality proves particularly valuable in geological studies and

natural resource exploration, where accurately locating mineral deposits is crucial. The ability to detect minerals from orbit broadens ECOSTRESS's scope, complementing its primary role in monitoring water stress and ET dynamics in vegetation while offering critical insights for Earth sciences.

The EMIT and ECOSTRESS satellites play a vital role in analyzing the spectral properties of various minerals, including apatite, quartz, calcite, dolomite, gypsum, sepiolite, palygorskite, kaolinite, illite, glauconite, and iron oxides like hematite and goethite. Each mineral has unique spectral signatures in the visible to short-wave infrared (SWIR) and thermal infrared (TIR) ranges, enabling precise identification and mapping across the Earth's surface. Understanding these properties is essential for assessing the impact of mineral dust on climate dynamics and environmental processes. In the following section, we will conduct a literature review on the spectral characteristics of these minerals in the SWIR and TIR ranges.



## 2.0.9 Spectral properties of minerals

### 2.0.10 Spectral properties of apatite

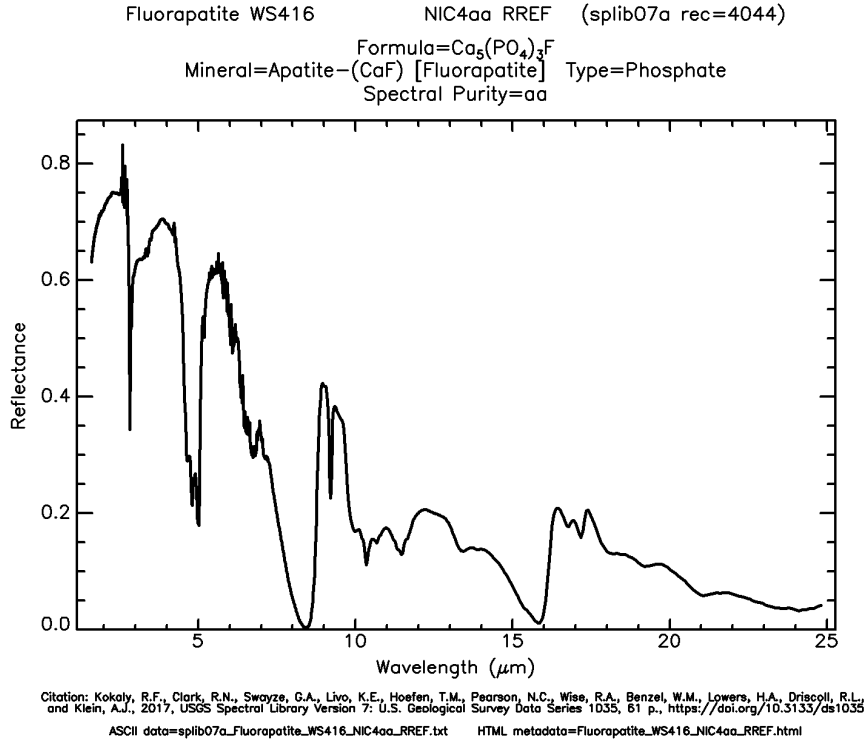


**Figure 2.5:** Reflectance Spectrum of Fluorapatite ( $\text{Ca}_5(\text{PO}_4)_3\text{F}$ ) from the USGS Spectral Library

Apatite, the most prevalent phosphate mineral, is identified by key features at 9160 nm and 9620 nm, both resulting from the asymmetric stretching of  $\text{PO}_4$ . Clavier et al. [46] provide information on the TIR-active vibrational modes of other phosphates, such as monazite and xenotime. The  $\text{PO}_4^{3-}$  anion in apatite can be easily substituted by  $\text{AsO}_4^{3-}$  and  $\text{VO}_4^{3-}$ , with Adler (1964) [47] summarizing the corresponding absorption features. Adler also described how the major TIR features shift to longer wavelengths when  $\text{P}^{5+}$ ,  $\text{As}^{5+}$ , and  $\text{V}^{5+}$  occupy the X position in  $\text{XO}_4^{3-}$ , correlating this shift with the increasing mass and ionic radius of the substituting elements.

The reflectance spectrum of pure fluorapatite in the Short-Wave Infrared (SWIR) range is typically featureless, as noted in the USGS Spectral Library [48]. However, the SWIR reflectance spectrum of this particular sample exhibits prominent absorption bands indicative of ferroan dolomite, specifically at 2318 nm and 2499 nm after continuum removal [49]. Additionally, subtle and narrow absorption

features appear within the broader Fe-related absorption around 1200 nm, likely attributable to  $\text{REE}^{3+}$ . The presence of ferroan dolomite signals is probably due to microscopic inclusions within the fluorapatite crystal. Nonetheless, it is also possible for carbonate to be a minor component in some fluorapatite and hydroxylapatite samples, as suggested by Fleet and Liu [50].

### 2.0.11 Spectral properties of Quartz

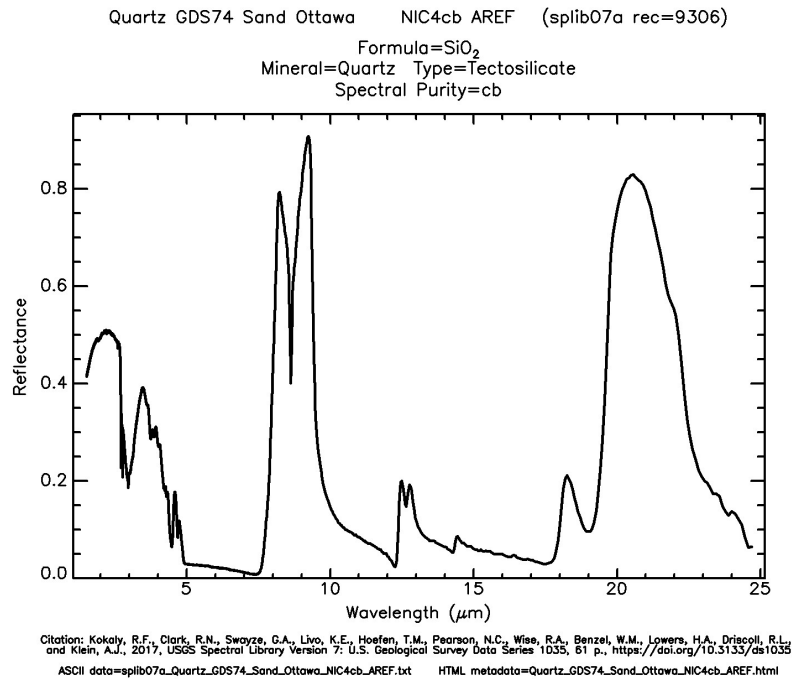


**Figure 2.6:** Reflectance Spectrum of Quartz ( $\text{SiO}_2$ ) from the USGS Spectral Library

Igisu et al. [51] identified four absorption features within the 4000 to 6000 nm wavelength range in the transmission spectra, attributing them to "Si-O bonds." Comparing these to the fundamental Si-O stretching vibrations (Si-O), they assigned the absorptions at 4470 nm, 4670 nm, and 4920 nm to the first overtones ( $2\nu\text{SiO}$ ) of the primary quartz reststrahlen bands in the thermal infrared (TIR) region. The fundamental stretching vibrations of silicates (SiO) produce the most intense features observable in the TIR wavelength region in reflectance spectra. The strongest group of reflection peaks, also known as reststrahlen bands [52], can create a relatively simple M-shaped signature in the reflectance spectra of less complex silicates like quartz. The primary reststrahlen bands of quartz are located

at 8150 nm, 8600 nm, and 9330 nm [53]. Additionally, a group of less intense fundamental stretching vibrations, referred to as secondary reststrahlen bands, are found around 12,550 nm.

## 2.0.12 Spectral properties of Dolomite

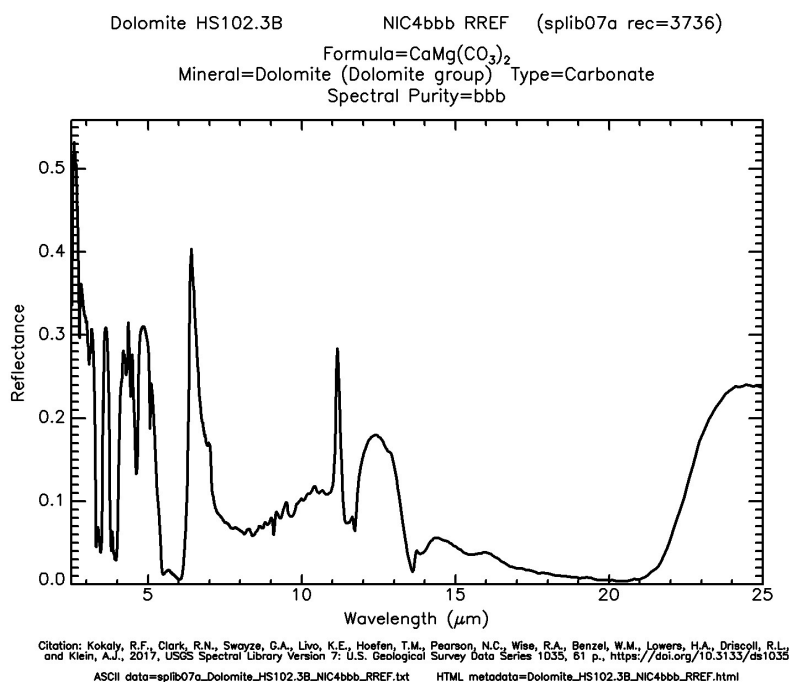


**Figure 2.7:** Reflectance Spectrum of Dolomite ( $\text{CaMg}(\text{CO}_3)_2$ ) from the USGS Spectral Library

Dolomite's absorption features in the SWIR band have also been studied extensively, showing distinct positions in different reports. Huang and Kerr [54] found that dolomite has an absorption band centered at 3.95  $\mu\text{m}$ . Hunt and Salisbury [55] reported dolomite's absorption band at 2.33  $\mu\text{m}$ . Gaffey [56] indicated that dolomite's absorption band is located around 2.31-2.32  $\mu\text{m}$ . Van der Meer [57] concluded that dolomite has an absorption band at 3.3039  $\mu\text{m}$ . In the TIR region, Huang and Kerr [54] observed a strong absorption band for dolomite at 11.35  $\mu\text{m}$ . Clark [58] noted that the absorption band positions of dolomite can shift slightly due to compositional differences.

Reig et al. [59] utilized FTIR spectroscopy to determine the absorption features of dolomite at 881  $\text{cm}^{-1}$  (11.35  $\mu\text{m}$ ) and 730  $\text{cm}^{-1}$  (13.70  $\mu\text{m}$ ).

Calcite and dolomite, being part of a solid-solution series, exhibit characteristic peak shifts in the 2330–2335 nm range. This behavior arises from the substitution of magnesium (Mg) for calcium (Ca) within their crystal structures. As the Mg content increases, the absorption peak shifts toward shorter wavelengths.

### 2.0.13 Spectral properties of Calcite

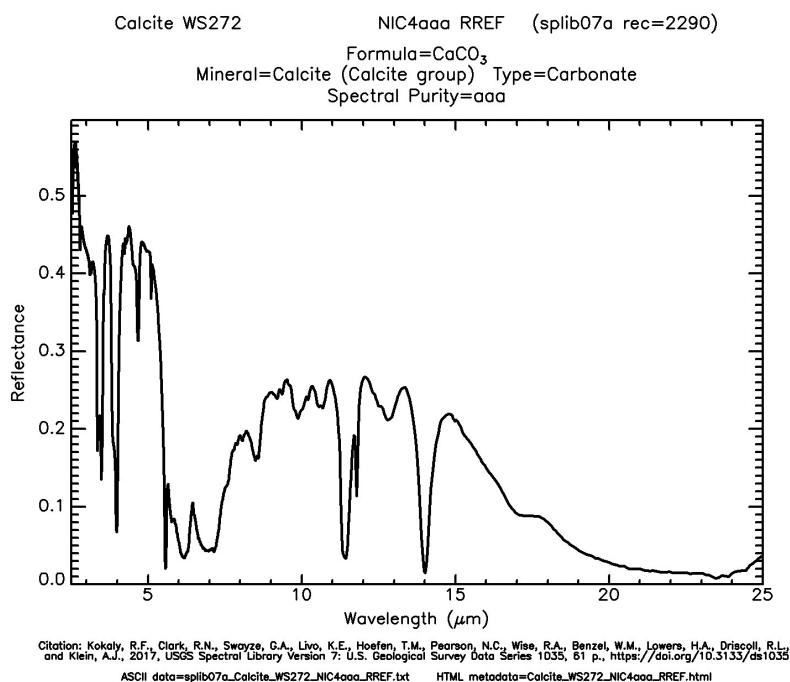


**Figure 2.8:** Reflectance Spectrum of Calcite (CaCO<sub>3</sub>) from the USGS Spectral Library

In the study of carbonate minerals' absorption features in the SWIR band, calcite shows significant variations in the precise position of its absorption bands as reported by various researchers. Huang and Kerr [54] observed that calcite has an absorption band centered at 3.92 μm. Hunt and Salisbury [55] found calcite's absorption band at 2.35 μm. Gaffey [56] reported that calcite's absorption is centered around 2.33-2.34 μm, while Van der Meer [57] concluded that the absorption band is at 2.3465 μm. In the TIR region, Huang and Kerr [54] indicated a strong absorption band for calcite at 11.40 μm. Clark [58] suggested that the position of the absorption band can slightly shift due to different compositions of calcite. Reig et al. [59] used FTIR spectroscopy to determine specific absorption features of calcite at 875 cm<sup>-1</sup> (11.43 μm) and 712 cm<sup>-1</sup> (14.04 μm).

## 2.0.14 Spectral properties of gypsum

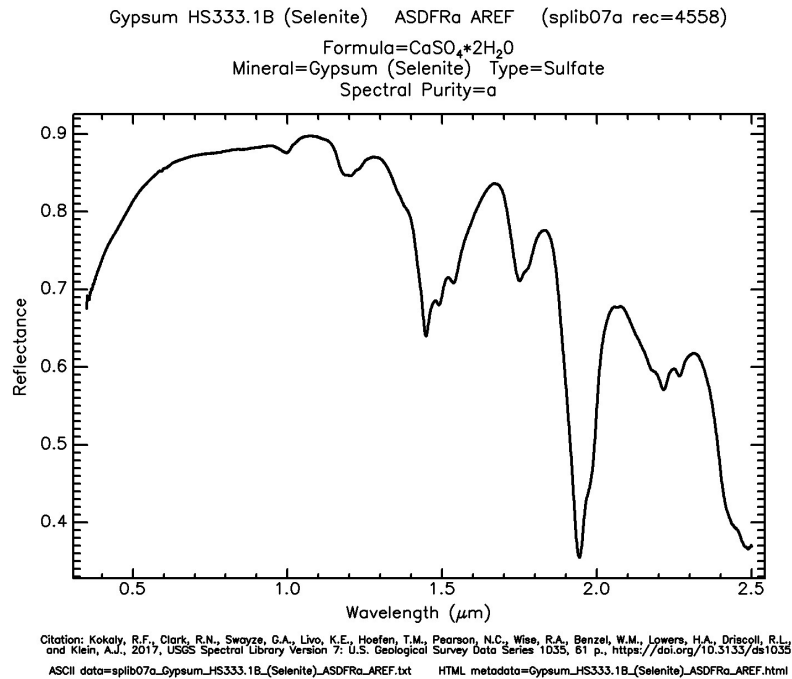


**Figure 2.9:** Reflectance Spectrum of Gypsum ( $\text{CaSO}_4 \cdot 2\text{H}_2\text{O}$ ) from the USGS Spectral Library

Gypsum exhibits specific spectral absorption features due to vibrational processes involving anion bonds [60]. In the VNIR and SWIR parts of the electromagnetic spectrum, these features are primarily due to water molecules in the gypsum crystals [55]. Key absorption characteristics include those near 1.2 microns, which result from the combination of H–O–H bending and the first overtone of O–H stretching [55] [60]. Between 1.38 to 1.61 microns, the first overtone of O–H stretching is prominent. At 1.75 microns, there is a combination of H–O–H bending and O–H stretching fundamentals, along with low-frequency vibrational modes of crystal water. Around 1.91 microns, the absorption features are due to the combined effect of O–H stretch and H–O–H bends. Finally, at approximately 2.21 microns, the absorption characteristics result from the combined effect of O–H stretching fundamental and the first overtone of water [61].

Applying and parameterizing spectral absorption features can be challenging due to overlapping signals from various sources, such as other soil components and atmospheric effects. Gypsum shows several characteristic absorption features, with prominent ones around 1.5 m, 1.75 m, and 2.2 m in the VNIR-SWIR spectral region [62]. However, the 1.5 m feature is unsuitable for remote sensing due to atmospheric

water vapor absorption. The 2.2 m doublet absorption can be confused with clay, making it problematic for spectral discrimination, especially in low-quality spectral data. Consequently, the 1.75 m feature is the best discriminator for quantifying gypsum absorption in common soil mixtures and conditions.

However, vegetation coverage and soil mixed with dry plant remains, such as starch, cellulose, and other biochemicals, may overlap with gypsum features and limit mapping capabilities. Dry plant pigments like cellulose and lignin absorb close to the 1.75 m gypsum absorption feature [63]. Additionally, hydrocarbons like oil and plastics, which have an absorption maximum of 1.73 m, can also overlap with gypsum features, particularly in polluted soils [64].

## 2.0.15 Spectral properties of Sepiolite

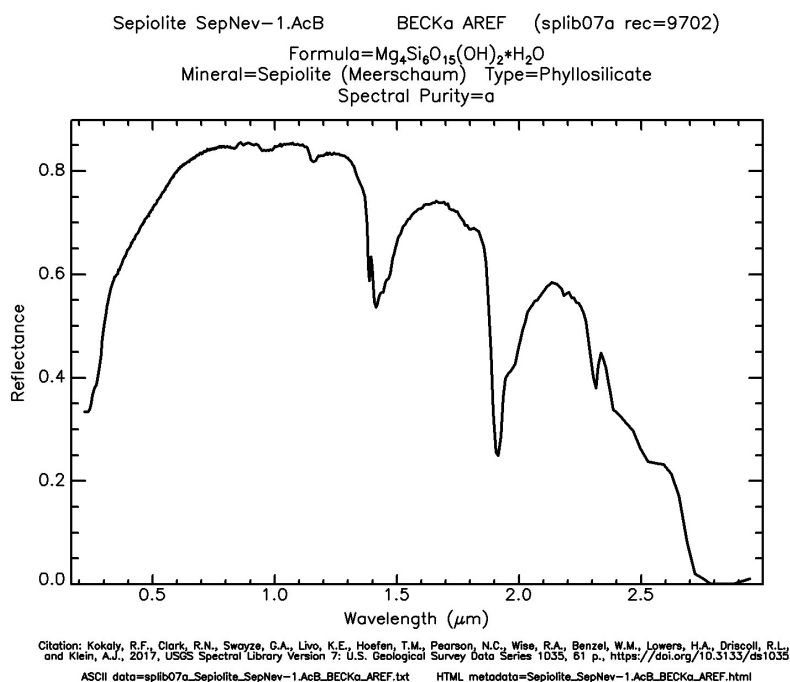


**Figure 2.10:** Reflectance Spectrum of Sepiolite ( $\text{Mg}_4\text{Si}_6\text{O}_{15}(\text{OH})_2 \cdot \text{H}_2\text{O}$ ) from the USGS Spectral Library

Sepiolite exhibits absorption features in the infrared region around 2340  $\mu\text{m}$ , primarily due to the vibrational modes of the silicate structure and the hydroxyl groups (OH) [62].

The VNIR spectra of sepiolite include features near 1.38, 1.42, 1.91, 2.18, and 2.31  $\mu\text{m}$  due to both Al and Mg in their structure [65].

The VNIR-SWIR spectra effectively identify the samples as sepiolite, with distinguishing features in the IR region. Sepiolite samples are characterized by a doublet of absorption bands at 1388 and 1415 nm, which originate from OH-group vibrations, and an absorption band at 1910 nm, caused by water vibrations related to their structure. Additionally, an absorption band at 2311 nm is observed due to Mg-OH vibrations [66].



## 2.0.16 Spectral properties of Kaolinite

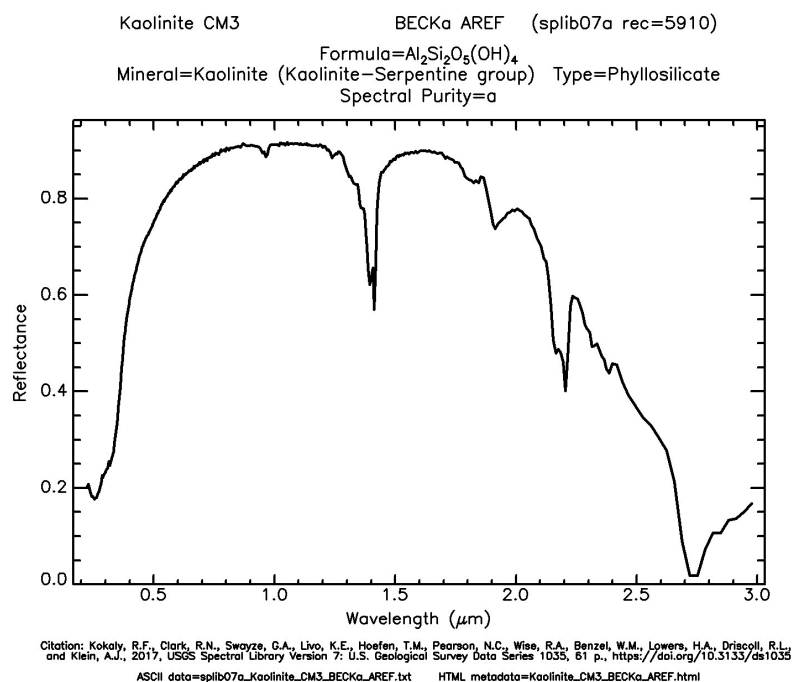


**Figure 2.11:** Reflectance Spectrum of Kaolinite ( $\text{Al}_2\text{Si}_2\text{O}_5(\text{OH})_4$ ) From the USGS Spectral Library

In kaolinite with high crystallinity, four bands are associated with the vibrational O-H process. Specifically, absorption bands at 1379 nm, 1393 nm, and 1345 nm are linked to inner-surface OH groups. In well-ordered kaolinite, near-infrared bands resulting from the combination of stretching and bending vibration modes of OH- groups form a doublet at 2180 nm and 2190 nm. Additionally, an absorption band centered at 2208 nm is associated with the combined stretching and bending modes of inner-surface hydroxyl groups. In disordered kaolinite, the shape of the OH- group bands resembles that found in the O-H stretching region, reflecting the degree of disorder. Localized absorption bands at 1340 nm, 1395 nm, and 1409 nm are linked to stretching processes in disordered kaolinite [67].

## 2.0.17 Spectral properties of Illite

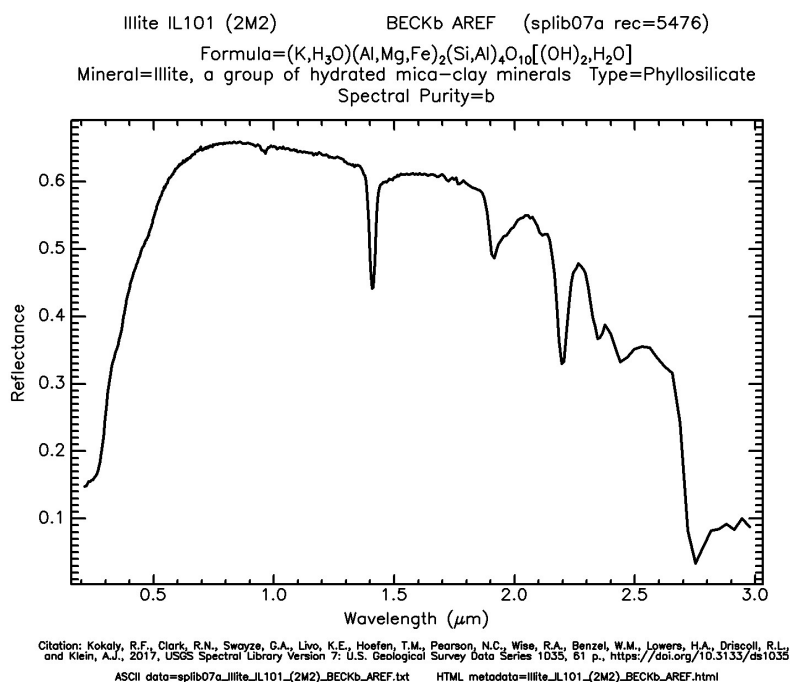


**Figure 2.12:** Reflectance Spectrum of Illite  $((\text{Mg}, \text{Al})_2\text{Si}_4\text{O}_{10}(\text{OH}) \cdot 4\text{H}_2\text{O})$  From the USGS Spectral Library

Illite has distinct absorption features at approximately 1410 nm, 1910 nm, and 2210 nm. Although these features are similar to those of illite-smectite and smectite, their intensities differ. The spectral distinction of illite can generally be determined by examining the ratio of the minima of the H<sub>2</sub>O absorption feature to the minima of the AlOH absorption feature [68].

## 2.0.18 Spectral properties of Palygorskite

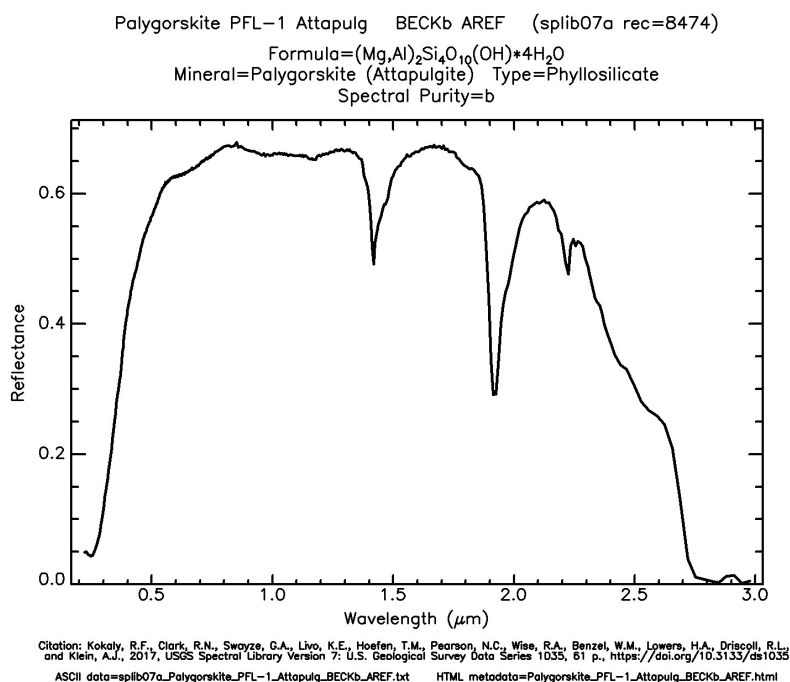


**Figure 2.13:** Reflectance Spectrum of Palygorskite ((Mg, Al)<sub>2</sub>Si<sub>4</sub>O<sub>10</sub>(OH) · 4H<sub>2</sub>O) From the USGS Spectral Library

For palygorskite samples, the VNIR-SWIR spectra reveal characteristic absorption bands at 1415 nm and 1910 nm, along with another band around 2207 nm due to Al-OH vibrations. In intermediate compositions, such as Al-sepiolite and Mg-palygorskite samples, the coexistence of features at 2207 and 2311 nm can be observed. These features are more distinctly seen in the second derivative of the spectra [66].

## 2.0.19 Spectral properties of Glauconite

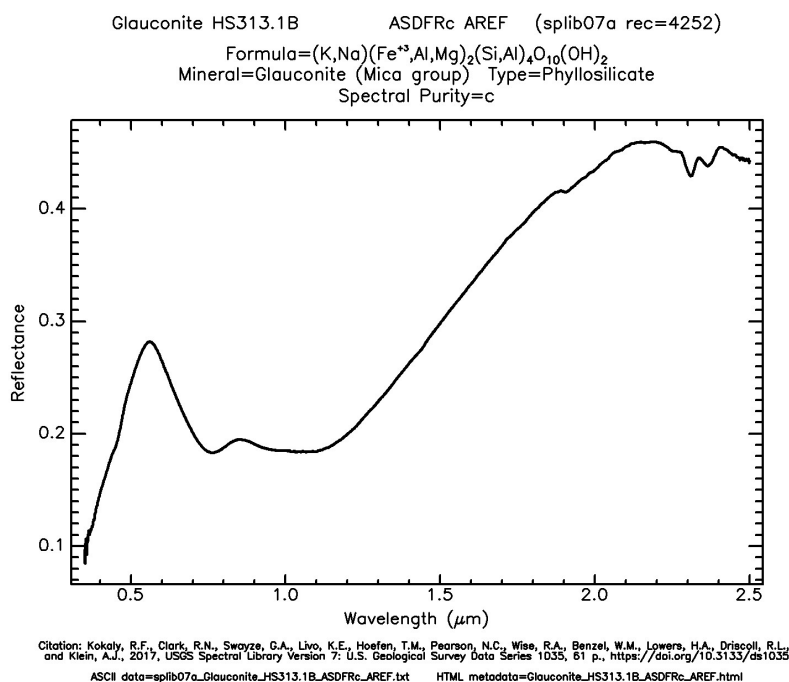


**Figure 2.14:** Reflectance Spectrum of Glauconite((K, Na(Fe<sup>3+</sup>, Al, Mg)<sub>2</sub>(Si, Al)<sub>4</sub>O<sub>10</sub>(OH)<sub>2</sub>)  
 From the USGS Spectral Library

Glauconite's spectral signatures are characterized by distinct absorption features in both the visible-short-wave infrared (SWIR) and mid-infrared (MIR) regions. In the SWIR region, glauconite shows absorption bands at approximately 0.77, 1.08, 1.9, and 2.3 m, which vary with its potassium oxide (K<sub>2</sub>O) content. The maturity of glauconite is indicated by the presence of metal-metal charge transfer (CT) and Fe<sup>2+</sup> absorption bands at 1.08 and 0.77 m, respectively. Additionally, H<sub>2</sub>O and OH signatures in the near-infrared (NIR) region reflect differences in molecular H<sub>2</sub>O content. In the MIR region, a shift of the Si-O stretch at 10 m towards lower wavelengths suggests a dominance of smectite layers in the glauconite structure [69].

## 2.0.20 Spectral properties of Iron Oxides (Hematite and Goethite)

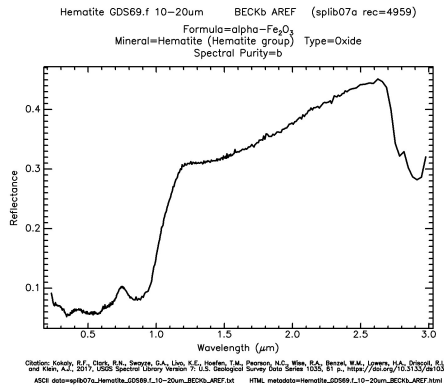


**Figure 2.15:** Reflectance Spectrum of Hematite  $\text{Fe}_2\text{O}_3$  From the USGS Spectral Library

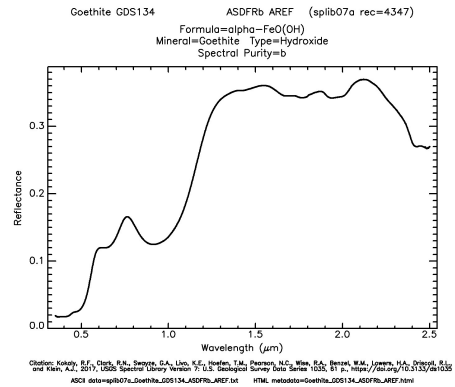


**Figure 2.16:** Reflectance Spectrum of Goethite  $\text{FeO(OH)}$  From the USGS Spectral Library

Iron oxides have distinct visible reflectance spectra due to  $\text{Fe}^{3+}$  absorptions. Hematite shows an absorption near 550 nm, 630, and 860 nm, giving it a red color, while goethite absorbs near 480 nm, 650, and 920nm resulting in a yellow-brown hue. When these two minerals mix, their absorption bands overlap, creating a peak somewhere between the two original positions. The exact location of this peak depends on the ratio of hematite to goethite and the strength of their absorption bands [70].

It is important to note certain limitations when using satellite images for spectral analysis. Due to atmospheric interference, particularly in regions around 1380 nm and 1900 nm associated with water vapor absorption, some diagnostic features cannot be used. As a result, only one or two robust features are selected for analysis. Additionally, satellite-acquired spectra are more affected by noise compared to laboratory or field spectra, requiring careful preprocessing and interpretation to ensure reliable results.

## Chapter 3

# Methodology

## 3.1 Methodology of Multi-Temporal NDVI Analysis

### 3.1.1 NDVI Analysis for year 2023

For this study, Landsat imagery was acquired for six months in 2023: February, March, April, June, July, and August. The selection of these months was intentional, aimed at capturing significant seasonal variations in vegetation dynamics. The time frames represent critical phenological stages, including early spring growth, peak summer vegetation, and late summer senescence. This targeted approach allows for a detailed examination of changes in vegetation cover and health throughout the year, providing insights into the seasonal response of vegetation to environmental conditions.

February marks the beginning of early spring growth, indicating the awakening of vegetation from dormancy. March continues this trend with increased activity as temperatures rise. April often reflects peak growth rates, resulting in lush landscapes. June captures the maximum biomass and health of plants during the summer growing season. July may still show peak vegetation but starts to indicate the onset of senescence in some species. Finally, August represents late summer, revealing signs of stress or decline due to prolonged heat and reduced moisture. The data sources utilized for this analysis include:

Time	Number						Type	Resolution
2023-02-03	LC08	L2SP	201037	20230203	20230209	02_T1_MTL	Landsat 8	30 m
2023-03-17	LC09	L2SP	201037	20230315	20230317	02_T1_MTL	Landsat 9	30 m
2023-04-18	LC09	L2SP	201037	20230416	20230418	02_T1_MTL	Landsat 9	30 m
2023-06-21	LC09	L2SP	201037	20230619	20230621	02_T1_MTL	Landsat 9	30 m
2023-07-08	LC09	L2SP	201037	20230705	20230708	02_T1_MTL	Landsat 9	30 m
2023-08-19	LC08	L2SP	201037	20230814	20230819	02_T1_MTL	Landsat 8	30 m

**Table 3.1:** Data sources for NDVI analysis

The Normalized Difference Vegetation Index (NDVI) is employed as a key metric in this analysis to assess vegetation health and density. NDVI leverages the unique spectral properties of healthy vegetation, which absorbs red light and reflects near-infrared (NIR) light. This relationship allows for effective differentiation between healthy and stressed vegetation. NDVI values range from -1 to +1, where values closer to +1 indicate dense, healthy vegetation, while lower values signify sparse or stressed vegetation cover.

The NDVI is calculated using the following formula:

$$\text{NDVI} = \left( \frac{\text{NIR} - \text{Red}}{\text{NIR} + \text{Red}} \right)$$

This formula provides a quantitative measure of vegetation health and enables a robust analysis of seasonal variations across the selected months.

### 3.1.2 Multi-Temporal NDVI Analysis for Land Cover Classification and Vegetation Dynamics

For a comprehensive assessment of land cover changes and vegetation dynamics, NDVI analysis was conducted using Landsat imagery spanning from 1985 to 2023. The selected dates prioritize periods of higher vegetation growth to capture seasonal and long-term trends. The data sources utilized for this analysis include: The

Time	Number	Type	Resolution
1985-03-14	LT05_L2SP_201037_19850314_20200918_02_T1_MTL	Landsat 5	30 m
1991-02-27	LT05_L2SP_201037_19910227_20200915_02_T1_MTL	Landsat 5	30 m
1999-03-21	LT05_L2SP_201037_19990321_20211203_02_T1_MTL	Landsat 5	30 m
2004-03-18	LT05_L2SP_201037_20040318_20200903_02_T1_MTL	Landsat 5	30 m
2009-01-27	LT05_L2SP_201037_20090127_20200828_02_T1_MTL	Landsat 5	30 m
2014-03-30	LC08_L2SP_201037_20140330_20200911_02_T1_MTL	Landsat 8	30 m
2017-04-07	LC08_L2SP_201037_20170407_20200904_02_T1_MTL	Landsat 8	30 m
2023-03-15	LC09_L2SP_201037_20230315_20230317_02_T1_MTL	Landsat 9	30 m

**Table 3.2:** Data sources for multi-temporal NDVI analysis

selection of March and April imagery for most years aims to capture peak vegetation stages, as these months typically exhibit more favorable climatic conditions for plant growth in the study area. The 2009 image, captured in January, was selected to maintain temporal continuity, despite being outside the preferred range.

Land cover categories were classified based on NDVI values:

- Bare land/urban areas: NDVI values between -0.2 to 0.2
- Shrubland: NDVI values between 0.2 to 0.3
- Cultivated land: NDVI values between 0.3 to 0.6
- Forest: NDVI values >0.6

This classification allowed for a clear differentiation between various land cover types. Bare land or urban areas, typically characterized by low to no vegetation, exhibit low NDVI values due to minimal photosynthetic activity. Shrubland, which consists of sparse vegetation, is identified by slightly higher NDVI values. Cultivated land shows moderate NDVI values, reflecting the seasonal presence of crops. Finally, Forest, representing dense, year-round plant growth, is distinguished by the highest NDVI values.

By selecting imagery from periods of higher vegetation cover (March-April), the analysis is optimized to capture the peak growing seasons. This methodological approach is particularly valuable for detecting phenological changes, which are critical for understanding both short-term vegetation dynamics and long-term



trends related to land use changes.

## 3.2 Methodology of Desertification Index

To assess the desertification trends in the Khouribga mine region, a multi-temporal analysis was conducted using Landsat satellite imagery over a 40-year period. The selected years include 1985, 1991, 1999, 2005, 2009, 2014, 2017, 2023 and 2024. The focus on February, March, and April was chosen deliberately to capture periods of higher vegetation growth, as these months represent the peak of the greener season in the region. The analysis was designed to detect changes in land cover, vegetation health, and desertification through the use of two key indices: the Modified Soil-Adjusted Vegetation Index (MSAVI) and Albedo.[37]

The Landsat satellite data used for this analysis includes as following and once the images were obtained, they were resized to focus on the area of interest:

Time	Number	Type	Resolution
1985-03-14	LT05_L2SP_201037_19850314_20200918_02_T1_MTL	Landsat 5	30 m
1991-02-27	LT05_L2SP_201037_19910227_20200915_02_T1_MTL	Landsat 5	30 m
1999-03-21	LT05_L2SP_201037_19990321_20211203_02_T1_MTL	Landsat 5	30 m
2005-03-21	LT05_L2SP_201037_20050321_20200902_02_T1_MTL	Landsat 5	30 m
2009-01-27	LT05_L2SP_201037_20090127_20200828_02_T1_MTL	Landsat 5	30 m
2014-03-30	LC08_L2SP_201037_20140330_20200911_02_T1_MTL	Landsat 8	30 m
2017-04-07	LC08_L2SP_201037_20170407_20200904_02_T1_MTL	Landsat 8	30 m
2023-03-15	LC09_L2SP_201037_20230315_20230317_02_T1_MTL	Landsat 9	30 m
2024-03-17	LC09_L2SP_201037_20240317_20240318_02_T1_MTL	Landsat 9	30 m

**Table 3.3:** Data sources for Desertification Index analysis

### 3.2.1 Indices for Desertification Assessment

Two indices were calculated to assess desertification and land cover changes: MSAVI and Albedo.

#### 1. MSAVI (Modified Soil Adjusted Vegetation Index)

MSAVI is an enhancement of the traditional NDVI. It reduces the soil reflectance noise, making it more effective in regions with sparse vegetation, which are typically prone to desertification. This makes MSAVI particularly suitable for arid and semi-arid regions like Khouribga, where soil exposure and sparse vegetation are common.

The formula used to compute MSAVI is:

$$\text{MSAVI} = \frac{2 \cdot \rho_{\text{NIR}} + 1 - \sqrt{(2 \cdot \rho_{\text{NIR}} + 1)^2 - 8 \cdot (\rho_{\text{NIR}} - \rho_{\text{red}})}}{2} \quad (3.1)$$

where:

b4 is the Near-Infrared (NIR) band, which is sensitive to vegetation.

b3 is the red band, which plants absorb for photosynthesis.

MSAVI is ideal for quantifying vegetation health, particularly in desertification studies where vegetation is sparse and the interaction between vegetation and soil becomes critical.

## 2. Albedo (Surface Reflectance):

Albedo measures the Earth's surface reflectivity. In the context of desertification, higher Albedo values are indicative of bare or degraded land, while lower values are typically associated with vegetated areas. By examining Albedo values over time, one can infer changes in surface conditions—whether land is becoming more barren or undergoing re-vegetation. The Albedo index is calculated using the following formula:

$$\text{Albedo} = 0.356 \times b_1 + 0.130 \times b_3 + 0.373 \times b_4 + 0.085 \times b_5 + 0.072 \times b_7 - 0.0018 \quad (3.2)$$

where:

b1 represents the blue band.

b3 represents the red band.

b4 represents the Near-Infrared (NIR) band.

b5 represents the Shortwave Infrared (SWIR1) band.

b7 represents the Shortwave Infrared (SWIR2) band.

### 3.2.2 Scatter Plot Analysis: Albedo vs. MSAVI

To better understand the relationship between vegetation cover and surface reflectance, a 2D scatter plot was generated, plotting MSAVI values on the x-axis and Albedo values on the y-axis as in figure 3.1. This scatter plot revealed a distinct linear correlation along the lower boundary of the Albedo-MSAVI feature space. Through this scatter plot, a clear linear correlation was observed along the lower boundary of the Albedo-MSAVI feature space. This trend was further examined by mapping the spatial distribution of surface cover types over the years. It became evident that the line connecting two key points, A and B, represented areas with

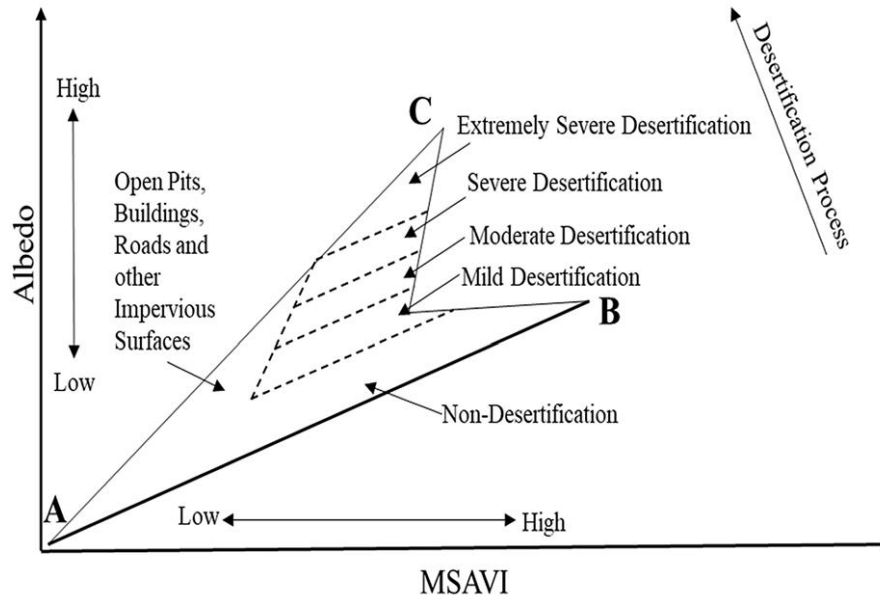


**Figure 3.1:** Albedo-MSAVI spatial features [37]

high vegetation coverage. Specifically, Point A corresponded to a water-saturated area, while Point B indicated a region with dense vegetation. The area surrounding Point A was identified as wetland, whereas Point C represented dry, bare land with high reflectance.

The scatter plot analysis revealed distinct ecological patterns: the A–B line, marking areas of high vegetation, exhibited the strongest correlation and was the most ecologically significant. In contrast, the A–C line displayed a lower correlation and represented a more chaotic ecological zone, with a mixture of desertification and water surfaces.

### 3.2.3 Approach to Pixel Classification

1. Severe Desertification (Red Cluster):

- Pixels that fall within a higher range of Albedo and lower MSAVI values, corresponding to the most degraded areas.
- These areas have the lowest vegetation coverage and the highest reflectance values due to soil exposure or barren land.

2. Moderate Desertification (Blue Cluster):

- Pixels in this class exhibit moderate Albedo and slightly higher MSAVI compared to severely desertified areas.

- Vegetation exists but is sparse, indicating regions experiencing some level of degradation, with partial vegetation loss.

3. Mild Desertification (Yellow Cluster):

- This class has low Albedo and moderate MSAVI, suggesting these areas still maintain some level of vegetation cover.

- These are areas with vegetation that is either under stress or thinning, marking the onset of land degradation.

4. Open Pits, Buildings, and Impervious Surfaces (Cyan Cluster):

- These areas have very high Albedo values and very low MSAVI, indicating man-made structures such as open mining pits, roads, and urban areas.

- There is little to no vegetation cover, and the surface reflectance is dominated by artificial structures.

5. Non-Desertification (Grey Cluster):

- This classification includes areas with low Albedo and high MSAVI, indicating healthy vegetation with no signs of desertification.

- These regions reflect optimal vegetative conditions with robust vegetation cover and low reflectance from soil or bare land.

The relationship between Albedo and MSAVI effectively highlighted changes in land cover and surface conditions driven by various biophysical processes. By analyzing the multi-temporal data through the Albedo-MSAVI feature space, shifts in vegetation health and land degradation could be classified, offering a valuable tool for studying land cover changes over time.

### 3.3 Methodology for Mineral Detection in Phosphate Mines Using Hyperspectral Analysis (ECOSTRESS/EMIT)

#### 3.3.1 Literature Review for Mineral Identification

The initial phase of the methodology involved conducting an in-depth literature review to identify the key mineral compositions typically associated with phosphate mines in Morocco. This review enabled the classification of minerals into three primary categories:

- **Main minerals:** These are the economically significant minerals that are the target of mining operations.

- **Gangue minerals:** Non-economic minerals that occur alongside the primary minerals, often requiring separation during processing.

- **Accessory minerals:** Minor minerals that may not contribute directly to the mine's economic value but can provide valuable geological or geochemical insights into the mining environment.

This classification was crucial for selecting relevant spectral signatures in the hyperspectral analysis. By focusing on these mineral groups, the subsequent steps of the methodology were designed to target specific spectral features associated with each category, ensuring accurate mineral detection.

### 3.3.2 Literature Review for Spectral Signatures in SWIR and TIR

Following the mineral identification, the next step involved a thorough review of the spectral signatures for the identified minerals within the Short-Wave Infrared (SWIR) and Thermal Infrared (TIR) regions of the electromagnetic spectrum. This review focused on the unique spectral absorption features and reflectance behaviors that are characteristic of each mineral type.

Why focus on SWIR and TIR?

These regions of the spectrum are especially useful in mineral detection because many minerals exhibit distinctive absorption features in these wavelengths. By identifying these unique spectral “fingerprints,” presence of specific minerals from hyperspectral data can be determined. SWIR, for instance, is known for capturing important hydroxyl, carbonate, and sulfide absorption features, while TIR is essential for detecting silicate and oxide minerals.

The goal of this review was to map out the spectral behaviors of the identified main, gangue, and accessory minerals. Each of these minerals has a unique way of interacting with light in the SWIR and TIR regions, and understanding these interactions would enable us to distinguish them in the hyperspectral data collected by the ECOSTRESS and EMIT sensors.

For example, minerals like calcite and dolomite, which are common gangue minerals, exhibit strong absorption features around 2.31–2.33 microns in the SWIR range. This particular feature helped guide our selection of relevant bands for analysis. Similarly, quartz, an accessory mineral, has distinctive reflectance peaks in the TIR region, typically between 8 to 9 microns, which provided another key diagnostic marker.

By thoroughly reviewing the spectral absorption characteristics of each mineral, a kind of “spectral checklist” for the study was created. For each mineral, it was documented as:

- Absorption band positions: These are the exact wavelengths where each mineral absorbs light. For example, phosphate minerals often have absorption bands around 2.16 microns in SWIR.
- Reflectance behaviors: This refers to how the mineral reflects light, particularly in the TIR range, where key minerals show unique patterns.

This knowledge served as the foundation for selecting the bands from the hyperspectral data that were most likely to detect each type of mineral. By zeroing in on these specific wavelengths, the presence and concentration of key minerals within the phosphate mine environment could be better identified.

The literature review was an essential part of this process, acting as a bridge between theoretical spectral knowledge and practical application in remote sensing. By consulting a variety of academic studies, spectral libraries, and past research on Moroccan phosphate mines, an understanding of how to approach the spectral analysis for each mineral group was acquired. The result was a well-defined set of spectral targets, which paved the way for the band math and mineral detection steps that followed in our analysis.

### 3.3.3 ECOSTRESS Image Processing

To prepare the ECOSTRESS data for mineral detection, a series of key steps were undertaken to ensure the accuracy and relevance of the data for hyperspectral analysis. These steps were essential in transforming the raw thermal emission data into actionable information for identifying surface minerals.

The ECOSTRESS images used in this study are Level 2 data, consisting of five spectral bands that capture thermal emission from the Earth's surface. In remote sensing, Level 2 data refers to products that have been pre-processed to a certain extent, including geo-correction, atmospheric correction, and calibration, making them suitable for specific scientific analyses. The Level 2 processing ensures that the data can provide accurate surface temperature and emissivity information, which is crucial for detecting mineral characteristics.

To work with the Level 2 ECOSTRESS images, the conversion from HDF5 format to GeoTIFF was accomplished using a script from NASA's GitHub repository, making the data suitable for GIS and remote sensing applications. For further processing, the Python package rasterio was employed, which is an efficient tool for handling geospatial raster data. Rasterio enables the reading, manipulation, and transformation of raster files, such as the ECOSTRESS data in GeoTIFF format. This package supports various operations, including resampling, reprojecting, and spatial subsetting, which facilitated the preparation and analysis of the thermal emission data for mineral detection in this study.

The ECOSTRESS images downloaded were captured during nighttime/early morning at (04:26:51 UTC) to minimize the impact of surface temperature fluctuations on the emissivity data. This timing helps reduce temperature variability, allowing for more accurate emissivity measurements, as surface temperature differences are less pronounced during these hours. The specific datasets worked with were:

ECOSTRESS-L2-LSTE-28137-005-20230623T042651-0601-01-Emis1-UTM.tif  
ECOSTRESS-L2-LSTE-28137-005-20230623T042651-0601-01-Emis2-UTM.tif  
ECOSTRESS-L2-LSTE-28137-005-20230623T042651-0601-01-Emis3-UTM.tif  
ECOSTRESS-L2-LSTE-28137-005-20230623T042651-0601-01-Emis4-UTM.tif  
ECOSTRESS-L2-LSTE-28137-005-20230623T042651-0601-01-Emis5-UTM.tif

Each of these files represents different wavelength bands in the thermal infrared region, capturing the thermal energy emitted from the Earth's surface. This information, when processed and analyzed, is key to understanding surface materials, including minerals in the phosphate mining region of study.

- The first step in processing the ECOSTRESS images was "georeferencing". This was a critical task to ensure that the spatial data was properly aligned with a known geographic coordinate system (WGS 1984, UTM-zone-29N). Without proper georeferencing, the images would not accurately reflect the real-world locations of the mining areas under investigation.

- One of the key aspects of working with ECOSTRESS data is understanding that it captures thermal emission rather than surface reflectance. However, since our goal was to detect surface minerals, a conversion from the thermal emittance data into reflectance values was needed. This transformation allows us to analyze how much of the incoming light is reflected by surface materials, which is essential for mineral identification.

-Reflectance Calculation from Emissivity:

To convert emissivity into reflectance, the following relationship derived from the Kirchhoff's law of thermal radiation was used:

$$R = 1 - \varepsilon \quad (3.3)$$

- R is the reflectance of the surface.

-  $\varepsilon$  is the emissivity of the surface.

The formula reflects that a surface with high emissivity will have low reflectance and vice versa. Using this band math, you can convert the emissivity data from the ECOSTRESS images into reflectance values for mineral identification.

To perform this conversion, band math techniques were applied. Band math involves applying mathematical operations to the pixel values in the spectral bands, transforming them from thermal emission to surface reflectance values. By doing this, the amount of light reflected from the surface was calculated, which enabled us to detect the spectral signatures of minerals.

- Layer Stacking: The ECOSTRESS images consist of five spectral bands, each capturing different wavelength data. These bands were integrated into a single

multi-band image through layer stacking. This process involved loading each band separately, combining them into a multi-dimensional array, and saving the array in a format such as GeoTIFF, which supports multi-band data. This step enabled comprehensive spectral analysis across all bands.

- Metadata Editing: To ensure that our spectral analysis was accurate, the metadata for the ECOSTRESS images was correctly configured. This included adding essential information about the wavelengths captured by each band and their Full Width at Half Maximum (FWHM) values, which represent the range of wavelengths covered by each band.

Together, these steps formed a robust methodology for processing the ECOSTRESS hyperspectral data, setting the stage for accurate mineral detection in the phosphate mining region. The combination of georeferencing, emittance-to-reflectance conversion, layer stacking, and careful metadata editing ensured that the images were properly prepared and ready for detailed spectral analysis.

### 3.3.4 EMIT Image Processing

The processing of EMIT hyperspectral data followed a structured approach. Each step in this process was designed to extract as much valuable data as possible from the EMIT images while tailoring it to the specific conditions of the phosphate mine under study.

The EMIT dataset used in this analysis,

**Dataset Name:** EMIT-L2A-RFL-001-20220819T140214-2223109-001

was captured on August 19, 2022, and contains reflectance data across 244 spectral bands with spectral range between 381 to 2493 nm. Each pixel in the image covers approximately 87.5 x 94.5 meters, which is detailed enough to detect the spatial variations of minerals across the phosphate mine. The image dimensions were 590 x 489 pixels, providing a comprehensive view of the area.

The key characteristics of the dataset included:

- Sensor: EMIT (Earth Surface Mineral Dust Source Investigation)
- Product Level: L2A
- Projection: UTM, Zone 32 North, using the WGS-84 datum

Reprojection and Resizing: The EMIT images were first reprojected to UTM, Zone 32 North to align with the study area's spatial reference system. The images were then resized to focus on the specific area of interest within the phosphate mine.

Vegetation Suppression: Vegetation in the image was suppressed using the algorithm of vegetation suppression in ENVI to isolate the mineral reflectance data. This



step was crucial for ensuring that the mineral signals were not masked or confused by vegetation cover, thus improving the accuracy of the mineral detection process.

### 3.3.5 Spectral Library Resampling

Once the images were prepared, the next step involved selecting the spectral signatures of the target minerals from the ENVI spectral library:

- SWIR and TIR Signatures: Minerals with SWIR spectral features were identified using Perkin and Beckman spectral analyzers, while those with TIR features were examined using Nicolet spectral analyzers. Data was sourced from the ASTER spectral library embedded within ENVI, which contains reference spectral data for a wide range of minerals.
- Resampling: The spectral signatures were resampled to match the spectral resolution and band configuration of the ECOSTRESS and EMIT sensors. This resampling ensured that the reference spectral data could be accurately compared with the hyperspectral data from the sensors, preserving the integrity of the mineral absorption features.

### 3.3.6 Development of Band Math Equations for Mineral Feature Detection

With the resampled spectral data, band math equations were developed to highlight the specific absorption features of the target minerals:

- Relative Absorption Band Depth (RBD): The RBD technique was used to enhance mineral absorption features in the hyperspectral images. This method involves calculating the ratio between the spectral channels at the absorption band shoulders and the band minimum, creating a diagnostic image for the target mineral.[46]
- Feature Detection and Stretching: Reflectance values from the band math equations were used to determine the absorption feature, applying a stretch value range of  $\pm 5$  percent to account for natural variations in reflectance. This fine-tuning ensured that the mineral features were detectable despite environmental variability.

### 3.3.7 Raster Color Slice for Mineral Visualization

To visualize the spatial distribution of the detected minerals, a raster color slice was applied to the processed images:

- Color Coding: The raster color slice assigned different colors to regions where the spectral features, as defined by the band math equations, fell within the calculated stretch value range. This technique provided an intuitive visual representation of the mineral occurrences within the phosphate mine.
- Mineral Mapping: By applying this color coding, areas with high concentrations

of specific minerals were easily identifiable, facilitating a clearer understanding of the mineral distribution patterns. This visualization was particularly useful for identifying regions of interest for further geological analysis or mining operations.

### **3.3.8 Validation**

To ensure the reliability of the mineral detection process, a validation step was included. This involved comparing spectral profiles from randomly selected pixels in color-sliced regions against reference spectra from the ENVI spectral library. These comparisons focused on key diagnostic wavelengths associated with the target minerals. A close spectral match between the field data and reference spectra, especially at critical absorption features, verified the accuracy of the detected mineral signatures. This validation provided additional confidence in the methodology by confirming the consistency between the extracted spectral features and established mineral characteristics.

## Chapter 4

# Results and Discussion

## 4.1 Results of NDVI Analysis

### 4.1.1 NDVI for the year 2023

The black-and-white NDVI analysis for 2023 provides a valuable grayscale portrayal of vegetation health across the Khouribga region, highlighting seasonal changes and environmental stress patterns. Through this monochromatic representation, monthly shifts in vegetation density and health become visually distinct, with lighter shades indicating areas of denser, healthier vegetation and darker shades reflecting sparser or more stressed plant cover. This chronological progression reveals the impact of seasonal dynamics on vegetation growth and decline, reflecting the cyclical patterns that influence vegetation health in response to varying temperatures and moisture availability throughout the year. By examining these trends, the analysis underscores the annual vegetation cycle within a semi-arid, mining-impacted landscape, where peak growth and subsequent seasonal decline are evident. This nuanced, month-by-month view sets the foundation for understanding how environmental factors shape vegetation resilience and degradation within the study area.

#### **February2023**

In February, the landscape appears mostly dark gray to medium gray, suggesting moderate vegetation health and coverage. This aligns with early spring, as vegetation is just beginning to emerge from dormancy, but the growth is still in its early stages.

#### **March2023**

March shows an increase in lighter areas, particularly in the central and southern regions, indicating a significant improvement in vegetation health. Compared to February, there is much lighter gray and white, suggesting that vegetation density has increased, likely due to early spring growth. March stands out as the month with the largest spread of healthy vegetation in the black-and-white series, showing a peak in plant coverage and health.

#### **April2023**

While April still shows a considerable amount of light gray and white areas, there is a slight decrease in vegetation density compared to March. This indicates that the vegetation has not grown much further or may have started to stabilize. The reduction in lighter areas suggests that April does not surpass the early surge seen in March.

### May2023

By May, there is a visible reduction in lighter areas, with the landscape appearing predominantly medium gray. This suggests that vegetation is starting to experience stress or decline, likely due to the increasing temperatures and reduced moisture levels as summer approaches.

### June2023

June shows a further landscape darkening, with fewer light gray areas and more dark gray regions. This suggests a continued decline in vegetation health, as the summer heat and drier conditions affect plant cover. Vegetation is sparser and less healthy compared to the previous months.

### July2023

July presents the darkest imagery in the sequence, with most of the landscape showing dark gray to black areas. This indicates that vegetation has significantly declined, with the plants experiencing stress, senescence, or even die-off. The health of the vegetation is at its lowest point, corresponding to the height of the summer season.

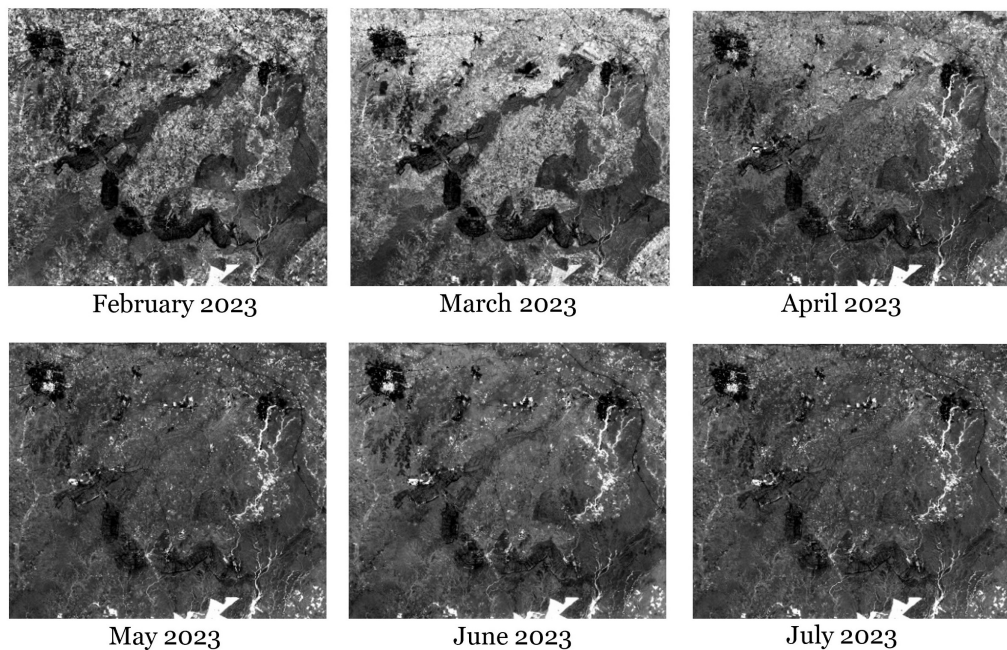







**Figure 4.1:** NDVI result for different months of 2023

### 4.1.2 Color-Sliced NDVI (Detailed Vegetation Health Classification)

The color-sliced NDVI analysis for 2023 offers a detailed classification of vegetation health, with each color representing specific NDVI value ranges that correlate with varying levels of vegetation density and health. By segmenting the landscape into distinct color-coded categories—ranging from dense, flourishing vegetation (yellow) to sparsely vegetated or stressed areas (black and blue)—this analysis allows for a clearer, more nuanced visualization of the vegetative landscape across different months. This method highlights seasonal patterns in vegetation health, illustrating how plant density and condition respond to environmental factors like temperature and moisture availability. Through this month-by-month assessment, significant trends emerge, with peak growth observed in early spring (March) followed by a gradual decline as summer progresses.

The color table breaks down the NDVI values into distinct categories:

	Color	Slice Min	Slice Max
1		-0.105339	0.000000
2		0.000000	0.170000
3		0.170000	0.250000
4		0.250001	0.350000
5		0.350001	0.853351

**Figure 4.2:** Classification table for raster color slice of 2023

Red (-0.105 to 0.0): Represents non-vegetative surfaces like bare soil or water bodies.

Black (0.0 to 0.17): Indicates sparsely vegetated areas or stressed vegetation.

Blue (0.17 to 0.25): It shows low vegetation health but still has some coverage.

Purple (0.25 to 0.35): Represents moderately healthy vegetation.

Yellow (0.35 to 0.85): Indicates dense, healthy, and flourishing vegetation.

The yellow areas represent the highest NDVI values (0.35 to 0.85), indicating the densest and healthiest vegetation, while black and blue areas indicate sparser or stressed vegetation.

#### February 2023

The NDVI values are distributed mostly across the lower range, with a lot of blue and purple areas. This suggests that vegetation is just starting to grow, as February marks the beginning of the early spring growth phase. There is a very limited

spread of yellow areas, which indicates that the vegetation health is not at its peak yet.

### **March 2023**

In March, there was a notable increase in yellow areas, which represented dense and healthy vegetation. March seems to show the largest spread of healthy vegetation for the year, with the greatest extent of high NDVI values (0.35 to 0.85). The early growth surge in March suggests very favorable conditions for vegetation growth, perhaps due to sufficient rainfall or optimal temperatures.

### **April 2023**

April shows a slight reduction in the extent of yellow areas compared to March. While the month is still characterized by healthy vegetation, with a fair amount of yellow and purple, it does not surpass March in terms of vegetation density. This may suggest that the vegetation reached an early peak in March and began stabilizing or declining slightly in April.

### **May 2023**

May shows a substantial reduction in yellow areas, with blue and purple becoming more dominant. This indicates that vegetation health is beginning to decline as the summer months approach, likely due to heat stress and reduced moisture availability. The overall plant density and health are lower than in the previous months.

### **June 2023**

June exhibits mostly blue and purple, with very limited yellow areas. This suggests a further decline in vegetation health, likely due to continued summer stress. The peak summer heat is affecting the vegetation, and the landscape shows signs of senescence or stress.

### **July 2023**

July continues the trend of declining vegetation health, with even more blue areas and a minimal presence of yellow. The vegetation is under significant stress due to the prolonged summer heat and lower moisture availability, leading to widespread senescence.

### 4.1.3 Multi temporal Time Series of NDVI for 40-year period

The multi-temporal NDVI analysis conducted from 1985 to 2023 offers a detailed understanding of land cover transformations, supported by both the classification results and the summarized data in the table and graph.

The histograms next to each NDVI map display the distribution of NDVI values across the study area for the corresponding year. In 1985 and 1991, the peak of the histogram leans towards higher NDVI values (indicating more vegetation). However, from 1999 onwards, the peak shifts toward lower values, showing a trend toward reduced vegetation cover and increased land degradation. In 2023, there is a slight rebound, with the histogram peak moving slightly higher again, reflecting some vegetation recovery.

#### Color Classification

##### Green (High NDVI Values, $>0.6$ )

Green areas represent dense, healthy vegetation, typically forests or regions with strong plant growth. In the earlier years (especially 1985, 1991, and 1999), significant patches of green are visible, indicating extensive forest cover. However, this green diminishes in later years, reflecting the loss of dense vegetation.

##### Yellow (Moderate NDVI Values, $0.3-0.6$ )

Yellow areas indicate cultivated lands or shrublands. These areas are still photosynthetically active but are less dense than forests. Yellow dominates much of the landscape throughout all the years, showing areas where crops or less dense vegetation persist. In 2023, yellow occupies large sections, signaling the continued presence of cultivated lands.

##### Brown (Low NDVI Values, $0.2-0.3$ )

These colors correspond to sparse or degraded vegetation, typically found in shrublands or semi-arid regions. In the maps from later years (2004 onwards), the brown color becomes more prevalent, particularly in areas that were once more vegetated. This shift suggests land degradation and the decline of healthier vegetation over time.

##### Black (Very Low NDVI Values, $<0.2$ )

Black areas signify bare land or urban areas with minimal to no vegetation. These areas experience little to no photosynthetic activity, often corresponding to regions



affected by human activities, like mining or construction. In 1985, black regions were relatively sparse, but by 2009 and later, black regions increased, showing an expansion of barren areas.

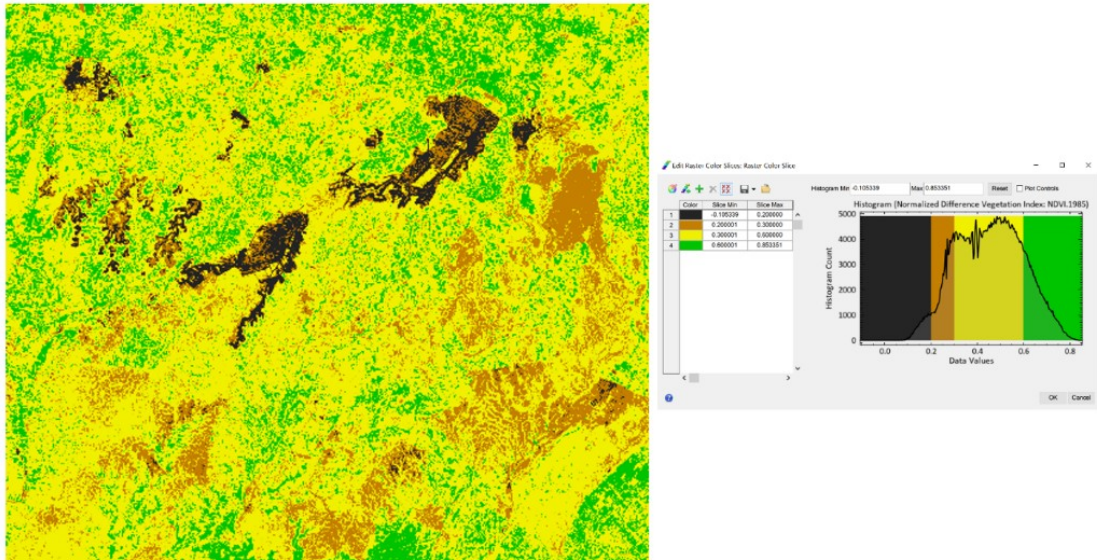


Figure 4.3: Color sliced NDVI trend for the year 1985

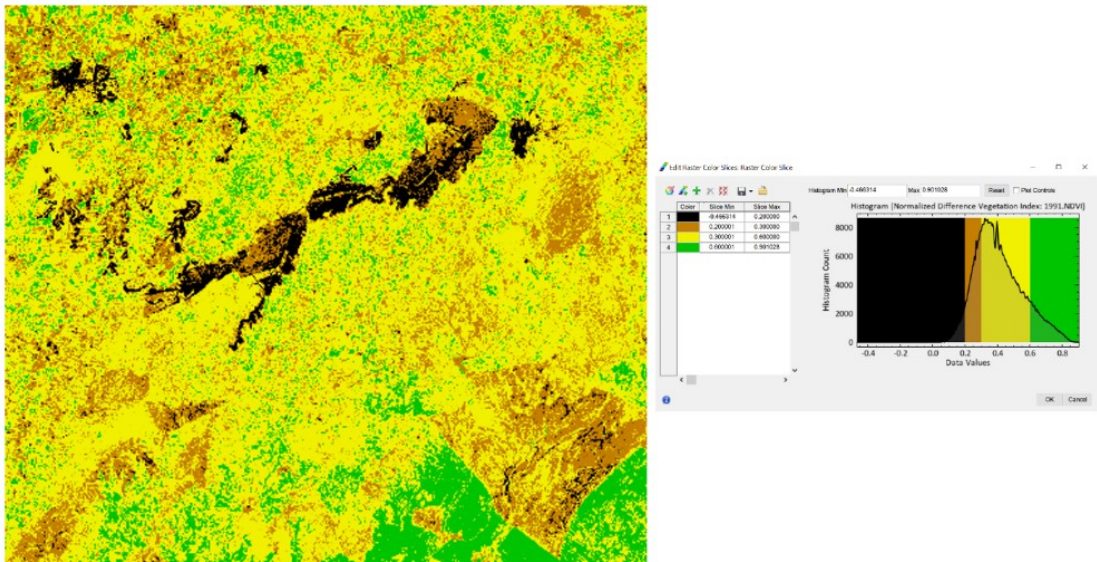


Figure 4.4: Color sliced NDVI trend for the year 1991

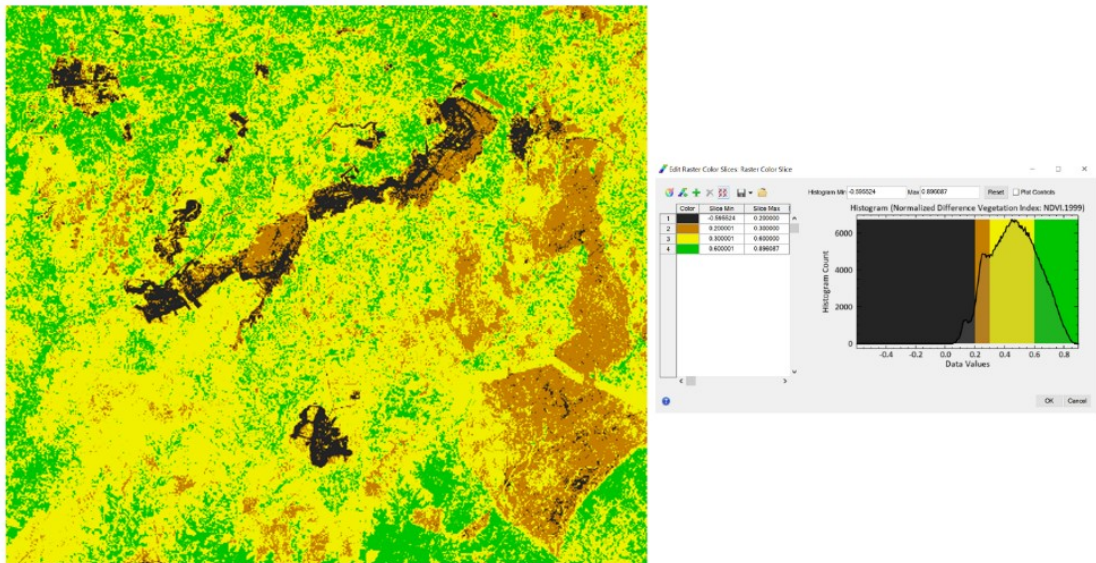


Figure 4.5: Color sliced NDVI trend for the year 1999

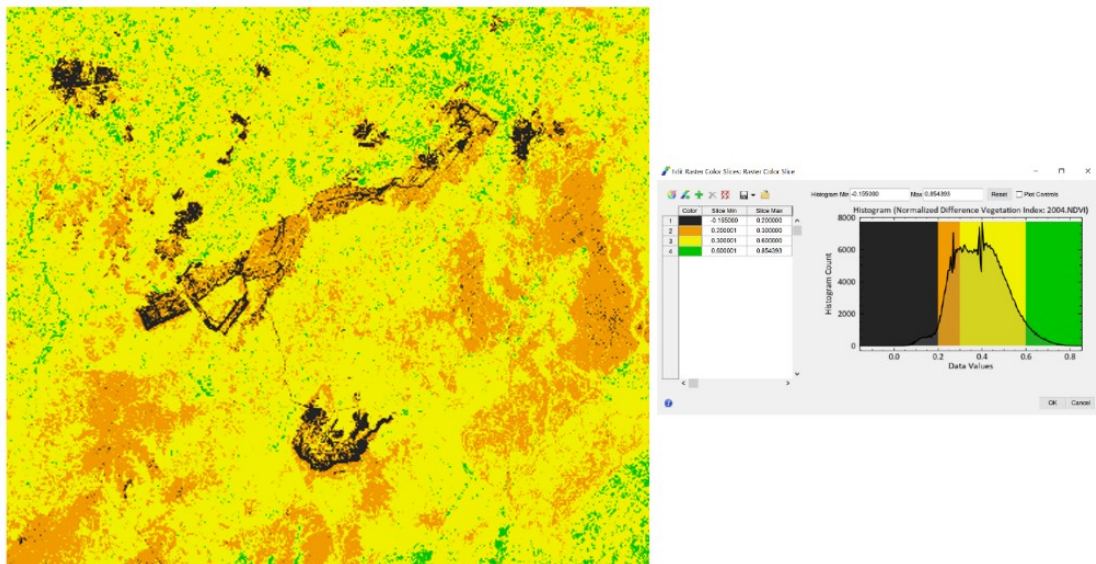


Figure 4.6: Color sliced NDVI trend for the year 2004



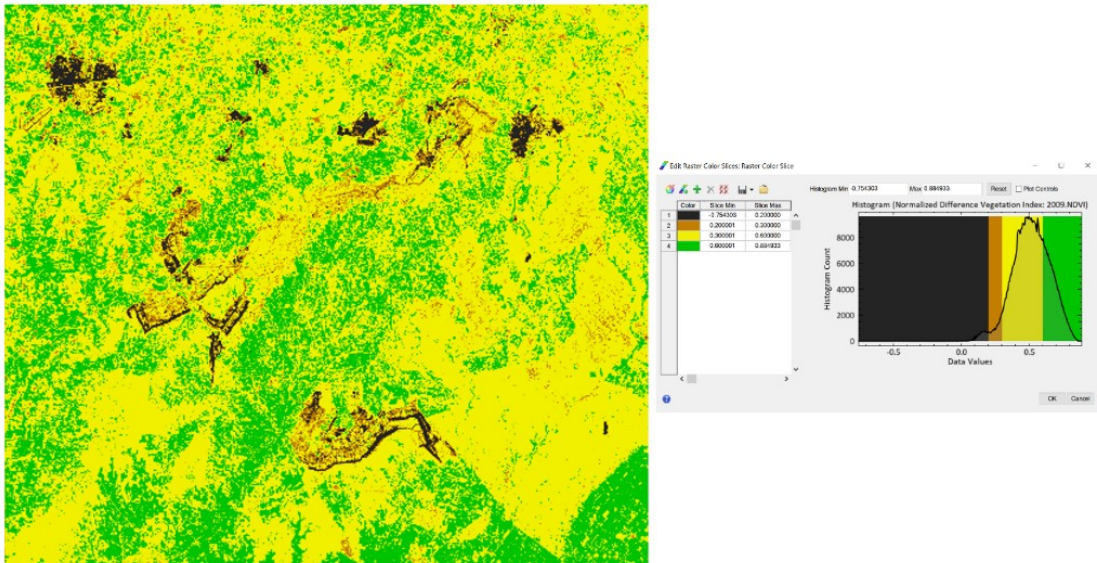


Figure 4.7: Color sliced NDVI trend for the year 2009

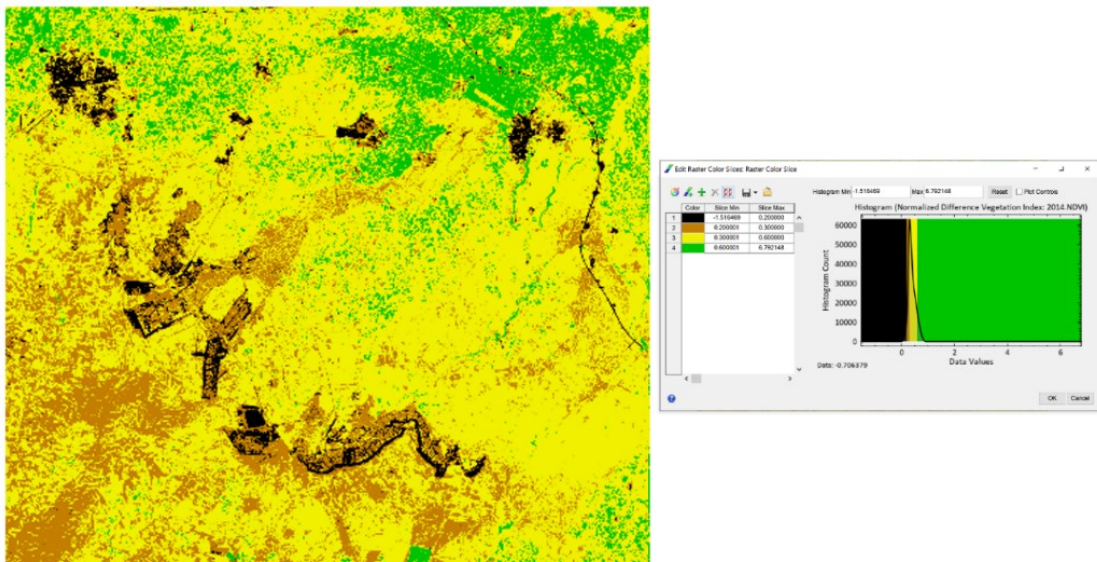


Figure 4.8: Color sliced NDVI trend for the year 2014

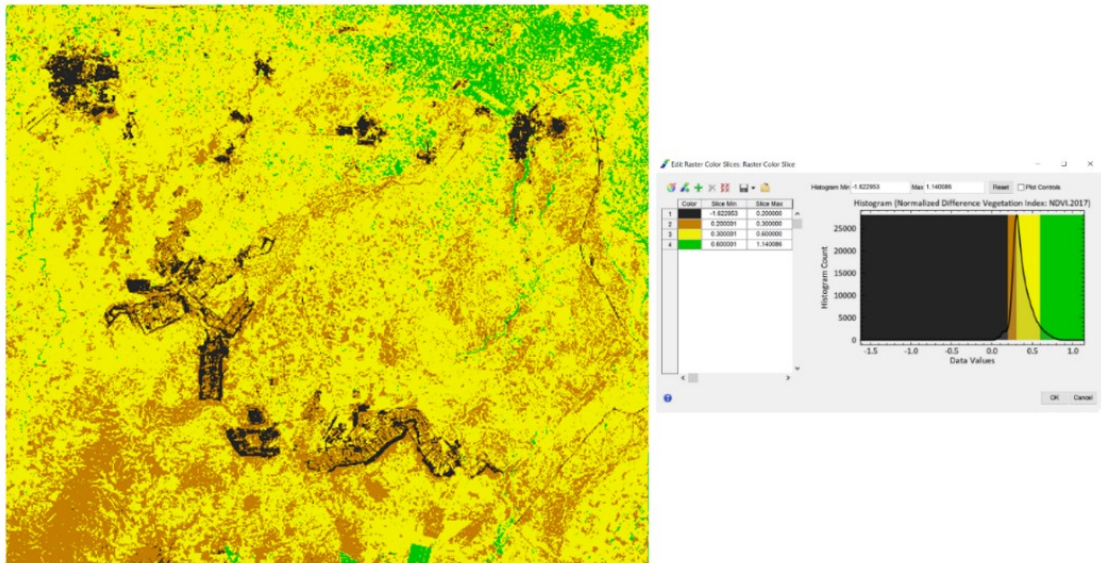


Figure 4.9: Color sliced NDVI trend for the year 2017

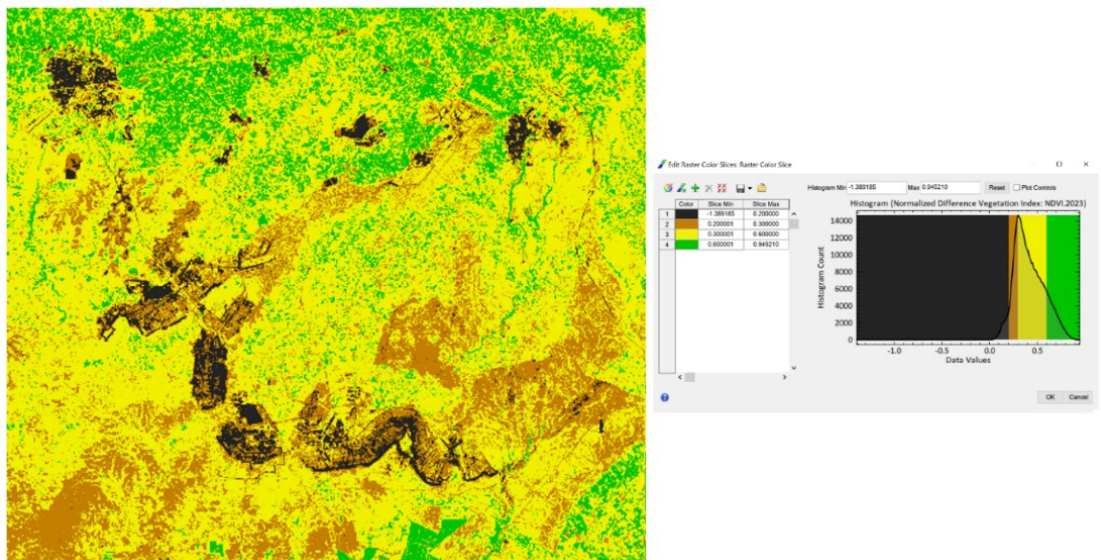
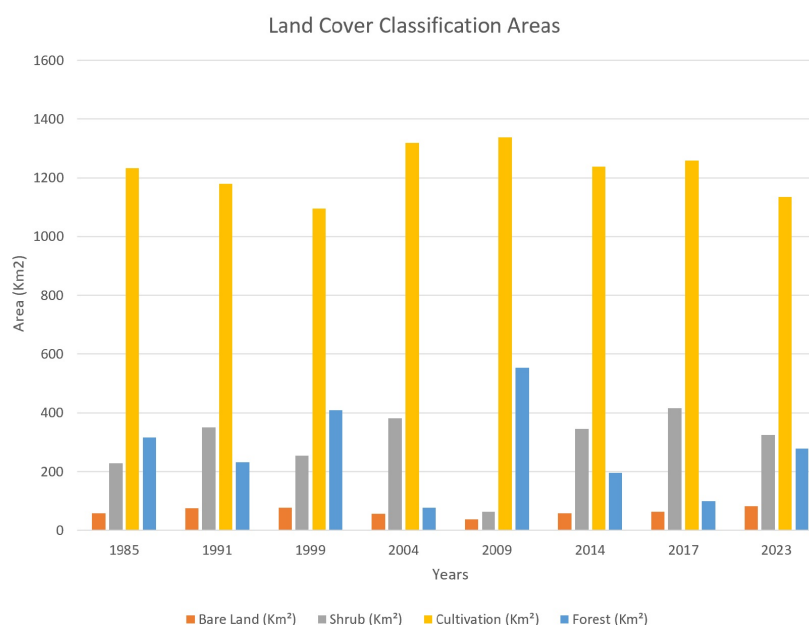


Figure 4.10: Color sliced NDVI trend for the year 2024

The table presents the areas (in square kilometers) for each of the four main vegetation types: bare land, shrubland, cultivated land, and forest over the selected years. The graph visually represents the fluctuations in these land cover types over the study period.

Year	Bare land area (Km2)	Shrub area (Km2)	Cultivation area (Km2)	Forest area (Km2)
1985	58.16	228.5	1233.7	316.1
1991	75.57	350	1179	231.9
1999	76.3	254.3	1096.2	409.7
2004	56.87	382.1	1319.8	77.69
2009	36.69	63.35	1337.7	554.3
2014	58.34	344.96	1238.3	194.8
2017	63.25	415.07	1258.9	99.24
2023	81.68	324.26	1135	277.6

**Table 4.1:** Land Cover and Vegetation Area Classification (Km<sup>2</sup>) from 1985 to 2023



**Figure 4.11:** Trends in Vegetation Classification Areas (1985-2023): Bare Land, Shrub, Cultivation, and Forest

### 1. Bare Land Area Expansion

According to the table and graph, bare land areas increased significantly from 1985 (58.16 km<sup>2</sup>) to 2023 (81.68 km<sup>2</sup>). This expansion is most prominent between 1991

and 1999, correlating with intensive mining activities and urban development in the region. The temporary decrease in 2009 (36.69 km<sup>2</sup>) is unusual but may be related to specific seasonal variations or re-vegetation efforts that later reverted. Overall, the progressive expansion of bare land reflects ongoing land degradation caused by anthropogenic factors such as mining, infrastructure development, and urban activities.

## **2. Shrubland Trends**

Shrubland, generally more resilient in semi-arid environments, fluctuated over the study period. In 1985, the area covered by shrubland was 228.5 km<sup>2</sup>, and it increased consistently, peaking in 2017 at 415.07 km<sup>2</sup>. However, it showed a slight decrease in 2023 to 324.26 km<sup>2</sup>. This dynamic indicates that shrublands are a transitional land cover that responds to land degradation but can also benefit from regrowth in degraded areas, depending on environmental management and land use practices.

## **3. Cultivated Land Decline**

Cultivated land exhibited significant changes, with its highest value in 2004 (1,319.8 km<sup>2</sup>) and a notable decline by 2023 (1,135 km<sup>2</sup>). The drop in cultivated area from its initial 1,233.7 km<sup>2</sup> in 1985 mirrors both the environmental impact of land degradation and possible shifts in agricultural practices. Increased urbanization and land being repurposed for mining operations likely contributed to the decline in cultivation. This reduction suggests a long-term shift away from agricultural sustainability in the region, further emphasizing the environmental stress imposed by mining.

## **4. Forest Area Degradation**

Forest areas were dramatically reduced from 316.1 km<sup>2</sup> in 1985 to 99.24 km<sup>2</sup> in 2017. This sharp decrease corresponds to widespread deforestation and land conversion for mining and urban development. However, by 2023, forested areas showed a promising recovery to 277.6 km<sup>2</sup>, suggesting that environmental policies or reforestation efforts may have been implemented to reverse some of the earlier damage. The fluctuating forest coverage in the graph demonstrates both the vulnerability of forest ecosystems to human activities and the potential for restoration under favorable conditions.



## 4.2 Results of Desertification Index

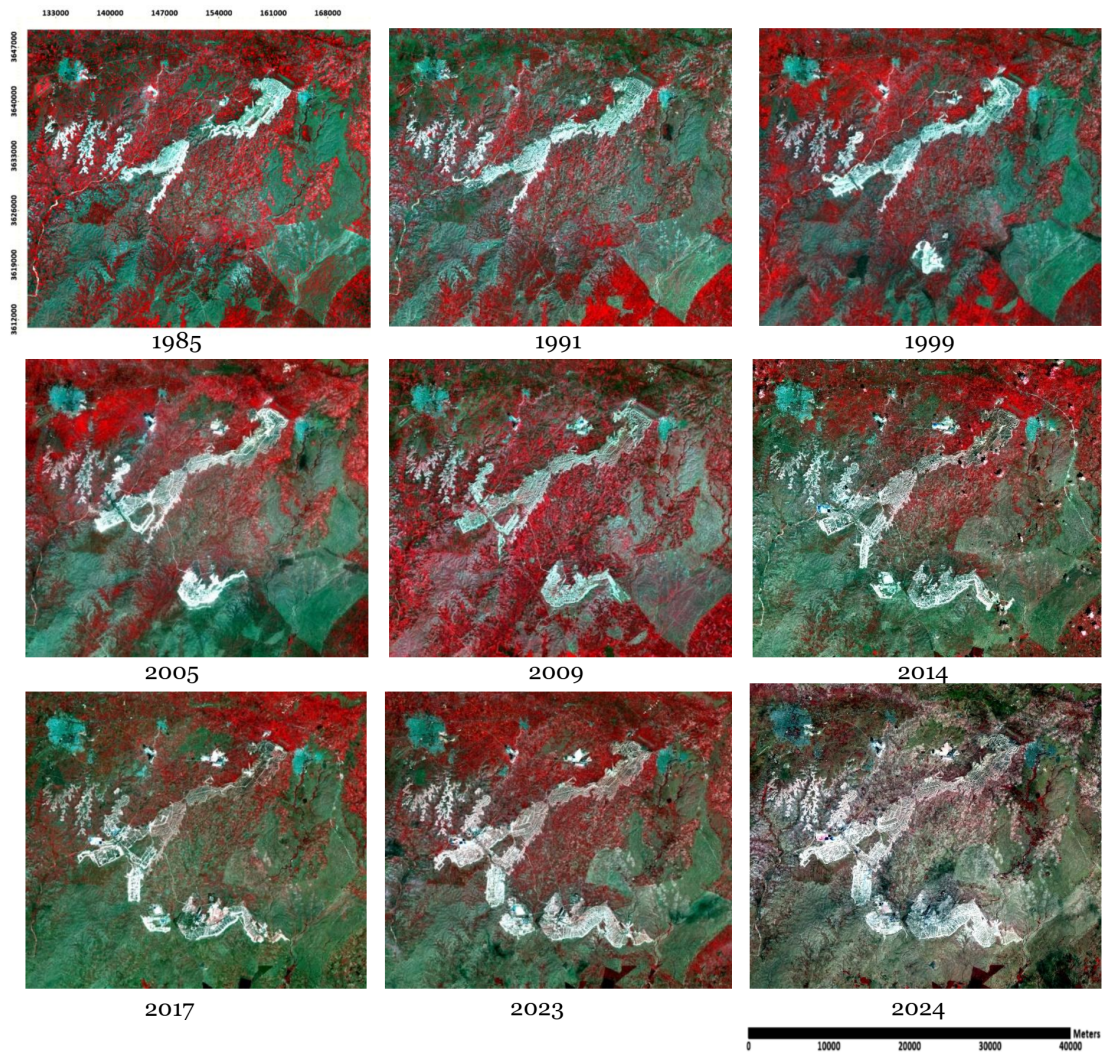
The multi-temporal desertification analysis for the Khouribga mine region, spanning from 1985 to 2024, provides a comprehensive assessment of ecological changes over nearly four decades. For each selected year, the analysis begins with Albedo and MSAVI imagery, which together capture critical information on surface reflectance and vegetation density. The Albedo images reveal patterns in soil and surface reflectivity, indicating areas with exposed soil and degradation, while the MSAVI images highlight vegetation density, offering insight into the health and spread of plant cover.

To further enhance understanding, a scatter plot classification is provided for each year, allowing for a detailed examination of land cover types based on the combined influence of MSAVI and Albedo values. This classification categorizes regions by land cover type and vegetation health, effectively distinguishing between barren areas, sparse vegetation, and densely vegetated zones. Finally, a classified map presents the spatial distribution of desertification intensity, identifying zones of severe, moderate, and mild land degradation within and around the mining area.



**Figure 4.12:** The classification of desertification for Khouribga region

Figure 4.13 categorizes desertification intensity within the Khouribga region into severe, moderate, and mild classifications, based on the calculated desertification index. Using color-coded zones, the map illustrates areas most affected by degradation, with severe desertification regions located in proximity to mining operations and other heavily impacted zones.



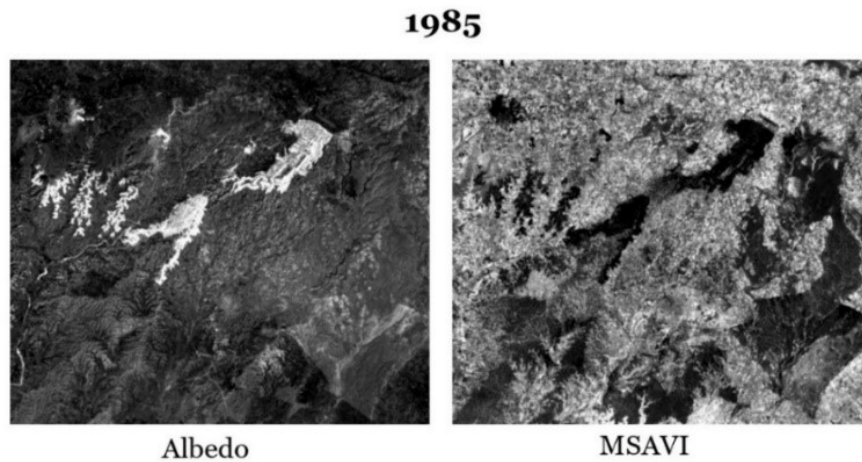
**Figure 4.13:** Desertification Index Assessment of the Khouribga Region: A Landsat-Based Temporal Study (1985–2024)

Figure 4.12 displays Landsat images for selected years, illustrating visible changes in land cover and vegetation around the Khouribga region over time.



1. 1985

Figure 4.16 illustrates that the land cover predominantly consists of areas experiencing moderate to severe desertification, particularly concentrated in the northern and central parts of the mining region. These areas are highlighted by fragmented red and blue patches, which indicate early signs of land degradation near mining activities. In contrast, the southwestern section is primarily characterized by yellow patches, representing mild desertification. This indicates a less degraded but still vulnerable landscape.



**Figure 4.14:** Albedo and MSAVI for Desertification Assessment in the Khouribga Region: 1985

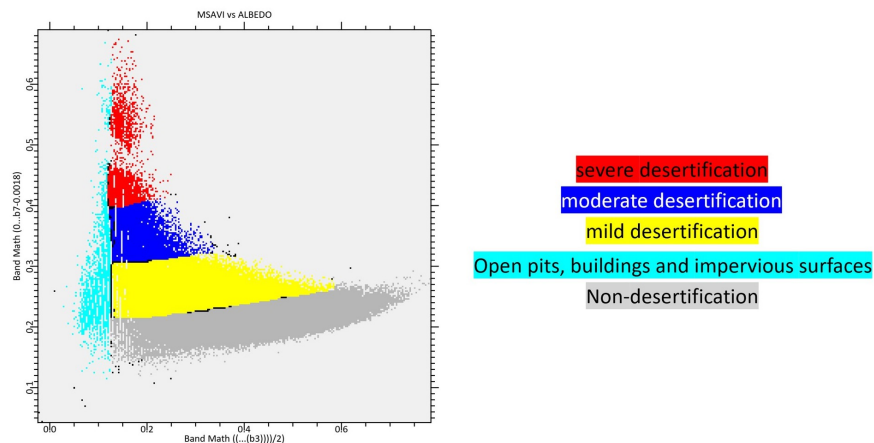


**Figure 4.15:** Albedo vs MSAVI scatter plot: 1985

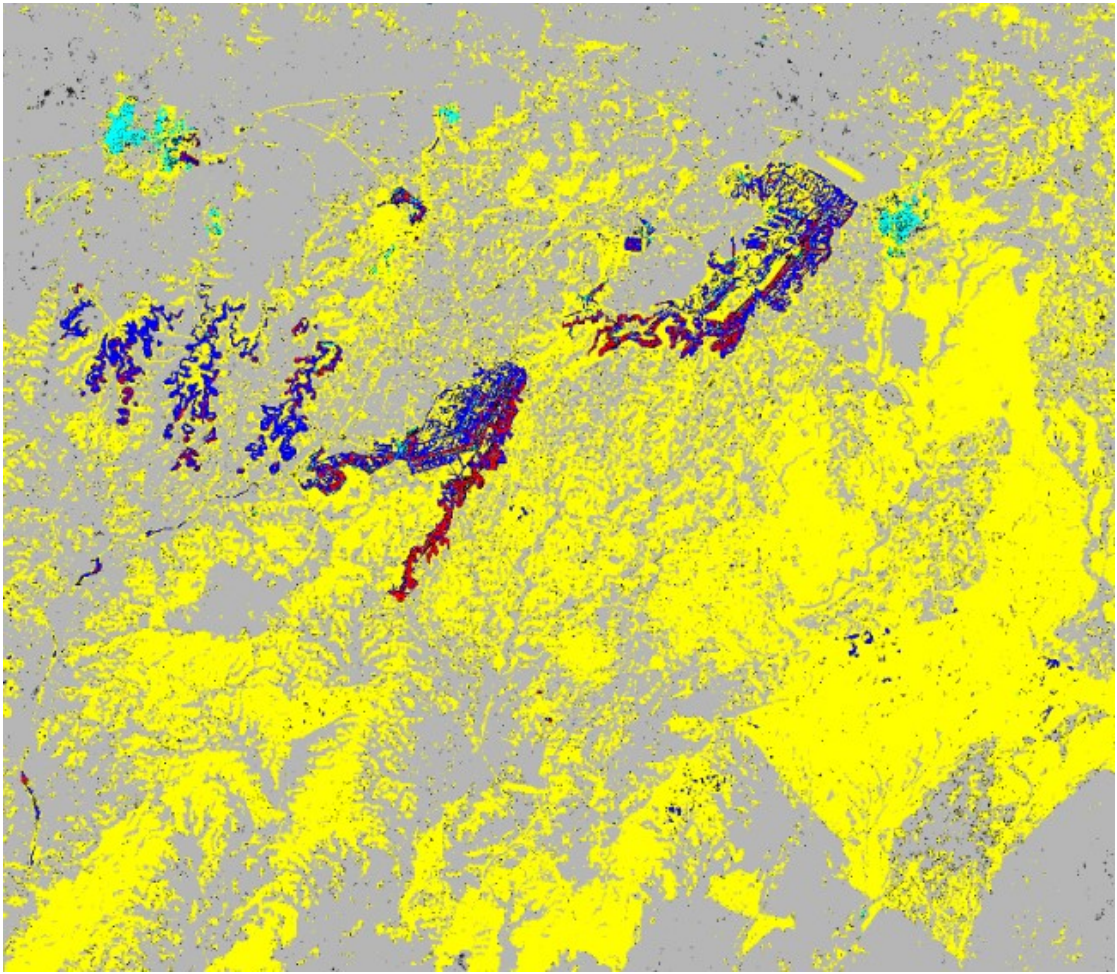


**Figure 4.16:** Spatial Distribution and Classification of Desertification: 1985

2. 1991

Figure 4.19 shows a slight expansion of red and blue areas compared to 1985, particularly in the central and northern parts of the map. The desertification process seems to advance in regions near active mining, reflecting increasing land degradation. Mild desertification (yellow) continues to spread towards the east.

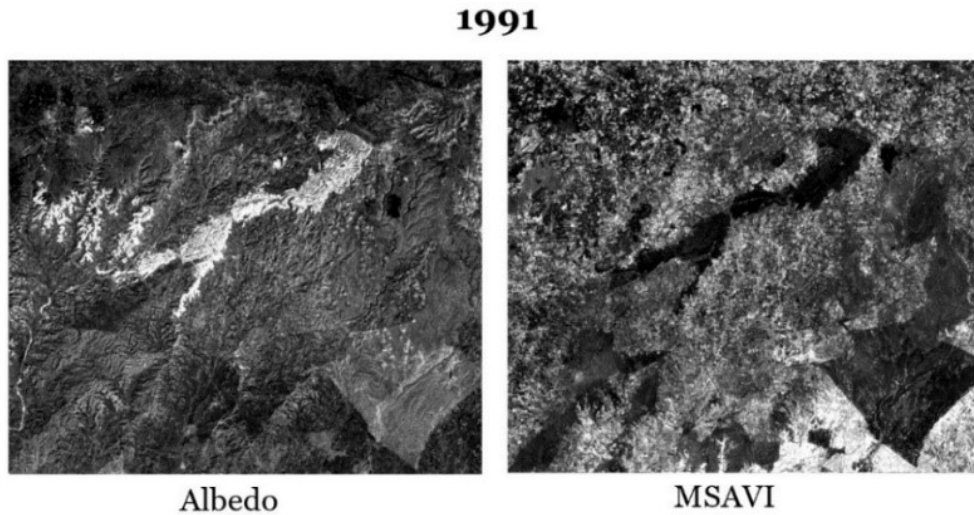


**Figure 4.17:** Albedo and MSAVI for Desertification Assessment in the Khouribga Region: 1991

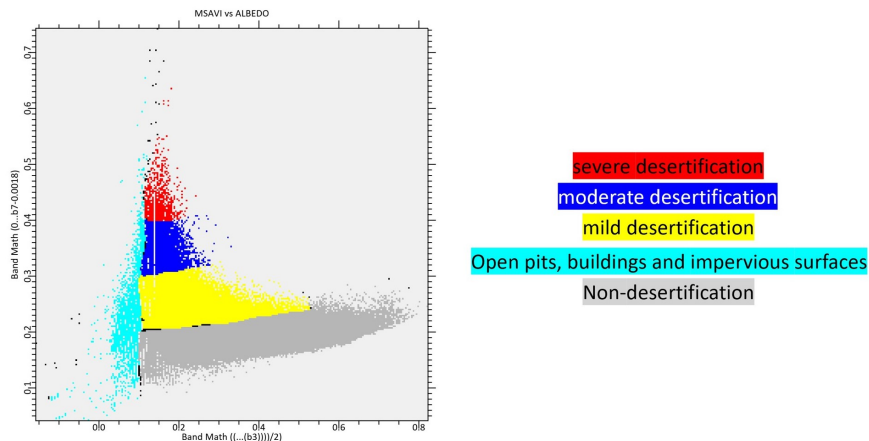


**Figure 4.18:** Albedo vs MSAVI scatter plot: 1991



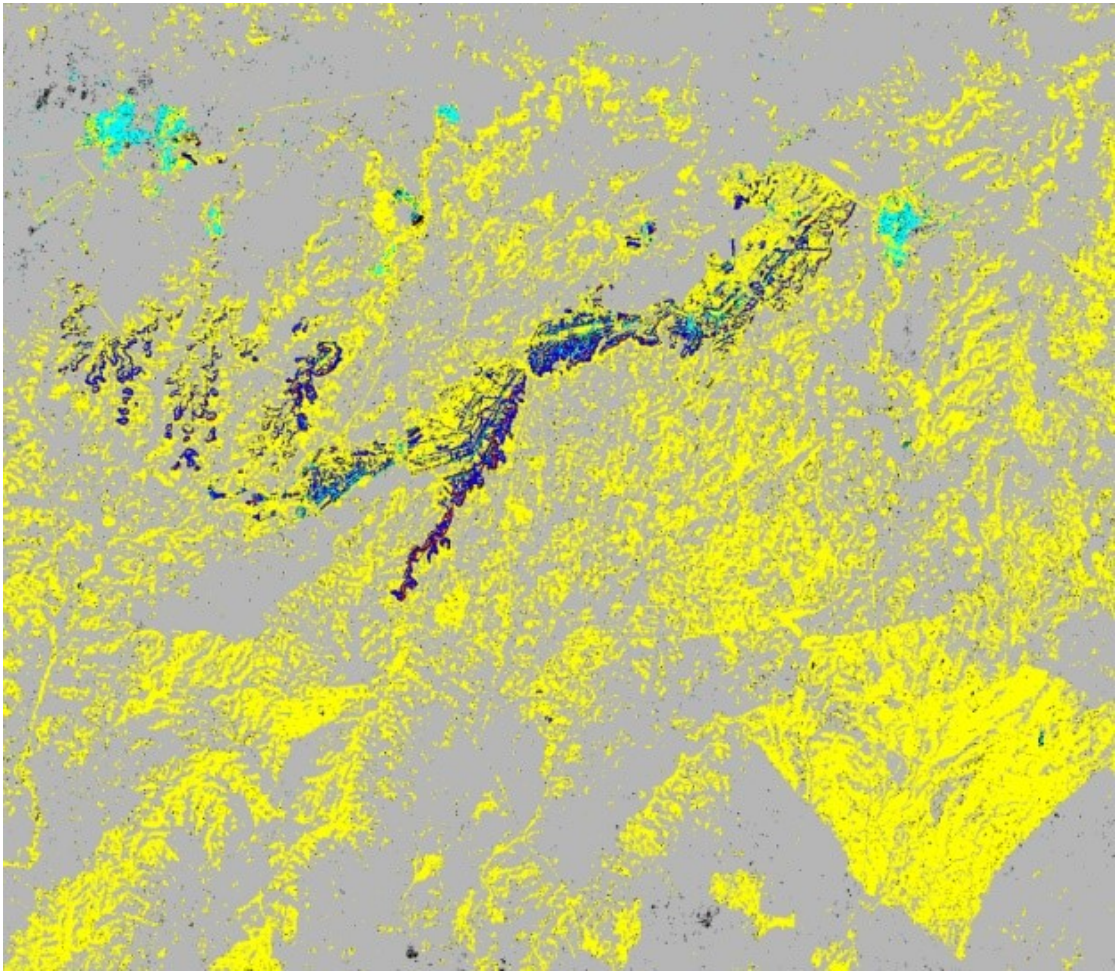


**Figure 4.19:** Spatial Distribution and Classification of Desertification: 1991

### 3. 1999

This year as in Figure 4.22 marks a continuation of desertification expansion, with severe and moderate areas (red and blue) becoming more prominent. The central region, where mining activities are likely more intensive, shows larger clusters of severe desertification. The yellow (mild desertification) areas also start covering more ground.

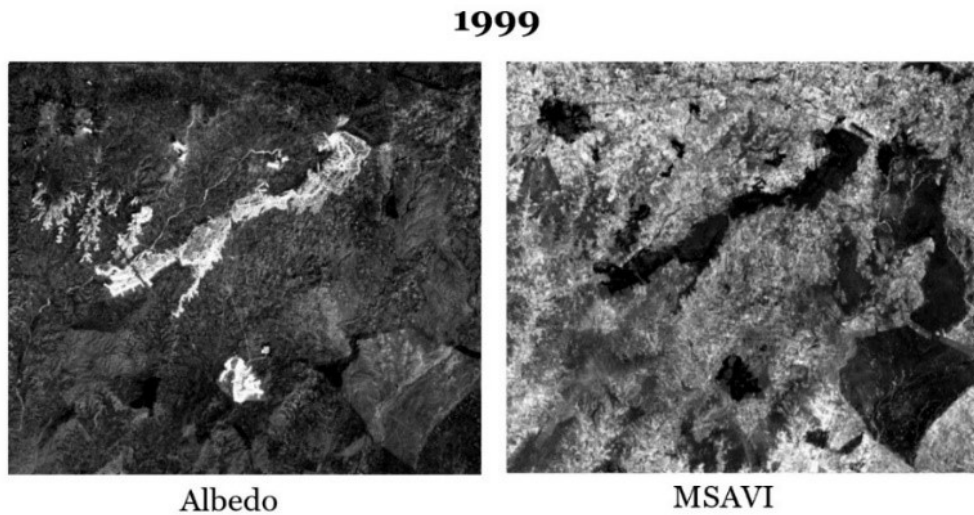


**Figure 4.20:** Albedo and MSAVI for Desertification Assessment in the Khouribga Region: 1999

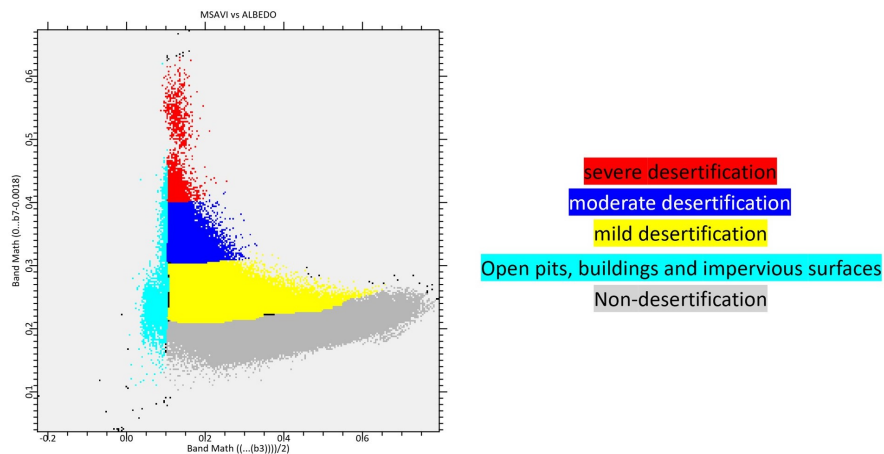


**Figure 4.21:** Albedo vs MSAVI scatter plot: 1999



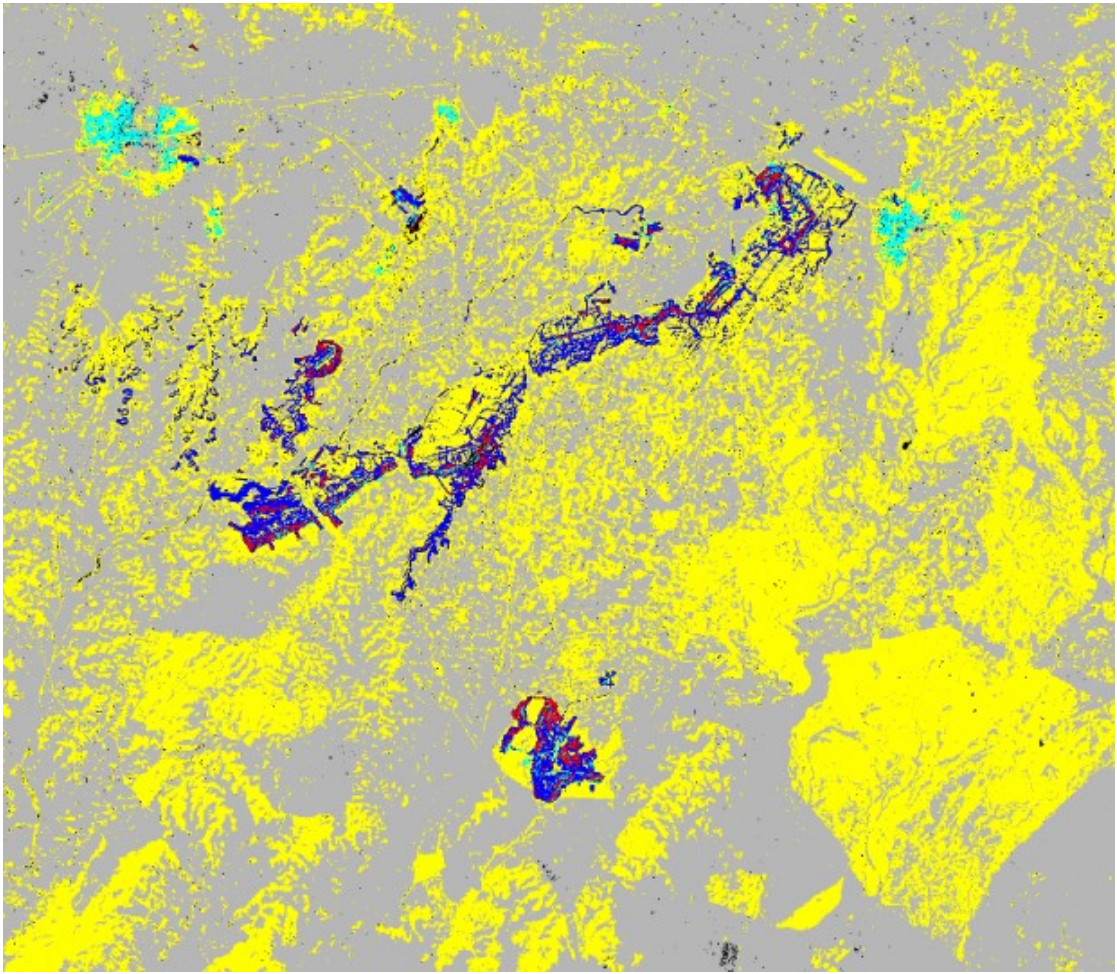


**Figure 4.22:** Spatial Distribution and Classification of Desertification: 1999

4. 2005

A notable reduction in severe desertification patches is observed as in Figure 4.25. Severe areas (red) shrink, potentially due to land restoration efforts or a temporary reduction in mining activities. However, blue and yellow areas expand further, indicating that while extreme degradation slowed, moderate and mild desertification continues to spread.

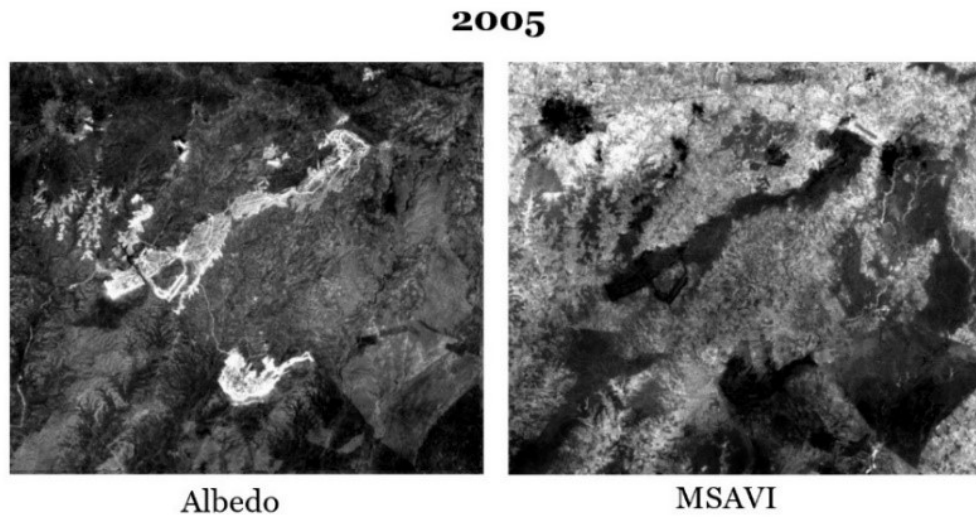


**Figure 4.23:** Albedo and MSAVI for Desertification Assessment in the Khouribga Region: 2005

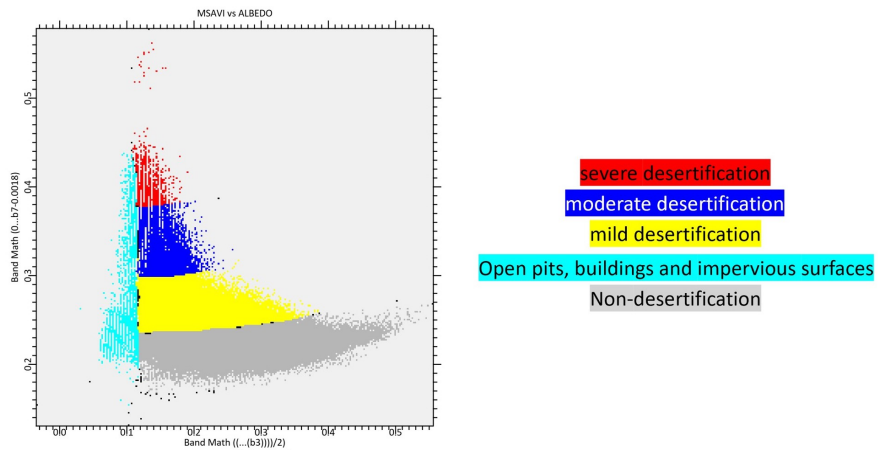


**Figure 4.24:** Albedo vs MSAVI scatter plot: 2005



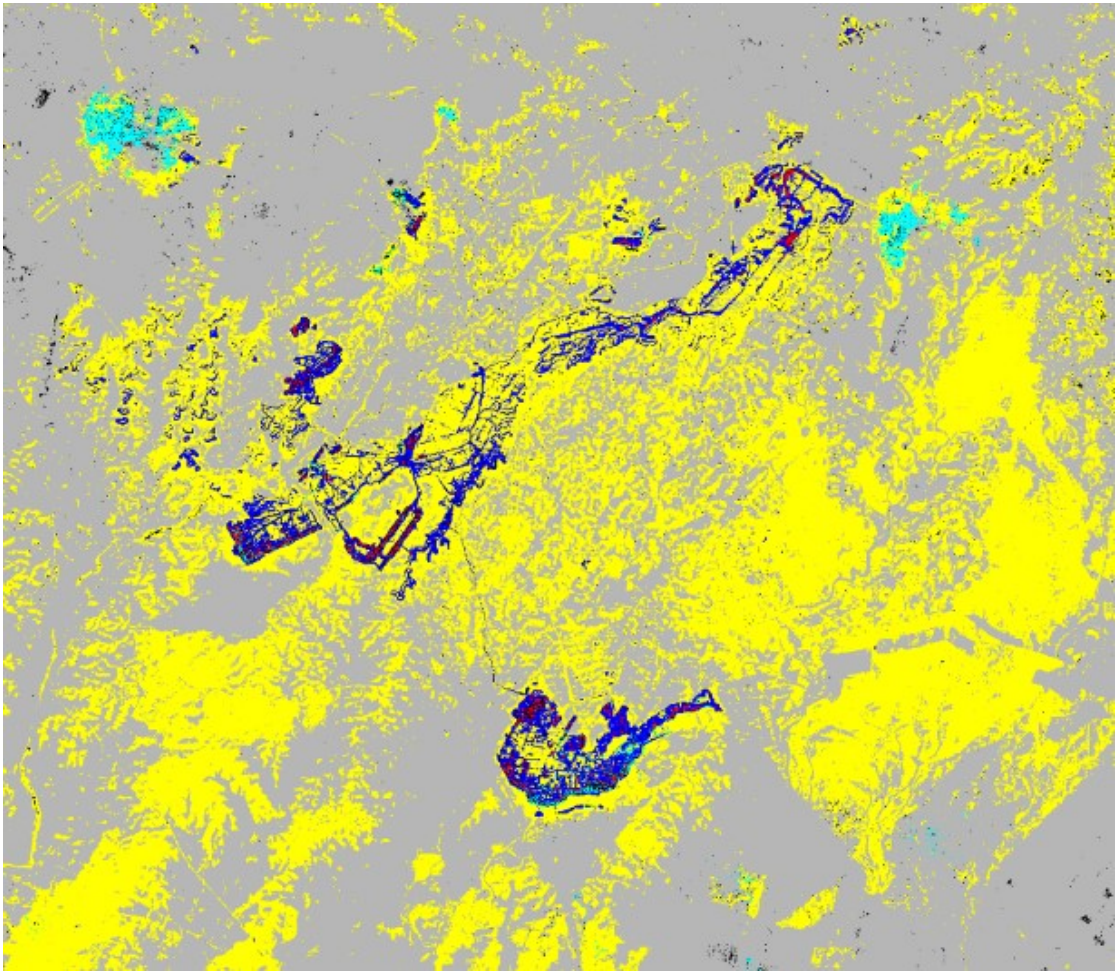


**Figure 4.25:** Spatial Distribution and Classification of Desertification: 2005



5. 2009

Figure 4.28 shows moderate desertification (blue) appears to stabilize, but yellow areas (mild desertification) expand considerably, especially in the central and western regions. The progression toward land degradation is evident, but the transition is gradual compared to previous years.

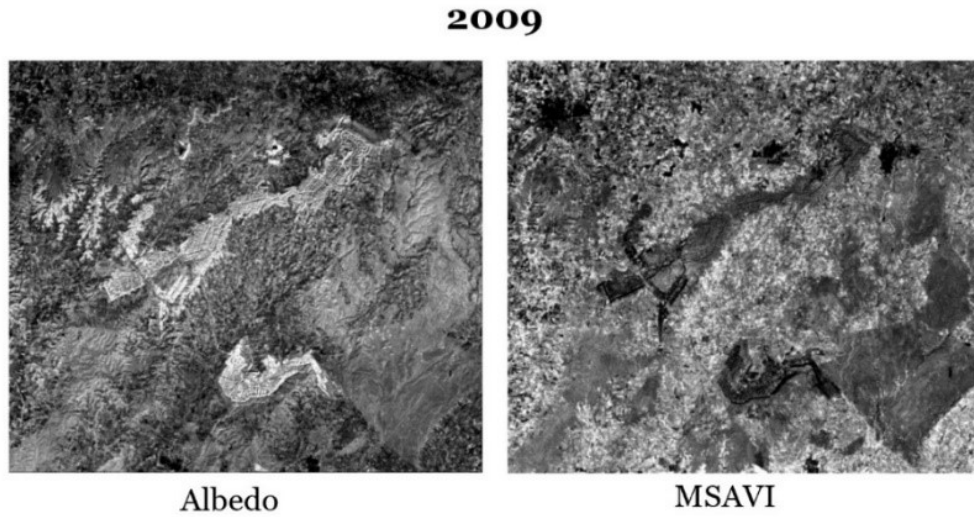


**Figure 4.26:** Albedo and MSAVI for Desertification Assessment in the Khouribga Region: 2009

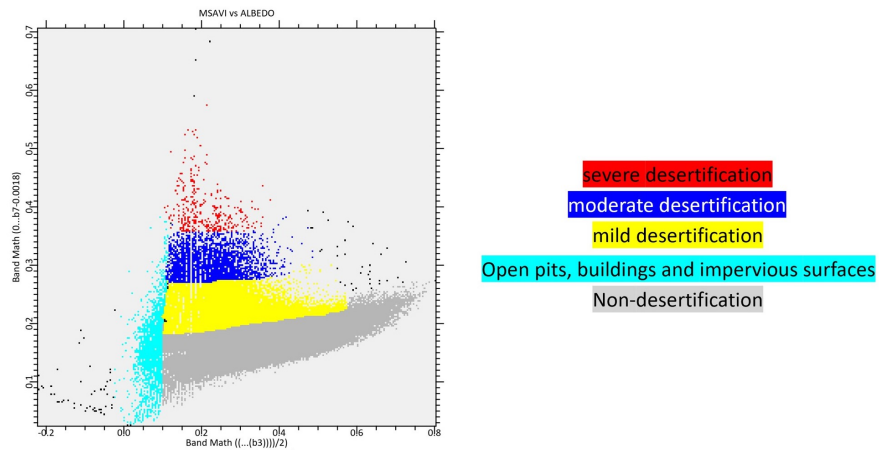


**Figure 4.27:** Albedo vs MSAVI scatter plot: 2009

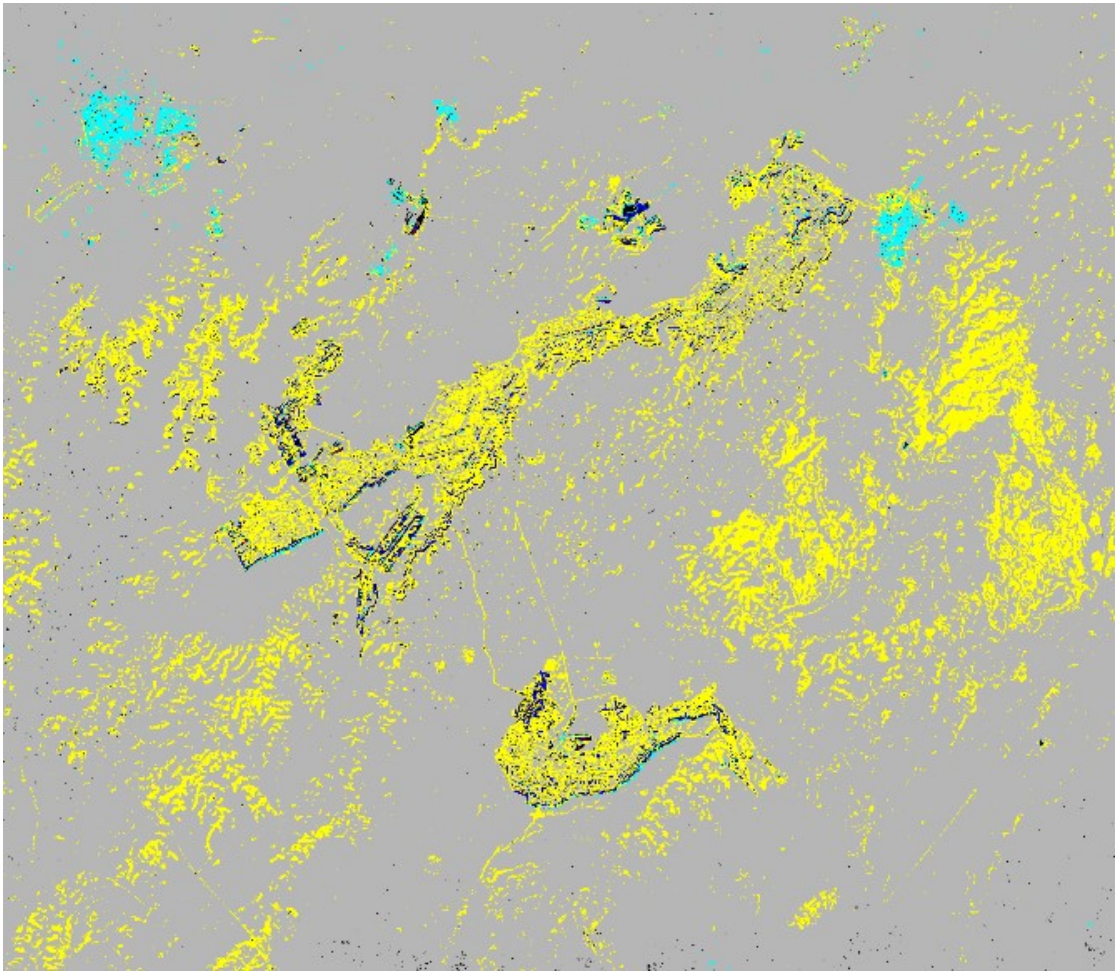


**Figure 4.28:** Spatial Distribution and Classification of Desertification: 2009

6. 2014

By this year, Figure 4.31, we see a resurgence of severe desertification (red) in the northern and central regions. The yellow and blue areas also become more pronounced, showing widespread mild and moderate desertification. The expansion of cyan regions suggests an increase in impervious surfaces and open pits, indicating more intense mining activities or infrastructure development.

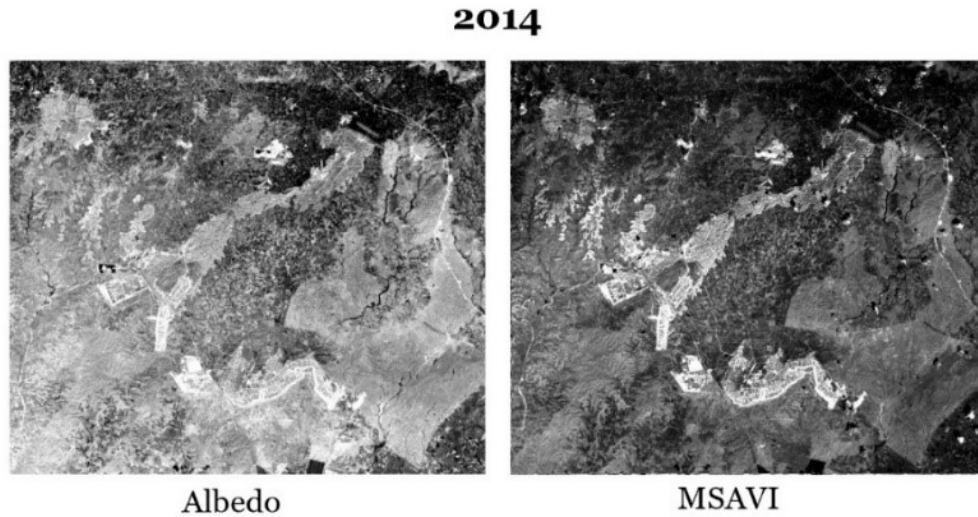


**Figure 4.29:** Albedo and MSAVI for Desertification Assessment in the Khouribga Region: 2014

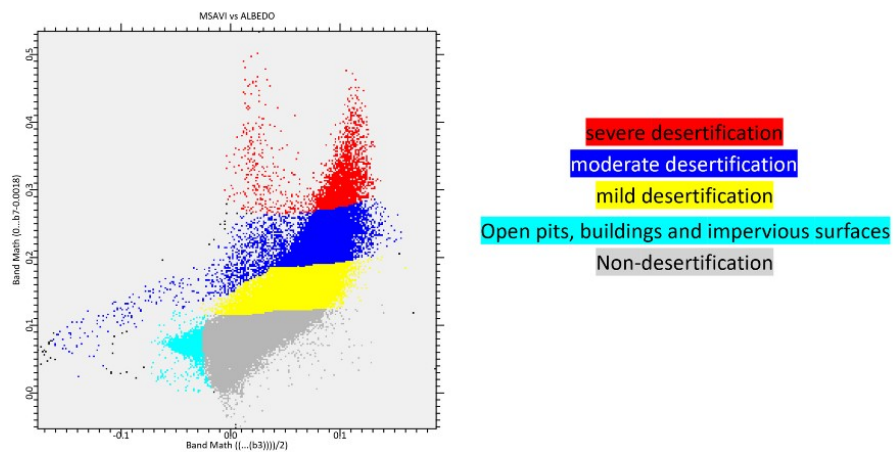


**Figure 4.30:** Albedo vs MSAVI scatter plot: 2014



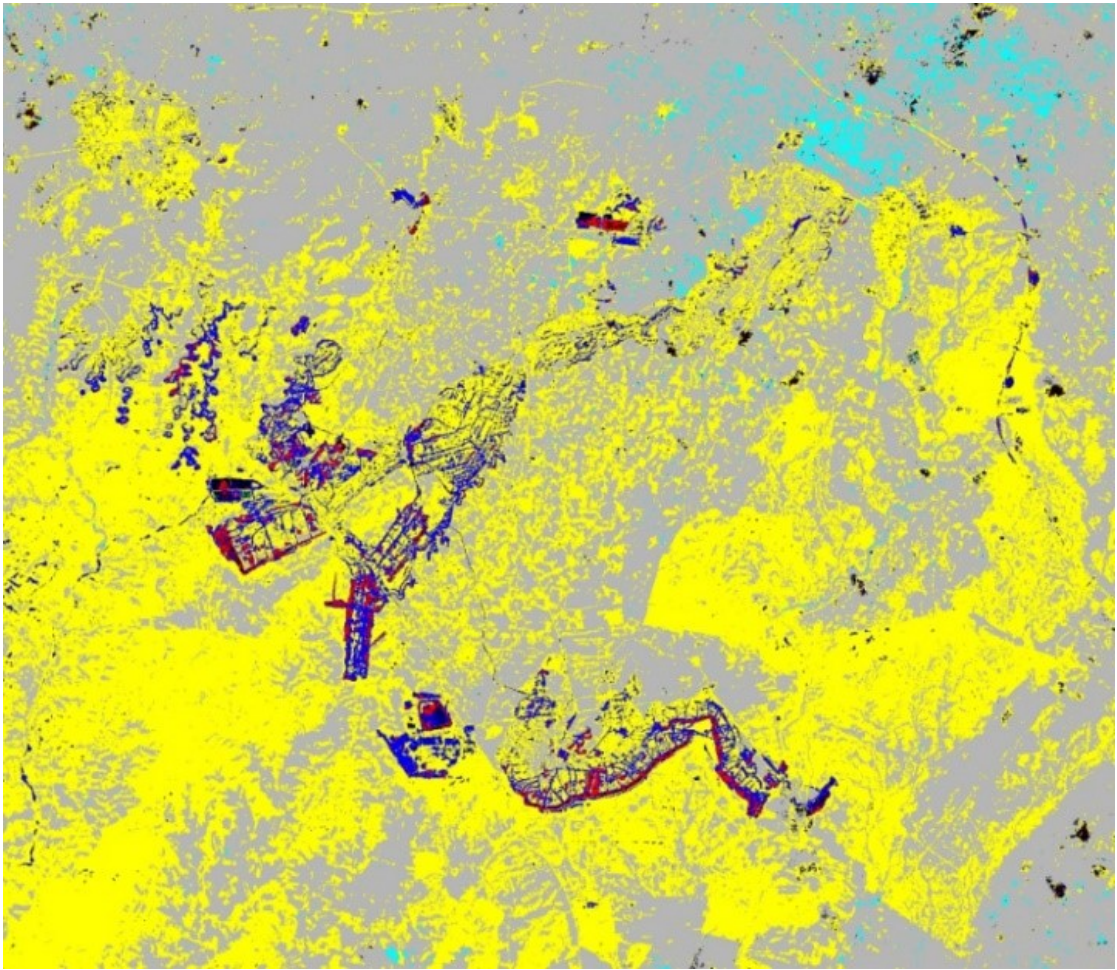


**Figure 4.31:** Spatial Distribution and Classification of Desertification: 2014

7. 2017

The trend of desertification continues, with an increase in severe (red) and moderate (blue) desertification patches as in Figure 4.34. Open pits (cyan) also expand, hinting at further mining infrastructure development. Mild desertification (yellow) now dominates much of the region, suggesting a high vulnerability to land degradation.

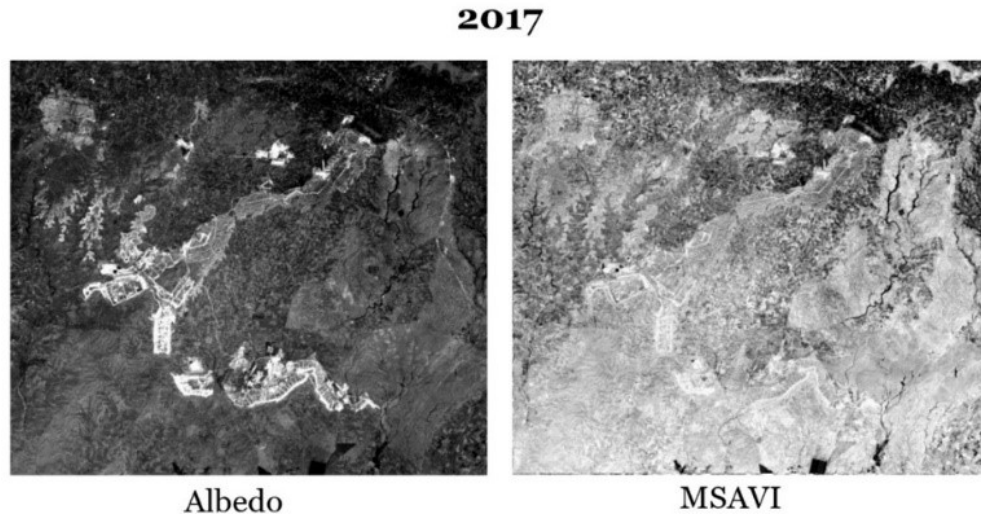


**Figure 4.32:** Albedo and MSAVI for Desertification Assessment in the Khouribga Region: 2017

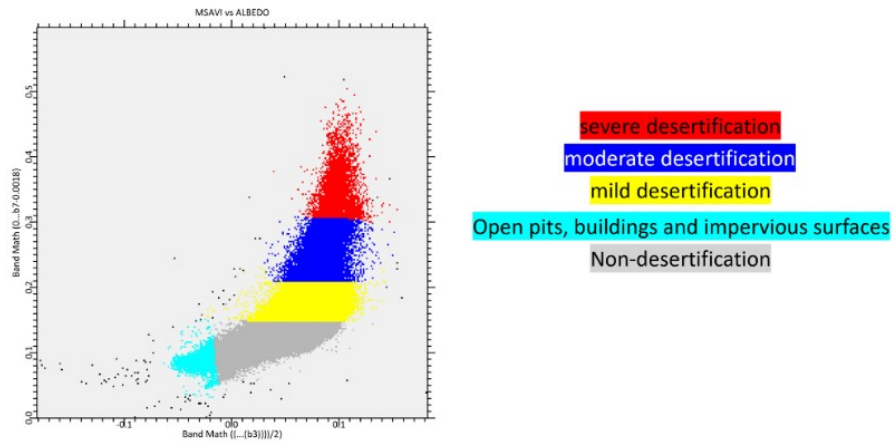


**Figure 4.33:** Albedo vs MSAVI scatter plot: 2017



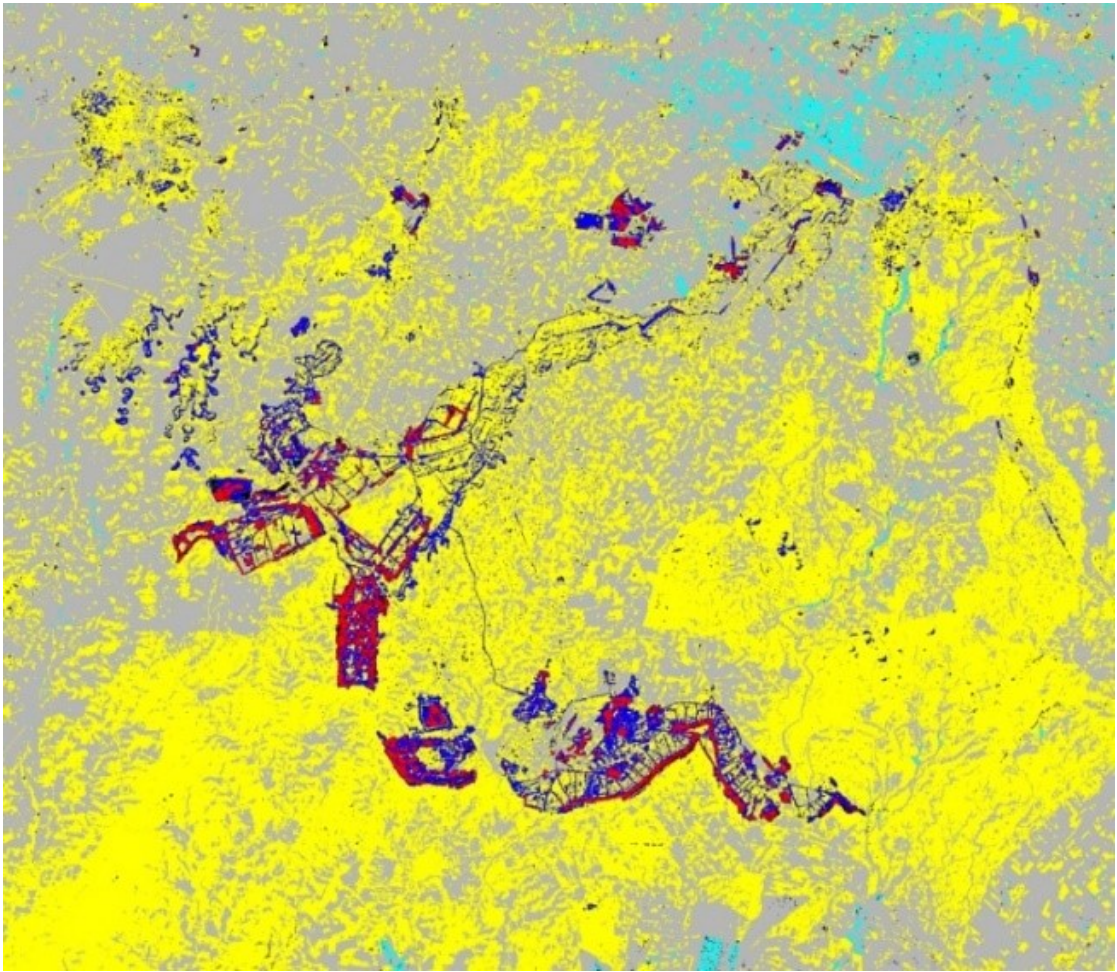


**Figure 4.34:** Spatial Distribution and Classification of Desertification: 2017

8. 2023

Figure 4.35 shows that Severe desertification (red) now dominates several areas, especially along central mining corridors, indicating significant land degradation. The cyan areas (open pits and impervious surfaces) continue to expand, correlating with ongoing mining. Mild desertification (yellow) is widespread, while moderate desertification (blue) persists in the northern regions.

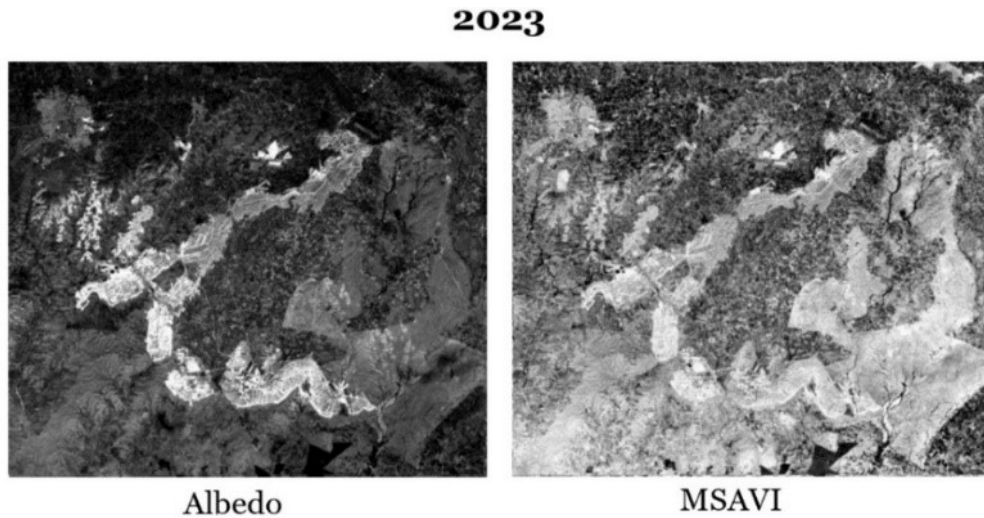


**Figure 4.35:** Albedo and MSAVI for Desertification Assessment in the Khouribga Region: 2023

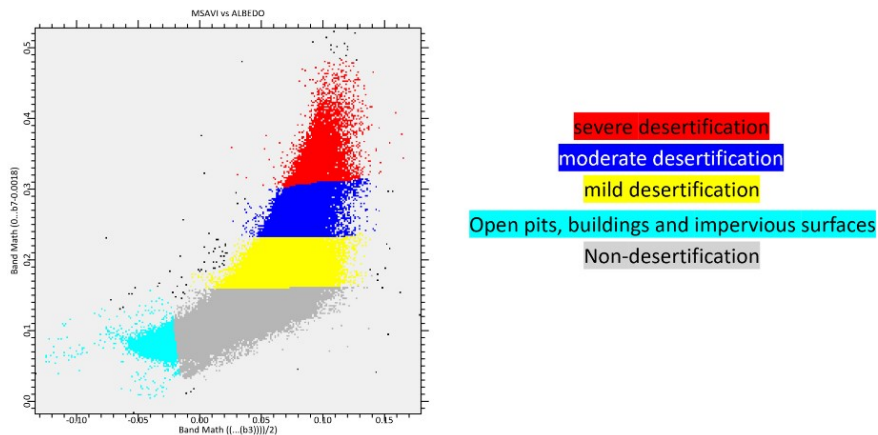


**Figure 4.36:** Albedo vs MSAVI scatter plot: 2023



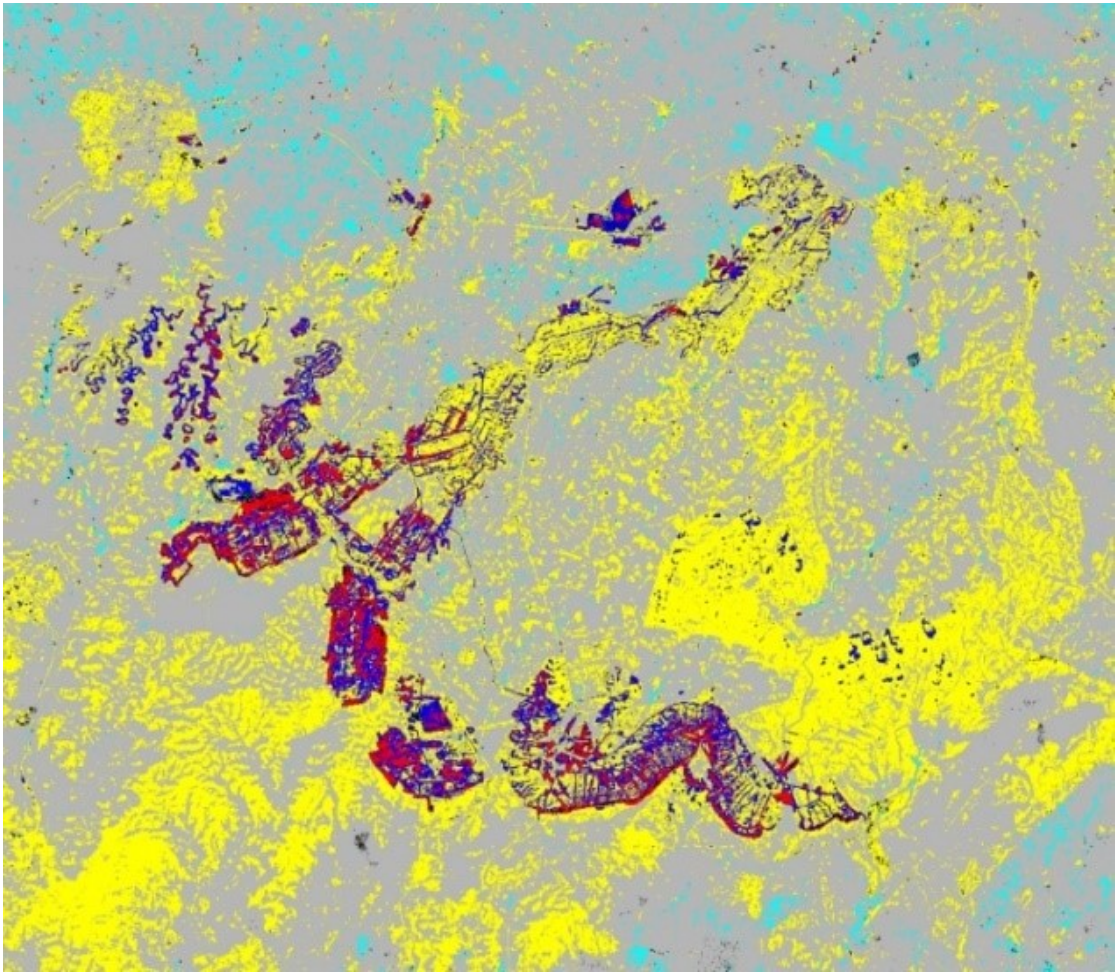


**Figure 4.37:** Spatial Distribution and Classification of Desertification: 2023



9. 2024

Figure 4.40, The most recent data shows the highest levels of severe desertification (red), with extensive patches spreading across the landscape. The northern and central parts of the region exhibit the most intense degradation. Moderate desertification (blue) has slightly expanded, while the cyan regions (impervious surfaces) have also grown. Mild desertification (yellow) remains the dominant feature, covering most of the region, indicating that the desertification process is pervasive but varies in intensity across different areas.

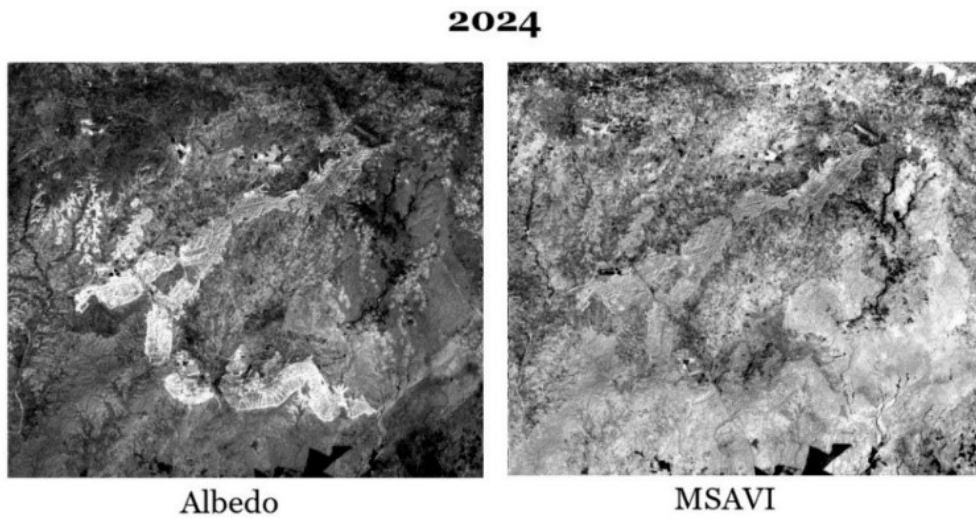


**Figure 4.38:** Albedo and MSAVI for Desertification Assessment in the Khouribga Region: 2024

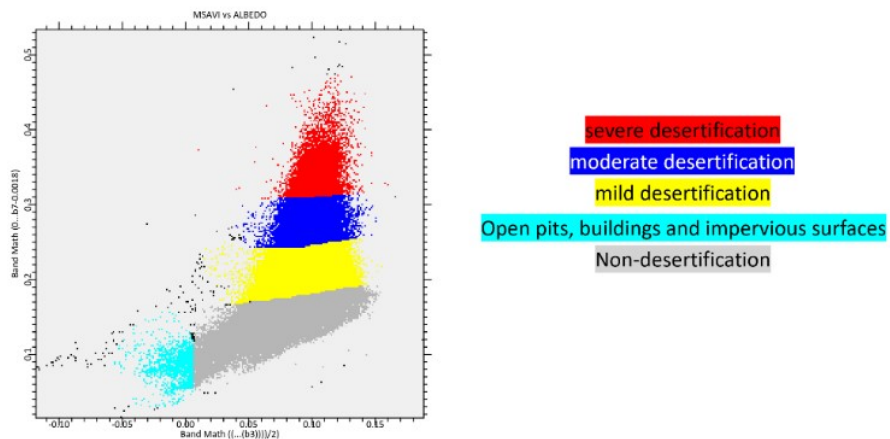


**Figure 4.39:** Albedo vs MSAVI scatter plot: 2024

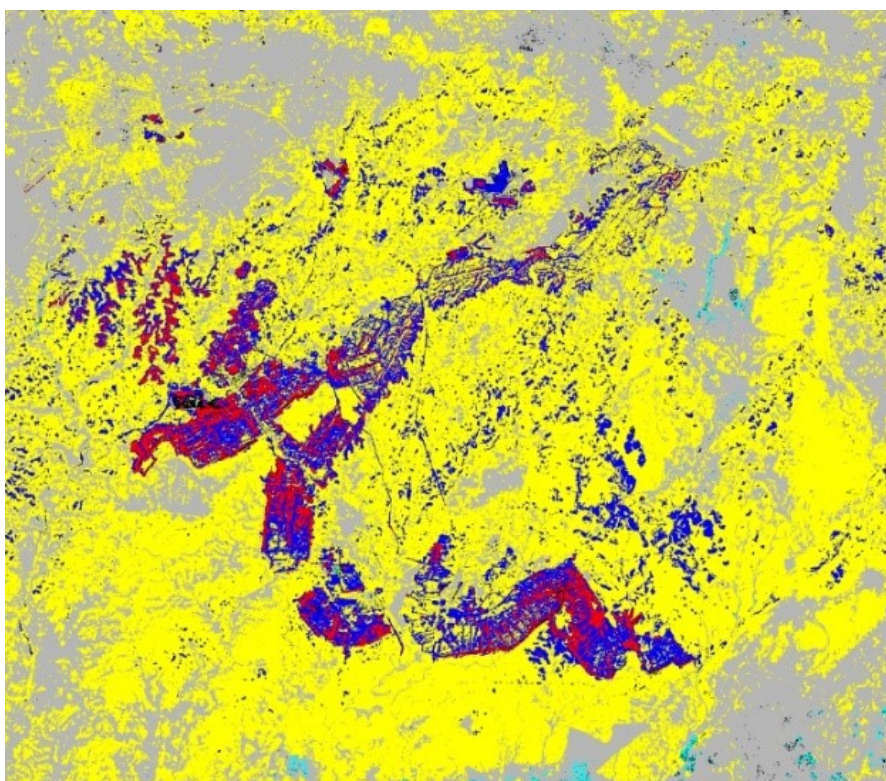


**Figure 4.40:** Spatial Distribution and Classification of Desertification: 2024

Severe Desertification (red) has steadily increased over time, especially in areas directly impacted by mining operations. This suggests that mining activities significantly contribute to land degradation, transforming once-vegetated areas into severely degraded zones.

Moderate Desertification (blue) shows a relatively stable but growing presence, particularly in areas adjacent to severe desertification zones. These regions are likely in transition, with vegetation gradually declining.

Mild Desertification (yellow) dominates large portions of the region, indicating widespread vulnerability to desertification. While not severely degraded, these areas are highly susceptible to future degradation if proper land management practices are not employed.

open pits and impervious surfaces (cyan) expand significantly over time, highlighting the increasing footprint of mining infrastructure. This is particularly evident in later years (2014, 2017, 2023, and 2024).

Non-desertification areas (gray) have shrunk significantly over the 40 years, especially in regions surrounding the mining zones. This indicates a reduction in healthy vegetated areas, particularly in regions where human activities (e.g., mining, infrastructure development) are concentrated.

### **4.3 Result of Mineral Detection in Phosphate Mines Using EMIT satellite**

In hyperspectral remote sensing, the identification of mineralogical compositions relies heavily on the unique spectral signatures that minerals exhibit across specific wavelengths. These spectral features, such as absorption troughs and reflectance peaks, enable the differentiation and mapping of minerals in various geological environments. By utilizing hyperspectral data from advanced sensors like EMIT (Earth Surface Mineral Dust Source Investigation), it is possible to perform detailed spectral analysis, identifying key minerals based on their distinct spectral characteristics. This section presents the spectral signatures and reflectance value ratios of various minerals, focusing on their unique absorption features in the SWIR (Short-Wave Infrared) and TIR (Thermal Infrared) regions. Minerals such as Dolomite, Calcite, Gypsum, Sepiolite, Kaolinite, Illite, and Hematite exhibit troughs or peaks at specific wavelengths, which can be detected using band ratios derived from the EMIT sensor's hyperspectral data. The use of band math, including combinations of reflectance values from different bands, allows for the quantification of these minerals in the study area. The Khouribga Phosphate Mine serves as the key case study, where these mineralogical analyses are conducted to map the distribution of economically significant and associated minerals.

The following table outlines the spectral signature wavelengths and type of feature for each mineral, highlighting the troughs and peaks that are instrumental in their identification using EMIT's bands.

Mineral	Wavelength (nm)	Type of Feature	Citation
Apatite	8400	Trough	[46]
	9160	Peak	
	9620		
Quartz	8150	Trough	[53]
	8600		
	9330		
Calcite	2340	Trough	[55]
	1140		[54]
	11430		[59]
	14040		
Dolomite	2330	Trough	[55]
	11350		[59]
	13700		[54]
Gypsum	1500	Trough	[55]
	1750		
	2210		
Sepiolite	2340	Trough	[55]
Kaolinite	1900	Trough	[67]
	2190		
Palygorskite	1415	Trough	[66]
	1910		
	2207		
Illite	1410	Trough	[68]
	1910		
	2210		
Glauconite	770	Trough	[69]
	1080		
	1900		
	2300		
Hematite	550	Trough	[70]
	630		
	860		
Goethite	480	Trough	[70]
	650		
	920		

**Table 4.2:** Spectral Features and Wavelength Characteristics of Minerals at Khouribga Phosphate Mine

This study targets key minerals at the Khouribga Phosphate Mine, including Dolomite, Calcite, Gypsum, Sepiolite, and Kaolinite, using spectral characteristics like absorption (troughs) and reflection (peaks) for identification. Band ratios are applied to highlight these features, enhancing detection by contrasting specific wavelengths. The following table presents the spectral signatures, corresponding EMIT bands, feature types (troughs or peaks), and associated band and reflectance value ratios for the minerals studied. Certain wavelengths have been excluded from the analysis due to atmospheric effects, as they are not visible in the satellite data.

Mineral	Wavelength of Spectral Signature ( $\mu\text{m}$ )	Equivalent Band in EMIT	Type of Feature	Band Ratio & Reflectance Value Ratio
Dolomite	2.31	Band 260	Trough	$B246+B268/B260$ $R2204+R2367/R2310$
Calcite	2.33	Band 263	Trough	$B244+B271/B263$ $R2182+R2389/R2330$
Gypsum	1.20	Band 111	Trough	$B100+B123/B111$ $R1111+R1275/R1200$
	1.66	Band 173	Peak	$B173/B156+B184$ $R1660/R1153+R1744$
	2.21	Band 247	Trough	$B226+B260/B247$ $R2056+R2308/R2210$
Sepiolite	2.137	Band 237	Peak	$B237/B214+B260$ $R2137/R1967+R2308$
	2.330	Band 263	Trough	$B260+B268/B263$ $R2308+R2367/R2330$
Kaolinite	2.204	Band 246	Trough	$B238+B251/B246$ $R2145+R2241/R246$
	2.234	Band 250	Peak	$B250/B246+B261$ $R2234/R2204+R2315$
Illite	2.211	Band 247	Trough	$B236+B256/B247$ $R2130+R2278/R2211$
Palygorskite	2.211	Band 247	Trough	$B238+B253/B247$ $R2145+R2256/R2211$
Glaucosite	2.308	Band 260	Trough	$B255+B264/B260$ $R2271+R2337/R2308$
Hematite	0.551	Band 24	Trough	$B18+B29/B24$ $R507+R589/R551$
	0.860	Band 43	Trough	$B48+B88/B43$ $R730+R1029/R860$

**Table 4.3:** Spectral Signatures, Reflectance Value Ratios, and Band Ratios of Minerals Using EMIT Data

### 4.3.1 Dolomite in EMIT

A relative band math analysis was conducted on the EMIT image using the spectral signature of dolomite at 2308 nm, corresponding to EMIT Band 260. Dolomite’s absorption features in the shortwave infrared (SWIR) band have been extensively studied, with significant absorption bands identified at 2.31  $\mu\text{m}$  (Gaffey, 1986) and 2.33  $\mu\text{m}$  (Hunt and Salisbury, 1971). The band math formula  $B246+B268/B260$  was employed, utilizing spectral features from 2.204  $\mu\text{m}$  (B246), 2.31  $\mu\text{m}$  (B260), and 2.367  $\mu\text{m}$  (B268). This approach leverages dolomite’s diagnostic absorption feature at 2.31  $\mu\text{m}$  in the SWIR range, serving as a key indicator of its presence.

Mineral	Wavelength of spectral signature	Equivalent Band in EMIT	Type of Feature	Band ratio & Reflectance value ratio
Dolomite	2.31 $\mu\text{m}$	Band 260	Trough	$B246+B268/B260$ $R2204+R2367/R2310$

**Table 4.4:** spectral signature of Dolomite observed in the SWIR range at a wavelength of 2308 nm corresponding to EMIT band 260.

A detailed summary of the reflectance values for Dolomite at three key feature wavelengths—2204 nm, 2310 nm, and 2367 nm—is provided. The reflectance data, which was obtained from the resampled Spectral Reflectance of Dolomite shown in Figure 4.41, is categorized by grain size—fine, medium, and coarse—and was measured using two spectral analyzers, Beckman and Perkin. For fine-grained Dolomite, the reflectance values are notably high, recorded at 74.67 (Beckman) and 77.53 (Perkin) at 2204 nm. In contrast, medium and coarse grains show lower reflectance, with values of 64.25 and 67.26 for medium grain, and 52.17 and 56.87 for coarse grain, respectively, at the same wavelength. The table also includes the stretch value range for each grain size, which is crucial for subsequent band math calculations.

Feature Wavelengths from Resampled Spectra (nm)	2204 nm		2310 nm		2367 nm		B246 + B268 / B260
Equivalent Band in EMIT	B246		B260		B268		
	Beckman	Perkin	Beckman	Perkin	Beckman	Perkin	Stretch Value Range
Reflectance for Dolomite (Fine Grain)	74.67	77.53	71.13	72.31	74.68	76.87	2.099 - 2.135
Reflectance for Dolomite (Medium Grain)	64.25	67.26	54.25	54.86	63.49	66.24	2.3 - 2.43
Reflectance for Dolomite (Coarse Grain)	52.17	56.87	40.95	43.10	51.27	55.78	2.52 - 2.61

**Table 4.5:** Reflectance Values and Band Math Calculation for Dolomite at Spectral Signature of 2310 nm. This table presents the reflectance values and band math calculations for Dolomite with fine, medium, and coarse grain sizes, calculated using Perkin and Beckman spectral analyzers, with data sourced from the ASTER library embedded in ENVI.

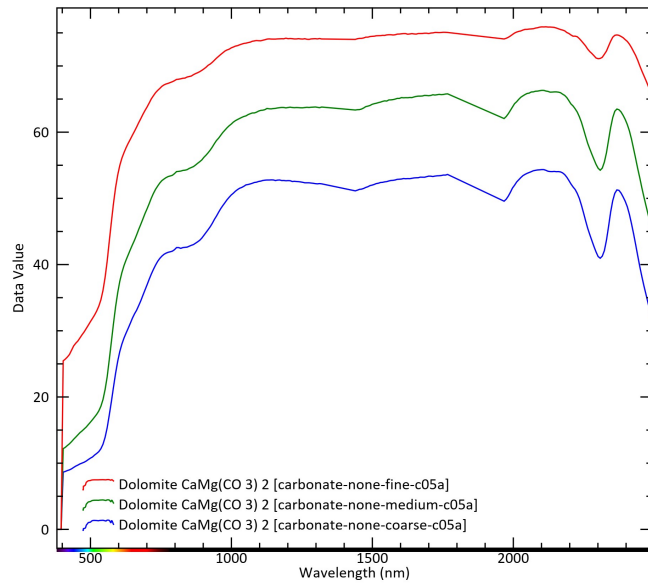


**Figure 4.41:** Resampled Spectral Reflectance of Dolomite for fine, medium, and coarse grain size, adjusted to the EMIT sensor resolution.

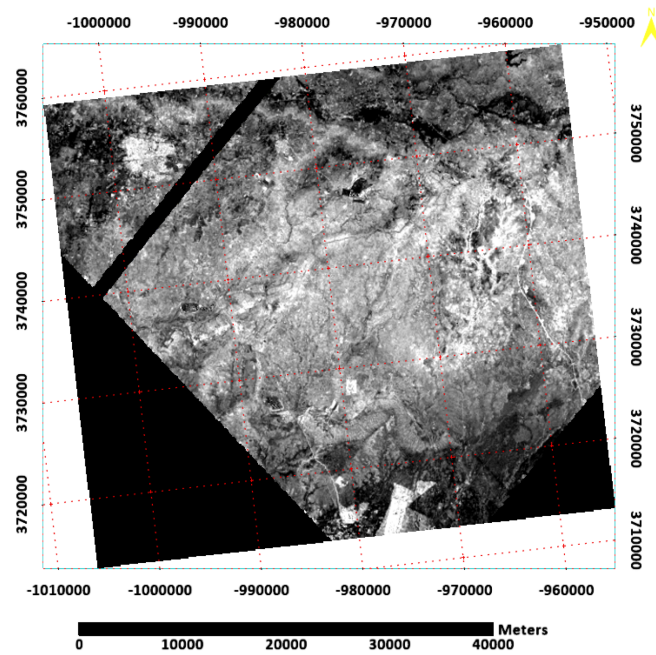


**Figure 4.42:** EMIT image of dolomite after application of relative band math at 2308 nm wavelength.



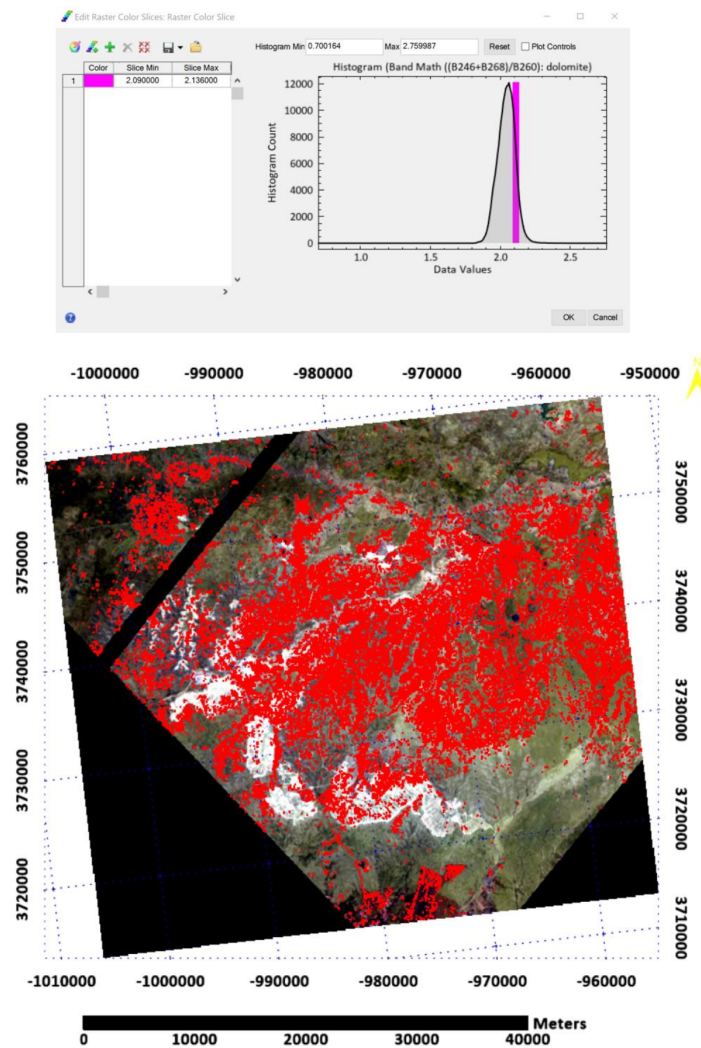


**Figure 4.43:** results of relative band math after applying raster color slice: The red color represents the range between 2.09 to 2.136, corresponding to the presence of the fine grain dolomite.

After conducting the EMIT image analysis of dolomite using the relative band math at the 2308 nm wavelength, the results were processed using raster color slicing. The red color on the map represents the range between 2.09 to 2.136, corresponding to the presence of fine-grained dolomite. In contrast, no color was associated with the medium and coarse grain sizes of dolomite, indicating that these sizes did not exhibit the specific spectral characteristics needed for identification in the selected ranges.



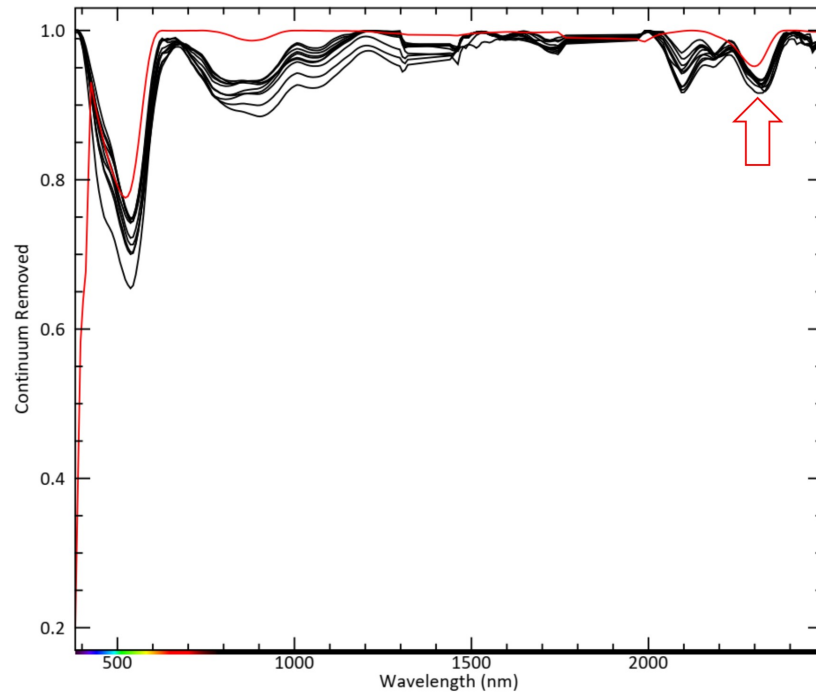


**Figure 4.44:** A comparison of the selected dolomite spectra from the ENVI spectral library (in red) with spectral profiles collected from multiple locations within the study area (in black)

The comparison of the spectral profiles from the selected pixels with the dolomite spectra from the ENVI spectral library demonstrates a notable similarity at 2.31 micrometers, validating the presence of dolomite in the spectral data. However, a slight shift in the peak center is observed, which is expected, as the spectra may represent a mixture of dolomite and calcite. To achieve this analysis, random pixels were selected within the areas highlighted in red through raster color slicing. The spectral profiles of these selected pixels were then compared with the spectra of dolomite, the main mineral under study. This analysis confirms that the spectral characteristics of the identified pixels closely align with those of dolomite, providing further evidence of its presence in the area.

### 4.3.2 Calcite in EMIT

Using EMIT’s spectral data, we analyzed the absorption features of calcite at 2330 nm (corresponding to Band 263 in EMIT). Calcite’s prominent absorption band at this wavelength falls within the shortwave infrared (SWIR) range, enabling us to distinguish it using specific band math techniques. The formula  $B244+B271/B263$  was applied, utilizing spectral features from 2.182 m (B244), 2.33 m (B263), and 2.389 m (B271), effectively highlighting calcite’s spectral response in this range.

Mineral	Wavelength of spectral signature	Equivalent Band in EMIT	Type of Feature	Band ratio & Reflectance value ratio
Calcite	2.33 $\mu\text{m}$	Band 263	Trough	$B244+B271/B263$ $R2182+R2389/R2330$

**Table 4.6:** spectral signature of Calcite observed in the SWIR range at a wavelength of 2330 nm corresponding to EMIT band 263.

Feature Wavelengths from Resampled Spectra (nm)	2182 nm		2330 nm		2389 nm		B244 + B271 / B263
Equivalent Band in EMIT	B244		B263		B271		
	Beckman	Perkin	Beckman	Perkin	Beckman	Perkin	Stretch Value Range
Reflectance for Calcite (Fine Grain)	82.86	86.82	73.24	75.00	80.63	83.34	2.23 - 2.26
Reflectance for Calcite (Medium Grain)	77.32	81.61	57.78	58.54	72.07	75.37	2.58 - 2.68
Reflectance for Calcite (Coarse Grain)	73.60	77.93	45.17	45.28	64.92	68.21	3.06 - 3.22

**Table 4.7:** Reflectance Values and Band Math Calculation for Calcite at Spectral Signature of 2330 nm. This table presents the reflectance values and band math calculations for Calcite with fine, medium, and coarse grain sizes, calculated using Perkin and Beckman spectral analyzers, with data sourced from the ASTER library embedded in ENVI.

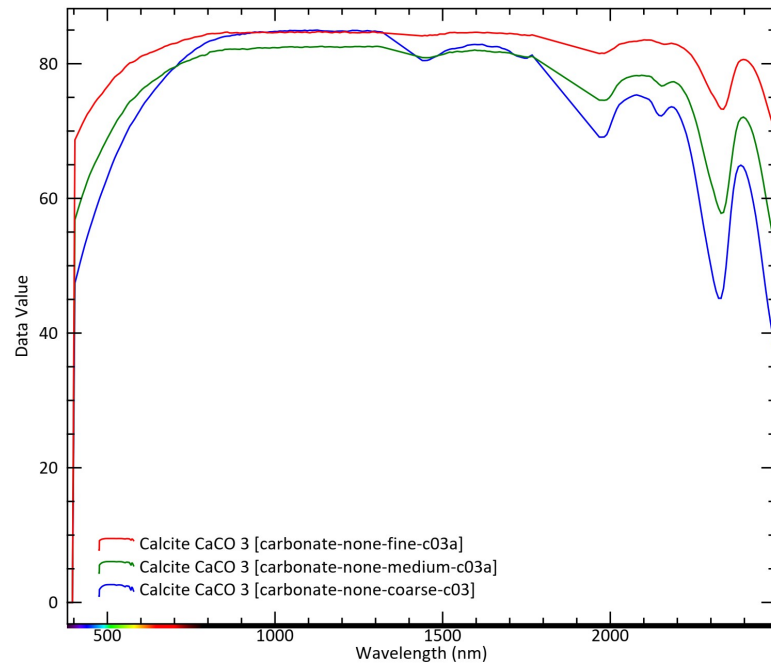


**Figure 4.45:** Resampled Spectral Reflectance of Calcite for fine, medium, and coarse grain size, adjusted to the EMIT sensor resolution.

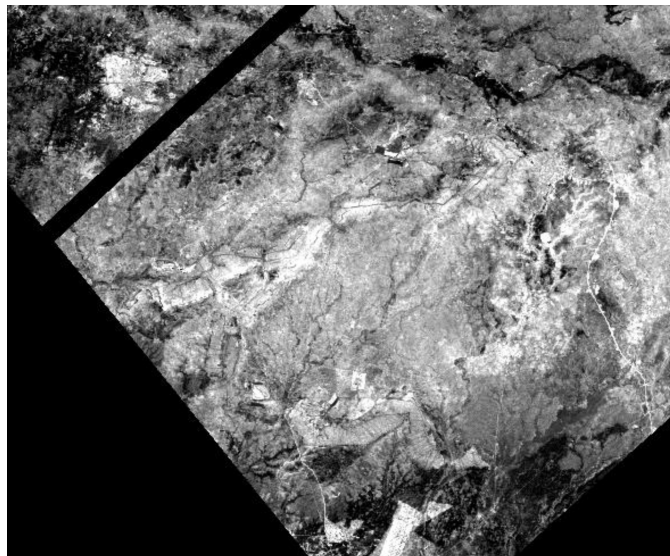


**Figure 4.46:** EMIT image of calcite after application of relative band math at 2330 nm wavelength.

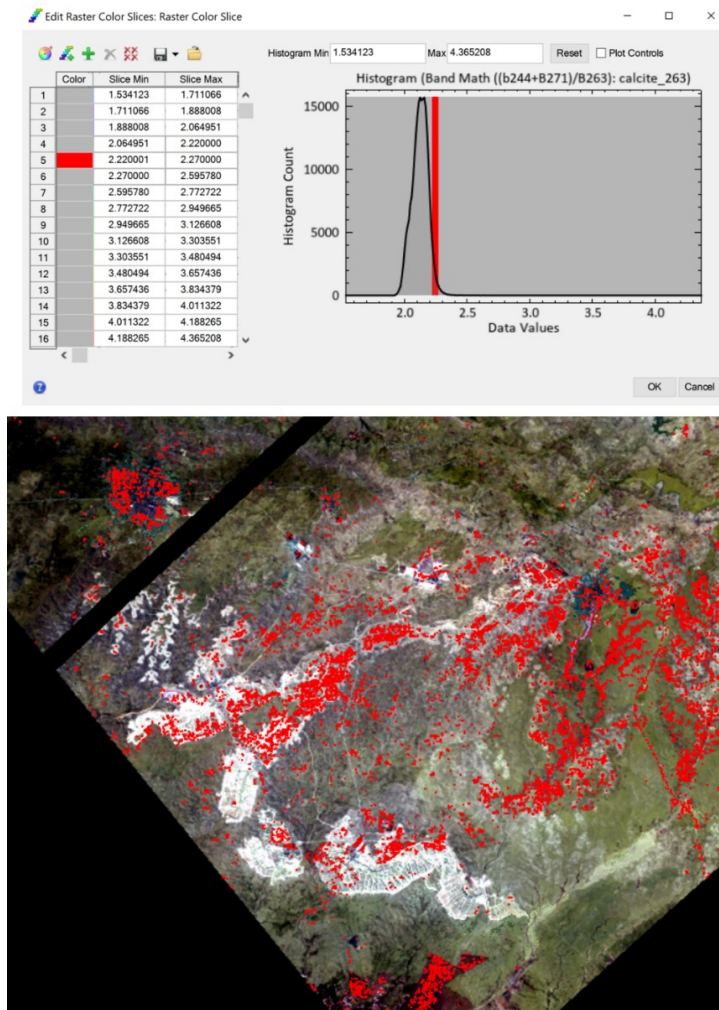


**Figure 4.47:** results of relative band math after applying raster color slice: The red color represents the range between 2.220 to 2.270, corresponding to the presence of the fine grain calcite.

Following the band math analysis on EMIT imagery, raster color slicing was performed. Areas corresponding to fine-grain calcite are highlighted in red within the reflectance range of 2.220 to 2.270. This visual representation aids in isolating regions with a higher likelihood of containing fine-grain calcite.

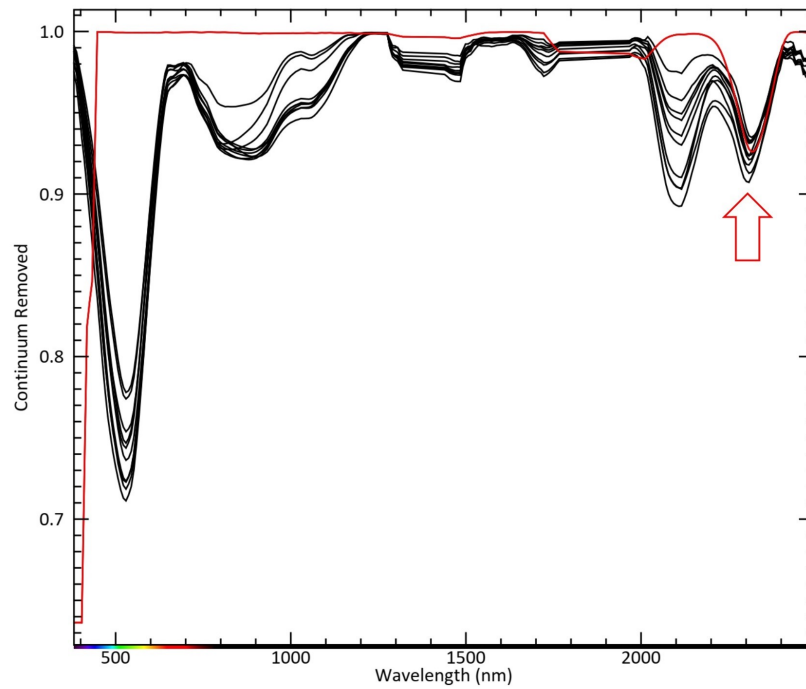


**Figure 4.48:** A comparison of the selected calcite spectra from the ENVI spectral library (in red) with spectral profiles collected from multiple locations within the study area (in black)

For validation, we compared random pixel profiles from the color-sliced regions with known calcite spectra from the ENVI library. The close match, especially at the diagnostic 2.33  $\mu\text{m}$  wavelength, confirms the identified calcite in the spectral data. This validation step strengthens our analysis by demonstrating consistency between field spectra and the spectral library.

### 4.3.3 Gypsum in EMIT

Gypsum is identifiable in the Shortwave Infrared (SWIR) range by distinct absorption features around three main wavelengths: 1200 nm, 1660 nm, and 2210 nm.

Mineral	Wavelength of spectral signature	Equivalent Band in EMIT	Type of Feature	Band ratio & Reflectance value ratio
Gypsum	1.20 $\mu\text{m}$	Band 111	Trough	$B100+B123/B111$ $R1111+R1275/R1200$
	1.66 $\mu\text{m}$	Band 173	Peak	$B173/B156+B184$ $R1660/R1153+R1744$
	2.21 $\mu\text{m}$	Band 247	Trough	$B226+B260/B247$ $R2056+R2308/2210$

**Table 4.8:** spectral signature of Gypsum observed in the SWIR range at a wavelength of 1200 nm, 1660 nm, and 2210 nm corresponding to EMIT band 111, 173, and 247 respectively.

At 1200 nm, gypsum shows a pronounced absorption trough, best represented in EMIT’s Band 111. This characteristic trough can be further quantified by the band math ratio  $(B100+B123)/B111$  or alternatively by the reflectance value ratio  $(R1111+R1275)/R1200$ , offering an effective method for distinguishing gypsum from other minerals in the spectral dataset.

Feature Wavelengths from Resampled Spectra (nm)	1126 nm		1200 nm		1290 nm		$B101+B123/B111$
Equivalent Band in EMIT	B101		B111		B123		
	Beckman	Perkin	Beckman	Perkin	Beckman	Perkin	Stretch Value Range
Reflectance for Gypsum Fine Grain	94.5	92.48	89.90	87.52	91.94	89.86	2.00 - 2.10
Reflectance for Gypsum Medium Grain	88.98	85.86	79.87	78.07	84.01	81.95	2.05 - 2.20
Reflectance for Gypsum Coarse Grain	89.01	88.31	74.08	74.32	80.47	80.45	2.20 - 2.30

**Table 4.9:** Reflectance Values and Band Math Calculation for Gypsum at Spectral Signature of 1200 nm. This table presents the reflectance values and band math calculations for Gypsum with fine, medium, and coarse grain sizes, calculated using Perkin and Beckman spectral analyzers, with data sourced from the ASTER library embedded in ENVI.

The second key spectral feature of gypsum is observed around 1660 nm, represented by a peak in EMIT’s Band 173. This peak can be highlighted through the band ratio  $B173/(B156+B184)$ .

At 2210 nm, gypsum exhibits a third distinct trough, represented in EMIT by Band 247. Here, the band math expression  $(B226+B260)/B247$  or the reflectance ratio  $(R2056+R2308)/2210$  provides a precise means of identifying gypsum within this wavelength range.

Feature Wavelengths from Resampled Spectra (nm)	1153 nm		1660 nm		1744 nm		B173/B156 + B184
Equivalent Band in EMIT	B156		B173		B184		
	Beckman	Perkin	Beckman	Perkin	Beckman	Perkin	Stretch Value Range
Reflectance for Gypsum Fine Grain	76.09	72.43	88.67	86.64	75.96	72.57	0.5 - 0.6
Reflectance for Gypsum Medium Grain	56.89	57.76	78.28	77.10	56.87	55.17	0.6 - 0.7
Reflectance for Gypsum Coarse Grain	44.11	44.72	71.86	72.63	44.10	45.02	0.8 - 0.85

**Table 4.10:** Reflectance Values and Band Math Calculation for Gypsum at Spectral Signature of 1660 nm. This table presents the reflectance values and band math calculations for Gypsum with fine, medium, and coarse grain sizes, calculated using Perkin and Beckman spectral analyzers, with data sourced from the ASTER library embedded in ENVI.

Feature Wavelengths from Resampled Spectra (nm)	2056 nm		2210 nm		2308 nm		(B226 + B260) / B247
Equivalent Band in EMIT	B226		B247		B260		
	Beckman	Perkin	Beckman	Perkin	Beckman	Perkin	Stretch Value Range
Reflectance for Gypsum Fine Grain	71.68	67.68	59.68	54.91	64.21	60.12	2.2 - 2.35
Reflectance for Gypsum Medium Grain	51.08	49.27	36.27	34.04	41.79	40.13	2.5 - 2.6
Reflectance for Gypsum Coarse Grain	37.69	38.70	23.50	23.70	28.06	28.97	2.7 - 2.9

**Table 4.11:** Reflectance Values and Band Math Calculation for Gypsum at Spectral Signature of 2210 nm. This table presents the reflectance values and band math calculations for Gypsum with fine, medium, and coarse grain sizes, calculated using Perkin and Beckman spectral analyzers, with data sourced from the ASTER library embedded in ENVI.

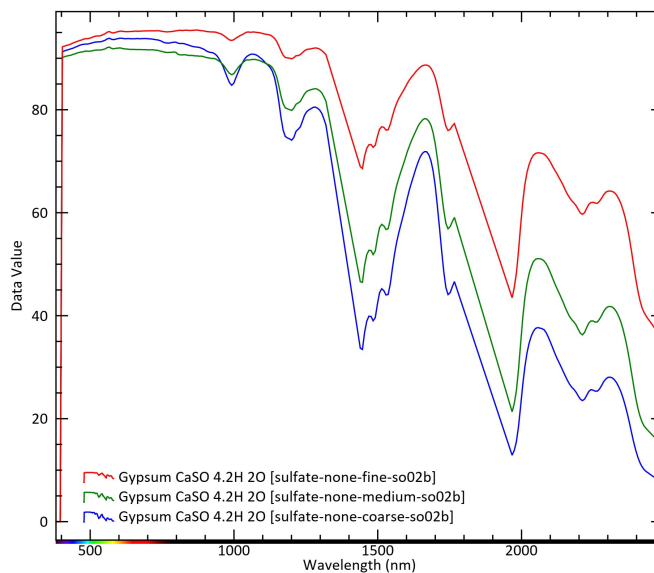


**Figure 4.49:** Resampled Spectral Reflectance of Gypsum for fine, medium, and coarse grain size, adjusted to the EMIT sensor resolution.



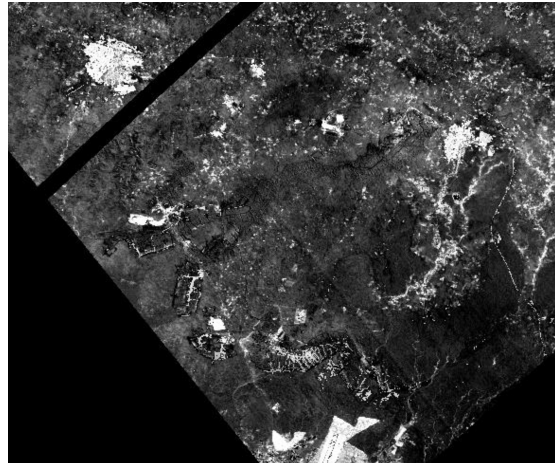


**Figure 4.50:** EMIT image of gypsum after application of relative band math at 1200 nm wavelength.

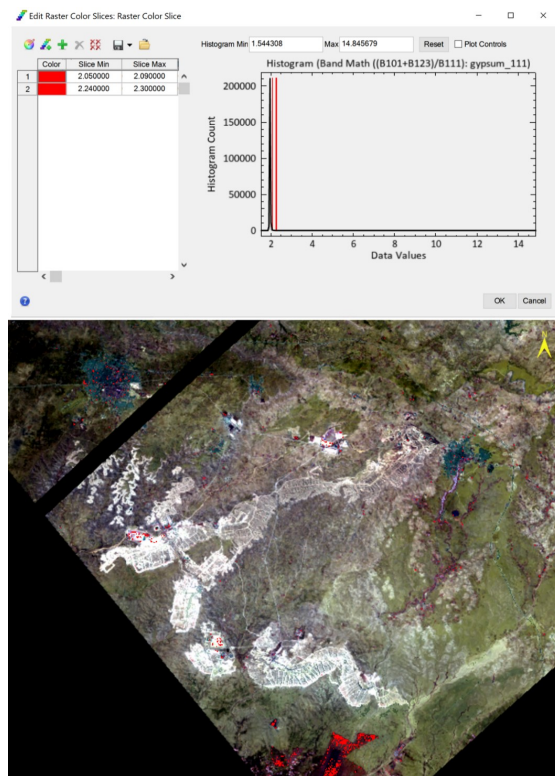


**Figure 4.51:** results of relative band math after applying raster color slice: The red color represents the range between 2.05 to 2.09 and 2.24 to 2.3 corresponding to the presence of the fine grain gypsum.



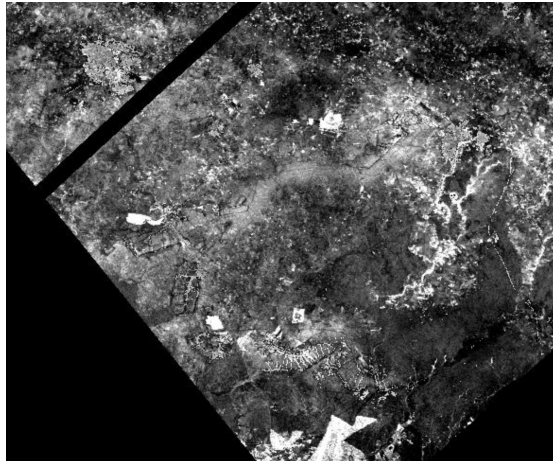


**Figure 4.52:** EMIT image of gypsum after application of relative band math at 1660 nm wavelength.

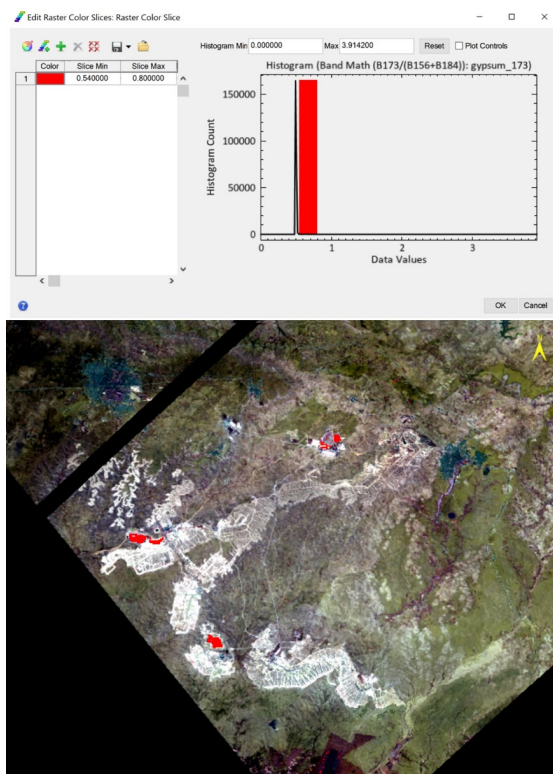


**Figure 4.53:** results of relative band math after applying raster color slice: The red color represents the range between 0.540 to 0.8, corresponding to the presence of the fine grain gypsum.

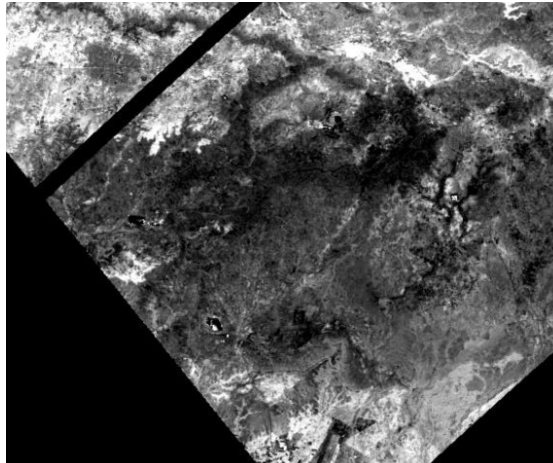


**Figure 4.54:** EMIT image of gypsum after application of relative band math at 2210 nm wavelength.

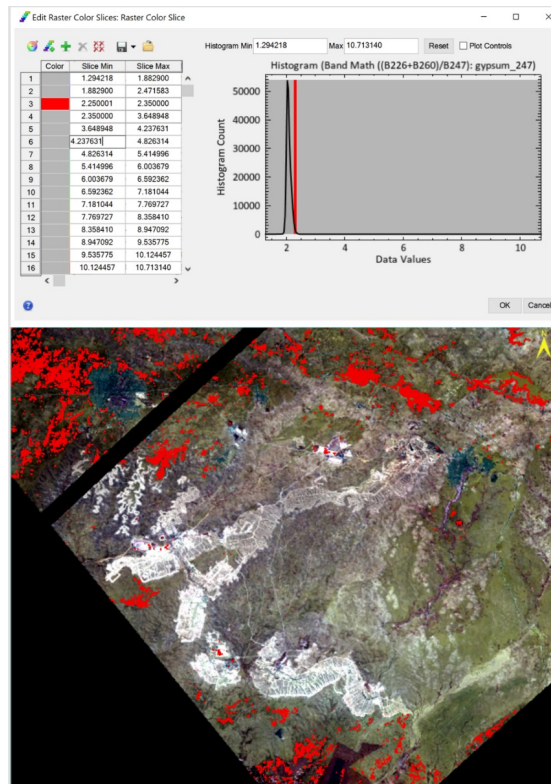


**Figure 4.55:** results of relative band math after applying raster color slice: The red color represents the range between 2.25 to 2.35, corresponding to the presence of the fine grain gypsum.

To support this analysis, Figures 4.50 through 4.56 illustrate the spatial distribution of gypsum in the EMIT images following band math applications at each of these characteristic wavelengths. Color slicing techniques are applied to highlight ranges specific to fine, medium, and coarse gypsum grains, with red hues denoting higher concentrations of fine-grain gypsum. For instance, the 1200 nm imagery reveals concentrations in the range of 2.05 to 2.09 and 2.24 to 2.3, while the 1660 nm wavelength shows values from 0.54 to 0.8, and 2210 nm highlights gypsum within the range of 2.25 to 2.35. This approach effectively delineates gypsum deposits, enabling researchers to assess both their spatial distribution and abundance across the study area. Finally, a comparison of selected gypsum spectra from the ENVI

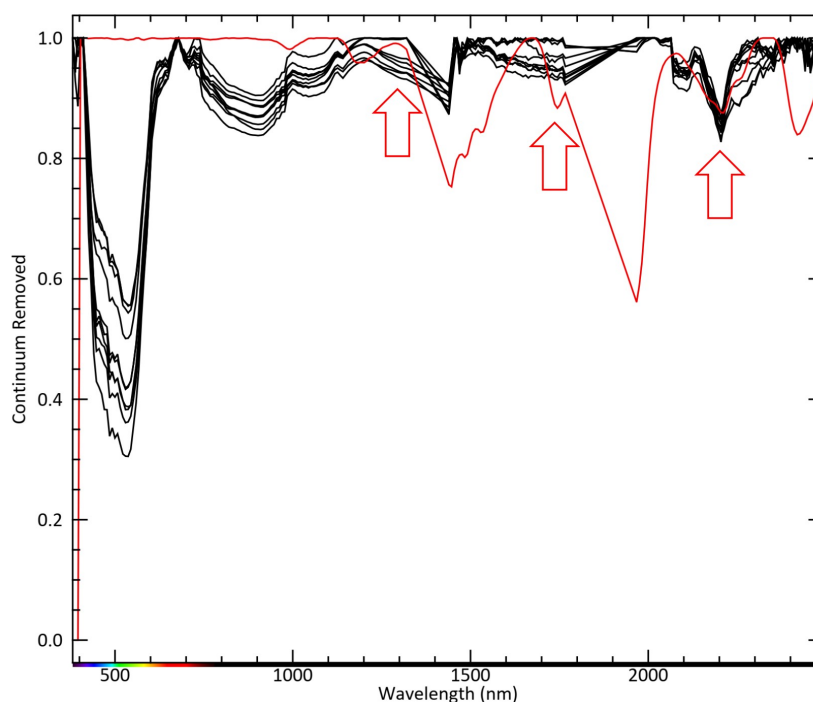


**Figure 4.56:** A comparison of the selected gypsum spectra from the ENVI spectral library (in red) with spectral profiles collected from multiple locations within the study area (in black) indicates notable similarities in 2210 nm.

spectral library with the spectral profiles gathered across various points in the study area reveals significant similarities around the absorption feature between 1600 and 1750 nm. This feature is the most diagnostic for gypsum in satellite data. However, the absorption feature at 2210 nm, while present, shows a widespread distribution likely attributed to the presence of clay minerals, such as illite or smectite, rather than gypsum.

### 4.3.4 Sepiolite in EMIT

Sepiolite, exhibits two distinct spectral features in the Shortwave Infrared (SWIR) range that make it identifiable through hyperspectral remote sensing. In EMIT data, sepiolite shows a prominent peak at around 2137 nm and a characteristic trough at 2330 nm, both of which help to distinguish it from other minerals in spectral analysis. The first key feature appears as a peak at 2137 nm, represented

Mineral	Wavelength of spectral signature	Equivalent Band in EMIT	Type of Feature	Band ratio &
				Reflectance value ratio
Sepiolite	2.137 $\mu\text{m}$	Band 237	Peak	$B237/B214+B260$ $R2137/R1967+R2308$
	2.330 $\mu\text{m}$	Band 263	Trough	$B260+B268/b263$ $R2308+R2367/R2330$

**Table 4.12:** spectral signature of Sepiolite observed in the SWIR range at a wavelength of 2137 nm and 2330 nm corresponding to EMIT band 237 and 263 respectively.

in EMIT by Band 237. This peak is quantified using the band ratio formula  $B237/(B214+B260)$  or the reflectance value ratio  $R2137/(R1967+R2308)$ . These ratios capture the enhanced reflectance at 2137 nm, a unique spectral signature of sepiolite, allowing for differentiation based on grain size. Fine-grain sepiolite reflects light at this peak within a range of 0.6 to 0.7, while medium-grain sepiolite has a higher reflectance, around 0.7 to 0.75. Coarse-grain sepiolite, exhibiting a stronger reflectance, ranges from 0.8 to 0.85, marking a notable progression as grain size increases.

Feature Wavelengths from Resampled Spectra (nm)	1967 nm		2137 nm		2308 nm		B237/B214 + B260
Equivalent Band in EMIT	B214		B237		B260		
	Beckman	Perkin	Beckman	Perkin	Beckman	Perkin	Stretch Value Range
Reflectance for Sepiolite Fine Grain	46.9	46.16	61.66	60.64	48.85	46.81	0.6 - 0.7
Reflectance for Sepiolite Medium Grain	41.46	40.68	59	58.46	41.66	39.72	0.7 - 0.75
Reflectance for Sepiolite Coarse Grain	28.02	30.23	45.54	49.02	28.69	30.11	0.8 - 0.85

**Table 4.13:** Reflectance Values and Band Math Calculation for Sepiolite at Spectral Signature of 2137 nm. This table presents the reflectance values and band math calculations for Sepiolite with fine, medium, and coarse grain sizes, calculated using Perkin and Beckman spectral analyzers, with data sourced from the ASTER library embedded in ENVI.

The second spectral feature, a trough at 2330 nm, is represented by EMIT’s Band 263. This trough is analyzed through the band math ratio  $(B260+B268)/B263$  or reflectance value ratio  $(R2308+R2367)/R2330$ , which emphasizes sepiolite’s

characteristic low reflectance in this range. The spectral behavior at this trough varies with the grain size of sepiolite: fine-grain sepiolite reflects within a stretch value range of 1.8 to 1.95, while medium-grain sepiolite spans from 1.7 to 1.9, and coarse-grain sepiolite maintains a range of 1.7 to 1.9.

Feature Wavelengths from Resampled Spectra (nm)	2308 nm		2330 nm		2367 nm		B260 + B268/B263
Equivalent Band in EMIT	B260		B263		B268		
	Beckman	Perkin	Beckman	Perkin	Beckman	Perkin	Stretch Value Range
Reflectance for Sepiolite Fine Grain	48.85	46.81	50.50	49.34	48.60	44.91	1.8 - 1.95
Reflectance for Sepiolite Medium Grain	41.66	39.72	44.01	43.49	41.81	38	1.7 - 1.9
Reflectance for Sepiolite Coarse Grain	28.69	30.11	30.77	33.58	28.68	28.17	1.7 - 1.9

**Table 4.14:** Reflectance Values and Band Math Calculation for Sepiolite at Spectral Signature of 2330 nm. This table presents the reflectance values and band math calculations for Sepiolite with fine, medium, and coarse grain sizes, calculated using Perkin and Beckman spectral analyzers, with data sourced from the ASTER library embedded in ENVI.

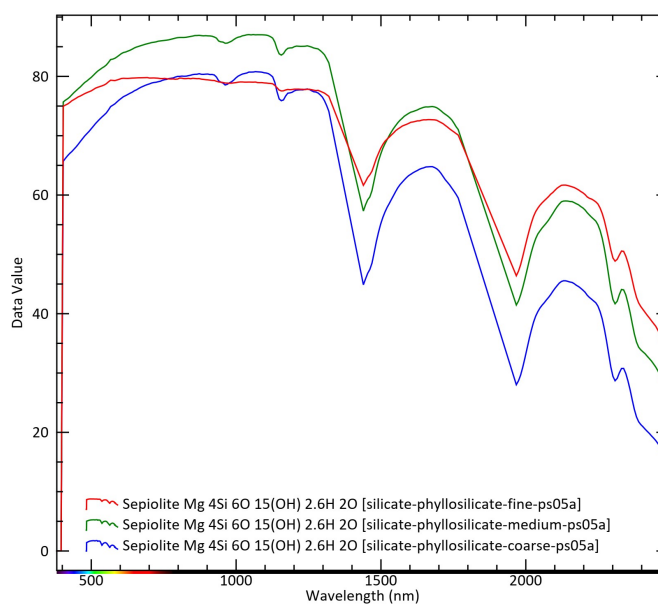


**Figure 4.57:** Resampled Spectral Reflectance of Sepiolite for fine, medium, and coarse grain size, adjusted to the EMIT sensor resolution.

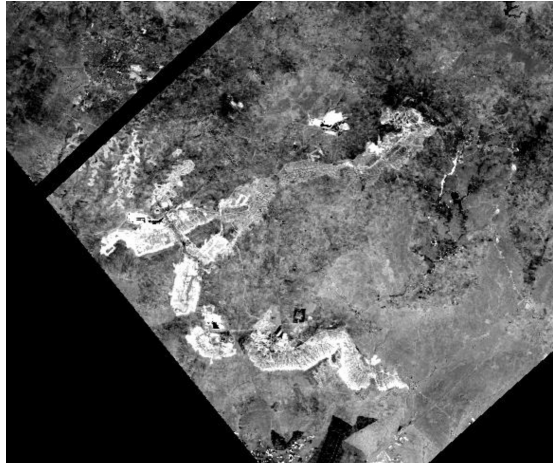


**Figure 4.58:** EMIT image of Sepiolite after application of relative band math at 2137 nm wavelength.

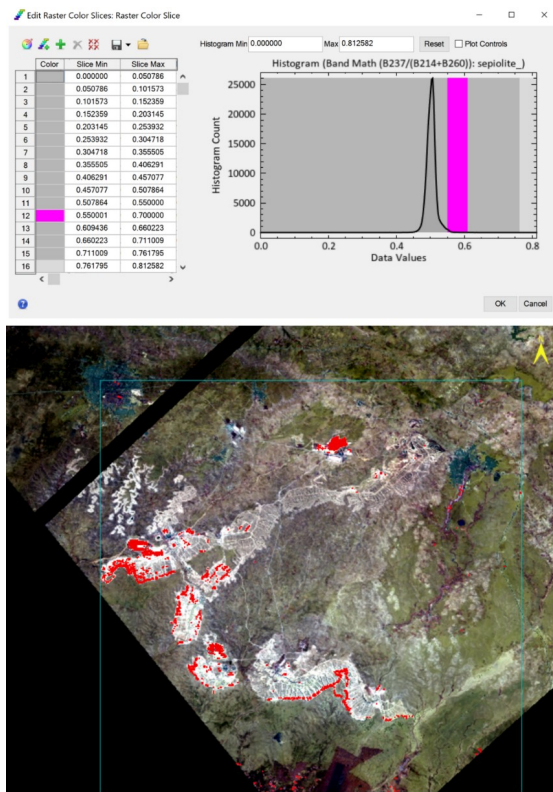


**Figure 4.59:** results of relative band math after applying raster color slice: The red color represents the range between 0.55 to 0.7, corresponding to the presence of the fine grain sepiolite.



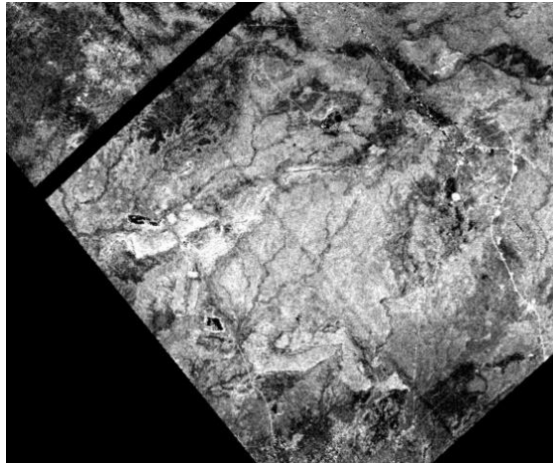


**Figure 4.60:** EMIT image of sepiolite after application of relative band math at 2330 nm wavelength.

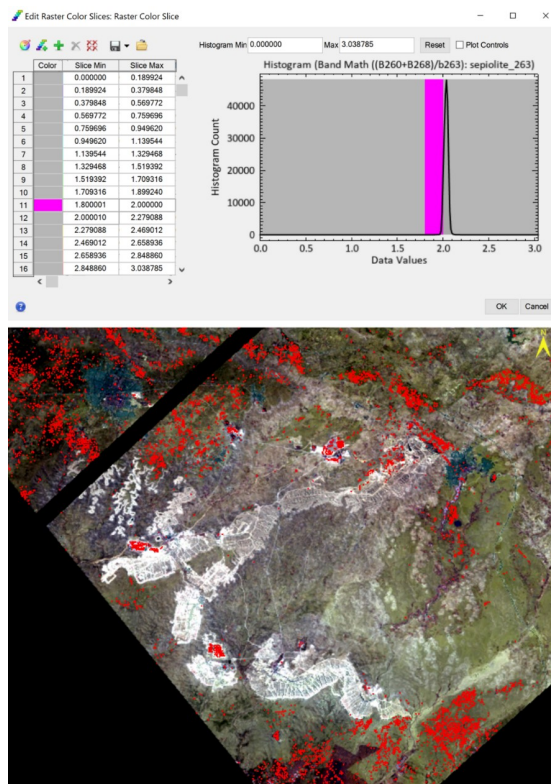


**Figure 4.61:** results of relative band math after applying raster color slice: The red color represents the range between 1.7 to 1.8, corresponding to the presence of the medium and coarse grain sepiolite.

Figures 4.57 to 4.61 illustrate these spectral patterns visually. For instance, Figure 4.58 showcases the EMIT image of sepiolite at 2137 nm. A raster color slice has been applied in Figure 4.59. Here, red hues highlight areas with reflectance values between 0.55 to 0.7, indicating the presence of fine-grain sepiolite in the study area. Similarly, Figure 4.60 presents the results of the 2330 nm band math, where shades of red pinpoint concentrations of medium and coarse-grain sepiolite, mapped between values of 1.7 to 1.8 in Figure 4.61. Finally, a comparison of

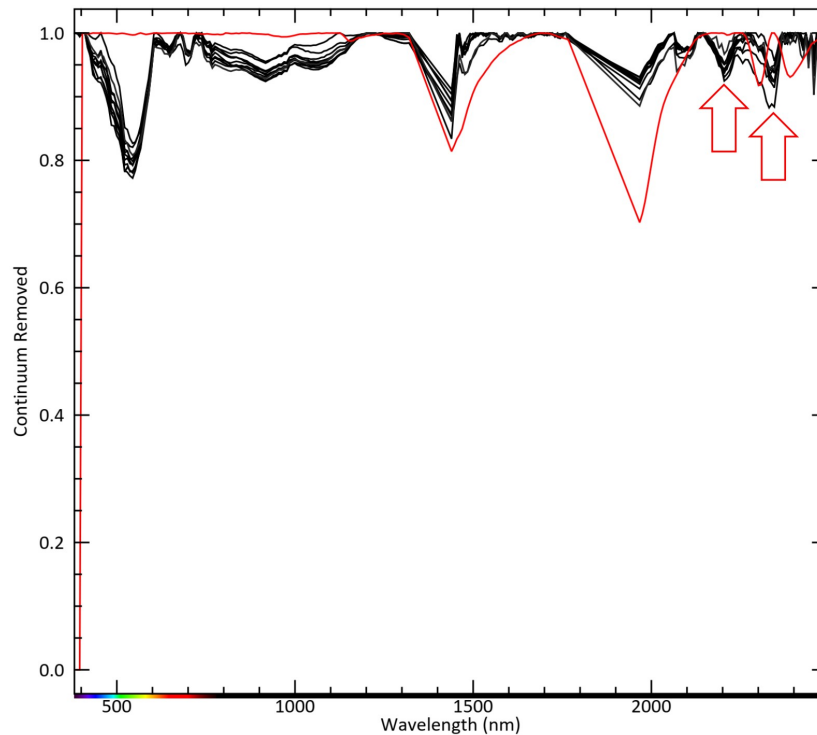


**Figure 4.62:** A comparison of the selected sepiolite spectra from the ENVI spectral library (in red) with spectral profiles collected from multiple locations within the study area (in black) indicates weak similarities in 2137 nm and good similarities in 2330 nm.

selected sepiolite spectra from the ENVI spectral library with spectral profiles collected across multiple locations within the study area, as shown in Figure 4.62, reveals a nuanced agreement. While a weak similarity is observed at 2137 nm, the feature at 2330 nm exhibits better alignment with the observed data. However, this feature is not a unique diagnostic marker for sepiolite, as it is also shared with dolomite. This overlap highlights the challenges in distinguishing sepiolite from carbonates using this spectral region alone.



### 4.3.5 Kaolinite in EMIT

Kaolinite, a clay mineral commonly formed through the weathering of aluminosilicates, reveals distinct spectral features in the SWIR range, which make it identifiable through EMIT’s high-resolution spectral bands. This mineral’s diagnostic spectral behavior is marked by a deep trough at 2204 nm and a characteristic peak at 2234 nm, offering a reliable approach for detecting and analyzing kaolinite in remote sensing data.

Mineral	Wavelength of spectral signature	Equivalent Band in EMIT	Type of Feature	Band ratio &
				Reflectance value ratio
Kaolinite	2.204 $\mu\text{m}$	Band 246	Trough	$B238+B251/B246$
	2.234 $\mu\text{m}$	Band 250	Peak	$R2145+R2241/R246$ $B250/B246+B261$ $R2234/R2204+2315$

**Table 4.15:** spectral signature of Kaolinite observed in the SWIR range at a wavelength of 2204 nm and 2334 nm corresponding to EMIT band 246 and 250 respectively.

The first significant spectral feature of kaolinite is the trough at 2204 nm, captured by EMIT Band 246. This trough is represented using the band ratio formula  $B238+B251/B246$  or the reflectance value ratio  $R2145+R2241/R2204$ , which highlights the low reflectance typical of kaolinite at this wavelength. For fine-grained kaolinite, reflectance values range from 2.5 to 2.7, which helps distinguish it from other minerals with overlapping SWIR spectra.

Feature Wavelengths from Resampled Spectra (nm)	2145 nm		2204 nm		2241 nm		B238 + B251/B246
Equivalent Band in EMIT	B238		B246		B251		
	Beckman	Perkin	Beckman	Perkin	Beckman	Perkin	Stretch Value Range
Reflectance for Kaolinite Fine Grain	66.59	55.19	52.83	42.01	66.99	57.08	2.5 - 2.7

**Table 4.16:** Reflectance Values and Band Math Calculation for Kaolinite at Spectral Signature of 2204 nm. This table presents the reflectance values and band math calculation for Kaolinite with fine grain size, calculated using Perkin and Beckman spectral analyzers, with data sourced from the ASTER library embedded in ENVI.

The second spectral feature of kaolinite, a peak at 2234 nm, is captured by EMIT Band 250 and analyzed through the band math ratio  $B250/(B246+B261)$  or reflectance value ratio  $R2234/(R2204+R2315)$ . This peak highlights kaolinite's increased reflectance in this spectral region, setting it apart from surrounding minerals. Fine-grain kaolinite shows a moderate reflectance range between 0.5 and 0.65

Feature Wavelengths from Resampled Spectra (nm)	2204 nm		2234 nm		2315 nm		B250/B246 + B261
Equivalent Band in EMIT	B246		B250		B261		
	Beckman	Perkin	Beckman	Perkin	Beckman	Perkin	Stretch Value Range
Reflectance for Kaolinite Fine Grain	57.97	40.59	71.14	57.13	63	48.27	0.5 - 0.65

**Table 4.17:** Reflectance Values and Band Math Calculation for Kaolinite at Spectral Signature of 2234 nm. This table presents the reflectance values and band math calculations for Kaolinite with fine grain size. The values were calculated using Perkin and Beckman spectral analyzers, with data sourced from the ASTER library embedded in ENVI.

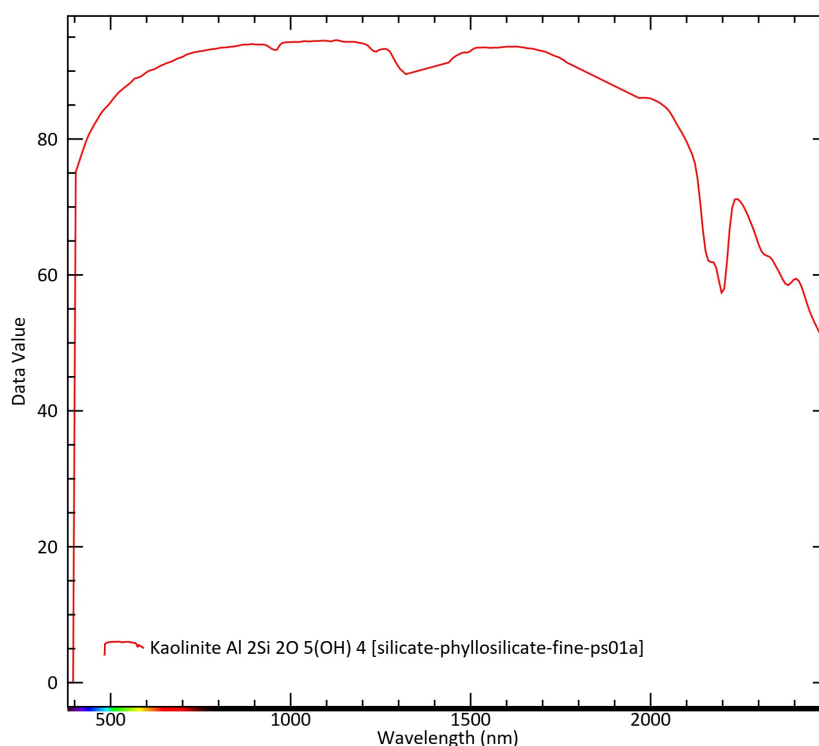


**Figure 4.63:** Resampled Spectral Reflectance of Kaolinite for fine, medium, and coarse grain size, adjusted to the EMIT sensor resolution.

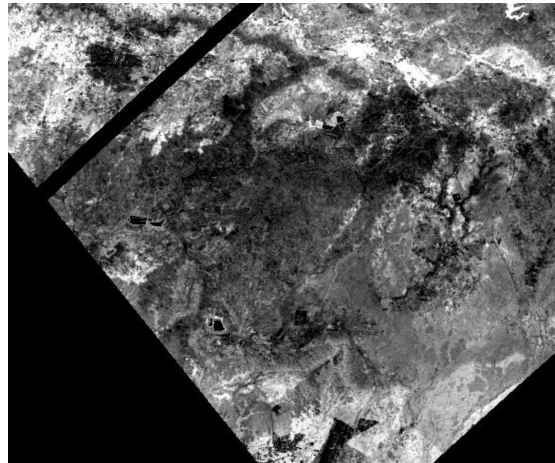


**Figure 4.64:** EMIT image of Kaolinite after application of relative band math at 2204 nm wavelength.

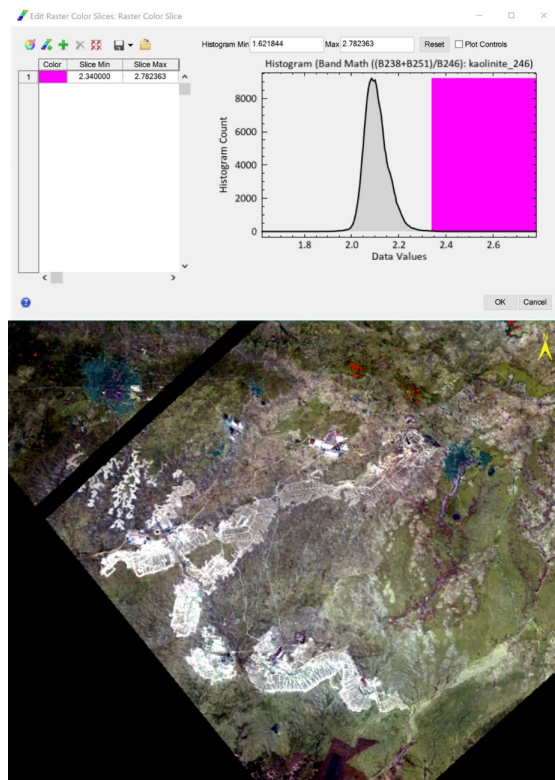


**Figure 4.65:** results of relative band math after applying raster color slice: The red color represents the range between 2.34 to 2.78, corresponding to the presence of the fine grain Kaolinite.

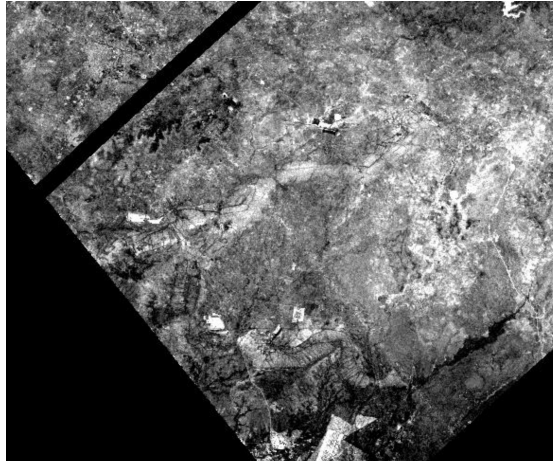


**Figure 4.66:** EMIT image of Kaolinite after application of relative band math at 2234 nm wavelength.

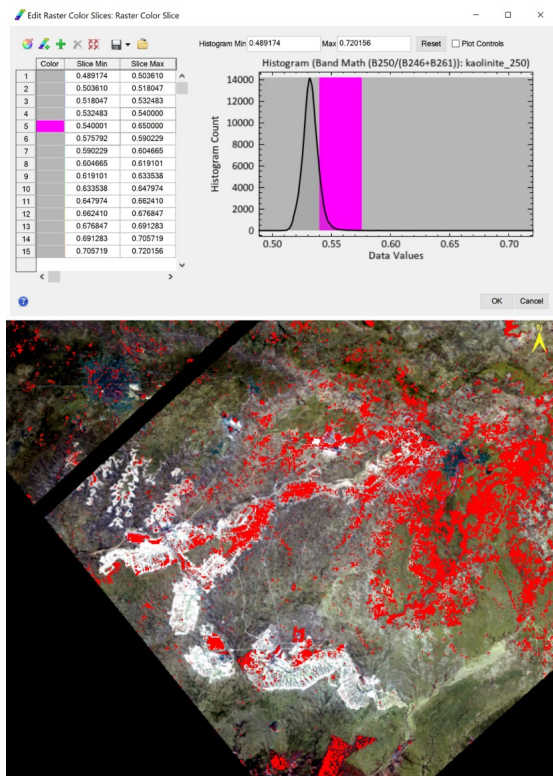


**Figure 4.67:** results of relative band math after applying raster color slice: The red color represents the range between 0.54 to 0.65, corresponding to the presence of the fine grain Kaolinite.

Figures 4.65 and 4.67 demonstrate the spatial distribution of kaolinite through color slicing, with red hues marking the presence of fine-grain kaolinite, supporting the reliability of the 2204 nm trough and 2234 nm peak as diagnostic features. These

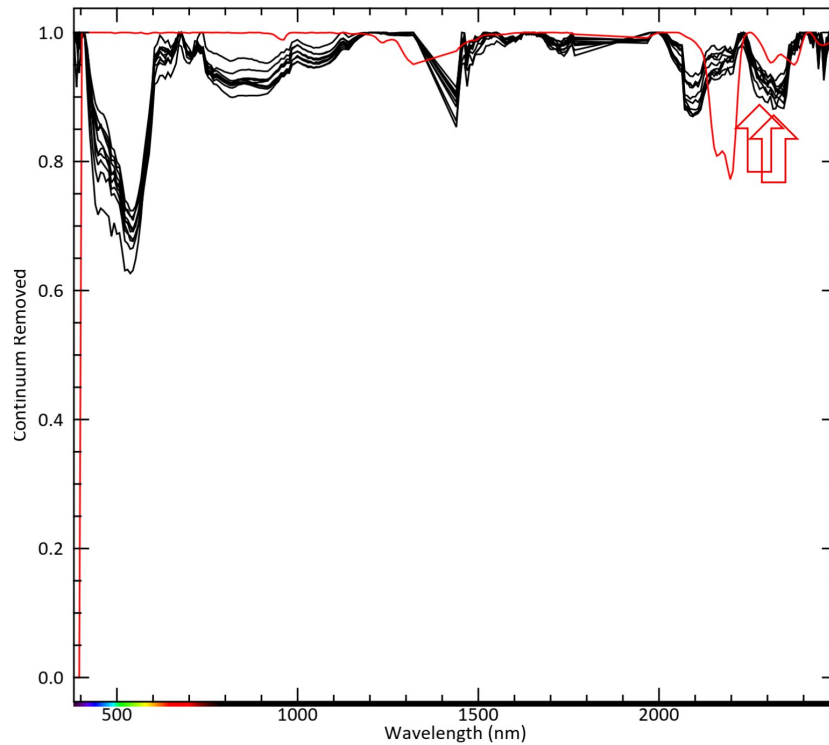


**Figure 4.68:** A comparison of the selected kaolinite spectra from the ENVI spectral library (in red) with spectral profiles collected from multiple locations within the study area (in black) indicates moderate similarities in 2200 nm and 2234 nm.

spectral characteristics are further validated in Figure 4.68, where a comparison of selected kaolinite spectra from ENVI's spectral library (in red) with real-world data (in black) reveals moderate agreement at both 2204 nm and 2234 nm. This confirms that kaolinite's distinct spectral response can be consistently detected across multiple locations.

### 4.3.6 Illite in EMIT

Illite, a mica-like clay mineral often found in sedimentary environments, displays unique spectral features in the SWIR range that make it readily identifiable through EMIT’s high-resolution spectral bands. This mineral is characterized by a pronounced spectral trough at 2211 nm, a signature captured by EMIT Band 247, which serves as a distinguishing marker when analyzing remotely sensed imagery.

Mineral	Wavelength of spectral signature	Equivalent Band in EMIT	Type of Feature	Band ratio & Reflectance value ratio
Illite	2.211 $\mu$ m	Band 247	Trough	$B236+B256/B247$ $R2130+R2278/R2211$

**Table 4.18:** spectral signature of Illite observed in the SWIR range at a wavelength of 2211 nm corresponding to EMIT band 247.

The trough at 2211 nm, a key spectral feature of illite, is highlighted using a band ratio of  $B236+B256/B247$  or a reflectance value ratio of  $R2130+R2278/R2211$ . This band math calculation effectively enhances illite’s lower reflectance at this specific wavelength, marking it as a spectral trough. When measured through Beckman and Perkin spectral analyzers and sourced from the ASTER library in ENVI, reflectance values for fine-grained illite exhibit a stretch range from 2.10 to 2.24, emphasizing the mineral’s distinctive reflectance dip.

Feature Wavelengths from Resampled Spectra (nm)	2130 nm		2211 nm		2278 nm		B236 + B256 / B247
Equivalent Band in EMIT	B236		B247		B256		
	Beckman	Perkin	Beckman	Perkin	Beckman	Perkin	Stretch Value Range
Reflectance for Illite Fine Grain	75.52	73.67	65.85	68.11	72.22	69.92	2.24 - 2.10

**Table 4.19:** Reflectance Values and Band Math Calculation for Illite at Spectral Signature of 2211 nm. This table presents the reflectance values and band math calculations for Illite with fine grain size. The values were calculated using Perkin and Beckman spectral analyzers, with data sourced from the ASTER library embedded in ENVI.

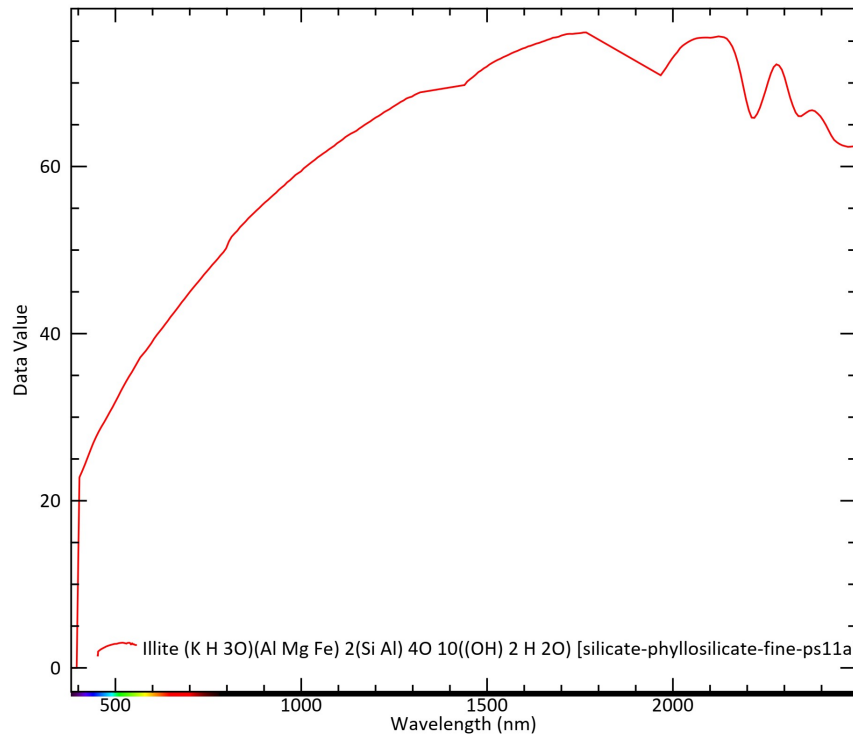


**Figure 4.69:** Resampled Spectral Reflectance of Illite for fine grain size, adjusted to the EMIT sensor resolution.

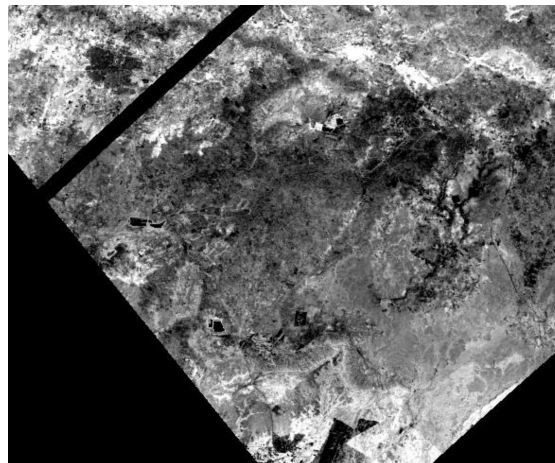


**Figure 4.70:** EMIT image of Illite after application of relative band math at 2211 nm wavelength.



The mapped reflectance values for illite provide insights into its distribution patterns within the study area, as visualized in Figures 4.70 and 4.71. Here, a relative band math approach highlights areas of fine-grained illite, with color slicing applied to raster data to enhance spatial detection. The resulting EMIT images use a red color range to indicate the presence of fine-grain illite in the 2.1 to 2.25 stretch range, offering a clear visual indicator of illite-rich zones across the landscape.

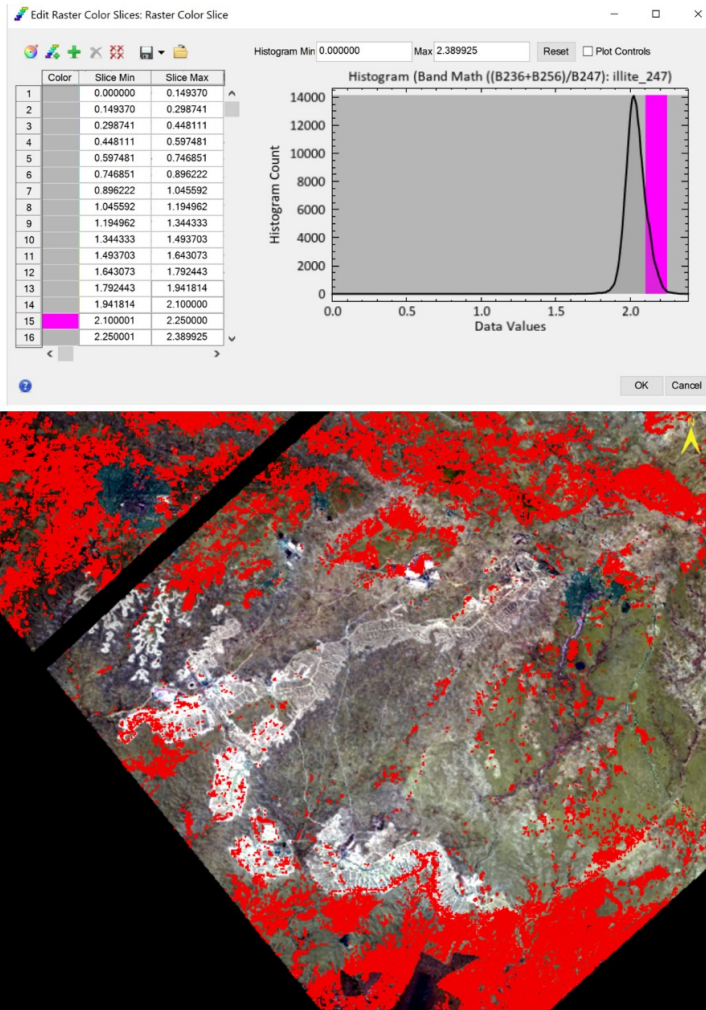


**Figure 4.71:** results of relative band math after applying raster color slice: The red color represents the range between 2.1 to 2.25, corresponding to the presence of the fine grain Illite.



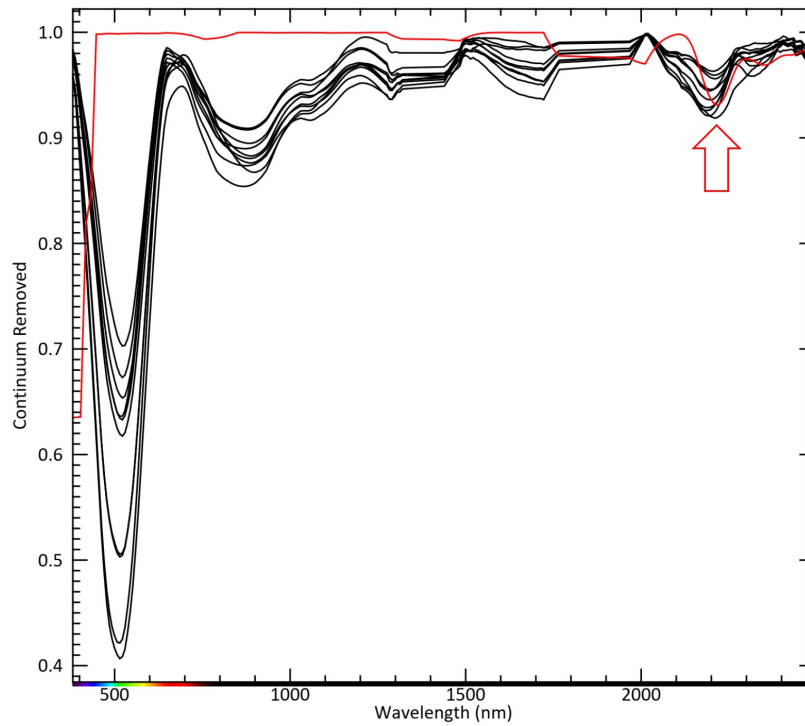


**Figure 4.72:** A comparison of the selected illite spectra from the ENVI spectral library (in red) with spectral profiles collected from multiple locations within the study area (in black) indicates notable similarities in 2211 nm.

The comparison presented in Figure 4.72 further confirms the reliability of the 2211 nm trough as an identifying feature for illite. The ENVI spectral library's signature (in red) is overlaid with actual spectral profiles collected from various study area locations (in black), revealing strong alignment at the 2211 nm wavelength.

### 4.3.7 Palygorskite in EMIT

Palygorskite, a fibrous clay mineral commonly associated with arid and semi-arid soils, shows distinct spectral characteristics in the shortwave infrared (SWIR) range, making it identifiable within EMIT’s bands. Notably, Palygorskite displays a spectral trough at 2211 nm, captured by EMIT Band 247, a feature that provides a reliable marker for detecting this mineral in complex geological environments.

Mineral	Wavelength of spectral signature	Equivalent Band in EMIT	Type of Feature	Band ratio & Reflectance value ratio
Palygorskite	2.211 $\mu\text{m}$	Band 247	Trough	$\frac{\text{B238}+\text{B253}}{\text{B247}}$ $\frac{\text{R2145}+\text{R2256}}{\text{R2211}}$

**Table 4.20:** spectral signature of Palygorskite observed in the SWIR range at a wavelength of 2211 nm corresponding to EMIT band 247.

The 2211 nm trough is emphasized through a band ratio of  $\text{B238}+\text{B253}/\text{B247}$  and a reflectance value ratio of  $\text{R2145}+\text{R2256}/\text{R2211}$ . This band math approach underlines Palygorskite’s absorption feature by enhancing the spectral dip at 2211 nm, a unique property of this mineral. Fine-grained Palygorskite samples analyzed with Beckman and Perkin instruments show a stretch range of 2.1 to 2.2, based on reflectance values from the ASTER library in ENVI.

Feature Wavelengths from Resampled Spectra (nm)	2145 nm		2211 nm		2256 nm		B238 + B253 / B247
Equivalent Band in EMIT	B238		B247		B253		
	Beckman	Perkin	Beckman	Perkin	Beckman	Perkin	Stretch Value Range
Reflectance for Palygorskite Fine Grain	66.34	64.13	59.87	56.22	62.03	59.08	2.1 – 2.2

**Table 4.21:** Reflectance Values and Band Math Calculation for Palygorskite at Spectral Signature of 2211 nm. This table presents the reflectance values and band math calculations for Palygorskite with fine grain size. The values were calculated using Perkin and Beckman spectral analyzers, with data sourced from the ASTER library embedded in ENVI.

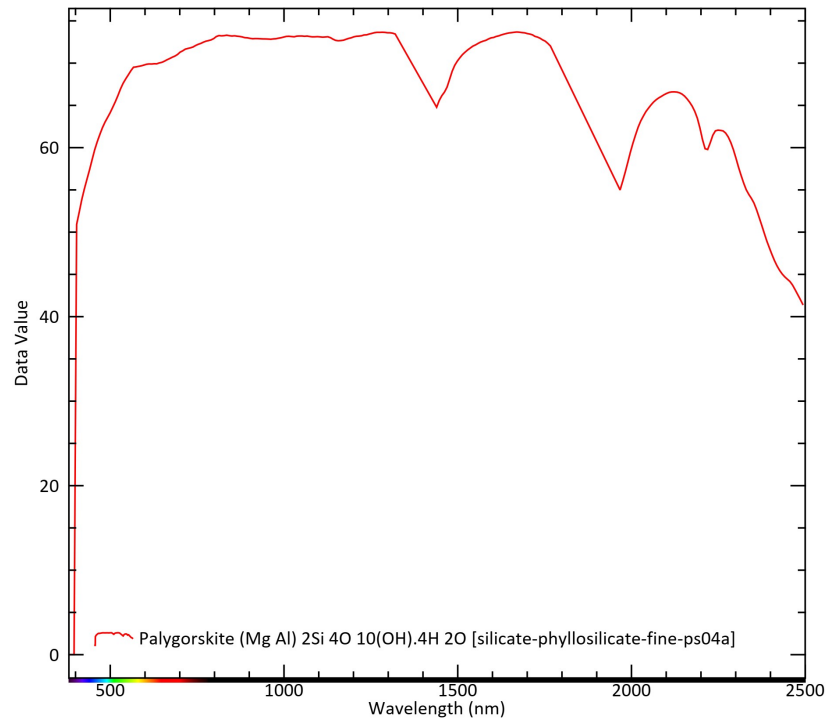


**Figure 4.73:** Resampled Spectral Reflectance of Palygorskite for fine grain size, adjusted to the EMIT sensor resolution.

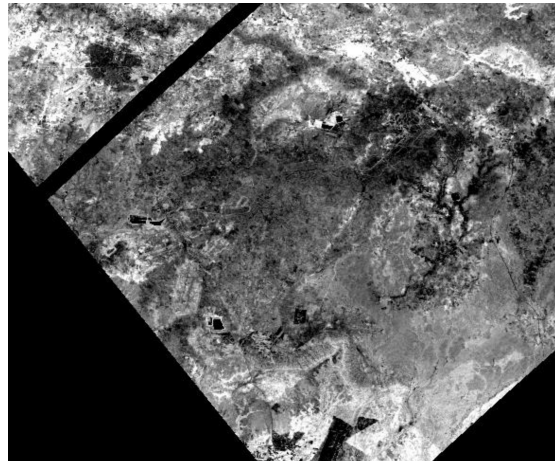


**Figure 4.74:** EMIT image of Palygorskite after application of relative band math at 2211 nm wavelength.

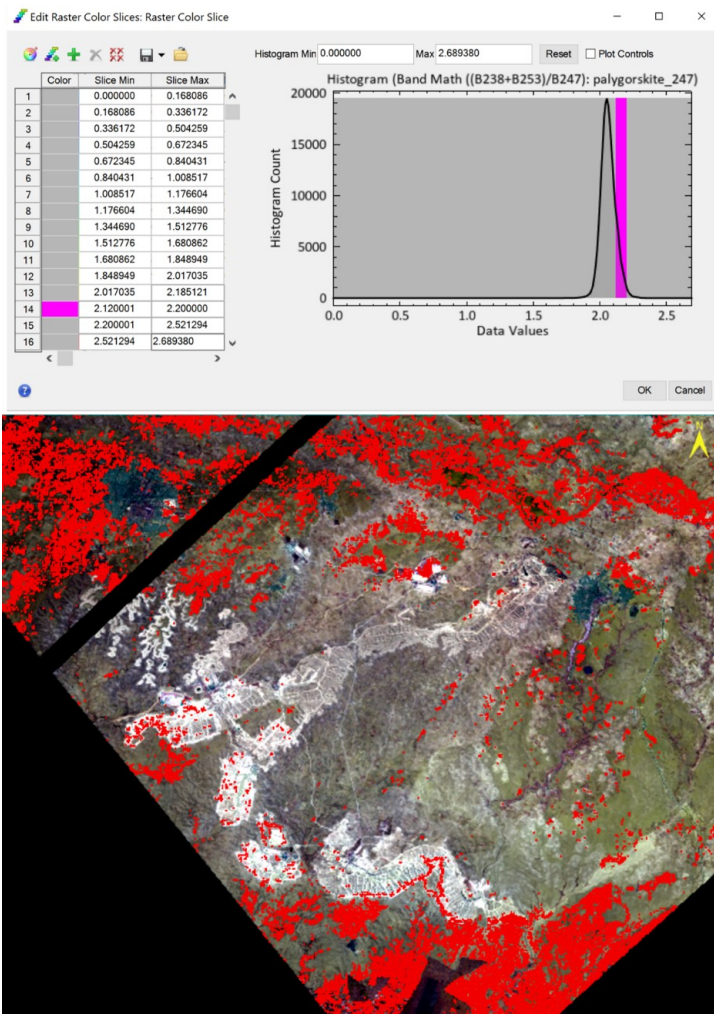


**Figure 4.75:** results of relative band math after applying raster color slice: The red color represents the range between 2.1 to 2.2, corresponding to the presence of the fine grain Palygorskite.

In Figures 4.74 and 4.75, the EMIT imagery reveals the spatial distribution of Palygorskite, highlighting areas where fine-grained particles are prevalent. The color-sliced raster data vividly represents Palygorskite in red, corresponding to the reflectance stretch range of 2.1 to 2.2.

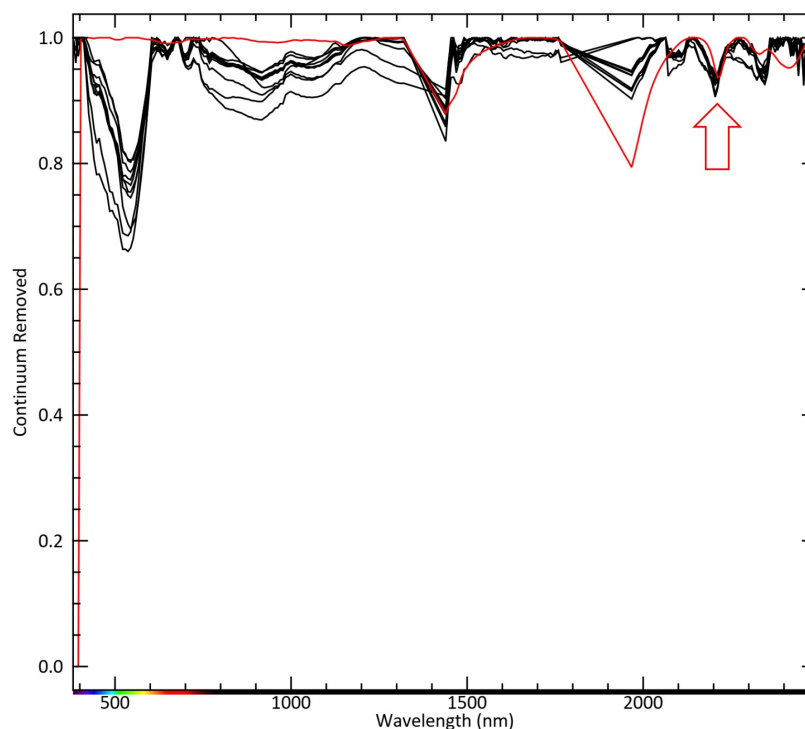


**Figure 4.76:** A comparison of the selected Palygorskite spectra from the ENVI spectral library (in red) with spectral profiles collected from multiple locations within the study area (in black) indicates notable similarities in 2211 nm.

The comparison of the Palygorskite spectral profile from the ENVI spectral library (in red) against collected spectra from multiple locations (in black) in Figure 4.76 further substantiates the mineral's spectral consistency, particularly at the 2211 nm marker. The alignment of these profiles confirms the characteristic absorption feature of Palygorskite, supporting the reliability of remote detection methods for this clay mineral.

The spectral analysis conducted for palygorskite and illite highlights that these minerals share similar absorption features, which makes differentiation challenging using the current technique. While the analyses were performed separately, the resulting mineral maps display comparable spatial distributions due to these shared spectral characteristics. As a result, the maps represent the combined distribution of illite and palygorskite in the study area.

### 4.3.8 Glauconite in EMIT

Glauconite, a greenish clay mineral often associated with marine environments, displays a signature trough at 2308 nm that provides a distinct spectral fingerprint in EMIT’s SWIR bands. The subtle depth of this trough, observed in Band 260, is essential for pinpointing glauconite in environments where clay minerals are abundant and visually similar. This absorption feature, captured by the band ratio  $B255+B264/B260$  and the reflectance value ratio  $R2271+R2337/R2308$ , reveals glauconite’s unique spectral behavior across different grain sizes.

Mineral	Wavelength of spectral signature	Equivalent Band in EMIT	Type of Feature	Band ratio & Reflectance value ratio
Glauconite	2.308 $\mu\text{m}$	Band 260	Trough	$B255+B264/B260$ $R2271+R2337/R2308$

**Table 4.22:** spectral signature of Glauconite observed in the SWIR range at a wavelength of 2308 nm corresponding to EMIT band 250 respectively.

Feature Wavelengths from Resampled Spectra (nm)	2271 nm		2308 nm		2337 nm		B255 + B264 / B260
Equivalent Band in EMIT	B255		B260		B264		
	Beckman	Perkin	Beckman	Perkin	Beckman	Perkin	Stretch Value Range
Reflectance for Glauconite Fine Grain	54.87	52.94	50.97	48.81	52.73	50.91	2.05 - 2.25
Reflectance for Glauconite Medium Grain	24.50	24.40	20.25	19.49	21.88	21.75	2.25 - 2.35
Reflectance for Glauconite Coarse Grain	11.04	11.40	8.23	8.15	9.19	9.53	2.40 - 2.60

**Table 4.23:** Reflectance Values and Band Math Calculation for Glauconite at Spectral Signature of 2308 nm. This table presents the reflectance values and band math calculations for Glauconite with fine, medium, and coarse grain sizes. The values were calculated using Perkin and Beckman spectral analyzers, with data sourced from the ASTER library embedded in ENVI.

Reflectance values for glauconite show clear differentiation among fine, medium, and coarse grains, with values stretching from 2.05–2.25 for fine grain sizes, increasing to 2.40–2.60 for coarser samples. The reflectance data, sourced from Beckman and Perkin measurements in the ASTER library within ENVI, demonstrates how glauconite’s grain size affects its spectral profile, with finer grains reflecting higher values due to their smoother surfaces.

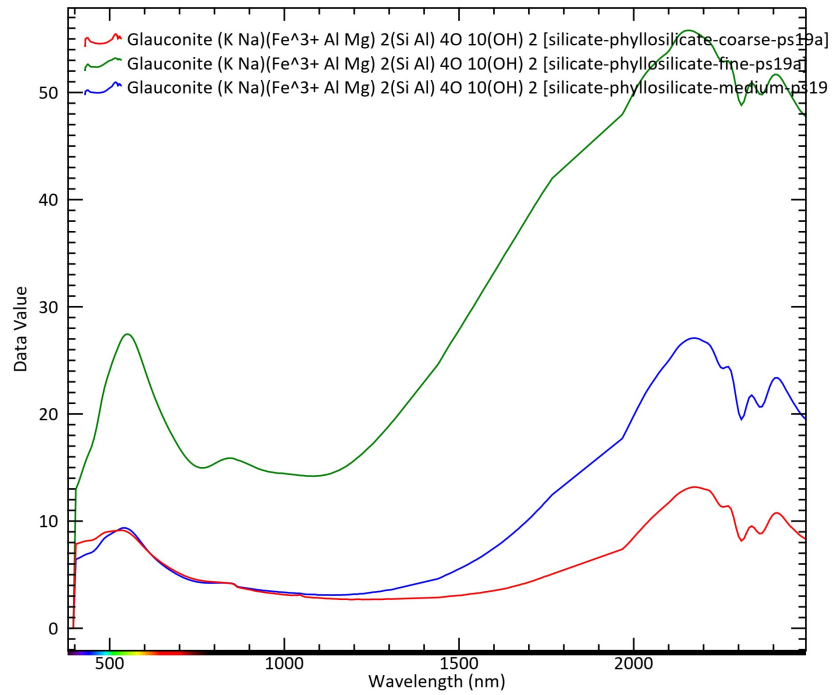


**Figure 4.77:** Resampled Spectral Reflectance of glauconite for fine, grain size, adjusted to the EMIT sensor resolution.

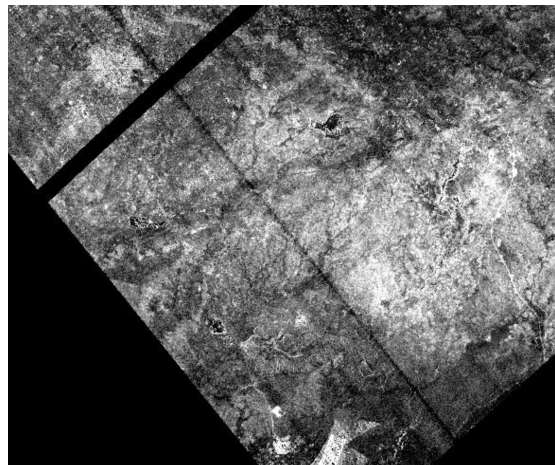


**Figure 4.78:** EMIT image of Glauconite after application of relative band math at 2308 nm wavelength.



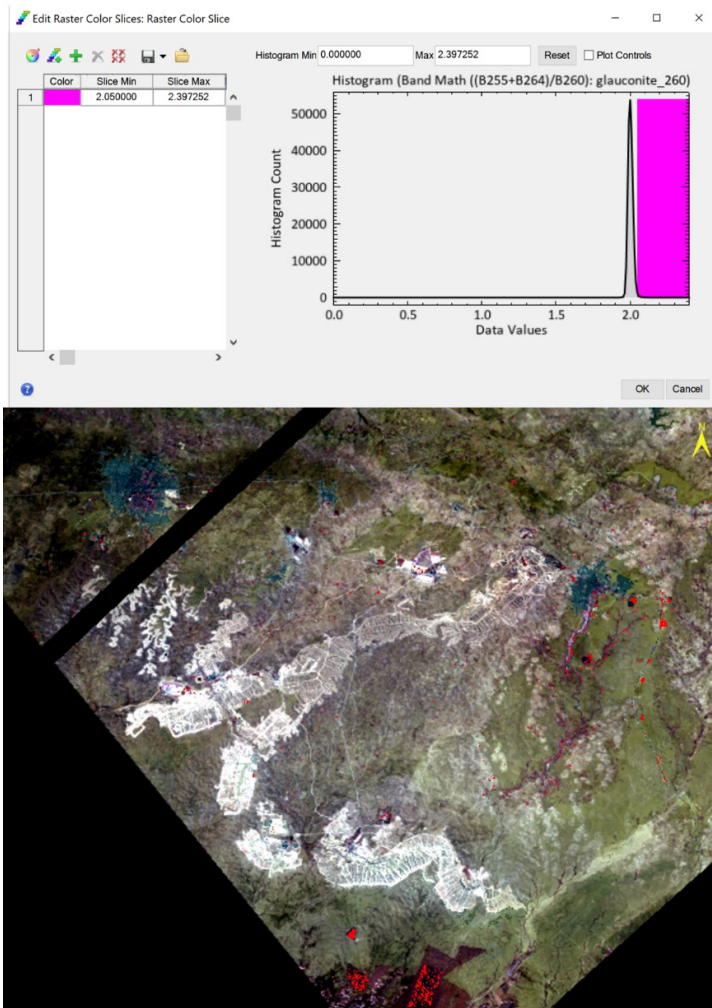


**Figure 4.79:** results of relative band math after applying raster color slice: The red color represents the range between 2.05 to 2.25, corresponding to the presence of the fine grain glauconite.

Figures 4.78 and 4.79 illustrate the spatial distribution of glauconite within EMIT imagery, where color-slicing emphasizes fine-grained glauconite with a red hue in areas with values ranging from 2.05 to 2.25. This color-sliced visualization provides an intuitive look at glauconite’s occurrence, mapping its spatial extent in regions.



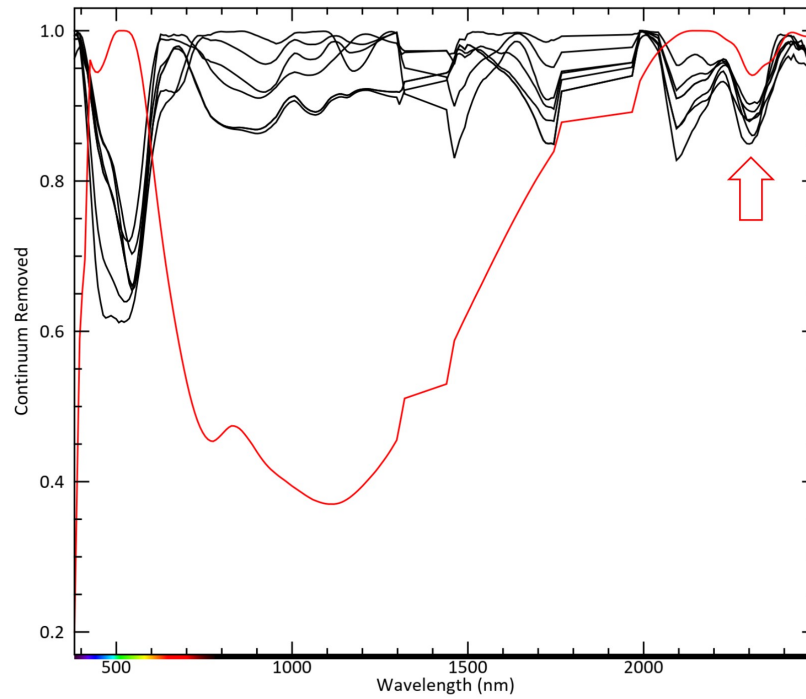


**Figure 4.80:** A comparison of the selected Glauconite spectra from the ENVI spectral library (in red) with spectral profiles collected from multiple locations within the study area (in black) indicates notable similarities in 2203 nm.

A comparison between glauconite's standard spectral profile from the ENVI library (in red) and on-site spectral readings (in black) from various study locations, as shown in Figure 4.80, underscores its characteristic absorption at 2308 nm.

### 4.3.9 Hematite in EMIT

Hematite, an iron oxide mineral recognized for its distinctive red-brown color, presents spectral signatures at 551 nm and 860 nm, corresponding to EMIT Bands 24 and 43, respectively. These troughs capture hematite’s reflective properties at both visible and near-infrared wavelengths, where its strong absorption serves as a key identifier for this mineral in natural landscapes. By employing band ratios, such as B18+B29/B24 for the 551 nm signature and B48+B88/B43 for the 860 nm range, along with the reflectance ratios R0.507+R0.589/R0.551 and R0.730+R1.029/R0.860, the spectral characteristics of hematite can be enhanced, aiding in distinguishing it from similar iron oxides.

Mineral	Wavelength of spectral signature	Equivalent Band in EMIT	Type of Feature	Band ratio & Reflectance value ratio
Hematite	0.551 $\mu$ m	Band 24	Trough	B18+B29/B24 R0.507+R0.589/R0.551
	0.860 $\mu$ m	Band 43	Trough	B48+B88/B43 R0.730+R1.029/R0.860

**Table 4.24:** spectral signature of Hematite observed in the SWIR range at a wavelength of 551 nm and 860 nm corresponding to EMIT band 24 and band 43.

Feature Wavelengths from Resampled Spectra (nm)	507 nm		551 nm		589 nm		B18 + B29 / B24
Equivalent Band in EMIT	B18		B24		B29		
	Beckman	Perkin	Beckman	Perkin	Beckman	Perkin	Stretch Value Range
Reflectance for Hematite (Fine Grain)	4.57	2.99	5.59	3.64	12.31	8.1	2.7 - 3.6
Reflectance for Hematite (Medium Grain)	6.32	6.48	6.95	7.14	8.57	9.48	2.1 - 2.35
Reflectance for Hematite (Coarse Grain)	6.59	6.63	7.12	7.24	8.45	9.3	2.11 - 2.2

**Table 4.25:** Reflectance Values and Band Math Calculation for Hematite at Spectral Signature of 551 nm. This table presents the reflectance values and band math calculations for Hematite with fine, medium, and coarse grain sizes, calculated using Perkin and Beckman spectral analyzers, with data sourced from the ASTER library embedded in ENVI.

Feature Wavelengths from Resampled Spectra (nm)	730 nm		860 nm		1029 nm		B48 + B88 / B43
Equivalent Band in EMIT	B48		B43		B88		
	Beckman	Perkin	Beckman	Perkin	Beckman	Perkin	Stretch Value Range
Reflectance for Hematite (Fine Grain)	24.3	18.02	21.29	15.28	30.49	23.62	2.4 – 2.6
Reflectance for Hematite (Medium Grain)	11.2	11.95	9.63	9.83	11.89	12.17	2.2 – 2.4
Reflectance for Hematite (Coarse Grain)	10.52	11.11	8.89	8.93	10.41	10.76	2.2 – 2.4

**Table 4.26:** Reflectance Values and Band Math Calculation for Hematite at Spectral Signature of 860 nm. This table presents the reflectance values and band math calculations for Hematite with fine, medium, and coarse grain sizes, calculated using Perkin and Beckman spectral analyzers, with data sourced from the ASTER library embedded in ENVI.

Reflectance measurements for hematite reveal substantial variations across fine, medium, and coarse grain sizes. For example, fine-grained hematite exhibits a higher reflectance, ranging from 2.7 to 3.6 for the 551 nm band and from 2.4 to 2.6 at 860 nm, as derived from ASTER library data using Perkin and Beckman spectral analyzers. Medium and coarse grains show a more constrained reflectance range, indicative of their reduced surface reflectivity compared to fine grains. These reflectance values, depicted in Tables 4.25 and 4.26, provide insight into hematite’s physical grain structure and how it interacts with light, making it possible to map hematite-rich regions in different geological settings accurately.

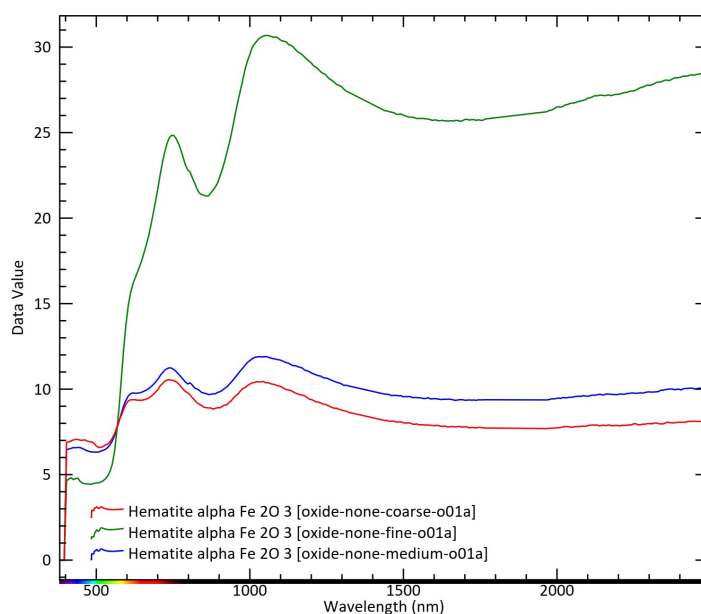


**Figure 4.81:** Resampled Spectral Reflectance of Hematite for fine, medium, and coarse grain size, adjusted to the EMIT sensor resolution.

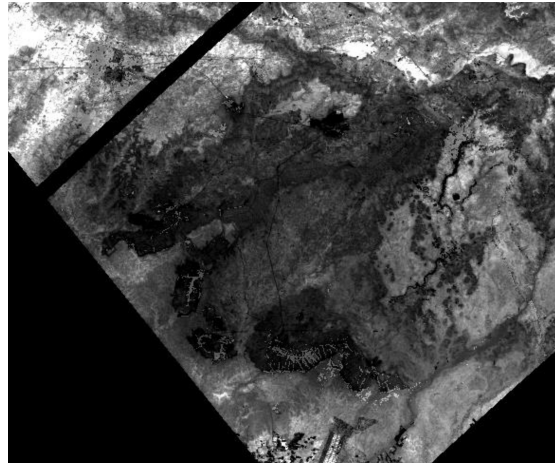


**Figure 4.82:** EMIT image of Hematite after application of relative band math at 551 nm wavelength.

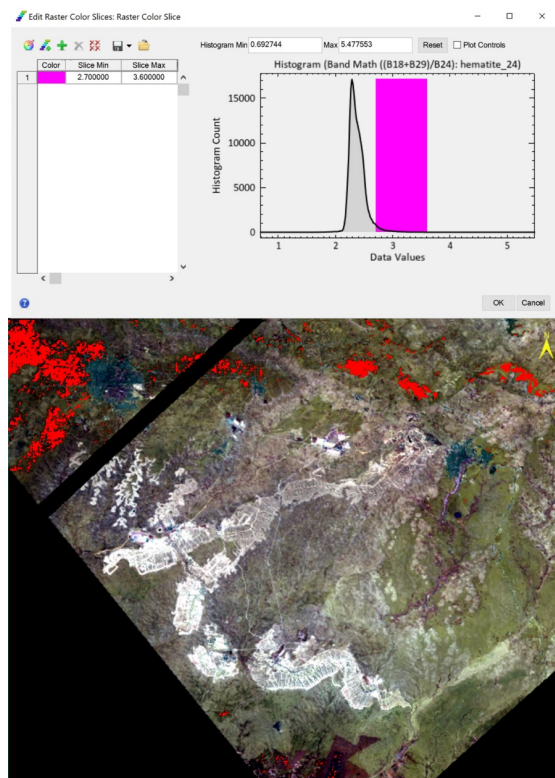


**Figure 4.83:** results of relative band math after applying raster color slice: The red color represents the range between 2.7 to 3.6, corresponding to the presence of the fine grain Hematite.

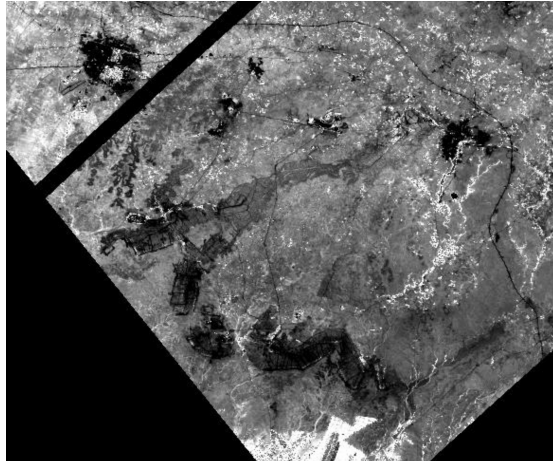


**Figure 4.84:** EMIT image of Hematite after application of relative band math at 860 nm wavelength.

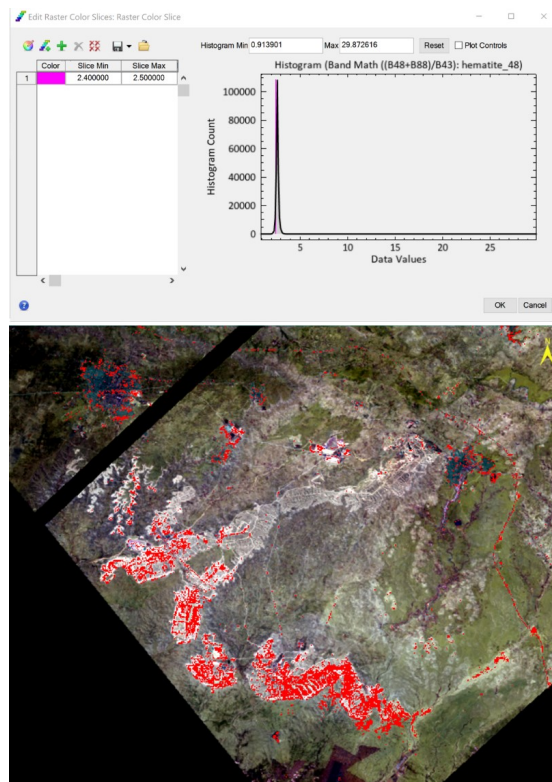


**Figure 4.85:** results of relative band math after applying raster color slice: The red color represents the range between 2.4 to 2.5, corresponding to the presence of the fine grain Hematite.

In Figures 4.82 and 4.84, EMIT imagery displays hematite using band math applications at 551 nm and 860 nm, respectively. Color slicing within these images, as shown in Figures 4.83 and 4.85, highlights fine-grained hematite in red, emphasizing reflectance values within the 2.7 to 3.6 and 2.4 to 2.5 ranges, which are indicative of high-purity hematite deposits. The spectral comparison illustrated

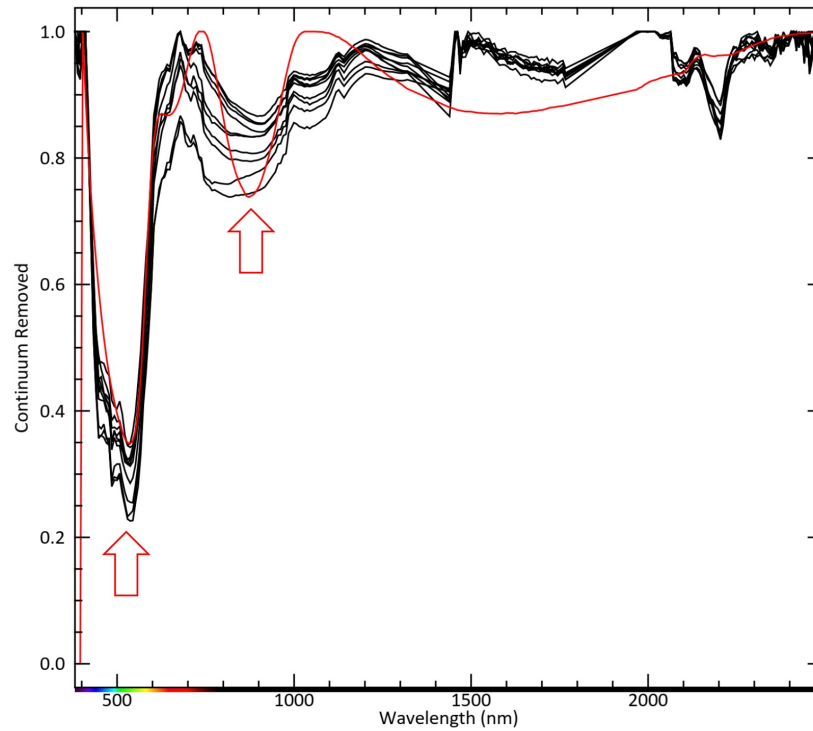


**Figure 4.86:** A comparison of the selected hematite spectra from the ENVI spectral library (in red) with spectral profiles collected from multiple locations within the study area (in black) indicates notable similarities in 551 nm and 860 nm.

in Figure 4.86, showing ENVI library data (in red) alongside field-collected spectra (in black), underscores the consistent spectral behavior of hematite at 551 nm and 860 nm.

## 4.4 Result of Mineral Detection in Phosphate Mines Using ECOSTRESS satellite

In this section, the application of ECOSTRESS satellite data for mineral detection within phosphate mines was studied, examining how the instrument’s spectral bands capture distinct mineral signatures crucial for identifying key components like apatite, quartz, calcite, and dolomite. By analyzing specific absorption features and leveraging tailored band and reflectance value ratios, ECOSTRESS enables a detailed differentiation of these minerals across the phosphate mining landscape. The ECOSTRESS sensor operates in the thermal infrared (TIR) range, making it particularly effective for detecting minerals with distinct spectral signatures in this part of the spectrum. Minerals like apatite, quartz, calcite, and dolomite were selected for this analysis due to their well-defined absorption features in the TIR region. Apatite, for example, shows prominent absorption at 8400, 9160, and 9620 nm, whereas quartz and dolomite have distinct spectral responses at alternative wavelengths. Specific band math techniques are applied to enhance mineral discrimination.

The following subsections discuss the findings in detail, revealing how ECOSTRESS data supports high-resolution mineral identification, informs resource management strategies, and highlights areas of geological interest within the mining context. Through this analysis, we demonstrate how ECOSTRESS’s capacity to detect subtle spectral variations plays an instrumental role in the remote sensing of mineral deposits.

Mineral	Wavelength of Spectral Signature (nm)	Type of Feature	Band Ratio and Reflectance Value Ratio
Apatite	8400	Absorption	$(B2 + B4) / B3$ $R8780 + R10490 / R9200$
	9160		
	9620		
Quartz	8150	Absorption	$(B2 - B4) / (B2 + B4)$ $R8780 - R10490 / R8780 + R10490$
	8600		
	9330		
Calcite	11430	Absorption	$B3 / B5$ $R9200 / R12090$
	14040		
Dolomite	11350	Absorption	$(B5 + B4) / B3$ $R12090 + R10490 / R9200$
	13700		

**Table 4.27:** Spectral Signatures, Reflectance Value Ratio, and Band Ratios of Minerals Using ECOSTRESS Data.

#### 4.4.1 Apatite In ECOSTRESS

Feature Wavelengths from Resampled Spectra ( $\mu\text{m}$ )	8.29 $\mu\text{m}$	8.78 $\mu\text{m}$	9.20 $\mu\text{m}$	10.49 $\mu\text{m}$	12.09 $\mu\text{m}$	Band Math for Apatite (B2 + B4) / B3
Equivalent Band in ECOSTRESS	B1	B2	B3	B4	B5	-
Reflectance Value for Apatite (Fine Grain)	5.95	11.82	15.94	10.64	20.39	1.4
Reflectance Value for Apatite (Medium Grain)	1.88	14.32	31.83	6.31	7.29	0.64
Reflectance Value for Apatite (Coarse Grain)	1.12	14.63	35.04	6.08	3.52	0.59

**Table 4.28:** Reflectance Values and Band Math Calculation for Apatite at a Spectral Signature of 9620 nm. This table presents the reflectance values and band math calculations for Apatite with fine, medium, and coarse grain sizes. The values were calculated using Nicolet spectral analyzers, with data sourced from the ASTER library embedded in ENVI.

Apatite, a key mineral in phosphate deposits, exhibits distinctive spectral features in the TIR range, particularly around 9.16 m and 9.62 m, as captured by the ECOSTRESS sensor.

Given the spectral characteristics of apatite, the following band math expression can be used to detect apatite:

$$\frac{B2 + B4}{B3}$$

The band math calculations in Table 4.28 show variations in reflectance across fine, medium, and coarse grains, with fine-grained apatite demonstrating reflectance values of 5.95 at 8.29 m and reaching a peak of 20.39 at 12.09 m. These values contrast significantly with medium and coarse grains, further validating the mineral's spectral distinctiveness and aiding in its identification within the phosphate mine.



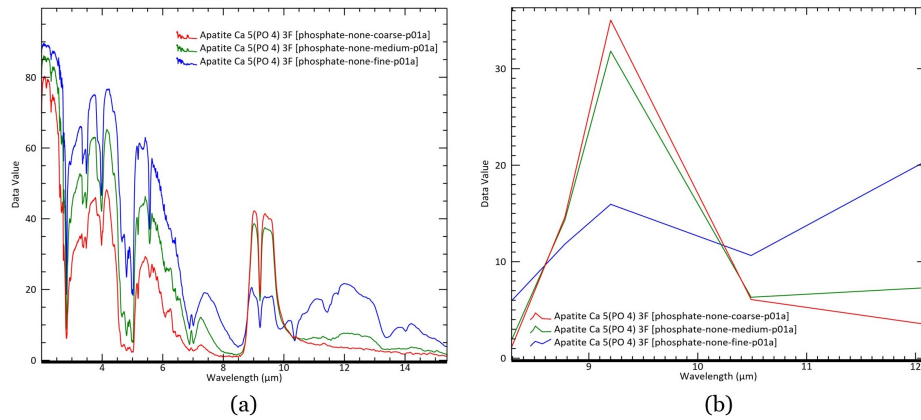


**Figure 4.87:** (a) Spectral Reflectance and (b) Resampled Spectral Reflectance of Apatite for fine, medium, and coarse grain size, adjusted to the ECOSTRESS sensor resolution.

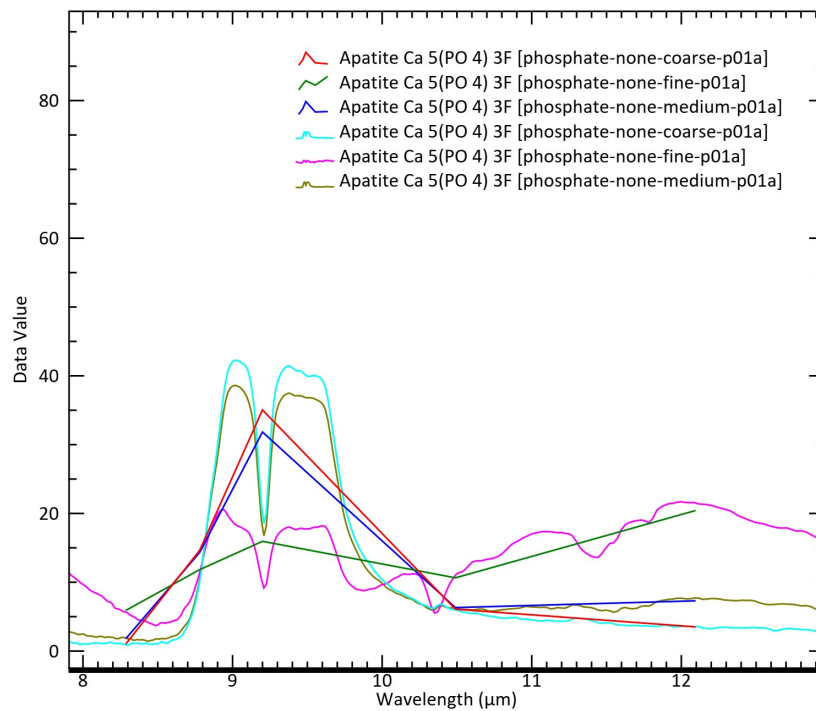


**Figure 4.88:** Spectral Reflectance and Resampled Spectral Reflectance of Apatite for fine, medium, and coarse grain size in one frame.

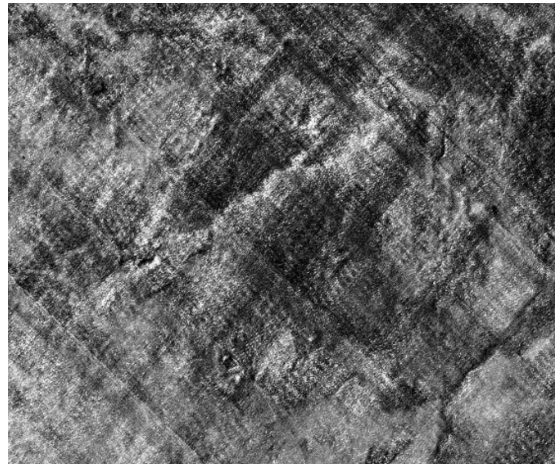


**Figure 4.89:** ECOSTRESS image of Apatite after application of relative band math at 9160 nm wavelength.

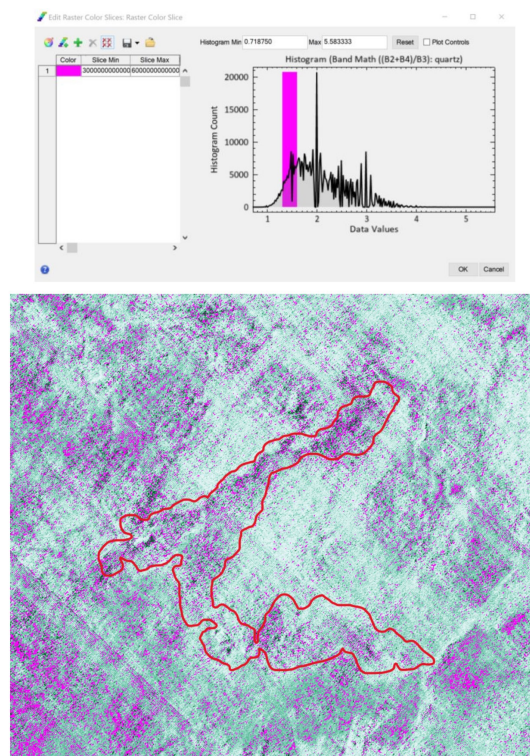


**Figure 4.90:** results of relative band math after applying raster color slice: The red color represents the range between 1.3 to 1.6, corresponding to the presence of the fine grain Apatite.

The grayscale image in Figure 4.89 presents the ECOSTRESS data of apatite after applying a specific band math formula at the 9160 nm wavelength. This wavelength is particularly significant due to its strong absorption feature for apatite in the thermal infrared (TIR) spectrum, as captured by the ECOSTRESS sensor. The variations in grayscale intensity likely represent different levels of reflectance corresponding to apatite concentrations across the surface. Areas with darker tones might indicate regions with lower reflectance or possibly lower apatite concentration, whereas lighter tones could signify higher reflectance, suggesting potential apatite-rich zones.

In Figure 4.90, the application of raster color slicing highlights areas with reflectance values corresponding to fine-grained apatite. The red color, representing a reflectance range of 0.3 to 0.6, indicates the potential presence of fine-grained apatite within the defined mine boundary. The outlined red area thus serves as a spatial reference, helping to visually locate the mine within the ECOSTRESS dataset. Although the mine's physical boundaries are not visible in the original grayscale image, the color-slicing technique isolates apatite concentrations within the mining area. In Figure 4.91, The close alignment of these spectra, particularly around the 9160 nm absorption feature, suggests a strong similarity between the field samples and the reference apatite, confirming the mineral's presence within the study area.

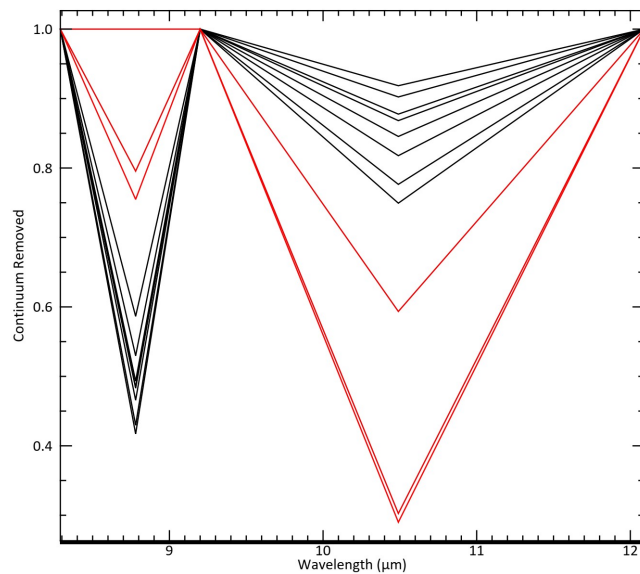


**Figure 4.91:** A comparison of the selected apatite spectra from the ENVI spectral library (in red) with spectral profiles collected from multiple locations within the study area (in black).

## 4.4.2 Quartz In ECOSTRESS

Feature Wavelengths from Resampled Spectra ( $\mu\text{m}$ )	8.29 $\mu\text{m}$	8.78 $\mu\text{m}$	9.20 $\mu\text{m}$	10.49 $\mu\text{m}$	12.09 $\mu\text{m}$	Band Math for Quartz (B2 - B4) / (B2 + B4)
Equivalent Band in ECOSTRESS	B1	B2	B3	B4	B5	-
Reflectance Value for Quartz (Fine Grain)	20.82	21.34	22.61	14.77	7.13	0.18
Reflectance Value for Quartz (Medium Grain)	42.05	48.65	48.89	7.61	3.88	0.72
Reflectance Value for Quartz (Coarse Grain)	48.02	58.38	54.82	7.73	3.74	0.76

**Table 4.29:** Reflectance Values and Band Math Calculation for Quartz at a Spectral Signature of 9330 nm. This table presents the reflectance values and band math calculations for Quartz with fine, medium, and coarse grain sizes. The values were calculated using Nicolet spectral analyzers, with data sourced from the ASTER library embedded in ENVI.

Quartz, a highly abundant and resilient mineral, is distinguishable by its unique spectral characteristics, especially in the thermal infrared (TIR) region. Its reststrahlen bands create a signature "M-shaped" reflectance pattern that peaks at specific wavelengths, particularly around 8.78  $\mu\text{m}$  and 10.49  $\mu\text{m}$ . Given the spectral characteristics of quartz, the following band math expression can be used to detect quartz:

$$\frac{B2 - B4}{B2 + B4}$$

(B2 - B4) highlights the drop in reflectance as the wavelength shifts from B2 (8.78  $\mu\text{m}$ ) to B4 (10.49  $\mu\text{m}$ ). Quartz is expected to show a higher reflectance at B2 due to its strong reststrahlen bands and a notable decrease in reflectance by B4. (B2 + B4) normalizes the difference, making the index more robust across varying illumination conditions and ensuring the output is within a consistent range. This band math expression effectively captures the M-shaped reststrahlen bands of quartz by emphasizing the spectral decrease from B2 to B4, characteristic of quartz in the TIR region.

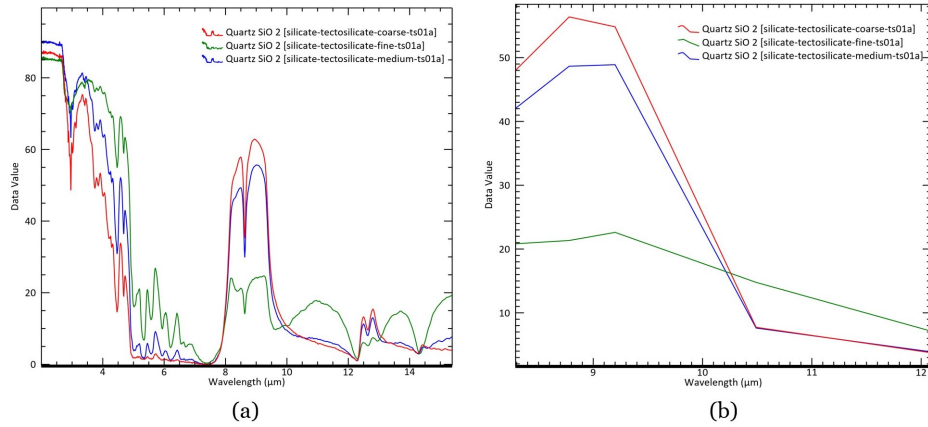


**Figure 4.92:** (a) Spectral Reflectance and (b) Resampled Spectral Reflectance of Quartz for fine, medium, and coarse grain size, adjusted to the ECOSTRESS sensor resolution.

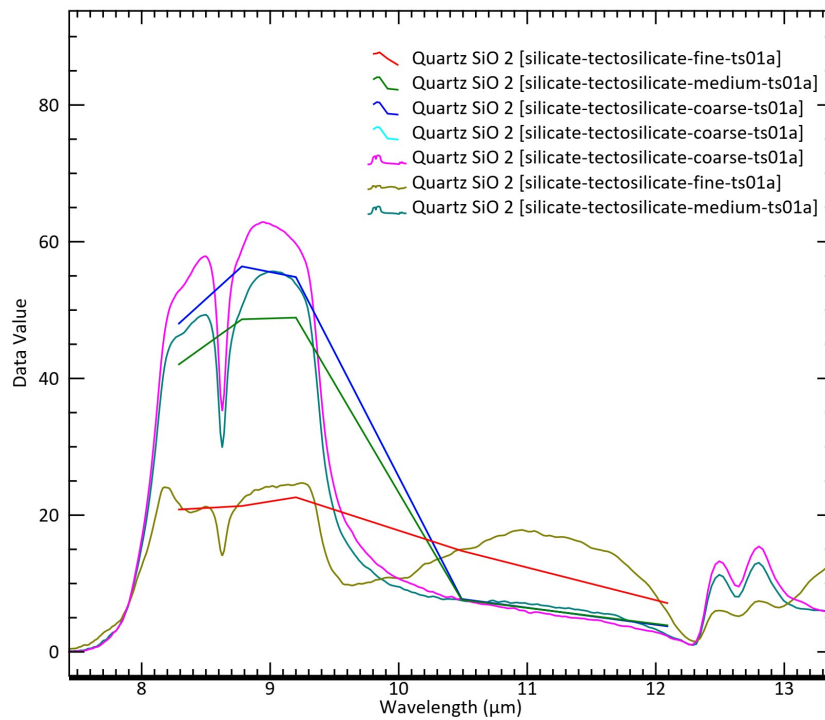


**Figure 4.93:** Spectral Reflectance and Resampled Spectral Reflectance of Quartz for fine, medium, and coarse grain size in one frame.



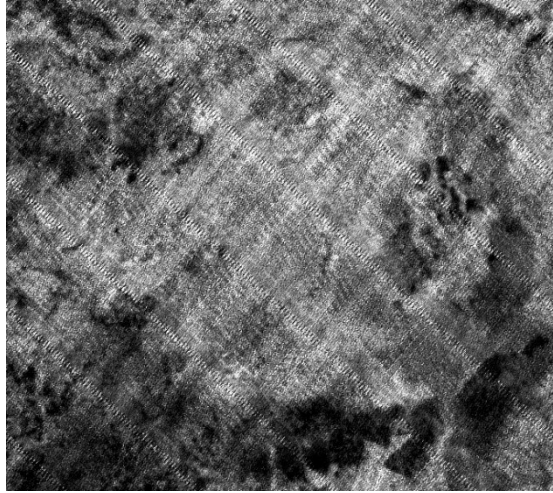


**Figure 4.94:** ECOSTRESS image of Quartz after application of relative band math at 9330 nm wavelength.

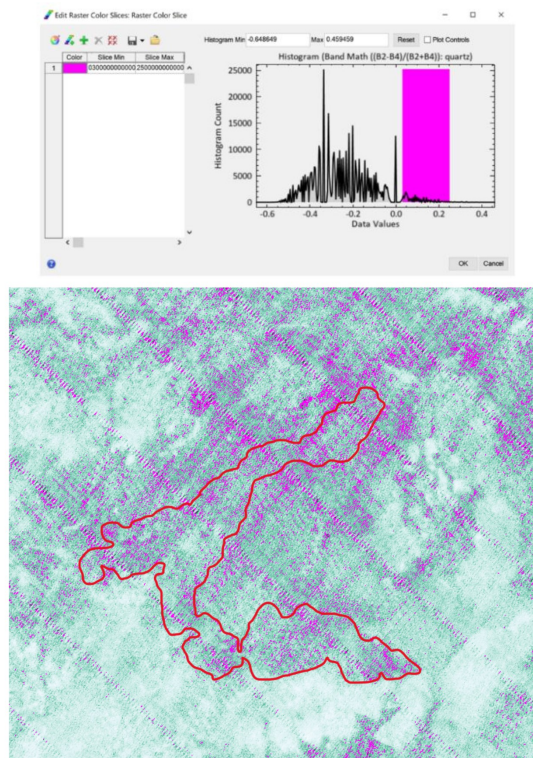


**Figure 4.95:** results of relative band math after applying raster color slice: The red color represents the range between 0.03 to 0.25, corresponding to the presence of the fine grain Quartz.

The results presented in Figures 4.94 and 4.95 highlight the effectiveness of using relative band math to isolate fine-grain quartz with ECOSTRESS data, specifically at the 9330 nm wavelength. In Figure 4.94, the grayscale image shows the initial output of the band math calculation, highlighting areas with spectral characteristics that suggest quartz. The texture and contrast of the image reveal variations in reflectance across the region, providing a foundation for further classification. Figure 4.95 builds on this by applying a raster color slice to the initial result, with red areas indicating where fine-grain quartz is present. The color slice was set to emphasize values between 0.03 and 0.25, capturing subtle spectral differences within the mining area. This visualization helps clarify the spatial distribution of quartz, highlighting regions with higher concentrations of fine-grain particles. This approach is particularly useful for mineral mapping and assessing resources. Figure 4.96 compares quartz spectra from the ENVI spectral library with spectral profiles collected from various locations in the study area, showing an apparent match. However, the slight discrepancies between the observed spectral signatures and the reference spectra are likely due to the presence of mixed pixels, indicating that the signal may include contributions from other minerals besides quartz.

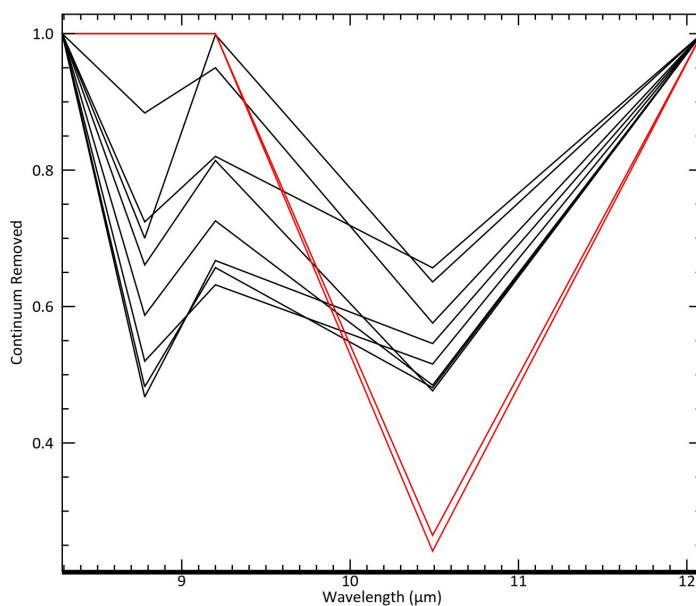


**Figure 4.96:** A comparison of the selected quartz spectra from the ENVI spectral library (in red) with spectral profiles collected from multiple locations within the study area (in black) indicates notable similarities in 9330 nm.

### 4.4.3 Dolomite In ECOSTRESS

Feature Wavelengths from Resampled Spectra ( $\mu\text{m}$ )	8.29 $\mu\text{m}$	8.78 $\mu\text{m}$	9.20 $\mu\text{m}$	10.49 $\mu\text{m}$	12.09 $\mu\text{m}$	Band Math for Dolomite (B5 + B4) / B3
Equivalent Band in ECOSTRESS	B1	B2	B3	B4	B5	-
Reflectance Value for Dolomite (Fine Grain)	21.94	16.28	14.48	25.58	26.27	3.6
Reflectance Value for Dolomite (Medium Grain)	7.78	6.69	6.06	12.09	12.29	4
Reflectance Value for Dolomite (Coarse Grain)	5.8	5.0	4.88	5.96	4.59	2.16

**Table 4.30:** Reflectance Values and Band Math Calculation for Dolomite at a Spectral Signature of 11350 nm. This table presents the reflectance values and band math calculations for Dolomite with fine, medium, and coarse grain sizes. The values were calculated using Nicolet spectral analyzers, with data sourced from the ASTER library embedded in ENVI.

Given the specific absorption features of dolomite, especially around 11.35  $\mu\text{m}$ , as indicated by multiple studies, the following band math expression can be used to detect dolomite:

$$\frac{B5 + B4}{B3}$$

(B5 - B4) captures the difference between the reflectance at 12.09  $\mu\text{m}$  (B5) and 10.49  $\mu\text{m}$  (B4). Since dolomite has a strong absorption around 11.35  $\mu\text{m}$ , we expect a notable decrease in reflectance from B5 to B4. This difference highlights the dolomite signature. (B3) as a normalizing factor ensures that the index is relative to the general reflectance behavior in the mid-infrared range, making the index more robust against other factors like surface conditions or overall brightness.

Dolomite, known for its distinctive spectral signature in the Thermal Infrared Region (TIR), exhibits notable absorption features, particularly around 11.35  $\mu\text{m}$ . However, after resampling the spectral data to the five bands of ECOSTRESS, as shown in Figure 4.98, the expected absorption features of dolomite become less pronounced. Specifically, the reflectance values are relatively flat between 11 and 12 micrometers, masking the distinctive dolomite signature. This lack of resolution in ECOSTRESS between Band 4 and Band 5 makes it difficult to effectively capture the characteristic absorption of dolomite, highlighting a limitation in using ECOSTRESS for detecting this mineral in its purest form.

Given the limitations of ECOSTRESS in capturing dolomite's spectral signature in the TIR range, we turn to EMIT images for more effective detection. Dolomite also has distinct signatures in the Shortwave Infrared (SWIR) range, which EMIT can capture more clearly. However, even after applying color slicing to the EMIT



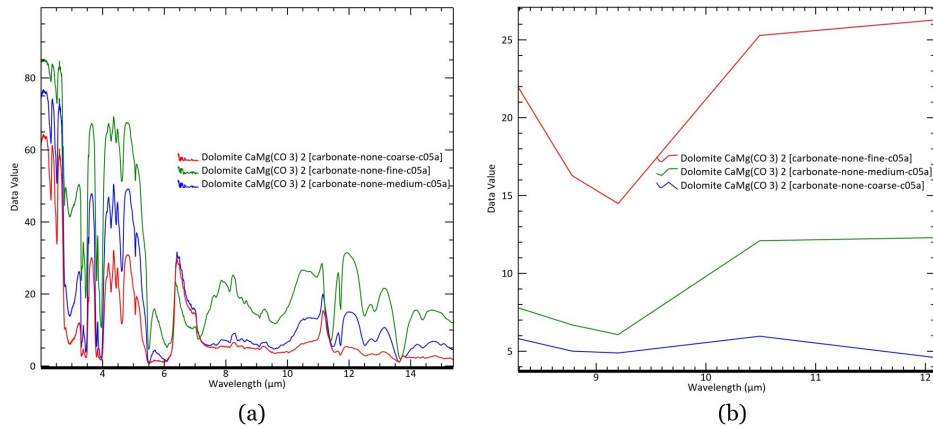


**Figure 4.97:** (a) Spectral Reflectance and (b) Resampled Spectral Reflectance of Dolomite for fine, medium, and coarse grain size, adjusted to the ECOSTRESS sensor resolution.

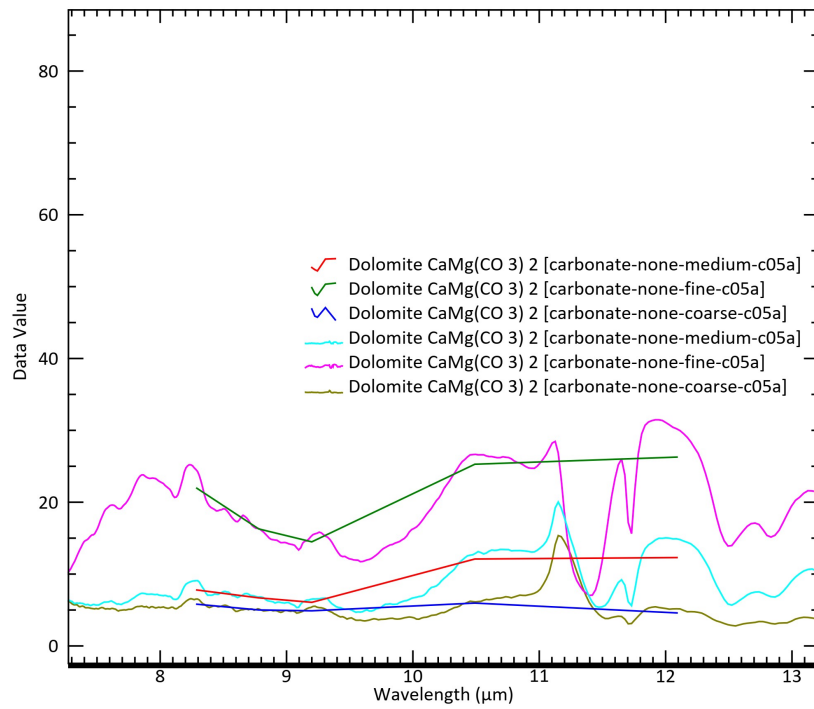


**Figure 4.98:** ECOSTRESS image of Dolomite after application of relative band math at 11350 nm wavelength.

data, the distribution of red colors remains constant and does not reveal significant geological patterns associated with dolomite.

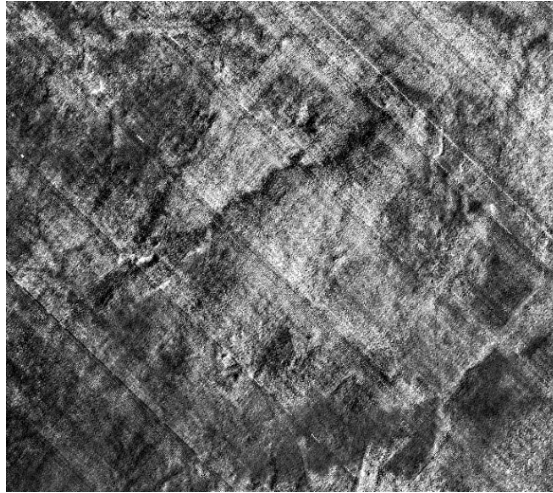


**Figure 4.99:** ECOSTRESS image of Dolomite after application of relative band math at 11430 nm wavelength.

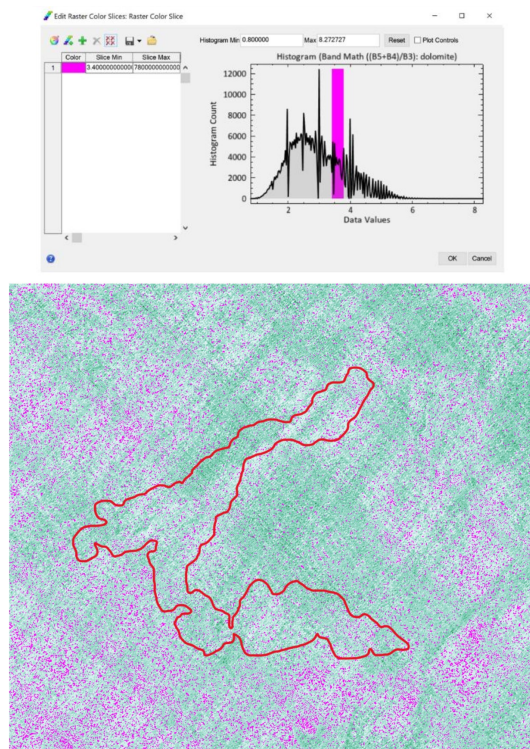


**Figure 4.100:** results of relative band math after applying raster color slice: The red color represents the range between 3.4 - 3.78 corresponding to the presence of the fine grain Calcite.

#### 4.4.4 Calcite In ECOSTRESS

Feature Wavelengths from Resampled Spectra ( $\mu\text{m}$ )	8.29 $\mu\text{m}$	8.78 $\mu\text{m}$	9.20 $\mu\text{m}$	10.49 $\mu\text{m}$	12.09 $\mu\text{m}$	Band Math for Calcite B3 / B5
Equivalent Band in ECOSTRESS	B1	B2	B3	B4	B5	-
Reflectance Value for Calcite (Fine Grain)	22.70	18.91	30.83	38.26	37.62	0.82
Reflectance Value for Calcite (Medium Grain)	7.62	6.31	12.59	18.52	17.37	0.72
Reflectance Value for Calcite (Coarse Grain)	4.94	3.97	6.50	10.44	7.29	0.89

**Table 4.31:** Reflectance Values and Band Math Calculation for Calcite at a Spectral Signature of 11430 nm. This table presents the reflectance values and band math calculations for Calcite with fine, medium, and coarse grain sizes. The values were calculated using Nicolet spectral analyzers, with data sourced from the ASTER library embedded in ENVI.

Given the specific absorption features of calcite, especially around 11.40  $\mu\text{m}$  as indicated by studies, the following band math expression can be used to detect calcite:

$$\frac{B3}{B5}$$

B3 (9.20  $\mu\text{m}$ ) represents a wavelength where calcite has relatively high reflectance before the significant absorption feature kicks in around 11.40  $\mu\text{m}$ . B5 (12.09  $\mu\text{m}$ ) is closer to the 11.40  $\mu\text{m}$  absorption feature. In regions with strong calcite absorption, reflectance here should be lower.

The ratio (B3 / B5) should help distinguish calcite by showing higher values where calcite's reflectance is higher at B3 than B5, highlighting areas where the absorption feature reduces reflectance at longer wavelengths.

However, similar to dolomite, after resampling the spectral data to ECOSTRESS's five available bands, as shown in Figure 4.102, the spectral signature of calcite is not fully captured. Specifically, there is a relatively flat response between 11 and 12 m, which prevents the bands from revealing the expected drop in reflectance associated with calcite's absorption feature. As a result, the characteristic signature of calcite is not as prominent, making detection via ECOSTRESS challenging.

When applying a raster color slice to the ECOSTRESS image (Figure 4.104), the red color distribution (representing values between 0.1 to 0.3 and 0.75 to 0.95) remains constant across the region, failing to highlight the geological variations that should correspond to calcite. This suggests that while ECOSTRESS can provide some insight into calcite's presence, its spectral resolution and sensitivity in the TIR and SWIR regions are not sufficient for effectively distinguishing calcite across the study area. Just as with dolomite, further refinement of processing techniques or the use of additional sensors may be required to improve the detection accuracy for calcite.

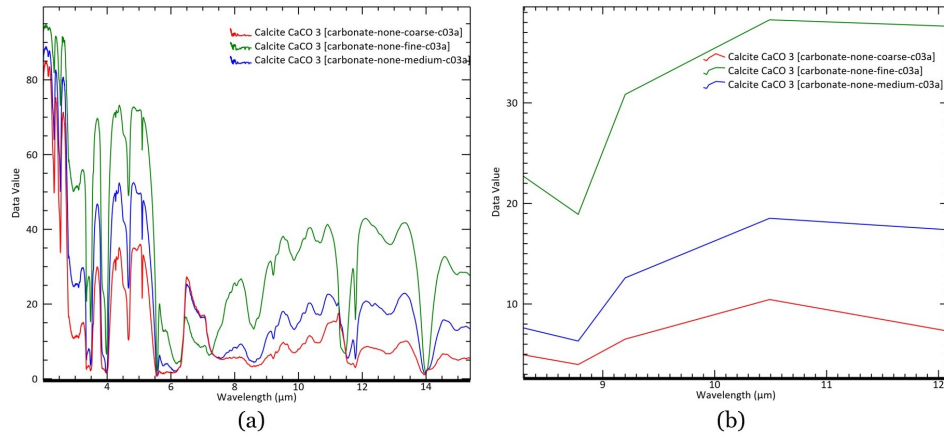


**Figure 4.101:** (a) Spectral Reflectance and (b) Resampled Spectral Reflectance of Calcite for fine, medium, and coarse grain size, adjusted to the ECOSTRESS sensor resolution.

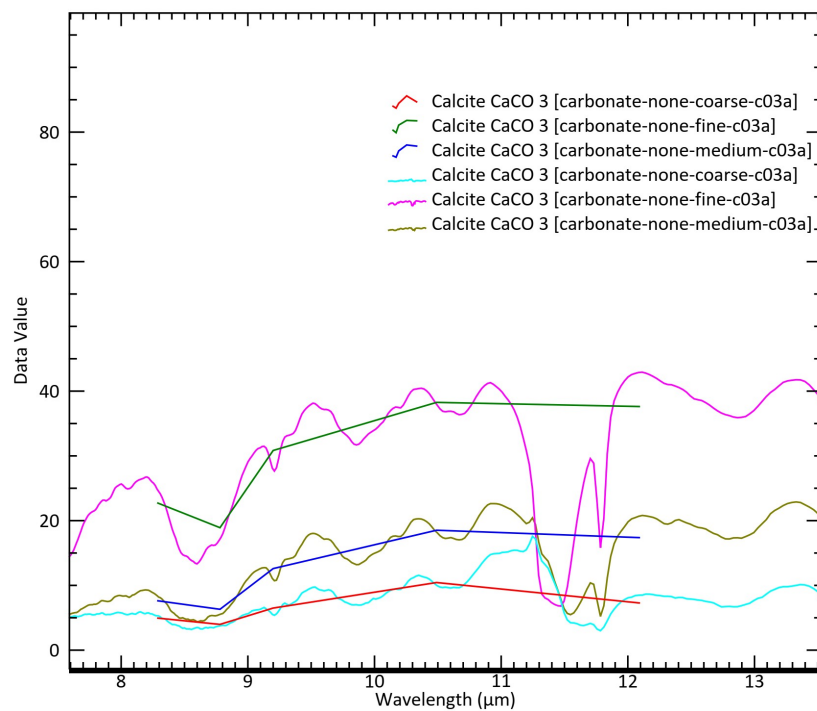


**Figure 4.102:** ECOSTRESS image of Calcite after application of relative band math at 11430 nm wavelength.

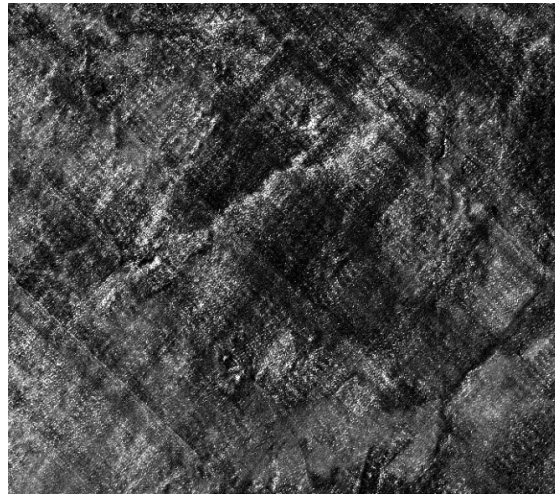


**Figure 4.103:** ECOSTRESS image of Calcite after application of relative band math at 11430 nm wavelength

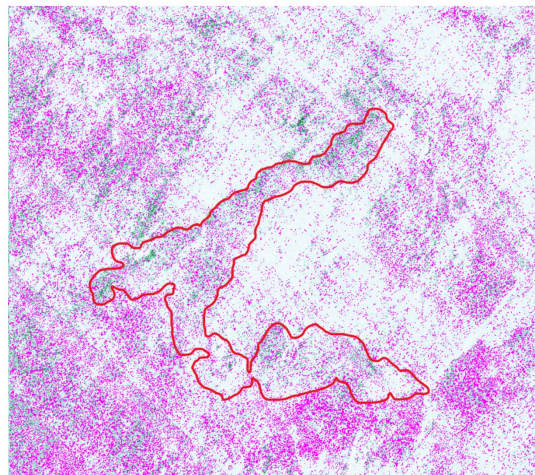
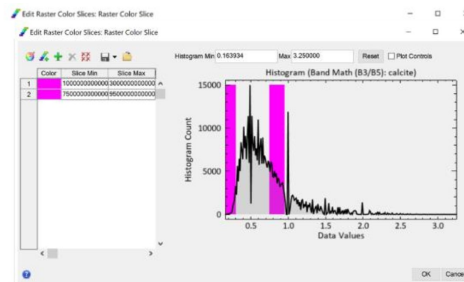


**Figure 4.104:** results of relative band math after applying raster color slice: The red color represents the range between 0.1 to 0.3 and 0.75 to 0.95 corresponding to the presence of the fine grain Calcite.

## Chapter 5

# Conclusion



### 5.0.1 Multitemporal and Vegetation Analysis

This study reveals significant environmental changes in the Khouribga region, emphasizing mining's impact on vegetation and the importance of sustainable solutions.

The 2023 NDVI analysis offers a detailed examination of seasonal vegetation dynamics, highlighting significant fluctuations throughout the year. In the black-and-white NDVI sequence, March 2023 emerges as the month with the highest vegetation density, as indicated by the large extent of light gray and white areas. April still shows healthy vegetation, though not as dense as March. From May onward, the landscape progressively darkens, reflecting a steady decline in vegetation health due to the summer season's heat and dryness, with July showing the most stressed and sparse vegetation.

In colored sliced NDVI, March 2023 stands out as the month with the healthiest and most extensive vegetation, evidenced by the large spread of yellow areas. April, while still showing healthy vegetation, does not reach the same extent of high NDVI values as March. As the months progress, vegetation health declines, with July showing the most stressed and sparse vegetation. This early peak in vegetation in March may be attributed to favorable early spring conditions that promoted strong early growth.

By integrating the NDVI multi-temporal analysis it is evident that the Khouribga phosphate mine area has undergone substantial environmental changes over the past 40 years. The seasonal selection of imagery as in Figure 5.1 to capture peak vegetation stages proved effective in detecting phenological trends. The recurring declines and recoveries of various vegetation types highlight the significant environmental pressures exerted by human activities, particularly mining, on the natural ecosystem. The 2009 image, taken in January, provided a useful temporal continuity despite being outside the preferred peak season and still aligned with general vegetation trends observed in the March-April imagery. The marked increase in bare land, along with the sharp decline in forest and cultivated areas, highlights the extensive impact of human activities, particularly mining. Although some vegetation recovery is visible in the more recent years, continued efforts in environmental management and sustainable land-use practices will be essential to maintain long-term ecosystem health. The results suggest that without significant intervention, the balance between development and environmental preservation will continue to be a challenge for the region.

The multi-temporal analysis of the Khouribga mine region over the past four decades provides clear evidence of escalating desertification processes, predominantly driven by intensive mining activities.

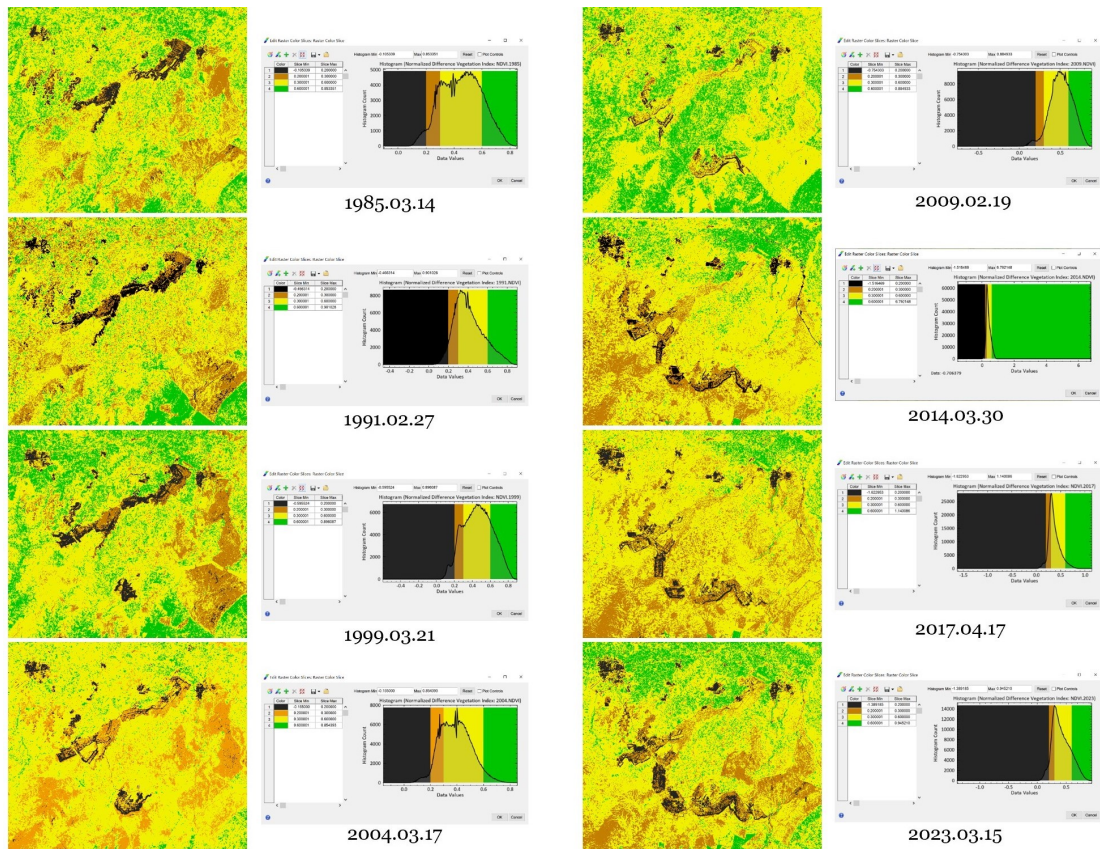


**Figure 5.1:** Multi-temporal NDVI of the Khouribga mine region from 1985 to 2023, showing vegetation and land cover changes

### 5.0.2 Desertification and Land Degradation

The use of MSAVI and Albedo indices allowed for a detailed assessment of vegetation health and surface reflectance, revealing a progressive transition from mild to moderate and severe desertification, particularly in areas of active mining and infrastructure expansion. These findings highlight the critical environmental impact of land use changes associated with resource extraction.

The spatial distribution of desertification, as mapped through the analysis in Figure 5.2, demonstrates a marked increase in severely degraded zones, with significant vegetation loss, as evidenced by the decline in MSAVI values, coupled with rising Albedo values indicative of barren and reflective surfaces. This pattern underscores the vulnerability of semi-arid ecosystems to anthropogenic pressures, leading to a degradation trajectory that threatens the ecological sustainability of the region.



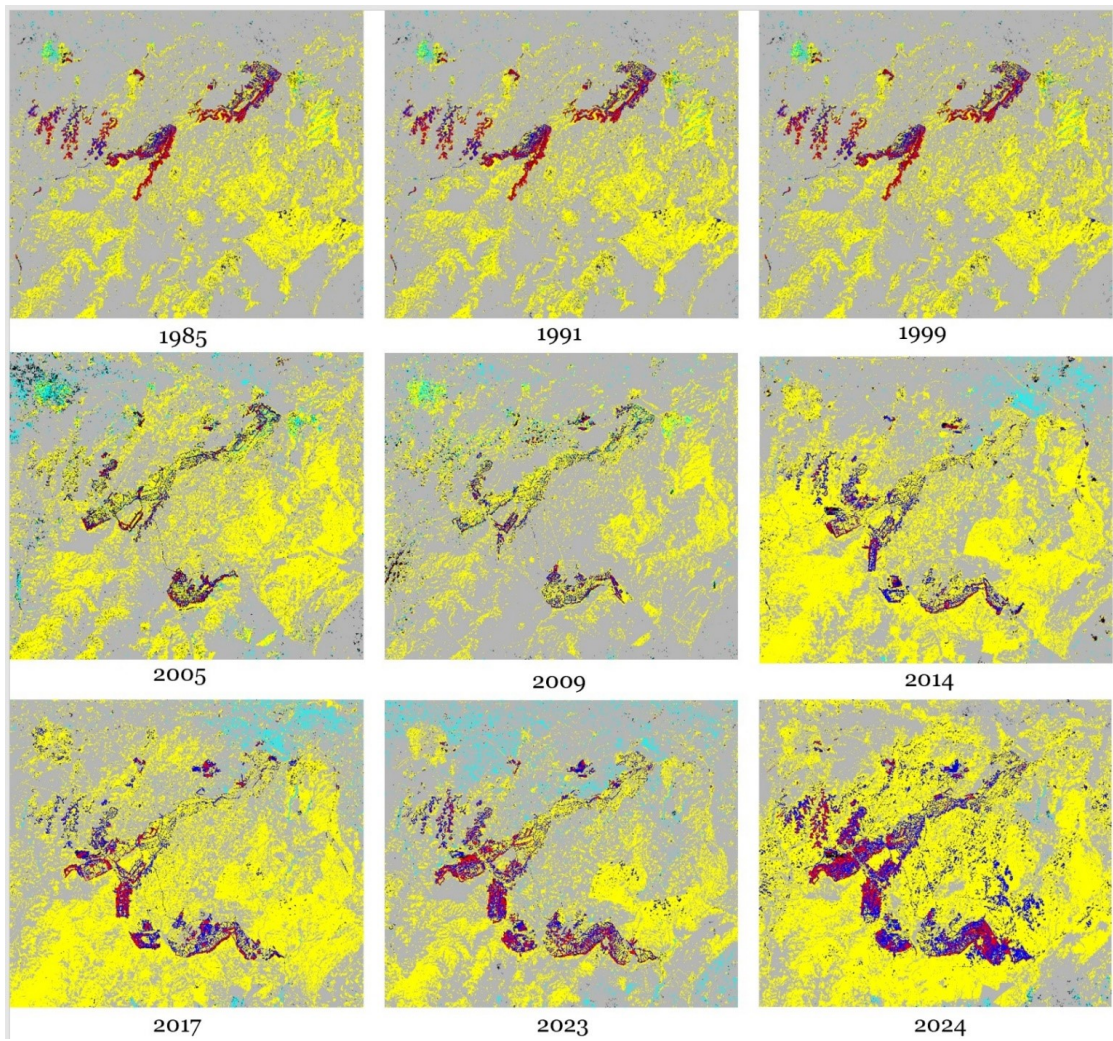


**Figure 5.2:** multi-temporal desertification trend of the Khouribga mine region over the past four decades

Given the observed trends, it is imperative to implement targeted land management strategies aimed at mitigating the environmental degradation caused by mining activities. These strategies should include reforestation efforts, erosion control measures, and the adoption of more sustainable mining practices that minimize land disturbance and promote vegetation recovery. Furthermore, continuous monitoring of desertification dynamics through remote sensing techniques is essential for tracking land cover changes and guiding restoration efforts.

The scatter plots of MSAVI versus Albedo for each selected year highlight changes

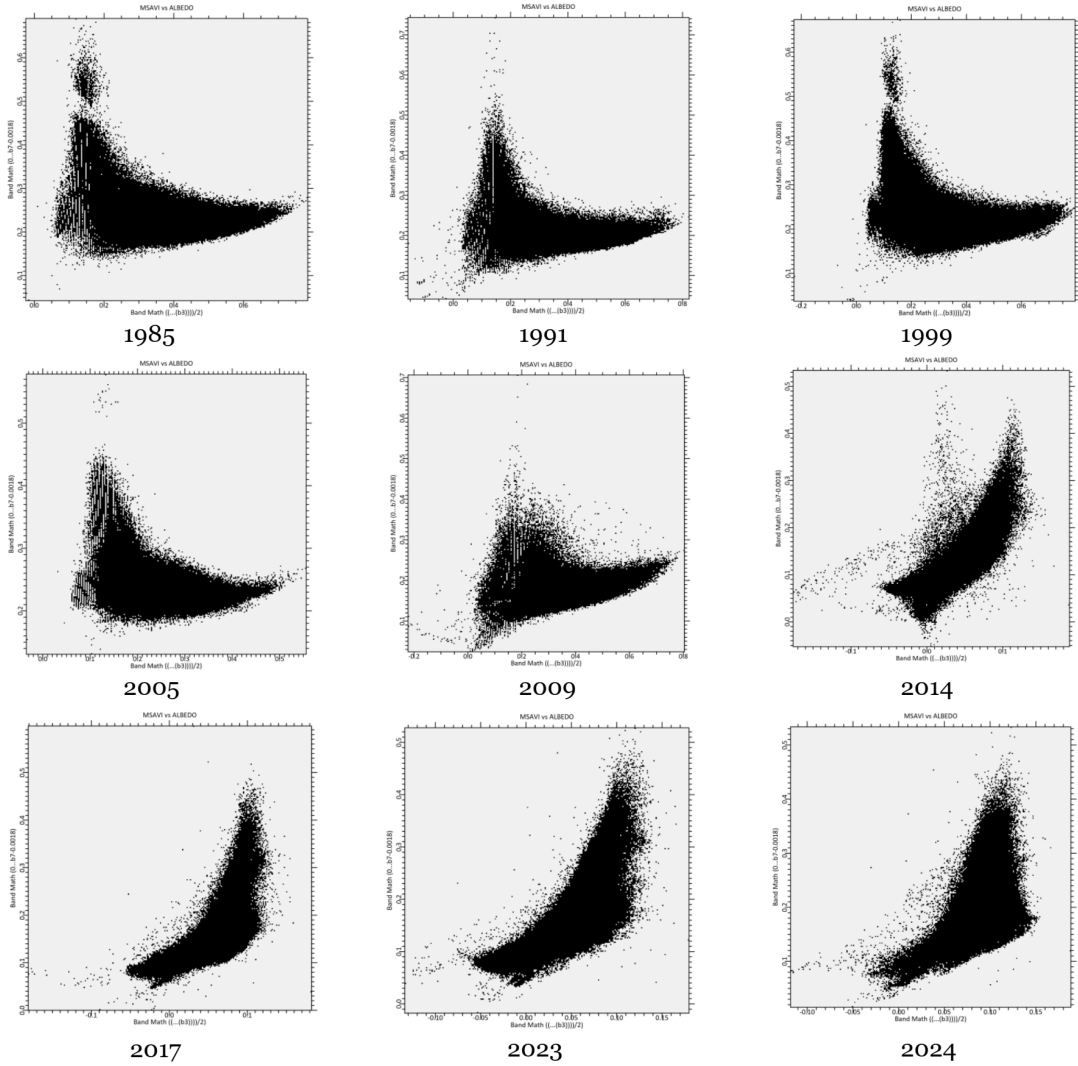


**Figure 5.3:** Scatter plot of multi-temporal desertification trend of Khouribga mine

in land cover and reflectance, which are influenced by both mining expansion and environmental degradation.

**1985-1991:** In the early years, the scatter plot shows a concentrated cluster in the lower to mid-albedo and MSAVI range, suggesting relatively undisturbed land with natural vegetation cover. The compact spread may indicate that vegetation cover and soil were more uniform.

**1999-2005:** During this period, the distribution begins to spread, particularly with points stretching towards higher albedo values. This spread reflects an increase in bare soil and mined areas, which have higher reflectance (albedo) due to reduced vegetation cover. The thinning of the MSAVI values suggests a decline in vegetation health and coverage, likely due to the expansion of mining activities.

**2009-2014:** The scatter further expands toward higher albedo and shows an even more dispersed range of MSAVI values. This change indicates a mix of degraded land and areas with low vegetation health, consistent with intensive mining expansion. The spread towards higher albedo values reflects exposed bare soil and disturbed areas.

**2017-2024:** The most recent years show a marked shift, with clusters shifting towards both high albedo and low MSAVI. This indicates significant land degradation and vegetation loss, with fewer areas showing signs of healthy vegetation. The distribution reflects large expanses of mined land and bare soil, highlighting the intensifying impact of phosphate mining on the environment.

From 1985 to 2024, the scatter plot has a clear progression from clustered, low-albedo, high-vegetation areas toward higher albedo and lower vegetation indices. This trend aligns with mining expansion in the Khouribga region, increasing bare land and reducing vegetation. The increase in albedo and MSAVI reduction over time reflects not only the physical footprint of mining but also the associated impacts on land degradation and vegetation health.

### 5.0.3 Key Findings of NDVI and Desertification Analysis

The study employed NDVI (Normalized Difference Vegetation Index) and MSAVI (Modified Soil Adjusted Vegetation Index) to monitor vegetation health and assess desertification trends in the Khouribga phosphate mine region. A multi-temporal analysis spanning nearly four decades (1985–2023) revealed significant environmental changes attributed to mining activities.

### **1. Seasonal NDVI Dynamics (2023):**

- March emerged as the peak vegetation month, showing the highest NDVI values and dense vegetation coverage, indicating favorable early spring conditions.
- As the months progressed, vegetation health declined sharply due to the summer season's heat and dryness, with July reflecting the most stressed and sparse vegetation.
- The color-sliced NDVI maps highlighted the spatial extent of vegetation, showing progressive reductions in healthy vegetation across seasons.

### **2. Long-Term Vegetation Changes:**

- Over 40 years, the study revealed recurring cycles of vegetation decline and recovery, with significant losses in forest and cultivated land near mining zones.
- By 2023, areas of bare land and urbanization had expanded considerably, emphasizing the ecological strain from mining activities.

### **3. Desertification Patterns (MSAVI and Albedo):**

- MSAVI analysis indicated declining vegetation health, while rising Albedo values highlighted the expansion of barren and reflective surfaces, signaling desertification.
- Scatter plots of MSAVI versus Albedo revealed a clear progression from vegetated areas with low Albedo and high MSAVI values in 1985 to barren, degraded landscapes with high Albedo and low MSAVI in 2023.

### **4. Spatial Desertification Trends:**

- Maps showed a marked increase in severely degraded zones, particularly in areas of active mining and infrastructure development.
- These trends underscore the vulnerability of semi-arid ecosystems to anthropogenic pressures, with significant vegetation loss and land degradation over time.

### **5. Implications for Land Management:**

- The results highlight the urgent need for targeted land management strategies, such as reforestation, erosion control, and sustainable mining practices, to mitigate the environmental impacts of mining.
- Continued remote sensing monitoring is essential for tracking desertification dynamics and guiding restoration efforts.

## 5.0.4 Limitations of NDVI and Desertification Analysis

### 1. Data and Temporal Constraints:

- Limited availability of historical and recent ground truth data hindered the validation of remote sensing findings.
- Temporal gaps in available imagery affected the continuity of multi-decadal analysis, potentially leaving critical events or trends unrecorded.

### 2. Indices' Sensitivity to Environmental Factors:

- NDVI and MSAVI are susceptible to interference from factors like soil brightness, cloud cover, and seasonal variations, which can affect the accuracy of vegetation health assessments.
- Albedo changes, while indicative of desertification, may also result from other surface modifications, such as urbanization or infrastructure development.

### 3. Exclusion of Ground Validation:

- The lack of field-based measurements and calibration limited the ability to directly validate desertification trends, reducing the certainty of observed patterns.

### 4. Limited Spatial and Spectral Resolution:

- While Landsat data provided valuable insights, its spatial and spectral resolution may overlook finer-scale vegetation dynamics or subtle land cover changes.

The analysis emphasizes the critical role of remote sensing tools like NDVI and MSAVI in assessing environmental impacts but underscores the need for integrated approaches combining satellite observations with field data for more robust and accurate monitoring of desertification processes.

### 5.0.5 Mineral Grouping and Shapefile Layout

Organizing shapefiles by mineral family or spectral similarity is essential to streamline the conclusion of the interpretation of mineral distributions and spectral responses across the study area.

**Carbonates:** Calcite and Dolomite

**Clays/Phyllosilicates:** Kaolinite, Illite, Sepiolite, Palygorskite, and Glauconite

**Iron Oxides:** Hematite and Goethite

**Sulfates:** Gypsum

**Phosphates:** Apatite

**Silicates:** Quartz

#### Carbonates Group

Minerals Included: **Calcite and Dolomite**

##### **Spectral Characteristics:**

**Calcite:** Shows a prominent absorption feature around 2330 nm (EMIT Band 263), which is utilized to identify its presence.

**Dolomite:** Exhibits significant absorption around 2308 nm (EMIT Band 260), making it identifiable in similar SWIR wavelengths.

Both minerals can be identified using SWIR-based band math, like the formulas  $B244+B271/B263$  for calcite and  $B246+B268/B260$  for dolomite.

Consistent Mapping: Since calcite and dolomite are both carbonates, this approach ensures that mapping is consistent across similar geological formations where both minerals may co-occur.

**Spectral Overlap:** Even within the carbonate group, there may be overlapping spectral responses, especially in areas with mixed mineral compositions, which could complicate precise identification.

This study performs a comparative analysis between images from ECOSTRESS and EMIT data to assess their effectiveness in detecting calcite and dolomite. EMIT's shortwave infrared (SWIR) data captured the spectral signatures of calcite effectively, with clear distinctions in the spatial distribution of calcite-rich areas after applying spectral feature extraction techniques Figure 5.4 (in red). The EMIT images highlight calcite accurately using its unique spectral features, which makes it valuable for precise mineral mapping.

However, ECOSTRESS, which operates primarily in the thermal infrared (TIR) region and has only five spectral bands, shows limitations in detecting calcite. Specifically, calcite's distinctive TIR spectral feature occurs around 11430 nm, but after resampling, ECOSTRESS's spectral response is flat in this part of the



spectrum. This lack of resolution and sensitivity in the key calcite spectral region results in a homogeneous appearance after color slicing, without the distinct calcite differentiation seen in EMIT data.

On the other hand, dolomite shows more promising results. In the EMIT image, dolomite features (in blue) exhibit a spatial distribution similar to what is partially captured in the ECOSTRESS TIR data. This similarity suggests that EMIT's SWIR data can provide useful complementary insights, especially when used alongside TIR data from ECOSTRESS, for better mapping of dolomite in the target region.

It is important to note that the interpretation of these images was significantly complicated by the presence of artifacts, which affected the overall quality of the data in ECOSTRESS. Nevertheless, despite these challenges, it was still possible to recover useful information regarding the distribution of calcite and dolomite. These findings underscore the potential of integrating TIR and SWIR spectral data from different satellite sources to enhance mineral detection. The limited calcite detection, combined with the challenges posed by data artifacts, highlights the need for further refinement, possibly through the integration of additional datasets or ground-truth verification.

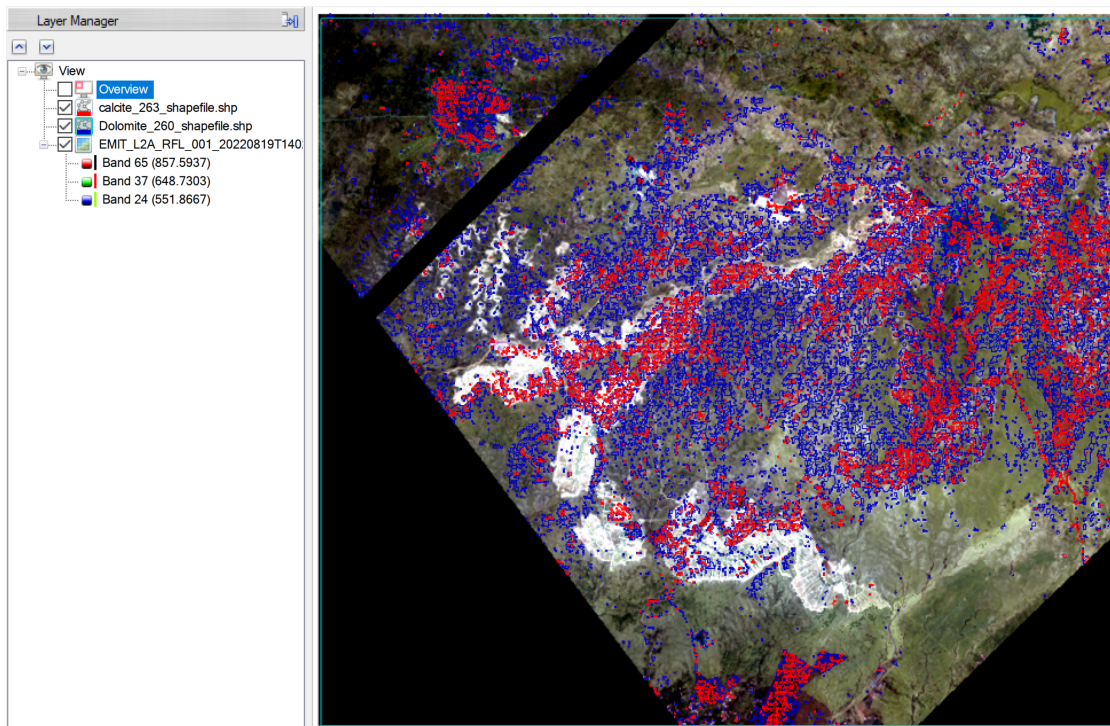


**Figure 5.4:** Calcite (in red) and dolomite (in blue) shapefile layout in EMIT.



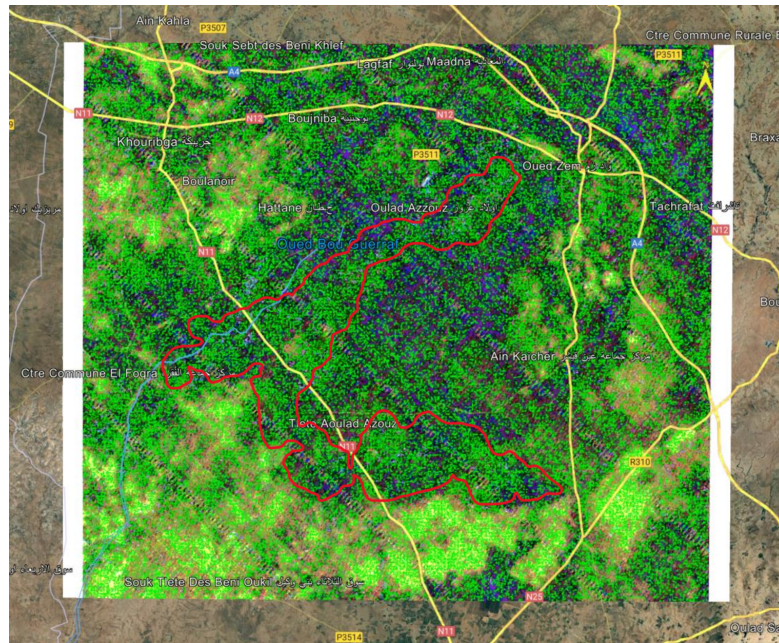


**Figure 5.5:** Shapefile (in green) represents the presence of Calcite in ECOSTRESS.

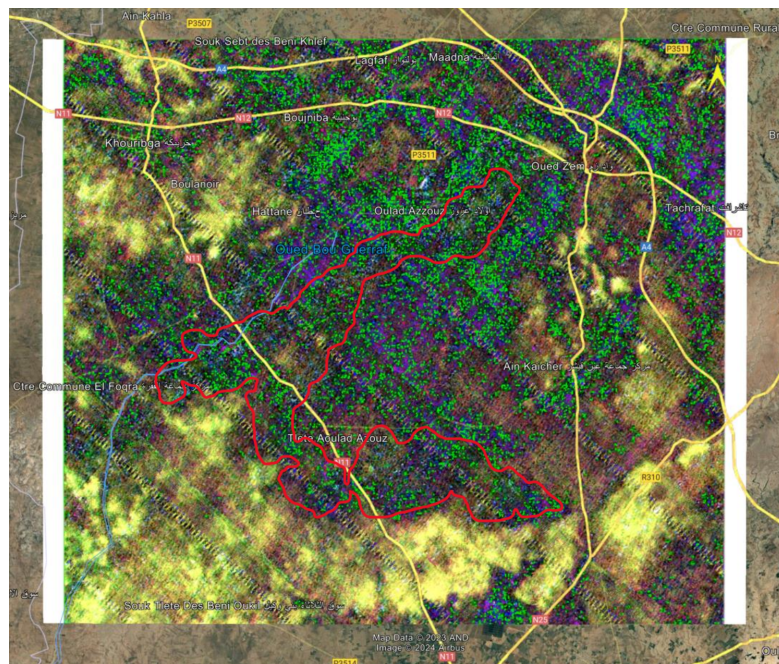


**Figure 5.6:** Shapefile (in green) represents the presence of dolomite in ECOSTRESS.

## Clay Minerals Group

Minerals Included: **Sepiolite, Kaolinite, Illite, Palygorskite Spectral Characteristics:**

**Sepiolite:** Exhibits a strong absorption feature around 2345 nm (EMIT Band 265), which is essential for identifying its presence in the SWIR range. Can be identified using the band math formula  $B244+B271/B263$ , where the absorption feature around 2345 nm is emphasized. This absorption band is particularly useful for distinguishing Sepiolite from other clays.

**Kaolinite:** Displays a characteristic absorption feature around 2200 nm (EMIT Band 248), which is prominent in SWIR data and helps isolate Kaolinite from other clay minerals. Identification is enhanced by the band math formula  $B245+B260/B248$ , which highlights the absorption at 2200 nm.

**Illite:** Has a significant absorption trough around 2211 nm (EMIT Band 247), making it easily identifiable. The trough at this wavelength is a key spectral marker for illite in complex geological environments. The 2211 nm absorption trough is highlighted using the formula  $B236+B256/B247$ , allowing for precise identification of illite in the imagery.

**Palygorskite:** Shows a distinctive absorption feature around 2211 nm (EMIT Band 247), similar to illite but can be separated using additional band math techniques. This feature is crucial for detecting Palygorskite in arid and semi-arid regions. The 2211 nm trough is also emphasized with the band math formula  $B238+B253/B247$ , isolating Palygorskite effectively from other minerals in the area.

**Consistent Mapping:** Since Sepiolite, Kaolinite, Illite, and Palygorskite are all clay minerals, this approach ensures that mapping is consistent across similar geological formations where these minerals may co-occur. Their unique absorption features in the SWIR range allow for accurate mapping and separation of these minerals in remote sensing data.

**Spectral Overlap:** Despite their distinct absorption features, these minerals may exhibit spectral overlap, particularly in regions with mixed mineral compositions. This could complicate the precise identification of individual clay minerals, requiring careful application of band math techniques and, in some cases, additional spectral data or ground truthing for validation.

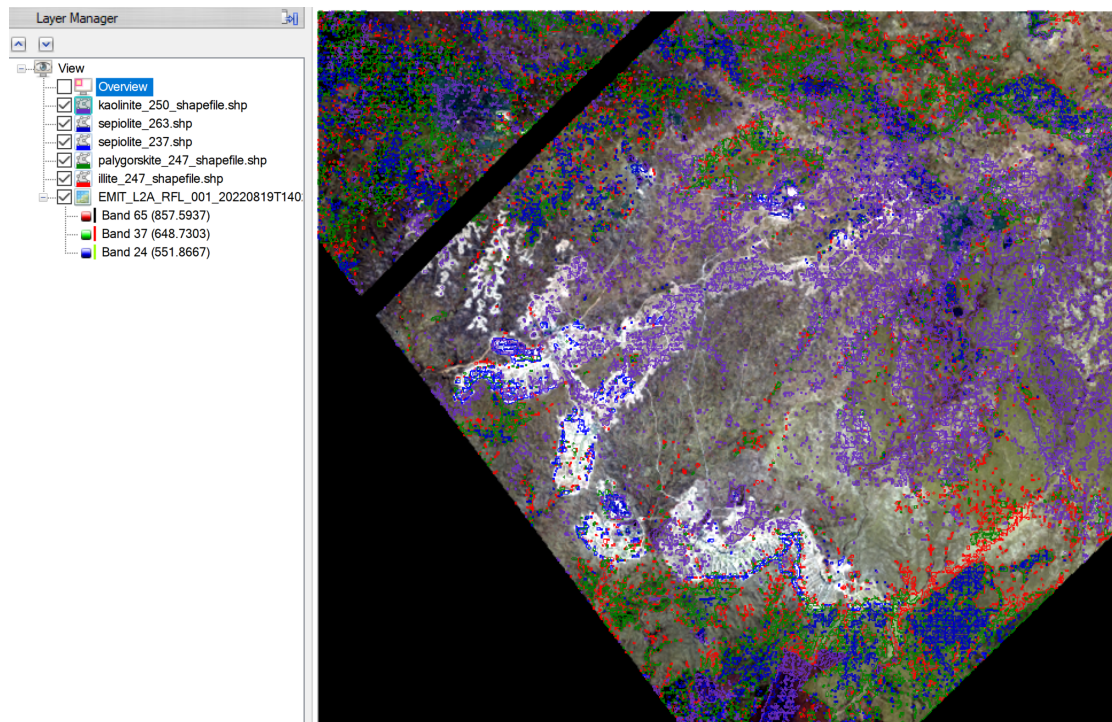


**Figure 5.7:** sepiolite (in blue), kaolinite dolomite (in purple), illite (in red) and palygorskite (in green) shapefile layout in EMIT.

## Iron Oxides Group

Mineral Included: **Hematite and goethite**

### Spectral Characteristics:

**Hematite:** Displays distinct absorption features at 551 nm and 860 nm, corresponding to EMIT Bands 24 and 43. These absorption troughs reflect hematite's unique spectral behavior in the visible and near-infrared regions, enabling effective differentiation from other minerals in natural landscapes.

Identification Using Band Math:

To enhance the identification of hematite, specific band math ratios  $B18 + B29 / B24$  and  $B48 + B88 / B43$  were written to focus on its spectral characteristics.

**Consistent Mapping:** The band math and reflectance ratios applied to hematite ensure consistent mapping of iron oxide-rich regions, capturing spatial distributions with a focus on variations in grain size and composition.

The stability analysis of iron-bearing minerals, particularly hematite and goethite, supports our findings from EMIT-based spectral analysis. According to the stability



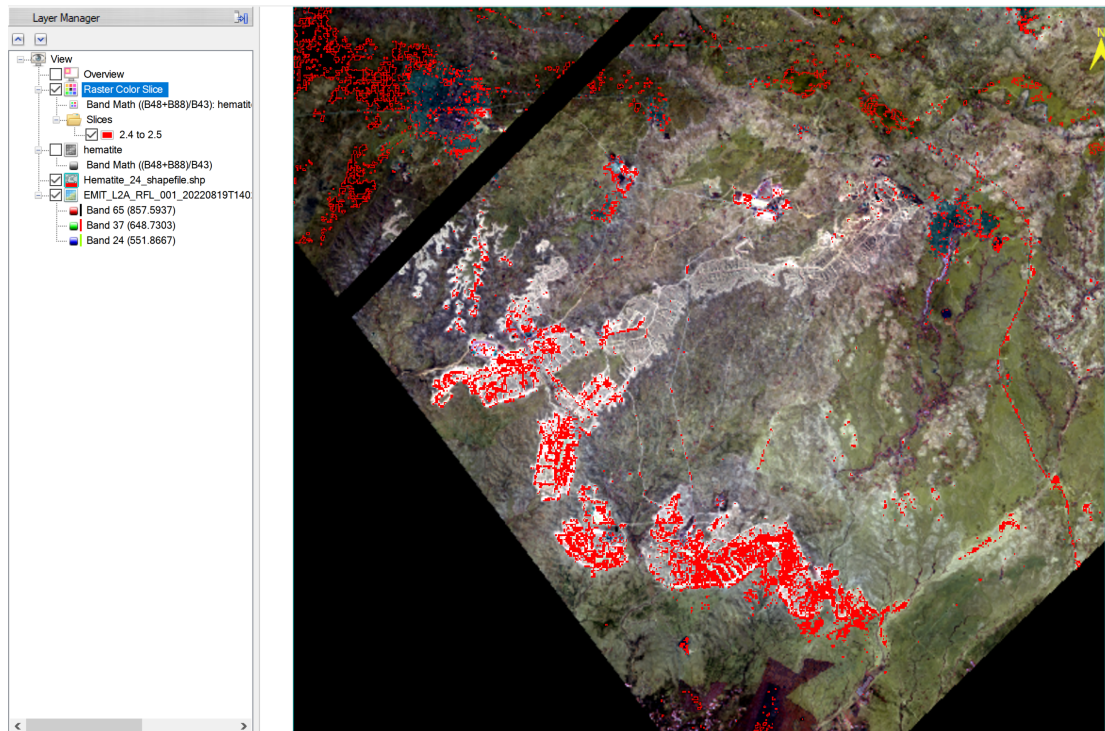


**Figure 5.8:** Shapefile (in red) represents the presence of hematite in EMIT.

diagram, hematite is resilient across a wide temperature range and maintains stability at elevated temperatures, making it well-suited to hot climates like Morocco's. In contrast, goethite is stable only within lower temperatures and narrower pH ranges, and it becomes unstable under high-temperature conditions.

In Morocco's warm environment, goethite likely transforms into hematite over time due to prolonged exposure to high temperatures, which limits the presence of goethite in the region. Consequently, our spectral analysis detected hematite prominently, whereas goethite was notably absent. This outcome aligns with the mineral stability characteristics depicted in the diagram, further emphasizing the influence of climatic factors on mineral composition in phosphate mining areas.

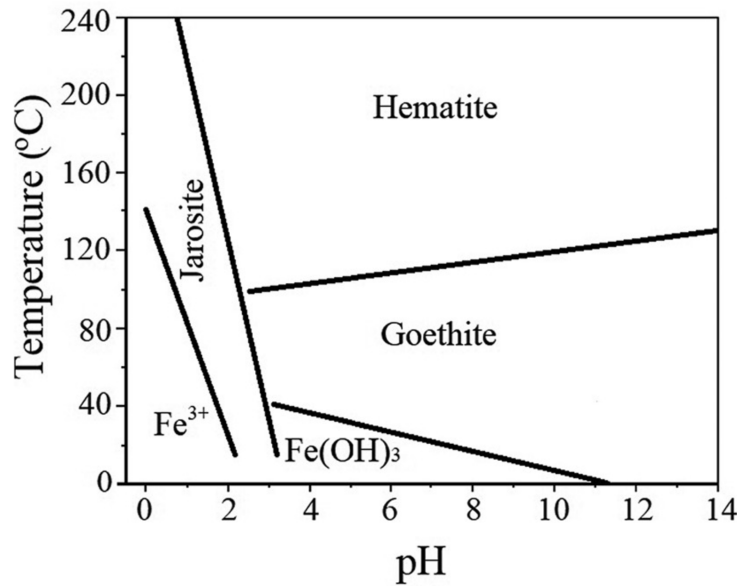


**Figure 5.9:** Stability of hematite, goethite, ferric hydroxide, and hydroxyl salts depending on temperature and pH

### Sulfates group

Mineral Included: **Gypsum**

#### Spectral Characteristics:

**Gypsum:** The spectral analysis of gypsum using EMIT data confirms the presence of distinct absorption features in the Shortwave Infrared (SWIR) range, notably at approximately 1200 nm, 1660 nm, and 2210 nm. Each of these wavelengths corresponds to specific bands in EMIT: Band 111 (1200 nm), Band 173 (1660 nm), and Band 247 (2210 nm), and they serve as key indicators for gypsum detection in the study area.

At 1200 nm, gypsum exhibits a pronounced absorption trough in EMIT Band 111, quantified through the band math ratio  $(B100+B123)/B111$  or the reflectance value ratio  $(R1111+R1275)/R1200$ . These calculations allow for effective differentiation of gypsum-based on this absorption feature, highlighting its potential as a distinguishing spectral signature.

The 1660 nm wavelength, represented by EMIT Band 173, shows a peak in gypsum's spectral profile. This feature is effectively captured by the band ratio  $B173/(B156+B184)$ , distinguishing it from surrounding materials.

**Spectral Overlap:** The third characteristic feature of gypsum, observed at 2210 nm, is represented by a trough in EMIT Band 247. The band math expression  $(B226+B260)/B247$  or the reflectance value ratio  $(R2056+R2308)/2210$  further enhances gypsum's detection, enabling accurate mapping in the study region.

The application of band math and color-slicing techniques across these key wave-

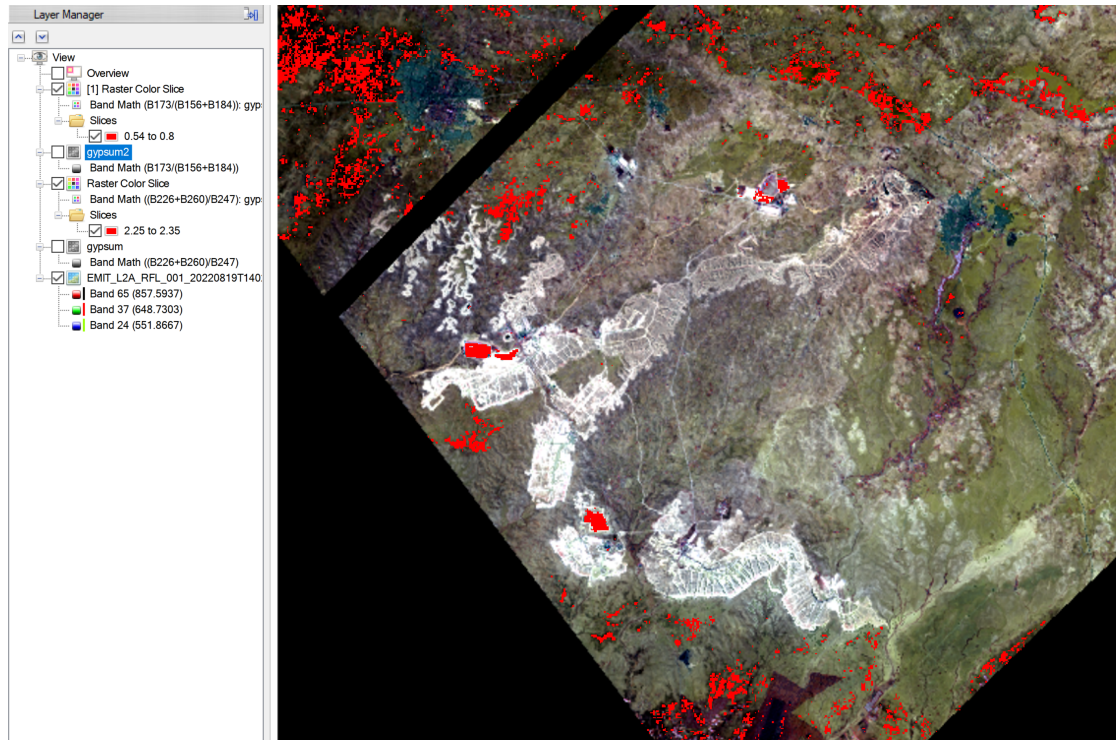


**Figure 5.10:** Shapefile (in red) represents the presence of gypsum in EMIT

lengths allowed for the visualization of gypsum's spatial distribution by grain size. For instance, fine-grain gypsum is highlighted by specific reflectance ranges at each wavelength: 2.05 to 2.09 and 2.24 to 2.3 at 1200 nm, 0.54 to 0.8 at 1660 nm, and 2.25 to 2.35 at 2210 nm. This stratification by grain size offers insights into both the concentration and extent of gypsum deposits in the area.

## Phosphates and Silicates group

Minerals Included: **Apatite and Quartz**

### Spectral Characteristics:

**Apatite:** Apatite, a primary mineral in phosphate deposits, exhibits a key absorption feature around 9160 nm, corresponding to ECOSTRESS Band 3. This feature is essential for detecting Apatite's fine-grain structure in phosphate mining



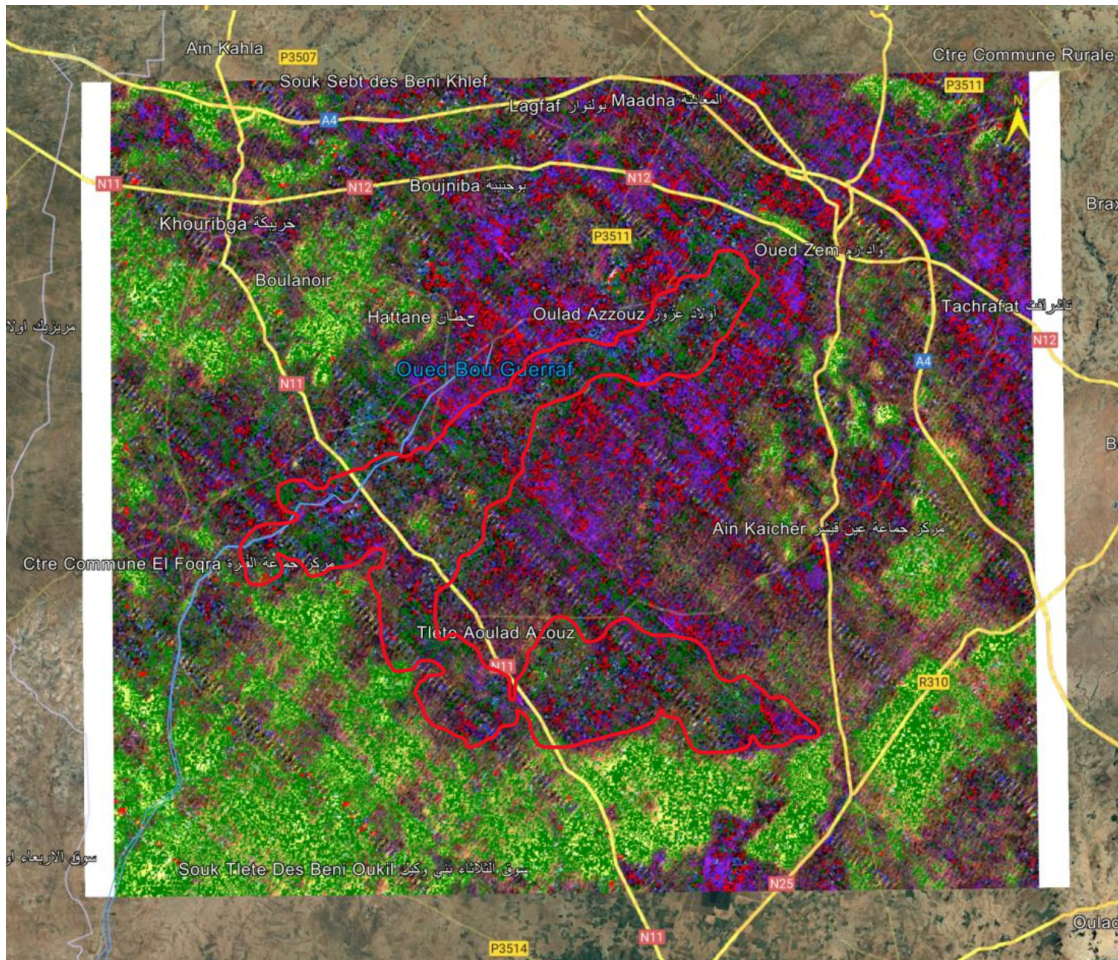


**Figure 5.11:** Apatite (in green) and quartz (in red) in ECOSTRESS

areas. The band math formula  $(B2 + B4)/B3$  highlights this absorption, with grain-size-dependent reflectance variations further refining identification. This spectral signature is particularly effective for distinguishing Apatite in mineral-rich regions.

**Quartz:** Quartz, an abundant and geologically significant mineral, shows a distinct "M-shaped" spectral pattern in the TIR range, with absorption features around 8.78 m and 10.49 m (ECOSTRESS Bands 2 and 4). These reststrahlen bands are emphasized using the formula  $(B2 - B4)/(B2 + B4)$ , capturing Quartz's unique reflectance profile. Variations in peak reflectance with grain size allow for precise differentiation, making Quartz identifiable even in complex geological settings.

**Consistent Mapping:** The application of ECOSTRESS TIR bands to both Apatite and Quartz provides a consistent mapping framework across mineral-rich areas. Their distinctive absorption features allow for reliable separation in regions



where they may co-occur with other TIR-sensitive minerals, ensuring targeted identification of these specific minerals.

**Spectral Overlap:** Though Apatite and Quartz possess unique spectral features, spectral overlap can occur, particularly in fine-grain regions with mixed mineral compositions. Careful application of band math and reflectance analysis across grain sizes helps isolate each mineral with precision.

**Conclusion:** The spectral analysis of Apatite and Quartz using TIR data from ECOSTRESS offers a robust methodology for mineral detection in mining environments. The distinctive absorption features captured through tailored band math formulas facilitate accurate mapping of these minerals, supporting resource management and sustainable mining. This approach, applicable to both phosphate mining and broader mineral exploration, provides insights into mineral distribution and enables informed environmental impact studies.

### 5.0.6 Key Findings of mineral detection

This study demonstrates the innovative application of ECOSTRESS and EMIT sensors, originally designed for environmental monitoring, in mineral detection and environmental impact assessment in the Khouribga phosphate mining region. Despite their design intent, the sensors proved effective in capturing spectral features crucial for identifying and characterizing both ore and host minerals. Key minerals detected included dolomite, calcite, gypsum, sepiolite, kaolinite, illite, palygorskite, glauconite, and hematite.

Mineral	EMIT band math using spectral signature	ECOSTRESS band math using spectral signature
Apatite	✗	✓
Quartz	✗	✓
Dolomite	✓	✓
Calcite	✓	✓
Gypsum	✓	✗
Sepiolite	✓	✗
Kaolinite	✓	✗
Illite	✓	✗
Palygorskite	✓	✗
Glauconite	✓	✗
Hematite	✓	✗

**Figure 5.12:** The capability of various satellites to detect different minerals.

- ECOSTRESS: Its thermal infrared (TIR) capabilities allowed for the detection of minerals with distinct thermal emissivity properties. ECOSTRESS proved effective for detecting Apatite and Quartz, as these minerals lack spectral signatures in the shortwave infrared (SWIR) range but can be identified through their thermal emissivity. However, ECOSTRESS was less effective in detecting Calcite and Dolomite, which have clearer spectral features in SWIR.

- EMIT: Its hyperspectral coverage in the shortwave infrared (SWIR) range enabled detailed mineral characterization, effectively detecting minerals such as Calcite, Dolomite, Gypsum, Sepiolite, Kaolinite, Illite, Palygorskite, Glauconite, and Hematite. However, EMIT was unable to detect Apatite and Quartz because these minerals do not exhibit distinct spectral features in the SWIR range.

The detection capabilities of EMIT and ECOSTRESS complement one another, offering unique strengths in identifying different minerals. While ECOSTRESS excels in detecting minerals with strong thermal emissivity properties, such as Apatite and Quartz, EMIT provides detailed discrimination of minerals with SWIR spectral signatures, such as Calcite and Dolomite.

Furthermore, integrating these satellite data with spectral libraries and band math techniques allowed the mapping of mineral distribution and their association with phosphate deposits. This study also revealed significant environmental impacts, including substantial vegetation loss and land degradation over four decades, driven by mining activities. NDVI, MSAVI, and Albedo analyses highlighted a clear progression toward desertification, emphasizing the vulnerability of semi-arid ecosystems.

### 5.0.7 Limitations of mineral detection

Despite the promising results, the study faced several challenges:

#### 1. Data Validation:

- A lack of publicly available mineralogical and geological data for the Khouribga region restricted the direct validation of findings.
- The absence of ground truthing, such as field sampling and on-site spectral measurements, limited the ability to cross-reference remote sensing results with actual mineral distributions.

#### 2. Sensor Limitations:

- ECOSTRESS: While effective in detecting thermal signatures, its limited spectral resolution reduced the ability to capture finer mineral distinctions, particularly in the thermal infrared range.
- EMIT: Despite its hyperspectral capabilities, differentiating minerals with overlapping spectral features in the SWIR range, such as kaolinite and illite, proved challenging. Atmospheric interference and the complexity of spectral responses

further complicated mineral separation.

### **3. Temporal and Spatial Constraints:**

- Data gaps due to sensor acquisition constraints hindered continuous monitoring of the region, affecting the comprehensiveness of the analysis.
- Variability in spectral signatures due to environmental factors, such as soil moisture and atmospheric conditions, introduced potential inaccuracies.

### **Recommendations**

Future research should prioritize ground truth validation to strengthen the reliability of remote sensing data. While incorporating additional sensors like Landsat and Sentinel could provide complementary spectral and temporal capabilities, their low spectral resolution does not offer significant advantages over the EMIT sensor. A possible direction for further development could be to explore techniques that are more sensitive to the shape of spectral features, rather than just their relative depth. Methods such as Gaussian fitting or polynomial fitting could be tested to improve mineral detection and land degradation assessments. Moreover, integrating field studies with advanced machine learning models could help address spectral ambiguities and enhance the overall accuracy of mineral classification and environmental monitoring.

# Bibliography

- [1] P. Pufahl and L. Groat. «Sedimentary and Igneous Phosphate Deposits: Formation and Exploration: An Invited Paper». In: *Geology, Environmental Science, Economic Geology* 112 (May 2017), pp. 486–516 (cit. on p. 2).
- [2] Gabriel Sophie, Poul Emsbo, Patrick I. McLaughlin, George N. Breit, Edward A. du Bray, and Alan E. Koenig. *Rare earth elements in sedimentary phosphate deposits: Solution to the global REE crisis?* Feb. 2015. DOI: 10.1016/j.gr.2014.10.008 (cit. on p. 2).
- [3] Saba Daneshgar, Arianna Callegari, Andrea G. Capodaglio, and David Vaccari. *The potential phosphorus crisis: Resource conservation and possible escape technologies: A review*. June 2018. DOI: 10.3390/resources7020037 (cit. on pp. 2, 9).
- [4] Dana Cordell and Stuart White. *Peak phosphorus: Clarifying the key issues of a vigorous debate about long-term phosphorus security*. 2011. DOI: 10.3390/su3102027 (cit. on p. 2).
- [5] Radouan El Bamiki, Michel Séranne, Hassane Chellaï, Gilles Merzeraud, Mohamed Marzoqi, and Carmen Melinte-Dobrinescu. «The Moroccan High Atlas phosphate-rich sediments: Unraveling the accumulation and differentiation processes». In: *Sedimentary Geology* (2020), p. 403. DOI: 10.1016/j.sedgeo.2020.105655. URL: <https://hal.umontpellier.fr/hal-02871048> (cit. on pp. 2, 7).
- [6] James Cooper, Rachel Lombardi, David Boardman, and Cynthia Carliell-Marquet. «The future distribution and production of global phosphate rock reserves». In: *Resources, Conservation and Recycling* 57 (Dec. 2011), pp. 78–86. ISSN: 09213449. DOI: 10.1016/j.resconrec.2011.09.009 (cit. on pp. 2, 9).
- [7] Yves Trambly, Wafae Badi, Fatima Driouech, Salaheddine El Adlouni, Luc Neppel, and Eric Servat. «Climate change impacts on extreme precipitation in Morocco». In: *Global and Planetary Change* 82-83 (Feb. 2012), pp. 104–114. ISSN: 09218181. DOI: 10.1016/j.gloplacha.2011.12.002 (cit. on pp. 2, 9).

- 
- [8] Noah S. Diffenbaugh and Filippo Giorgi. «Climate change hotspots in the CMIP5 global climate model ensemble». In: *Climatic Change* 114.3-4 (Oct. 2012), pp. 813–822. ISSN: 01650009. DOI: 10.1007/s10584-012-0570-x (cit. on pp. 2, 9).
- [9] Fatima Driouech, Michel Déqué, and Emilia Sánchez-Gómez. *Weather regimes-Moroccan precipitation link in a regional climate change simulation*. May 2010. DOI: 10.1016/j.gloplacha.2010.03.004 (cit. on pp. 2, 9, 10).
- [10] Reto Knutti, Joeri Rogelj, Jan Sedláček, and Erich M. Fischer. *A scientific critique of the two-degree climate change target*. Jan. 2016. DOI: 10.1038/ngeo2595 (cit. on pp. 2, 10).
- [11] Faten Khelifi, Antonio G. Caporale, Younes Hamed, and Paola Adamo. «Bioaccessibility of potentially toxic metals in soil, sediments and tailings from a north Africa phosphate-mining area: Insight into human health risk assessment». In: *Journal of Environmental Management* 279 (Feb. 2021). ISSN: 10958630. DOI: 10.1016/j.jenvman.2020.111634 (cit. on pp. 3, 4, 11, 12).
- [12] Bilal Boumaza, Tatiana Vladimirovna Chekushina, Rabah Kechiched, Nouara Benabdeslam, Lemya Brahmi, Dmitry Evgenievich Kucher, and Nazih Yacer Rebouh. «Environmental Geochemistry of Potentially Toxic Metals in Phosphate Rocks, Products, and Their Wastes in the Algerian Phosphate Mining Area (Tébessa, NE Algeria)». In: *Minerals* 13.7 (July 2023). ISSN: 2075163X. DOI: 10.3390/min13070853 (cit. on pp. 3, 12).
- [13] Mohammad Al-Hwaiti, Mustafa Al Kuisi, Ghazi Saffarini, and Khitam Alzughoul. «Assessment of elemental distribution and heavy metals contamination in phosphate deposits: Potential health risk assessment of finer-grained size fraction». In: *Environmental Geochemistry and Health* 36.4 (2014), pp. 651–663. ISSN: 02694042. DOI: 10.1007/s10653-013-9587-y (cit. on pp. 3, 12).
- [14] H. Lebrahimi, M. Fekhaoui, A. Bellaouchou, M. Elabidi, and L. Tahri. «Assessment of groundwater quality in Khouribga region, Morocco». In: *Journal of Materials and Environmental Science* 9.1 (2018), pp. 161–171. ISSN: 20282508. DOI: 10.26872/jmes.2018.9.1.20 (cit. on pp. 4, 11).
- [15] J.A Kent. *Phosphorus and Phosphates*. Springer, Boston, MA, Aug. 2015 (cit. on p. 7).
- [16] Muhammad Ouabid, Otmane Raji, Jean-Marie Dautria, Jean-Louis Bodinier, Fleurice Parat, Hicham El Messbahi, Carlos Garrido, Youssef Ahechach, and al Petrological and. «Petrological and geochemical constraints on the origin of apatite ores from Mesozoic alkaline intrusive complexes, Central High-Atlas, Morocco». In: *Ore Geology Reviews* 136 (2021), p. 104250. DOI:

- 10.1016/j.oregeorev.2021.104250{"i"}. URL: <https://hal.science/hal-03437822> (cit. on pp. 7, 9).
- [17] Jo Èrg Trappe. *A nomenclature system for granular phosphate rocks according to depositional texture*. Tech. rep. Institute of Geology, University of Bonn, Nov. 2000. URL: [www.elsevier.com/locate/sedgeo](http://www.elsevier.com/locate/sedgeo) (cit. on p. 7).
- [18] Y. Nathan, J.O Nriagu, and P.B. Moore. *The Mineralogy and Geochemistry of Phosphorites*. In *Phosphate Minerals*; Springer. Berlin/Heidelberg, Germany, 1984, pp. 275–291 (cit. on p. 7).
- [19] Arthur J.G. Notholt. «Phosphorite resources in the Mediterranean (Tethyan) phosphogenic province : a progress report». In: *Sciences Géologiques, bulletins et mémoires* 77 (1985), pp. 9–17 (cit. on p. 7).
- [20] Alain Piqué and Mohamed Knidiri. *Géologie du Maroc les domaines régionaux et leur évolution structurale*. Vol. 1. PUMAG, Marrakech, 1994 (cit. on p. 8).
- [21] Y Nati-Ian 'r, N Benalioulhaj, L L'rrv&r, and J Lucas'. *The geochemistry of cadmium in the phosphate-rich and organic-rich sediments of the Oulad-Abdoun and Timahdit basins (Morocco)*. Tech. rep. 1. 1956, pp. 17–27 (cit. on p. 7).
- [22] Steven J Van Kauwenbergh. *World Phosphate Rock Reserves and Resources*. Tech. rep. 2010. URL: [www.ifdc.org](http://www.ifdc.org) (cit. on p. 7).
- [23] «mcs2021-phosphate». In: () (cit. on p. 8).
- [24] Cheikh Elwali Malainine, Otmame Raji, Muhammad Ouabid, Abdou Khouakhi| Jean Louis Bodinier, Ahmed Laamrani, Hicham El Messbahi, Nasrrddine Youbi, and Moulay Ahmed Boumehdi. «An integrated ASTER-based approach for mapping carbonatite and iron oxide-apatite deposits». In: *Geocarto International* 37.22 (2022), pp. 6579–6601. ISSN: 10106049. DOI: 10.1080/10106049.2021.1953617 (cit. on p. 9).
- [25] Elena Xoplaki et al. «Large-scale atmospheric circulation driving extreme climate events in the mediterranean and its related impacts». In: *The Climate of the Mediterranean Region*. Elsevier Inc., 2012, pp. 347–417. ISBN: 9780124160422. DOI: 10.1016/B978-0-12-416042-2.00006-9 (cit. on p. 10).
- [26] M. G. Donat et al. «Changes in extreme temperature and precipitation in the Arab region: Long-term trends and variability related to ENSO and NAO». In: *International Journal of Climatology* 34.3 (Mar. 2014), pp. 581–592. ISSN: 08998418. DOI: 10.1002/joc.3707 (cit. on p. 10).

- [27] S. Filahi, M. Tanarhte, L. Mouhir, M. El Morhit, and Y. Trambly. «Trends in indices of daily temperature and precipitations extremes in Morocco». In: *Theoretical and Applied Climatology* 124.3-4 (May 2016), pp. 959–972. ISSN: 14344483. DOI: 10.1007/s00704-015-1472-4 (cit. on p. 10).
- [28] F. Driouech, S. Ben Rached, and T. El Hairech. «Climate variability and change in North African countries». In: *Climate Change and Food Security in West Asia and North Africa*. Springer Netherlands, Jan. 2013, pp. 161–172. ISBN: 9789400767515. DOI: 10.1007/978-94-007-6751-5 (cit. on p. 10).
- [29] Dorte Verner, David Tréguer, John Redwood, Jens Christensen, Rachael Mcdonnell, Christine Elbert, Yasuo Konishi, and Saad Belghazi. *CLIMATE VARIABILITY, DROUGHT, AND DROUGHT MANAGEMENT IN MOROCCO'S AGRICULTURAL SECTOR*. Tech. rep. Morocco: world bank group, Oct. 2018 (cit. on p. 10).
- [30] Jon Higgins. *Environmental Aspects of Phosphate and Potash Mining*. Tech. rep. United Nations Environment Programme International Fertilizer Industry Association, 2001. URL: [www.uneptie.org](http://www.uneptie.org) (cit. on p. 11).
- [31] M. Lghoul, A. Maqsoud, R. Hakkou, and A. Kchikach. «Hydrogeochemical behavior around the abandoned Kettara mine site, Morocco». In: *Journal of Geochemical Exploration* 144.PC (2014), pp. 456–467. ISSN: 03756742. DOI: 10.1016/j.gexplo.2013.12.003 (cit. on p. 11).
- [32] S. Rodríguez et al. «Transport of desert dust mixed with North African industrial pollutants in the subtropical Saharan Air Layer». In: *Atmospheric Chemistry and Physics* 11.13 (2011), pp. 6663–6685. ISSN: 16807316. DOI: 10.5194/acp-11-6663-2011 (cit. on p. 11).
- [33] Eduardo Ferreira da Silva, Ammar Mlayah, Celso Gomes, Fernando Noronha, Abdelkrim Charef, Cristina Sequeira, Valdemar Esteves, and Ana Raquel Figueiredo Marques. «Heavy elements in the phosphorite from Kalaat Khasba mine (North-western Tunisia): Potential implications on the environment and human health». In: *Journal of Hazardous Materials* 182.1-3 (Oct. 2010), pp. 232–245. ISSN: 03043894. DOI: 10.1016/j.jhazmat.2010.06.020 (cit. on p. 12).
- [34] Najoua Mghazli, Laila Sbabou, Rachid Hakkou, Ahmed Ouhammou, Mariam El Adnani, and Odile Bruneel. «Description of Microbial Communities of Phosphate Mine Wastes in Morocco, a Semi-Arid Climate, Using High-Throughput Sequencing and Functional Prediction». In: *Frontiers in Microbiology* 12 (July 2021). ISSN: 1664302X. DOI: 10.3389/fmicb.2021.666936 (cit. on p. 12).



- [35] Rachid Hakkou, Mostafa Benzaazoua, and Bruno Bussière. «Valorization of Phosphate Waste Rocks and Sludge from the Moroccan Phosphate Mines: Challenges and Perspectives». In: *Procedia Engineering*. Vol. 138. Elsevier Ltd, 2016, pp. 110–118. DOI: 10.1016/j.proeng.2016.02.068 (cit. on p. 12).
- [36] Bilal Boumaza, Tatiana V. Chekushina, Kirill A. Vorobyev, and Leonid E. Schesnyak. «The heavy metal pollution in groundwater, surface and spring water in phosphorite mining area of Tebessa (Algeria)». In: *Environmental Nanotechnology, Monitoring and Management* 16 (Dec. 2021). ISSN: 22151532. DOI: 10.1016/j.enmm.2021.100591 (cit. on p. 12).
- [37] Zhenhua Wu, Shaogang Lei, Zhengfu Bian, Jiu Huang, and Yong Zhang. «Study of the desertification index based on the albedo-MSAVI feature space for semi-arid steppe region». In: *Environmental Earth Sciences* 78.6 (Mar. 2019). ISSN: 18666299. DOI: 10.1007/s12665-019-8111-9 (cit. on pp. 13, 36, 38).
- [38] D. W. Brickey, J. K. Crowley, and L. C. Rowan. «Analysis of airborne imaging spectrometer data for the Ruby Mountains, Montana, by use of absorption-band depth images». In: *Third Airborne Imaging Spectrometer Data Analysis Workshop, NASA-JPL Publ.* (1987), pp. 143–147 (cit. on p. 14).
- [39] James K. Crowley, David W. Brickey, and Lawrence C. Rowan. «Airborne Imaging Spectrometer Data of the Ruby Mountains, Montana: Mineral Discrimination Using Relative Absorption Band-Depth Images». In: *U.S. Geological Survey* (1989), pp. 121–134 (cit. on p. 14).
- [40] National Aeronautics and Space Administration. «EMIT\_Fact\_Sheet\_FINAL». In: *www.nasa.gov* (2022). URL: <https://earth.jpl.nasa.gov/emit/resources/99/emit-fact-sheet/> (cit. on pp. 15, 16).
- [41] NASA. *EMIT Mission: Destination*. 2024. URL: <https://earth.jpl.nasa.gov/emit/mission/destination/> (cit. on p. 16).
- [42] NASA Jet Propulsion Laboratory. *"EMIT Instrument Overview," Earth Science Division: EMIT*. Nov. 2024. URL: <https://earth.jpl.nasa.gov/emit/instrument/overview/> (cit. on pp. 16, 17).
- [43] U.S. Geological Survey. *"LP DAAC - EMIT Overview,"* Nov. 2024. URL: <https://www.usgs.gov> (cit. on p. 17).
- [44] NASA Jet Propulsion Laboratory. *"ECOSTRESS Science,"* Nov. 2024. URL: <https://ecostress.jpl.nasa.gov/science> (cit. on p. 18).
- [45] NASA Jet Propulsion Laboratory. *"ECOSTRESS Instrument,"* Nov. 2024. URL: <https://ecostress.jpl.nasa.gov/instrument> (cit. on p. 18).

- [46] N. Clavier, A. Mesbah, S. Szenknect, and N. Dacheux. «Monazite, rhabdophane, xenotime & churchite: Vibrational spectroscopy of gadolinium phosphate polymorphs». In: *Spectrochimica Acta - Part A: Molecular and Biomolecular Spectroscopy* 205 (Dec. 2018), pp. 85–94. ISSN: 13861425. DOI: 10.1016/j.saa.2018.07.016 (cit. on pp. 20, 79).
- [47] Nans H. Adler. *INFRARED SPECTRA OF PHOSPHATE MINERALS: SYMMETRY AND SUBSTITUTIONAL EFFECTS IN THE PYROMORPHITE SERIES*. Tech. rep. 1964 (cit. on p. 20).
- [48] Roger N. Clark, Gregg A. Swayze, K. Eric Livo Richard A. Wise, Todd M. Hoefen, Raymond F. Kokaly, and Stephen J. Sutley. *USGS Digital Spectral Library splib06a*. Tech. rep. U.S. Geological Survey, 2007 (cit. on p. 20).
- [49] SuseN J Gerssvt. *Spectral reflectance of-carbonate minerals in the visible and near infrared (0.35-2.55 microns): calcite, aragonite, and dolomite*. Tech. rep. 1986, pp. 151–162 (cit. on p. 20).
- [50] Michael E. Fleet and Xi Liu. «Accommodation of the carbonate ion in fluorapatite synthesized at high pressure». In: *American Mineralogist* 93.8-9 (2008), pp. 1460–1469. ISSN: 0003004X. DOI: 10.2138/am.2008.2786 (cit. on p. 21).
- [51] Motoko Igisu, Yuichiro Ueno, Mie Shimojima, Satoru Nakashima, Stanley M. Awramik, Hiroyuki Ohta, and Shigenori Maruyama. «Micro-FTIR spectroscopic signatures of Bacterial lipids in Proterozoic microfossils». In: *Precambrian Research* 173.1-4 (Sept. 2009), pp. 19–26. ISSN: 03019268. DOI: 10.1016/j.precamres.2009.03.006 (cit. on p. 21).
- [52] H Rubens, Heinrich Rubens, and E F Nichqls. *HEAT RAYS OF GREAT WAVE LENGTH*. Tech. rep. 1897, pp. 418–462 (cit. on p. 21).
- [53] H Ysi and Cal Review. *Infrared Lattice Bands of Quartz*. Tech. rep. 1961 (cit. on pp. 22, 79).
- [54] C K Huang and Paul F Kerr. *INFRARED STUDY OF THE CARBONATE MINERALS*. Tech. rep. new york: columbia university, 1960 (cit. on pp. 23, 24, 79).
- [55] G.R. Hunt, J.W. Salisbury, and C.J. Lehnoff. «Visible and near infrared spectra of minerals and rocks. II. Carbonates». In: *Modern Geology* 2 (Jan. 1971), pp. 195–205 (cit. on pp. 23–25, 79).
- [56] Susan J. Gaffey. *Spectral reflectance of-carbonate minerals in the visible and near infrared (0.35-2.55 microns): calcite, aragonite, and dolomite*. Tech. rep. 1986, pp. 151–162 (cit. on pp. 23, 24).

- [57] F.D. van der Meer. «Sequential indicator conditional simulation and indicator kriging applied to discrimination of dolomitization in GER 63 - channel imaging spectrometer data». In: *Nonrenewable Resources (Springer)* 3.2 (June 1994), pp. 146–164 (cit. on pp. 23, 24).
- [58] Roger N Clark. *USGS Spectroscopy Lab: Spectroscopy of Rocks and Minerals, and Principles of Spectroscopy Spectroscopy of Rocks and Minerals, and Principles of Spectroscopy*. Tech. rep. 1999. URL: <http://speclab.cr.usgs.gov><http://speclab.cr.usgs.gov/PAPERS.refl-mrs/> (cit. on pp. 23, 24).
- [59] F. Bosch Reig, J. V.Gimeno Adelantado, and M. C.M. Moya Moreno. «FTIR quantitative analysis of calcium carbonate (calcite) and silica (quartz) mixtures using the constant ratio method. Application to geological samples». In: *Talanta* 58.4 (Oct. 2002), pp. 811–821. ISSN: 00399140. DOI: 10.1016/S0039-9140(02)00372-7 (cit. on pp. 23, 24, 79).
- [60] James K. Crowley. «Visible and near-infrared (0.4-2.5  $\mu\text{m}$ ) reflectance spectra of playa evaporite minerals». In: *Journal of Geophysical Research* 96 (1991), pp. 16231–16240 (cit. on p. 25).
- [61] N. Serkan Öztan and Mehmet Lutfi Süzen. «Mapping evaporate minerals by ASTER». In: *International Journal of Remote Sensing* 32 (Mar. 2011), pp. 1651–1673 (cit. on p. 25).
- [62] HUNT GR, SALISBURY JW, and LENHOFF CJ. «VISIBLE AND NEAR-INFRARED SPECTRA OF MINERALS AND ROCKS. IV. SULPHIDES AND SULPHATES.» In: *MOD. GEOL* 3 (1971), pp. 1–14 (cit. on pp. 25, 27).
- [63] Raymond F Kokaly and Roger N Clark. *Spectroscopic Determination of Leaf Biochemistry Using Band-Depth Analysis of Absorption Features and Stepwise Multiple Linear Regression The measurement of plant biochemical content by*. Tech. rep. 1999 (cit. on p. 26).
- [64] F. Kühn, K. Oppermann, and B. Hörig. «Hydrocarbon Index - An algorithm for hyperspectral detection of hydrocarbons». In: *International Journal of Remote Sensing* (June 2004), pp. 2467–2473 (cit. on p. 26).
- [65] Janice L. Bishop. «Visible and Near-Infrared Reflectance Spectroscopy». In: *Remote Compositional Analysis*. Cambridge University Press, Nov. 2019, pp. 68–101. DOI: 10.1017/9781316888872.006 (cit. on p. 27).
- [66] Javier García-Rivas, Emilia García-Romero, Ángel Santamaría-López, and Mercedes Suárez. «VNIR-SWIR spectroscopic study of samples from the sepiolite-palygorskite polysomatic series». In: *Revista de la Sociedad Española de Mineralogía* (2022) (cit. on pp. 27, 30, 79).

- [67] Andrea García-Vicente, Adrián Lorenzo, Juan Morales, Emilia García-Romero, and Mercedes Suárez. «Field Spectroscopy Applied to the Kaolinite Polytypes Identification». In: MDPI AG, June 2021, p. 16. DOI: 10.3390/iecms2021-09353 (cit. on pp. 28, 79).
- [68] Mark P Simpson. *Reflectance spectrometry [SWIR] of alteration minerals surrounding the Favona epithermal vein. Waihi vein system, Hauraki Goldfield*. Tech. rep. 2022. URL: <https://www.researchgate.net/publication/282933781> (cit. on pp. 29, 79).
- [69] Arindam Guha, Shovan Lal Chatteraj, Snehamoy Chatterjee, K. Vinod Kumar, P. V.N. Rao, and Ajoy K. Bhaumik. «Reflectance spectroscopy-guided broadband spectral derivative approach to detect glauconite-rich zones in fossiliferous limestone, Kachchh region, Gujarat, India». In: *Ore Geology Reviews* 127 (Dec. 2020). ISSN: 01691368. DOI: 10.1016/j.oregeorev.2020.103825 (cit. on pp. 31, 79).
- [70] Cécile Gomez and Phillipe Lagacherie. «Mapping of Primary Soil Properties Using Optical Visible and Near Infrared (Vis-NIR) Remote Sensing». In: *Land Surface Remote Sensing in Agriculture and Forest*. Elsevier Inc., Sept. 2016, pp. 1–35. ISBN: 9780081011836. DOI: 10.1016/B978-1-78548-103-1.50001-7 (cit. on pp. 32, 79).